Carew, Michael John (2004) ***Controls on Cu-Au mineralisation and Fe oxide metasomatism in the Eastern Fold Belt, N.W. Queensland, Australia.*** **PhD thesis, James Coook University.**

CHAPTER 3:

FLUID –ROCK INTERACTION AND SULPHIDE MINERALISATION WITHIN THE MOUNT FORT CONSTANTINE EXPLORATION LEASE, NW QUEENSLAND, AUSTRALIA

FLUID-ROCK INTERACTION AND SULPHIDE MINERALISATION WITHIN THE MOUNT FORT CONSTANTINE EXPLORATION LEASE, NW QUEENSLAND, AUSTRALIA

3.1. INTRODUCTION

Whole-rock geochemistry of veins and related alteration selvages can provide information regarding mass transfer associated with fluid-rock interaction and what components are added, depleted or recycled within a particular alteration system (Oliver, 1996). Several workers have documented the geochemical mass transfer associated with Na-Ca alteration in the Eastern Fold Belt (EFB) and their relationship to Fe oxide (±Cu-Au) mineralisation (Williams, 1994; Pollard, 2000; Oliver et al., 2004). These studies have shown that components liberated during Na-Ca alteration (e.g. K and Fe) are similar to components gained during Fe oxide metasomatism, particularly peripheral to several of the major IOCG deposits in the district, and also propose various processes in the formation of Fe oxide (±Cu-Au) mineralisation in the EFB.

Na-Ca veins and alteration within the FC12 prospect are particularly interesting due to their chalcopyrite content, which is scarce in most other Na-Ca alteration assemblages in the district. The previous chapter demonstrated that these Na-Ca alteration assemblages are similar to pre-mineralisation alteration assemblages at the Ernest Henry (Cu-Au) deposit, although the genetic relationship between these two alteration types is not well understood. This chapter focuses on the mass transfer associated with weakly mineralised Na-Ca alteration at the FC12 prospect via a combination of Gresens analysis, isocon diagrams and elemental profiling across vein and alteration interfaces. These results are then compared with Na-Ca alteration systems from elsewhere in the EFB.

3.2. PROCESSES ASSOCIATED WITH MASS TRANSFER: OPEN Vs CLOSED SYSTEMS

The mineral assemblages and chemical composition of veins and their associated alteration selvages can be controlled by a number of factors including vein geometry, temperature, pressure and the type of fluid-rock interaction (Fig. 3.1). Based on these above factors, Oliver (1996) categorised differing scenarios related to fluid-rock

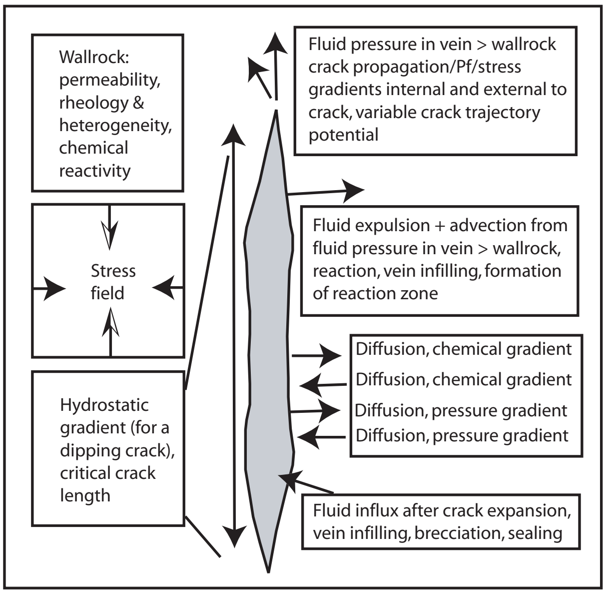

Figure 3.1: Factors and processes acting around fluid-filled cracks that influence propagation, termination, vein infilling and mass transfer to produce wall rock alteration (from Oliver and Bons, 2001)

interaction in metamorphic terrains. Two main subgroups of the Oliver (1996) classification are pertinent here: open system and closed system veining and alteration. These systems refer to whether chemical components within the vein or alteration halo are derived locally (closed system; millimetre to centimetre scale) or externally (open system; metre to kilometre scale). A brief summary of these fractured (veined) systems is provided below.

3.2.1 Closed systems

Closed system (fractured)

These systems refer to mass transfer over millimetre to centimetre scales, where fluid and/or mass are derived either from local devolatilisation or solution transfer (Oliver, 1996). Examples of fractured closed systems occur across a large range of metamorphic grades, e.g. lower greenschist (Cartwright et al., 1994; central Australia) to eclogite facies (Selverstone et al., 1992; Alpine subduction zone).

Diffusion is the dominant process whereby components become mobile in closed system situations, and can be driven by temperature, pressure and/or chemical gradients. A fluid in chemical disequilibrium with the host rock can cause local mass transfer diffusion if the fluid is present within the fracture for a sufficient amount of time (Oliver and Bons, 2001). Changes in pressure associated with heterogeneous layering, fluid-filled cracks and/or between individual grains can cause local diffusion of mobile components (e.g. silica and carbonate), resulting in depleted zones within the wall rock (Oliver, 1996; Oliver and Bons, 2001). In fractured systems, this may result in mass balance, whereby mass loss from the alteration selvage is proportional to mass gain within the vein (Oliver, 1996).

3.2.2 Open systems

Open system fractured, closed wall rocks

These systems refer to the infiltration of externally-derived fluids through fractures where no isotopic or chemical interaction with the surrounding wall rock is observed. This situation can arise when fluid infiltration is rapid and reaction with the wall rock is limited, and is particularly common where brittle fracturing is prominent and fluid pressures are high (Oliver, 1996).

Open system fractured, partly open system wall rocks

When the rate of fluid flow is reduced enough, or when rocks are permeable or chemically reactive, an externally derived fluid is able to react with the surrounding wall rock, resulting in alteration selvages that are isotopically and mineralogically distinct from the surrounding wall rock. This may result from infiltration of fluid into or out of the wall rock (advection) and/or diffusion across the fracture / wall rock interface (Oliver, 1996). The size of the alteration selvage is predominately governed by the degree of chemical disequilibrium between the fluid and the host rock and the rate of fluid flow or diffusive mass transfer through the wall rocks. These processes are particularly important for the deposition of vein-style or shear-hosted epigenetic ore, where direct wall rock interaction (e.g. redox) or changes in fluid state and composition are all important mechanisms. Examples of these veins have been well documented in the EFB by numerous workers (e.g. Oliver et al., 1993 and de Jong and Williams, 1995).

3.3. Na-Ca ALTERATION WITHIN THE FC12 PROSPECT

The overall spatial distribution and composition of Na-Ca veining within the FC12 prospect is discussed in detail in chapter 2, and the location of each sample is presented in figure 3.2 in this chapter. Unfortunately, due to the pervasive and intense nature of alteration at FC4NW, no samples were analysed from FC4NW. A description of the mineralogy and location of each sample from FC12 is presented in table 3.1. Na-Ca alteration and veining affects coarse-grained tholeiitic gabbroic rocks in samples FTCD249/86 (249/86, refers to 249 metres down hole FTCD1086), FTCD262.3/86 and FTCD203/86, whereas for sample FTCD346.9/82, the host rock is a medium-grained gabbro (Fig. 3.3, 3.4). Both rock types have a similar mineralogy, except the medium-grained gabbro contains approximately 40 modal % orthopyroxene, which is rare or absent in the coarser-grained varieties (Fig. 3.4a). The alteration selvage associated with veining is typically green (chlorite), although pink coloured patches and bands are also observed in most samples (Fig. 3.3). In thin section, the alteration selvage is dominated by chlorite replacing primary biotite, clinopyroxene and orthopyroxene, albitic plagioclase replacing primary plagioclase and titanite replacing ilmenite (Fig. 3.3). The veins themselves all contain similar mineral assemblages, however thin sections show that the proportions of these minerals vary.

	Rock type	***Location***	***Sample component***	***Mineral assemblages***
FTCD246/26	Coarse-grained tholeiitic gabbro	Hole No: FTCD1086 246 m depth	Unaltered rock	Apatite, biotite, clinopyroxene, hornblende, ilmentite, magnetite, pyrite, chalcopyrite
		Hole No: FTCD1086 248.2 m depth	Alteration selvage	Chlorite, (clinopyroxene), titanite, albite, quartz, hematitic albite, biotite, magnetite, (ilmenite), actinolite
		Hole No: FTCD1086 248.2 m depth	Vein	Calcite, actinolite, titanite, albite, magnetite
FTCD262.3/86	Coarse-grained tholeiitic gabbro	Hole No: FTCD1086 262.3 m depth	Unaltered rock	Clinopyroxene, biotite, quartz, ilmenite, magnetite, pyrite, chalcopyrite
		Hole No: FTCD1086 265.4 m depth	Alteration selvage	Chlorite, muscovite, hematitic albite, actinolite, magnetite, pyrite, titanite
		Hole No: FTCD1086 265.4 m depth	Vein	Albite, specular hematite, calcite, actinolite, titanite, magnetite, pyrite, chalcopyrite
FTCD346.9/82	Medium-grained tholeiitic gabbro	Hole No: FTCD1082 346.9 m depth	Unaltered rock	Orthopyroxene, biotite, ilmenite, magnetite, pyrite, plagioclase
		Hole No: FTCD1082 346 m depth	Alteration selvage	Albite, chlorite, actinolite, titanite, magnetite, pyrite
		Hole No: FTCD1082 346 m dep	Vein	Calcite, actinolite, titanite, apatite, albite, magnetite, pyrite, chalcopyrite
FTCD203/86	Coarse-grained tholeiitic gabbro	Hole No: FTCD1086 203 m depth	Unaltered rock	Clinopyroxene, orthopyroxene, biotite, magnetite, ilmenite, pyrite.
		Hole No: FTCD1086 209.8 m depth	Alteration selvage	Chlorite, actinolite, hematitic albite, titanite, muscovite, magnetite, ilmenite, pyrite
		Hole No: FTCD1086 209.8 m depth	Vein	Calcite, actinolite, albite, titanite, magnetite, pyrite, chalcopyrite

Table 3.1: Description of samples used in this study including drill hole number and depth, host rock type, and the mineralogy of each sample component. Note the 6.8 m interval between the unaltered and altered rock for sample FTCD203/86 due to poor core yield.

These veins typically exhibit an elongate, blocky appearance with large crystals of actinolite ± magnetite ± titanite on the vein margins and calcite ± specular hematite ± albite ± pyrite ± chalcopyrite within the central part of the vein (Fig. 3.3b, c, 4b, d). The presence of magnetite, actinolite and titanite at the vein margins may indicate small scale diffusional processes from the wall rock into the vein. This is especially pertinent for titanite, because Ti is typically immobile in aqueous solution except those containing high fluoride (Goldschmidt, 1958). Crystals can measure up to 1 cm in diameter suggesting that the fracture containing the vein was open for a significant period of time (*c.f.* Oliver and Bons,

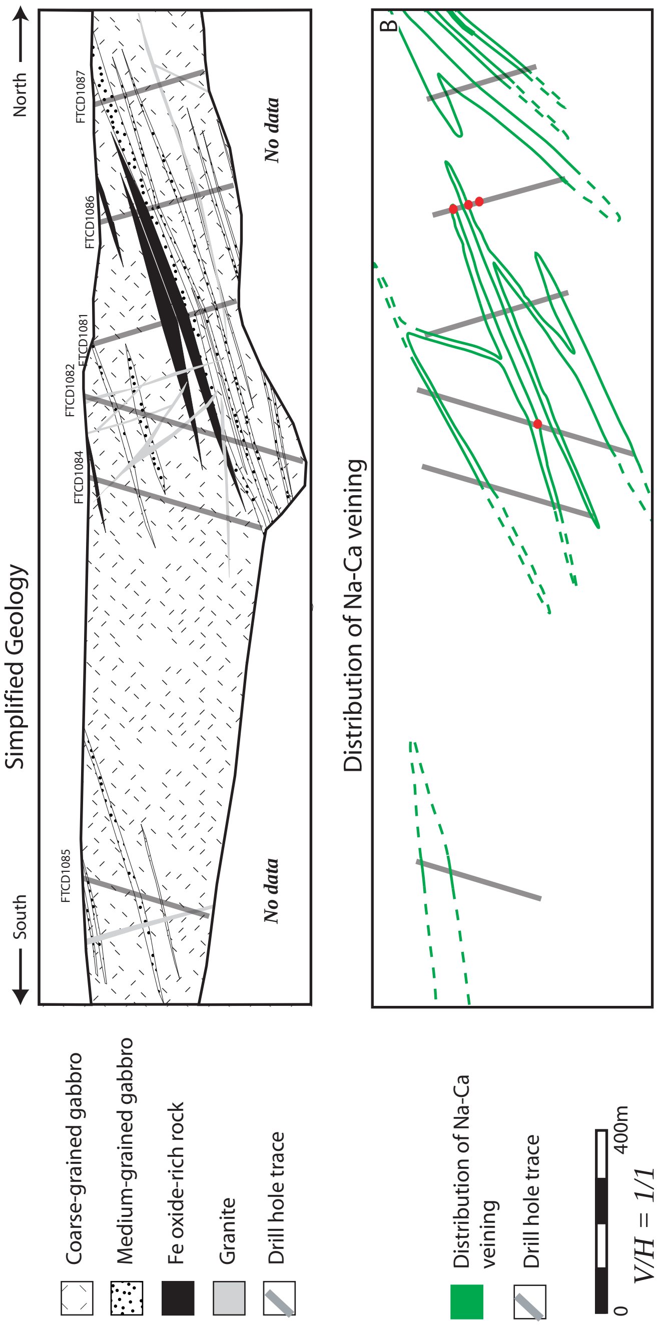

Figure 3.2: Interpreted geological cross-section showing the distribution of rock types and Na-Ca alteration and veining in diamond drill core at the FC12 prospect. A) The dominant rock type at FC12 is coarse-grained tholeiitic gabbro intercalated with equigranular medium-grained gabbro and Fe oxide-rich rocks. Variably albitised felsic igneous rocks are cutting each of these rock types. B) Na-Ca veining and related alteration is more prominent toward the north. These veins commonly contain visible pyrite and chalcopyrite that occur within the central part of the veins. The red dots on the cross-section indicate the location of samples used in this study.

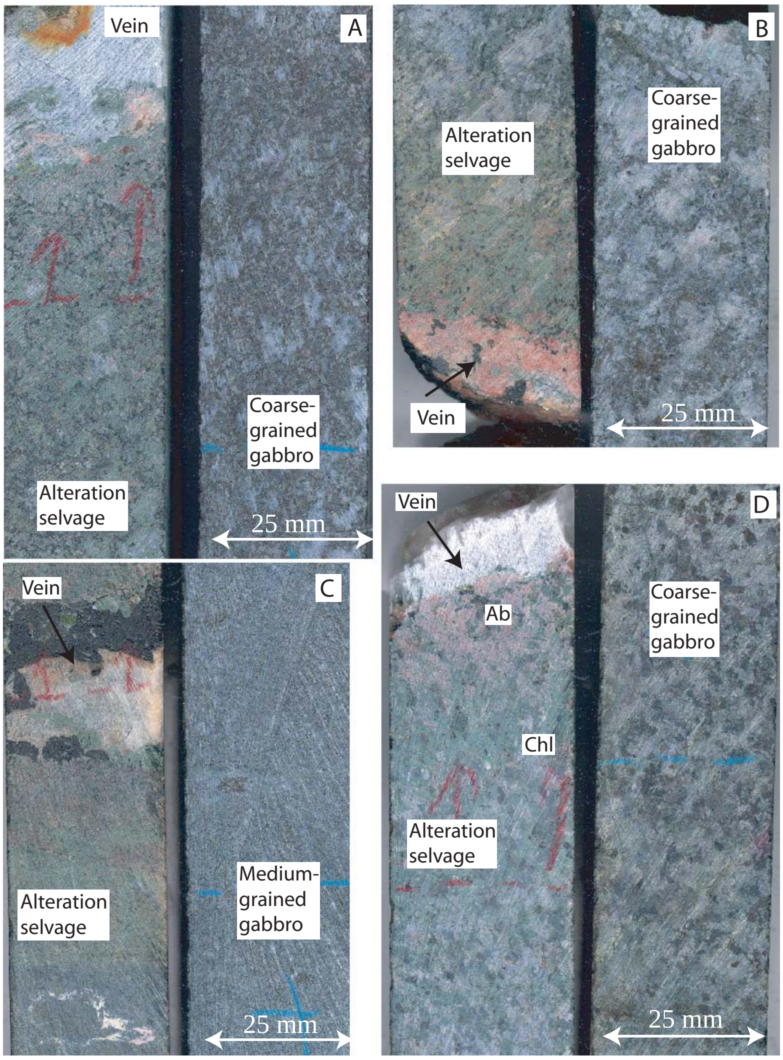

Figure 3.3: Photographs of gabbroic rocks from the FC12 prospect cut by Na-Ca veining and alteration. Photographs here represent the samples used in this study.
A) Coarse-grained gabbroic rock cut by actinolite + calcite + albite + chalcopyrite + pyrite vein. The alteration selvage is dominated by chlorite after clinopyroxene, orthopyroxene and biotite. FTCD1086. 248.2 m (altered rock) and 249 m (unaltered rock).
B) Coarse-grained gabbroic rock cut by albite + calcite + magnetite + hematite + pyrite + chalcopyrite. Alteration selvage associated with vein is composed of chlorite and minor albite. FTCD1086. 265.4 m (altered rock) and 262.3 m (unaltered rock).
C) Medium-grained gabbroic rock cut by calcite + albite + actinolite + magnetite vein and chlorite + albite alteration. FTCD1082. 347 m (altered rock) and 346.9 m (unaltered rock).
D) Coarse-grained gabbroic rocks cut by calcite + actinolite vein and chlorite + albite alteration. Note the alteration zoning where albite occurs adjacent to the vein whereas chlorite is more pronounced further away from the vein. FTCD1086. 209.8 m (altered rock) and 203 m (unaltered rock). Abbreviations: Chl=chlorite, ab=albite. Abbreviations after Kretz (1983).

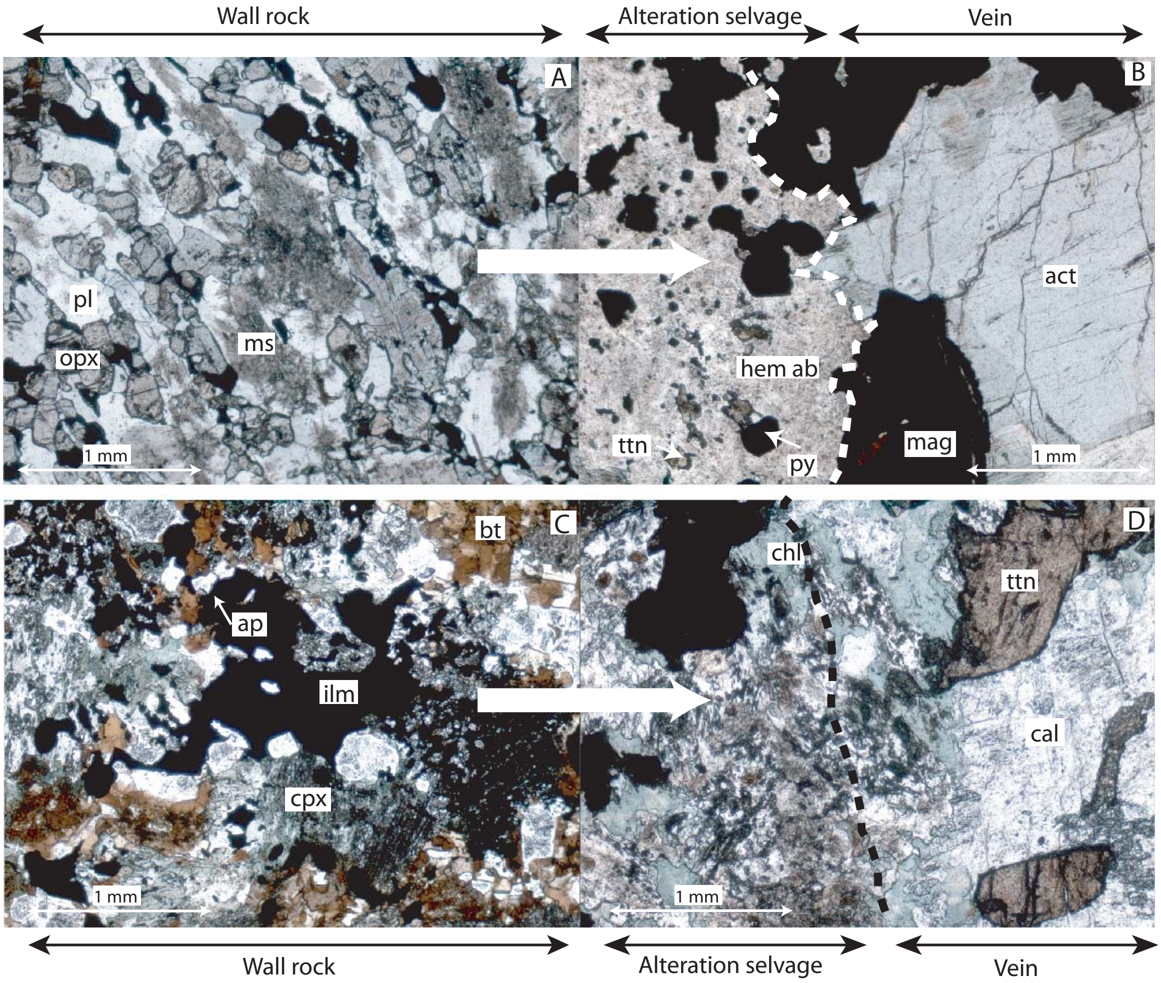

Figure 3.4: Photomicrographs of unaltered gabbroic rocks and their altered equivalent associated veins.

A) Medium-grained gabbroic rock with orthopyroxene, plagioclase magnetite and ilmenite (and minor muscovite). Note the distinct foliation in this sample. FTCD1082. 346.9 m.

B) Altered equivalent of (A) with hematite-stained albite and chlorite in the alteration selvage and actinolite + magnetite + calcite in the vein. Note the large size of the crystals in the vein and the breakdown of ilmenite to titanite in the alteration selvage. White line represents the boundary between the wall rock and the vein. FTCD1082. 347 m.

C) Coarse-grained gabbroic rock composed of biotite + ilmenite + magnetite + apatite + clinopyroxene. FTCD1086. 249 m.

D) Altered equivalent of (C) with chlorite + albite in the alteration selvage and large titanite and calcite crystals in the vein. Black line represents the boundary between the wall rock and the vein. FTCD1086. 248.2 m. Abbreviations: Hem ab=hematised albite, ttn=titanite, py=pyrite, mag=magnetite, act=actinolite, cal=calcite, chl=chlorite, ms=muscovite, bt=biotite, pl=plagioclase, opx=orthopyroxene, cpx=clinopyroxene, ap=apatite, ilm=ilmenite. Abbreviations after Kretz (1983).

2001). The occurrence of large amphibole, clinopyroxene and magnetite crystals in Na±Ca veins has been documented in calc-silicate and metadolerite rocks within the Mary Kathleen Fold Belt (Oliver and Bons, 2001), as well as other localities throughout the Eastern Fold Belt (e.g. de Jong and Williams, 1995), although sulphides are relatively uncommon within these veins.

3.4. ANALYTICAL TECHNIQUES

3.4.1 Samples and major/trace element geochemistry

In this study, 4 pairs of altered rock and their unaltered equivalents were analysed in addition to the associated veins (Table 3.1). Samples 246/86, 262.3/862 and 203/86 were collected from the FTCD1086 diamond drill hole within the FC12 prospect, while sample 346.9/82 was collected from the FTCD1082 diamond drill hole. Samples were chosen according to how representative they were of typical Na-Ca assemblages at FC12 and whether any other alteration phases had effected the rocks. The unaltered rock samples and their altered equivalents were each analysed for their major and trace element geochemistry. With the exception of the vein from 346.9/82, all veins were analysed as a bulk geochemical sample due to the small amount of material and relatively coarse grainsize. In this study, equal weights of powders from each sample were blended together for consistency. Implications of this sampling technique are described below.

Representative portions of all samples were crushed with a tungsten carbide-plated hydraulic press and powdered in a clean tungsten carbide bowl using a tema mill. All samples were analysed for major elements (SiO_2, TiO_2, Al_2O_3, Fe_2O_3 (total), MnO, MgO, CaO, Na_2O, K_2O, P_2O_5 and SO_3) and trace elements (Ba, V, Cr, Co, Ni, Cu, Zn, Ga, Pb, Rb, Sr, Y, Zr and Nb) at the James Cook University Advanced Analytical Centre (AAC) (Table 3.2, 3.3). Powders were roasted to 1000˚C for at least eight hours to determine the loss on ignition (LOI), and were then analysed by X-Ray Fluorescence using a Siemens SRS303 spectrometer fitted with an end-window rhodium tube. Samples were also analysed for As, Hf, Ce, Eu, La, Lu, Sm, Sc, Tb, Th and Yb by instrumental neutron activation analysis (INAA) at Becqueral Laboratories, Sydney (Table 3.2, 3.3).

		FTCD246/26		***FTCD262/86***		***FTCD346/82***		***FTCD203/86***	
SAMPLE	detection limit	altered rock	unaltered rock	altered rock	unaltered rock	altered rock	unaltered rock	altered rock	unaltered rock
Major elements (wt %)									
SiO_2		34.3	35.5	40.3	43.0	41.7	47.7	37.9	46.9
TiO_2		6.07	6.00	5.64	5.36	2.52	2.55	2.92	1.79
Al_2O_3		9.8	9.9	13.7	14.2	13.1	14.8	14.5	16.7
Fe_2O_3T		19.3	19.6	18.3	16.3	16.1	14.4	21.0	12.1
MnO		0.12	0.20	0.13	0.19	0.08	0.21	0.09	0.16
MgO		10.34	9.09	8.26	6.30	9.25	6.15	11.66	7.95
CaO		11.10	11.25	4.69	9.22	6.29	9.33	3.07	8.10
Na_2O		1.69	1.44	3.59	2.63	3.80	3.27	2.38	2.69
K_2O		0.74	2.66	0.79	1.77	0.21	1.15	0.35	1.95
P_2O_5		3.67	3.59	0.28	0.30	0.76	0.88	0.20	0.18
SO_3		0.02	0.09	0.15	0.05	0.02	0.04	0.12	0.02
Cl		0.038	0.311	0.023	0.085	0.033	0.065	0.014	0.199
F		0.27	0.33	0.04	0.04	0.02	0.06	0.03	0.03
LOI		3.3	0.7	2.50	1.0	3.7	0.30	2.20	2.0
SUM		100.4	100.0	98.4	100.3	97.5	100.9	96.5	100.5
Trace elements (XRF) (ppm)									
Ba	**10**	103	372	127	300	26	255	42	372
V	**8**	456	578	488	489	180	254	195	168
Cr	**5**	-	-	665	-	207	285	243	306
Co	**2**	14	72	40	65	516	56	110	61
Ni	**3**	27	29	29	36	30	21	34	64
Cu	**3**	29	91	9	84	3	33	3	37
Zn	**3**	44	42	15	69	-	80	bd	88
Ga	**3**	23	18	27	21	28	22	32	17
Pb	**10**	4	5	-	6	-	-	-	4
Rb	**2**	35	159	23	90	-	58	10	98
Sr	**2**	91	128	50	232	75	248	31	306
Y	**2**	81	42	25	19	48	35	17	14
Zr	**3**	71	56	62	68	101	53	49	46
Nb	**2**	14	8	13	9	23	17	10	5
Trace elements (INAA) (ppm)									
As	1.00	4.90	3.58	-	-	-	-	-	-
Ce	2.00	243.00	94.30	150.00	24.80	196.00	82.30	88.40	21.80
Eu	0.50	5.26	1.93	3.14	1.03	3.90	2.21	1.89	0.99
Hf	0.50	1.91	1.85	2.63	1.88	-	2.23	-	1.41
La	0.50	116.00	47.00	58.90	11.80	81.30	39.90	40.60	11.20
Lu	0.20	0.61	0.29	0.36	0.21	0.37	0.42	-0.20	-0.20
Sm	0.20	22.00	11.20	8.02	3.24	13.30	8.70	5.01	2.50
Sc	0.10	38.10	48.70	56.60	53.80	34.10	39.80	41.10	33.30
Tb	0.50	2.99	1.53	1.15	0.56	1.66	1.41	0.65	na
Th	0.50	2.72	1.03	2.45	0.67	3.33	1.01	1.70	0.69
Yb	0.50	4.92	2.43	2.49	1.43	2.80	3.19	1.35	1.07

Table 3.2: Major and trace element composition of unaltered and altered gabbro from the FC12 prospect determined by XRF (X-ray Fluorescence) and INAA (neutron activation analysis). Notes: "-" = elements below detection. Sample number refers to depth down hole and hole number respectively (see appendix 1)

3.4.2 Method for determining chemical composition of veins

An attempt was made to 'back calculate' the major element chemical composition of each vein from samples 246/86, 262.3/86 and 203/86 via the estimated modal mineralogy and the chemical formula for each mineral. This was necessary because the large grain size and the small vein width prohibited accurate XRF on individual drill core samples. This was first tested on sample 346.9/82 to see whether a similar chemical composition could be obtained in comparison to the results from XRF, since this sample was more even-grained than the other veins and so was analysed separately. Firstly, the modal percentages of each mineral were converted to mass (g) by multiplying the modal % with the density of each mineral in the vein. The calculated mass (g) for each mineral was then converted to a percentage of the total mass of the

SAMPLE	***FTCD346/82***	***FTCD246/26, FTCD262/86 and FTCD203/86 combined***
Major elements (wt %)		
SiO_2	17.303	26.621
TiO_2	0.23	1.692
Al_2O_3	3.238	6.14
Fe_2O_3T	28.48	9.632
MnO	0.072	0.07
MgO	1.494	2.353
CaO	26.498	28.408
Na_2O	2.671	2.945
K_2O	0.125	0.129
P_2O_5	0.168	0.109
SO_3	2.956	4.76
Cl	N/A	N/A
F	N/A	N/A
LOI	16.9	15.47
SUM	100.135	98.33
Trace elements (XRF) (ppm)		
Ba	-	39
V	211	132
Cr	147	23
Co	98	37
Ni	21	32
Cu	**89**	**12377**
Zn	**-**	**29**
Ga	**N/A**	**9**
Pb	**10**	**40**
Rb	**-**	**-**
Sr	**35**	**74**
Y	**18**	**33**
Zr	**-**	**7**
Nb	1	**2**
Trace elements (INAA)		
As	12.40	3.99
Ce	15.50	229.00
Eu	-0.50	3.73
Hf	-	-
La	6.95	103.00
Lu	0.25	0.49
Sm	1.27	11.60
Sc	7.30	5.70
Tb	-0.50	1.56
Th	0.51	3.33
Yb	1.61	3.46

Table 3.3: Major and trace element composition of veins from the FC12 prospect determined by XRF (X-ray Fluorescence) and INAA (neutron activation analysis). High LOI values can be attributed to CO_2 released during combustion from calcite .Notes: "N/A = elements not measured, "-" = below detection. Sample number refers to depth down hole and hole number respectively (see appendix 1).

vein (Deer et al., 1992) (Table 3.4). The major element concentration for each mineral was determined by the following equation:

$$C_{mn} = \%mass \times \frac{W_{element}}{W_{mn}} \quad \text{................equation 3.1}$$

Where:
C_{mn} = Major element concentration in mineral
% mass = Normalised mass % of each mineral
$W_{element}$ = Atomic weight of element
W_{mn} = Total atomic weight of mineral (cf. Deer et al., 1992; Table 3.4)

Each major element was then converted to an oxide and added together to give the overall geochemical composition of the vein, in addition to the excess volatile content (LOI) released during combustion (Table 3.5, appendix 3).

Table 3.5 shows that the values obtained for the major elements from these calculations are similar to the original XRF results for sample 346.9/82 (Table 3.3), although an estimate of the composition of K_2O and MnO could not be determined as no Mn- and K-rich minerals were observed in thin section and therefore could not be added to the calculations. The XRF results, however, show a small concentration of K_2O (0.13 wt %) and MnO (0.07 wt %) which presumably occurs as minor solid solution within the silicates, which therefore did not greatly affect the calculations for the other elements. These calculations were employed for the other veins (Table 3.5), and the results for all three veins were averaged and compared to the bulk chemical composition obtained from XRF (Table 3.5 and 3.3). The results from these calculations were similar to the XRF results suggesting that the calculated values shown in table 3.5 are realistic and are a reasonable indication of the chemical composition of each individual vein.

3.4.3 Isocon analysis

The isocon method (Grant, 1986) was applied to the unaltered rock and alteration selvage from each sample to quantify the geochemical changes during alteration. This method is usually robust in the sense that elements considered to be immobile in hydrothermal systems will usually plot as a linear array on this dimensionless X-Y diagram, reflecting no relative mass gains or losses of these elements during alteration.

Total molecular weight of minerals

Mineral	Chemical Formula	Mol. Weight
Magnetite	$Fe_2O_3.FeO$	231.55
Hematite	Fe_2O_3	159.70
Titanite	$CaTiSiO_4$	180.07
Actinolite	$Ca_2(MgFe)_5(Si_8O_{22})(OH)_2$	1017.60
Pyrite	FeS_2	119.97
Chalcopyrite	$CuFeS_2$	184.72
Apatite	$Ca_5(PO_4)_3(OH)$	502.31
Calcite	$CaCO_3$	100.09
Albite	$NaAlSi_3O_8$	262.24

Table 3.4: Table showing the molecular formulas for each mineral identified in thin section within the veins at FC12 and the total mass of each mineral based on their molecular formulas.

Calculated vein chemical compositions

Element	*FTCD346/82**	*FTCD246/86*	*FTCD262/86*	*FTCD203/86*	*Average of 246/86, 262/86 and 203/86*
SiO_2	20.32	19.44	36.68	17.87	24.66
TiO_2	1.30	4.80	0.95	0.50	2.09
Al_2O_3	3.15	0.67	9.52	4.43	4.87
Fe_2O_3T	29.76	10.98	21.16	10.14	14.09
MgO	1.72	2.82	0.49	0.39	1.23
CaO	24.82	37.07	12.31	35.54	28.31
Na_2O	1.92	0.41	5.79	2.69	2.96
K_2O	0.00	0.00	0.00	0.00	0.00
P_2O_5	0.43	0.00	0.00	0.00	0.00
S	0.88	0.00	5.00	1.45	2.15
Cu	0.06	0.00	1.45	0.51	0.65
LOI	15.63	23.81	6.66	26.48	18.98
Tot	100.00	100.00	100.00	100.00	100.00

Table 3.5: Major element composition of Na-Ca veins at FC12 determined by back calculating the modal proportion of minerals and molecular weight of each mineral with respect to density (Appendix 3). The first column represents the calculated chemical composition of sample 346.9/82 which is similar to the chemical composition determined by XRF (Table 3.3). The remaining samples were averaged together and presented in the final column. These values are similar to the average chemical composition of samples 246/86, 262.3/86 and 203/86 in table 3.3. Note: the Mg and Fe ratio of 3:2 for actinolite in these veins was based on mineral chemistry data of actinolite in similar veins within the FC12 prospect (chapter 2). See appendix 3 for further details on these calculations.

For each sample pair, individual elements were multiplied or divided by a chosen factor that conveniently distributed the elements on an X-Y diagram. As only the ratios of the elements are important for constructing the isocons, the absolute values are not necessary, as long as the particular element is multiplied by the same factor in both the unaltered and altered equivalent. A line of best fit can then be drawn through elements considered immobile in hydrothermal systems (Goldschmidt, 1958). The slope of the isocon defines the overall mass change between the rocks, and the departure of a particular element from this line defines its relative gain or loss. Isocons with a slope greater than one indicate an overall mass loss (i.e. dissolution) and those less than one indicate mass gain (if both rocks have similar density).

3.4.4 Method for combining the composition of veins and alteration

In order to investigate the overall mass transfer associated with Na-Ca alteration at FC12, components added in the vein need to be combined with components gained or lost in the alteration selvage and compared to the original rock composition. The relative concentration of components in the unaltered rock, altered rock and vein can provide information regarding which components are mobile on a small scale via diffusion, and which components are being added or depleted by larger-scale advection. The first step is to determine the change in concentration (Xm) from unaltered rock to the alteration selvage using the Gresens equation (equation 3.2).

$$Xm = (Fv\frac{\rho^b}{\rho^a}C_m^b - C_m^a) \times 100$$

……………….Equation 3.2 (Gresens 1967)

Where:
X_m=Change in concentration of mobile element (m)
For major elements: g per 100g
For trace elements: ppm per 100g
Fv=Volume factor
ρ^b=Density of altered rock.
ρ^a=Density of unaltered rock
$C_m{}^b$=Concentration of mobile element (m) in altered rock
$C_m{}^a$=Concentration of mobile element (m) in unaltered rock.

The value for Fv (volume factor) can be calculated by the relative change in the concentration of interpreted immobile elements (e.g. Ti, Al, Zr) over a range of arbitrary values using composition-variation diagrams (Gresens, 1967 (Fig. 3.5). The

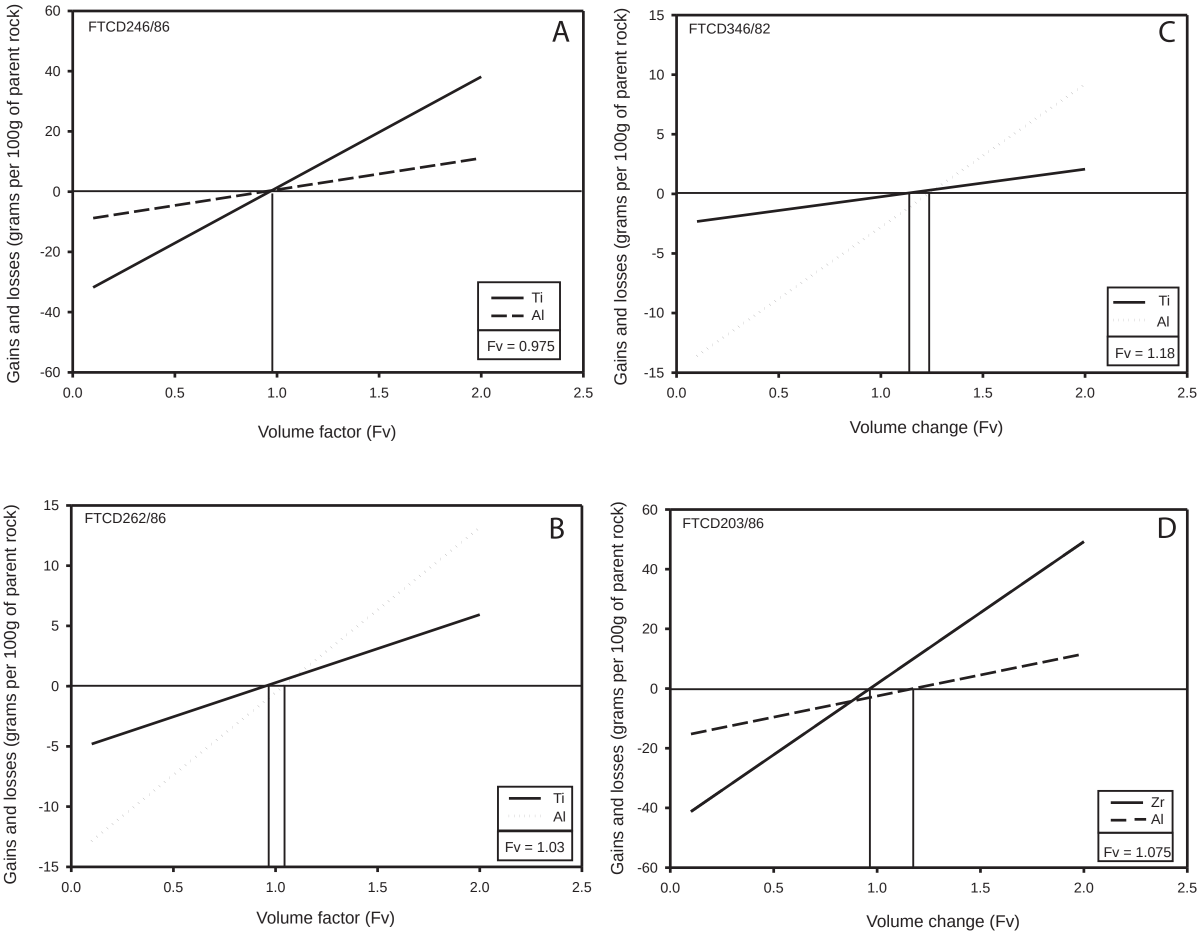

Figure 3.5: Composition - volume diagrams (after Gresens, 1967) showing the change in elemental gains and losses (Y-axis) associated with arbitrary values of Fv (X-axis) of elements that are interpreted to exhibit immobile behaviour during Na-Ca alteration. A), B), and C) are constrained by Ti and Al while D) is constrained by Zr and Al. Ti was found to be inconsistent with immobile behaviour for sample FTCD203/86, probably due to the small sample size. The average of the two points in which each line crosses the X axis is deemed the average volume change (Fv). Ti, Al and Zr were chosen after isocon analyses revealed they were the most likely immobile elements (see figure 3.6)

change in concentration (X_m) for each sample calculated from the above Gresens equation is presented in table 3.6.

In order to directly compare the chemical changes during alteration with components in the vein, the bulk density was determined for each sample (*c.f.* Deer et al., 1992). This is done by multiplying the modal % (estimated visually using a petrographic microscope) for each mineral by its density. This bulk density (g/cm^3) can then be multiplied by the volume (cm^3) of each sample component (i.e. vein and alteration selvage), giving the average bulk weight (g) of a 1 cm^2 cross section integrated across the vein and selvage width (Table. 3.7, appendix 4). While the bulk density of the alteration selvage and vein can be determined by the above calculations, the unaltered rock portion cannot be calculated in the same way because it lacks a width dimension. A value for the volume of the precursor unaltered rock that produced the observed selvage can be calculated by dividing the volume of the alteration selvage (in a 1 cm^2 channel with area and length the same as the width of the alteration zone) with the proportional change in volume (Fv) between the unaltered rock and altered equivalent from the C-V diagrams described above. This calculated volume (cm^3) can then be multiplied by the bulk density (g/cm^3) of the unaltered rock to give the bulk weight (g) of the unaltered rock for this volume, suitable then for comparing with the altered rock and vein (Table 3.7, appendix 4). The change in concentration (X_m) during alteration can now be converted to a percentage of the bulk weight (g) of the original rock. The results of these calculations are shown in table 3.8.

Table 3.9 shows the elemental/oxide vein composition presented as a percentage of the bulk weight of the vein. A comparison of these tables provides a means of directly comparing which components have been added or depleted in the alteration selvage (table 3.8) relative to components added in the vein (table 3.9), taking into account the relative density. Only the major elements were calculated for samples 246/86, 262/86 and 203/86 because trace elements concentrations could not be ‘back calculated’ in the same way (section 3.4.2). Elements which are enriched in the vein and show little change from unaltered to altered rock can be interpreted as having been introduced from outside the system. Alternatively, if Xm values for components added to the vein equal the depletion in the alteration selvage, this may indicate local diffusion from the wall rock into the vein.

	Change in concentration (Xm)			
SAMPLE	*FTCD246/86*	*FTCD262/86*	*FTCD346/82*	*FTCD203/86*
SiO2 (wt%)	-2.23	-2.25	-3.39	-7.48
TiO2 (wt%)	-0.12	0.34	0.13	1.25
Al2O3 (wt%)	-0.39	-0.41	-0.89	-1.55
Fe2O3 (wt%)	-0.88	2.22	2.66	9.77
MnO (wt %)	-0.08	-0.06	-0.13	-0.07
MgO (wt%)	0.93	2.04	3.67	4.17
CaO (wt%)	-0.49	-4.48	-2.65	-4.91
Na2O (wt%)	0.20	1.00	0.76	-0.22
K2O (wt%)	-1.94	-0.97	-0.93	-1.59
P2O5 (wt%)	-0.03	-0.02	-0.07	0.03
SO3 (wt%)	-0.07	0.10	-0.02	0.10
Ba (ppm)	-272.17	-171.72	-227.39	-328.34
V (ppm)	-136.03	3.92	-62.88	34.70
Cr (ppm)			-65.22	-53.40
Co (ppm)	-58.43	-24.60	491.87	53.35
Ni (ppm)	-2.83	-6.71	10.85	-28.66
Cu (ppm)	-62.89	-74.91	-29.81	-33.88
Zn (ppm)	0.65	-53.85		
Ga (ppm)	4.29	6.27	7.73	16.26
Pb (ppm)	-1.12			
Rb (ppm)	-125.08	-66.77		-87.60
Sr (ppm)	-39.80	-181.50	-168.37	-273.78
Y (ppm)	36.51	6.25	15.96	3.67
Zr (ppm)	12.82	-5.37	54.24	4.94
Nb (ppm)	5.57	4.13	7.42	5.40
Ce (ppm)	141.22	126.71	125.80	70.09
Eu (ppm)	3.17	2.14	1.93	0.97
La (ppm)	65.43	47.69	46.42	31.00
Lu (ppm)	0.30	0.15	-0.03	-0.01
Sm (ppm)	10.12	4.86	5.42	2.71
Sc (ppm)	-11.77	3.37	-3.59	9.42
Tb (ppm)	1.37	0.60	0.35	1.18
Th (ppm)	1.61	1.80	2.53	1.08
Yb (ppm)	2.34	1.09	-0.22	0.33

Table 3.6: Elemental mass changes (Xm) for unaltered rock to alteration selvages from the FC12 prospect determined using Gresens equation (equation 3.2). Volume change is specified by the average of Ti and Al on the Gresens plot except for sample 203/86 where the volume change was defined by Zr and Al (Fig. 3.5). Mass changes are in grams and 10^{-5} *grams per 100 grams of parent rock for major elements and trace elements respectively. Bd = below detection.*

Bulk weight (g) of sample components			
	Vein	Alteration selvage (x2)	Unaltered rock
FTCD246/86	8.06	31.58	32.58
FTCD262.3/86	8.14	22.37	22.14
FTCD346.9/82	7.36	18.68	17.59
FTCD203/86	5.12	53.78	60.22

Table 3.7: Bulk weight (g) of the unaltered rock, alteration halo and vein for each sample calculated for volume with a 1 cm^2 cross section profile ("trench") across the vein. Based on calculations shown in appendix 4.

	Change in concentration from original bulk weight (g)			
	FTCD246/86	*FTCD262/86*	*FTCD346/82*	*FTCD203/86*
SiO2	-0.73	-0.50	-0.60	-4.506
TiO2	-0.04	0.07	0.02	0.750
Al2O3	-0.13	-0.09	-0.16	-0.931
Fe2O3T	-0.29	0.49	0.47	5.884
MnO	-0.03	-0.01	-0.02	-0.040
MgO	0.30	0.45	0.65	2.512
CaO	-0.16	-0.99	-0.47	-2.956
Na2O	0.06	0.22	0.13	-0.130
K2O	-0.63	-0.22	-0.16	-0.955
P2O5	-0.01	0.00	-0.01	0.017
SO3	-0.02	0.02	0.00	0.063
Ba	-88.67	-38.02	-40.01	-197.74
V	-44.32	0.87	-11.06	20.90
Cr	0.00	0.00	-11.47	-32.16
Co	-19.04	-5.45	86.54	32.13
Ni	-0.92	-1.49	1.91	-17.26
Cu	-20.49	-16.59	-5.25	-20.41
Zn	0.21	-11.92	0.00	0.00
Ga	1.40	1.39	1.36	9.79
Pb	-0.37	0.00	0.00	0.00
Rb	-40.75	-14.78	0.00	-52.76
Sr	-12.97	-40.19	-29.62	-164.88
Y	11.89	1.38	2.81	2.21
Zr	4.18	-1.19	9.54	2.97
Nb	1.81	0.91	1.31	3.25
Ce	46.01	28.06	22.13	42.21
Eu	1.03	0.47	0.34	0.59
La	21.32	10.56	8.17	18.67
Lu	0.10	0.03	0.00	0.00
Sm	3.30	1.08	0.95	1.63
Sc	-3.84	0.75	-0.63	5.68
Tb	0.45	0.13	0.06	0.71
Th	0.52	0.40	0.44	0.65
W	37.49	4.86	2791.34	4323.21
Yb	0.76	0.24	-0.04	0.20

Table 3.8: The change in concentration from unaltered rock to altered rock calculated as a percentage of the bulk weight of the unaltered rock. Solution to the Gresens equation for each component using Fv's determined in figure 3.5 (Appendix 4).

	Bulk weight of element in vein (g)			
	FTCD246/86	FTCD262/86	FTCD346/82	FTCD203/86
SiO_2	1.57	2.99	1.27	0.91
TiO_2	0.39	0.08	0.02	0.03
Al_2O_3	0.05	0.77	0.24	0.23
Fe_2O_3T	0.89	1.72	2.10	0.52
MnO	0.00	0.00	0.01	0.00
MgO	0.23	0.04	0.11	0.02
CaO	2.99	1.00	1.95	1.82
Na_2O	0.03	0.47	0.20	0.14
K_2O	0.00	0.00	0.01	0.00
P_2O_5	0.00	0.00	0.01	0.00
SO_3	0.00	0.41	0.22	0.07
Ba	-	-	bd	-
V	-	-	15.53	-
Cr	-	-	10.82	-
Co	-	-	7.21	-
Ni	-	-	1.55	-
Cu	-	-	6.55	-
Zn	-	-	bd	-
Pb	-	-	0.74	-
Rb	-	-	bd	-
Sr	-	-	2.58	-
Y	-	-	1.32	-
Zr	-	-	bd	-
Nb	-	-	0.07	-
Ce	-	-	1.14	-
Eu	-	-	bd	-
La	-	-	0.51	-
Lu	-	-	0.02	-
Sm	-	-	0.09	-
Sc	-	-	0.54	-
Tb	-	-	bd	-
Th	-	-	0.04	-
Yb	-	-	0.12	-

Table 3.9: Concentration of elements in the vein as a percentage of the bulk weight calculated in appendix 4 in a "trench" of 1 cm^2 section across a vein . Trace element values were only obtained for sample 346.9/82 because this sample was analysed separately to the bulk analysis for samples 246/86, 262.3/86 and 203/86 (see text for further information).

3.5. RESULTS

3.5.1 Isocon plots

Four rocks affected by Na-Ca alteration and veining along with their unaltered equivalents from the FC12 prospect were compared using the isocon method to determine the elemental exchange involved during replacement (Fig. 3.6). The results from the isocon analysis show that the mass changes of specific components are similar between samples. For samples 246/86, 262.3/86 and 346.9/82, an isocon was constructed through Ti and Al with the assumption that these elements are relatively

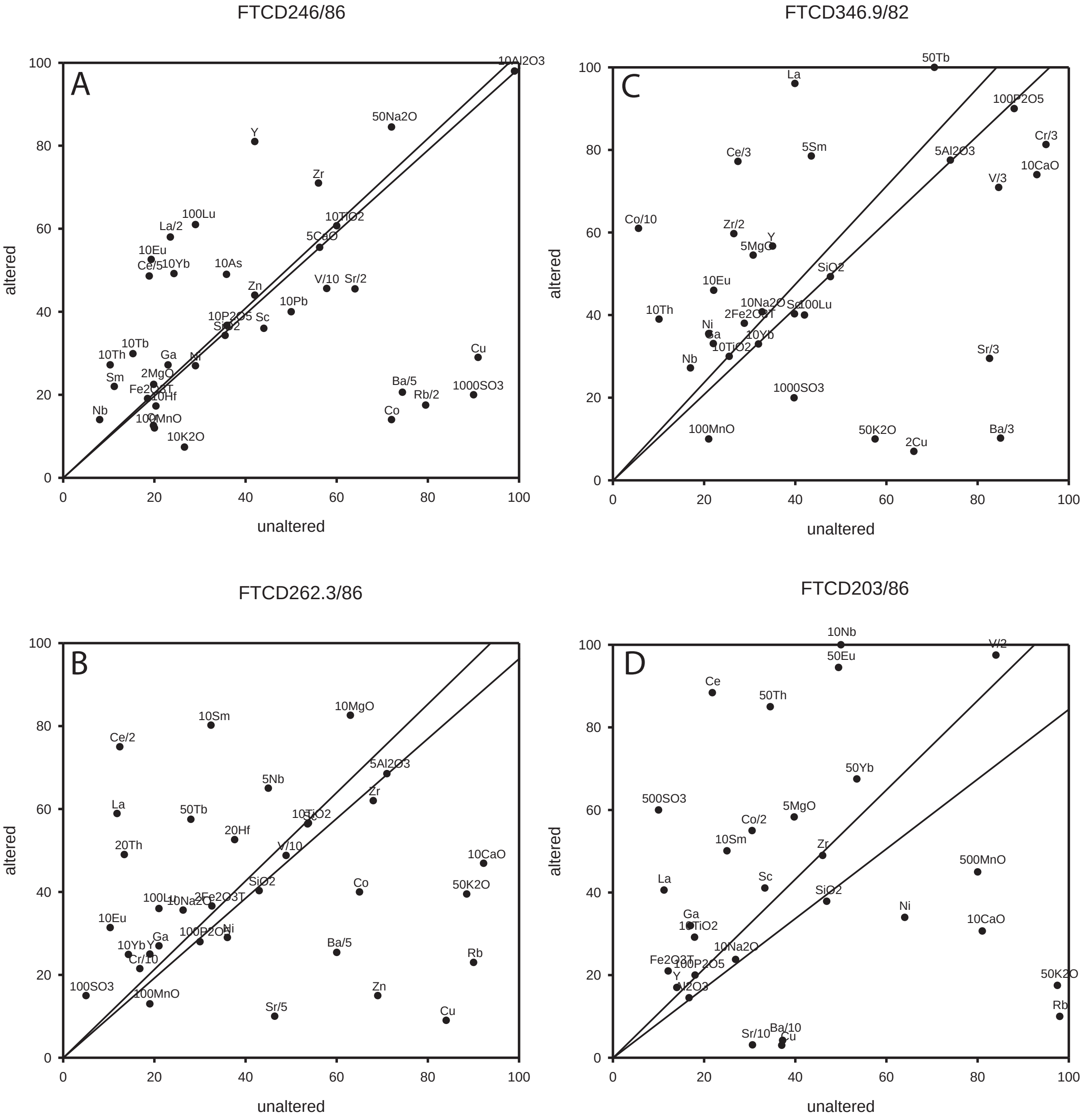

Figure 3.6: Isocon plots (after Grant, 1986) comparing rocks affected by alteration associated with Na-Ca veins and their unaltered equivalents from the FC12 prospect. Each isocon compares a coarse-grained gabbro affected by chlorite + albite + titanite alteration with a pristine gabbro except C) where the host rock is a medium-grained gabbro with higher orthopyroxene content than the coarser-grained varieties. The isocons are defined by the best fit between TiO_2 and Al_2O_3 for samples 246/86, 262.3/86 and 346.9/82, whereas for samples 203/86 the isocon is defined by Al_2O_3 and Zr, assuming in each case that these elements have remained immobile during alteration. Major elements are plotted as wt %; trace elements are plotted as ppm. Multiplication factors are shown for each element. Note the consistent gains in the REE (Ce, Eu, Sm and La), Na and Mg and losses in Cu, Ca, K, Ba and Sr associated with alteration. The location of each sample is shown in figure 3.2.

immobile compared to other elements (Fig. 3.6a, b, c) (Goldschmidt, 1958). For rock sample 203/86, Ti concentration appears to be relatively high in the altered rock with respect to the unaltered rock suggesting it may be mobile, or initially had an irregular distribution and was not therefore sampled evenly between unaltered and altered rock (Fig. 3.6d). In some high temperature systems, Ti mobility has been documented, although only over small scales (millimetre to centimetre) (Van Baleen, 1993) possibly by diffusion or small scale advection. The local presence of titanite on the vein boundaries in these samples and other examples of Na-Ca alteration elsewhere in the EFB (Mark and Foster, 2000) suggests that Ti may occasionally diffuse over millimetre scales in these systems. In any case, the isocon sample 203/86 was constructed through Al and Zr.

For each sample, the isocons indicate little to no volume change during alteration, consistent with thin section analysis of each sample which indicates that the original gabbroic texture has been preserved. Other components besides Ti, Al and Zr that appear immobile (or nearly so) during alteration include Si and P. Components consistently depleted in the alteration selvage include K, Ba, Rb, Sr, Ca, Mn, and Cu, while Ce, Mg, Ga, Th, Eu, La, and Sm are all enriched (Fig. 3.6). Na is enriched in samples 246/86, 262.3/86 and 346.9/82 but is immobile in sample 203/86, while S is enriched in samples 262.3/86 and 203/86 and depleted in sample 246/86. In sample 346.9/82, S content is below detection. Other elements that exhibit variable mobility between samples include Fe, Co, Yb, Y and V.

3.5.2 Elemental profiles: effects of bulk density and vein widths

Elemental profiles (Fig. 3.7) represent a useful way of visualising the relative changes in concentration between the unaltered rock, the alteration selvage and related vein (e.g. Oliver and Bons, 2001). More precise changes are presented in figure 3.8 and 3.9 based on the calculations presented above. Ti and Al show patterns consistent with their limited mobility in aqueous solutions, with a small component of Al sequestered into albite and Ti sequestered into titanite within the vein. The pattern of Al and Ti expressed across the wall rock/vein interface provides a useful reference frame for the relative mobility of other elements. All veins exhibit significant increases in Ca, predominately due to the presence of calcite (Fig. 3.7, 8a, 9). Interestingly, Ca is

Figure 3.7: Mineral assemblages and raw major element concentrations of alteration selvages developed around Na-Ca veins within the FC12 prospect. Each example shows clear evidence for the addition and depletion of specific components. The modal minerals proportions are shown in the top profile for each sample. The geochemical profiles were each constructed from XRF data not corrected for density differences. For all samples, Ca and Cu (sample 346.9/82) is depleted in the wall rock and enriched in the vein and may indicate some of these components in the vein were derived from diffusion and/or local advection (irrespective of the slight density differences inferred from figure 3.6). K is also depleted from the wall rock but is also very low to absent in the veins, suggesting that it has moved outside the scale of the alteration system presented here. Fe is relatively immobile in the wall rock and enriched in the vein suggesting it was introduced into the system by the external fluid. Ab=albite, act=actinolite, ap=apatite, bt=biotite, ccp=chalcopyrite, cct=calcite, chl=chlorite, cpx=clinopyroxene, hem ab=hematised albite, ilm=ilmenite, mag=magnetite, ms=muscovite, opx=orthopyroxene, pl=plagioclase, py=pyrite, ttn=titanite. Abbreviations after Kretz (1983).

Sample 246/86

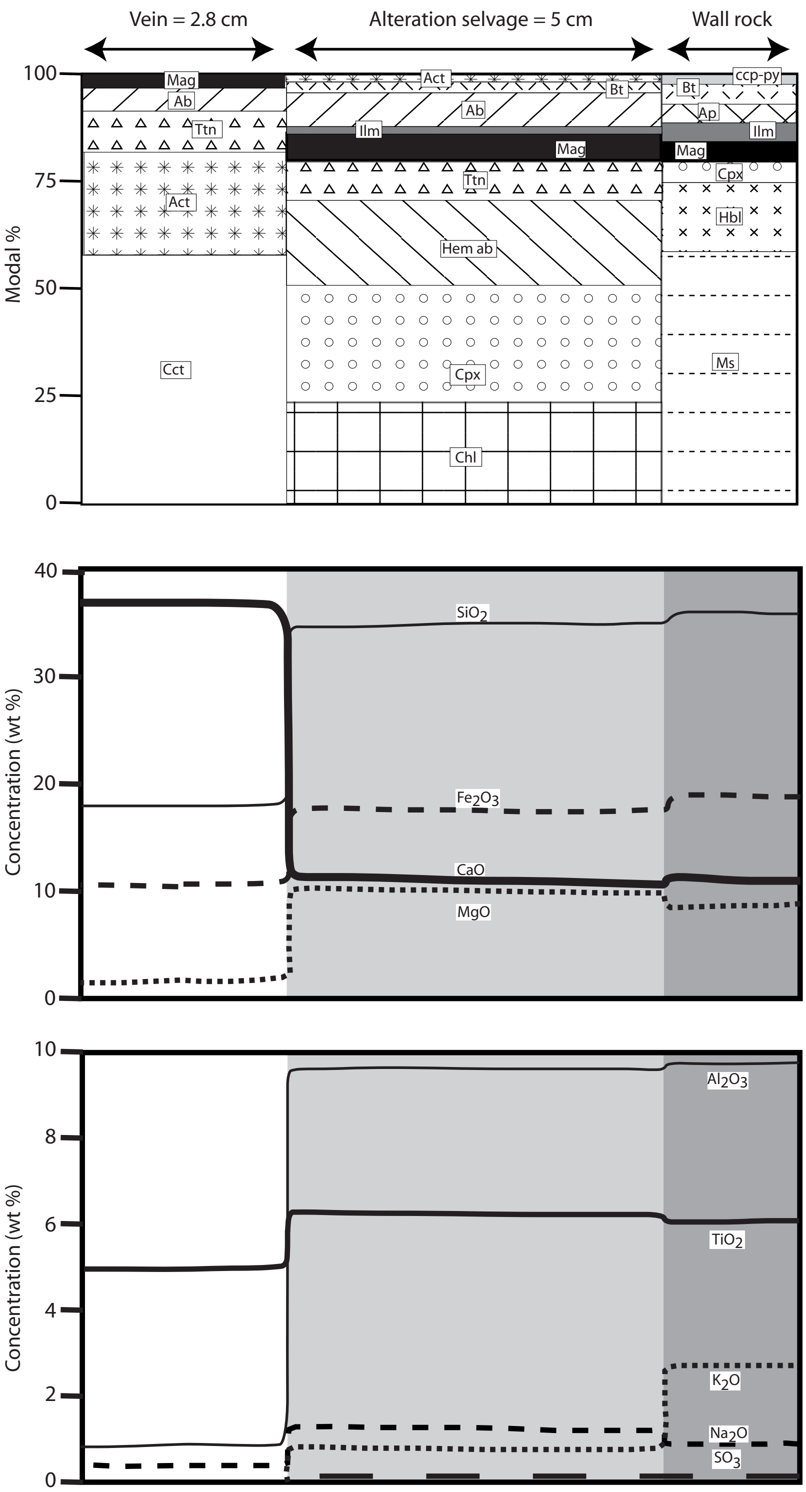

Sample 262.3/86

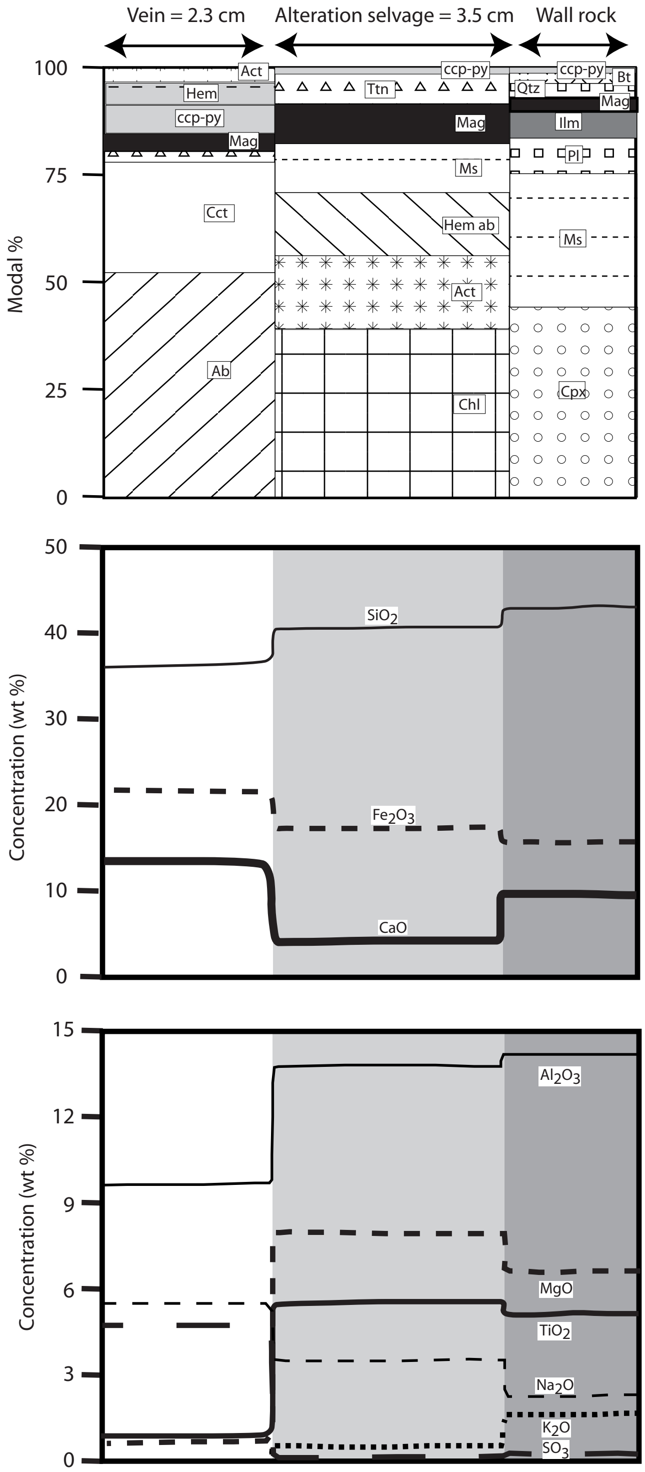

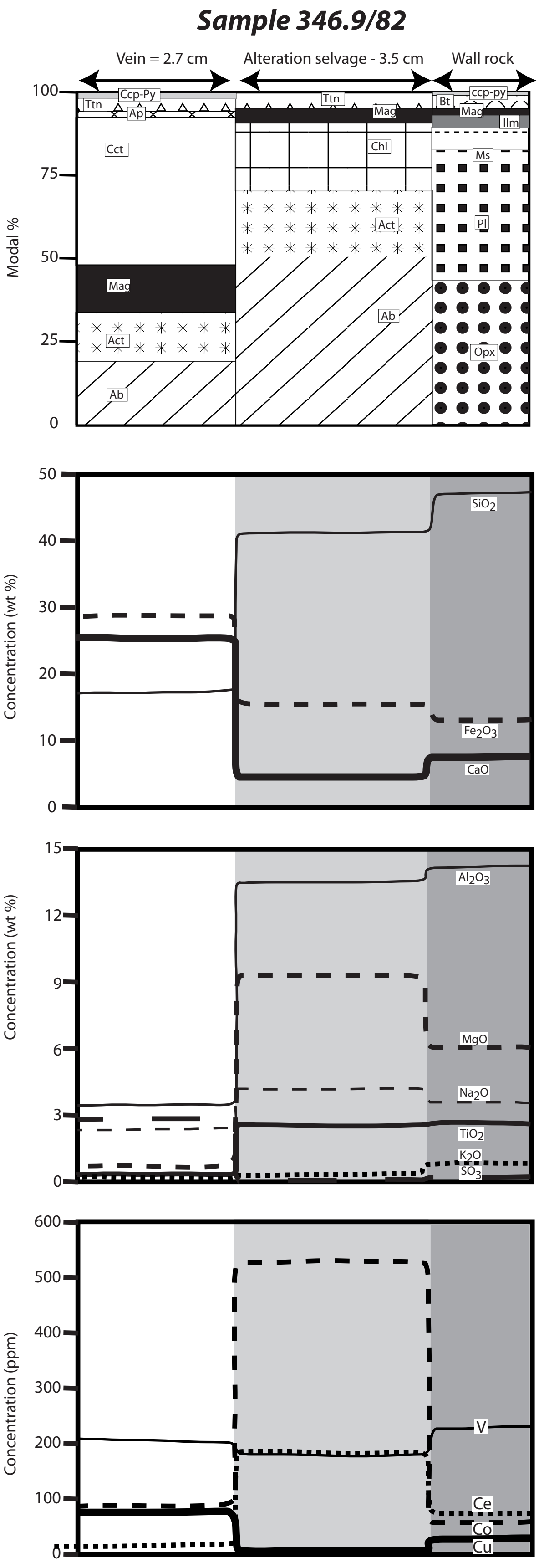
Sample 346.9/82
Vein = 2.7 cm
Alteration selvage - 3.5 cm
Wall rock
Modal %
100
75
50
25
0
Ccp-Py
Ttn
Ap
Cct
Mag
Act
Ab
Ttn
Mag
Chl
Act
Ab
Bt
ccp-py
Mag
Ilm
Ms
Pl
Opx
Concentration (wt %)
50
40
30
20
10
0
SiO2
Fe2O3
CaO
Concentration (wt %)
15
12
9
6
3
0
Al2O3
MgO
Na2O
TiO2
K2O
SO3
Concentration (ppm)
600
500
400
300
200
100
0
V
Ce
Co
Cu

Sample 203/86

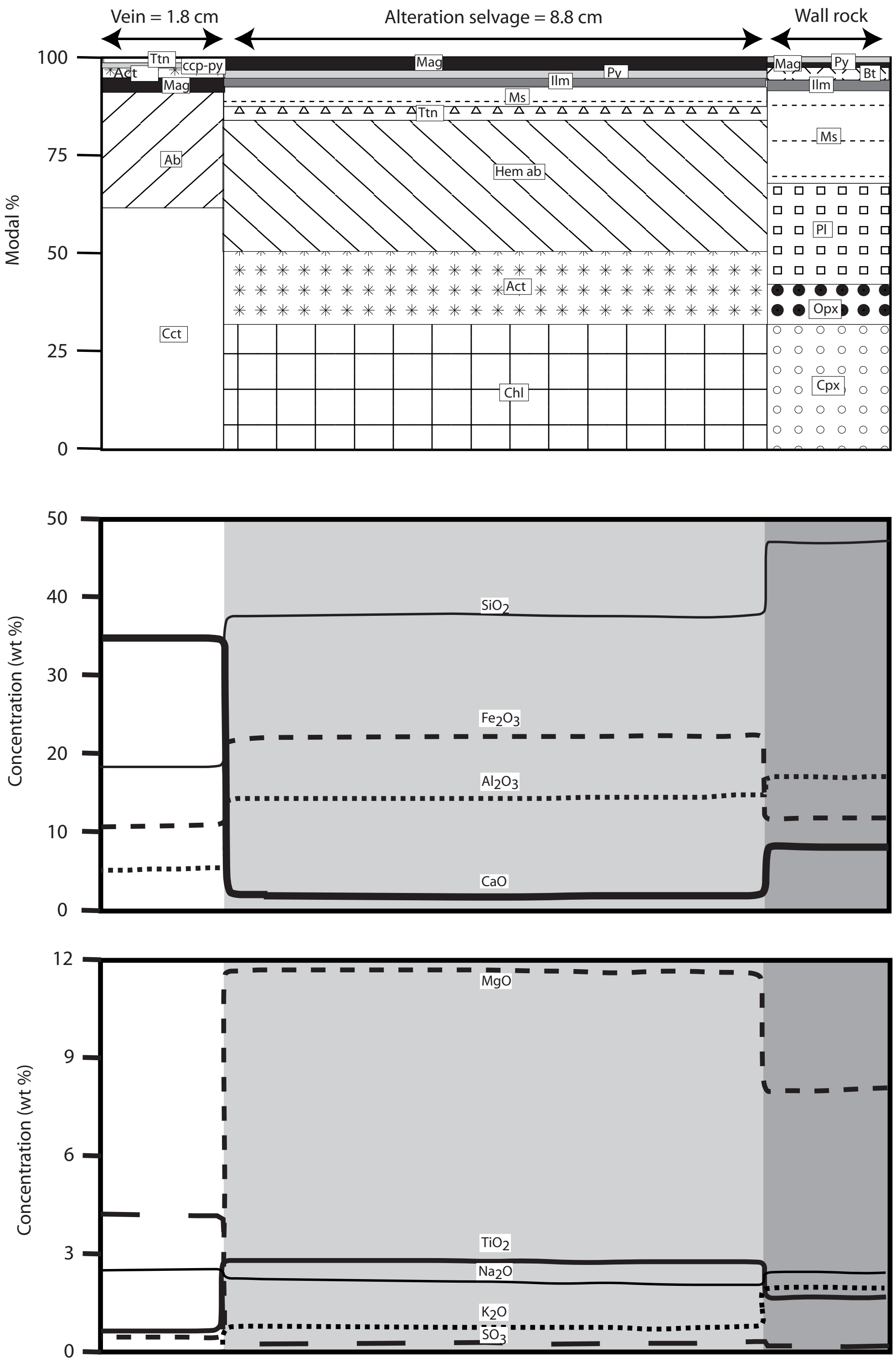

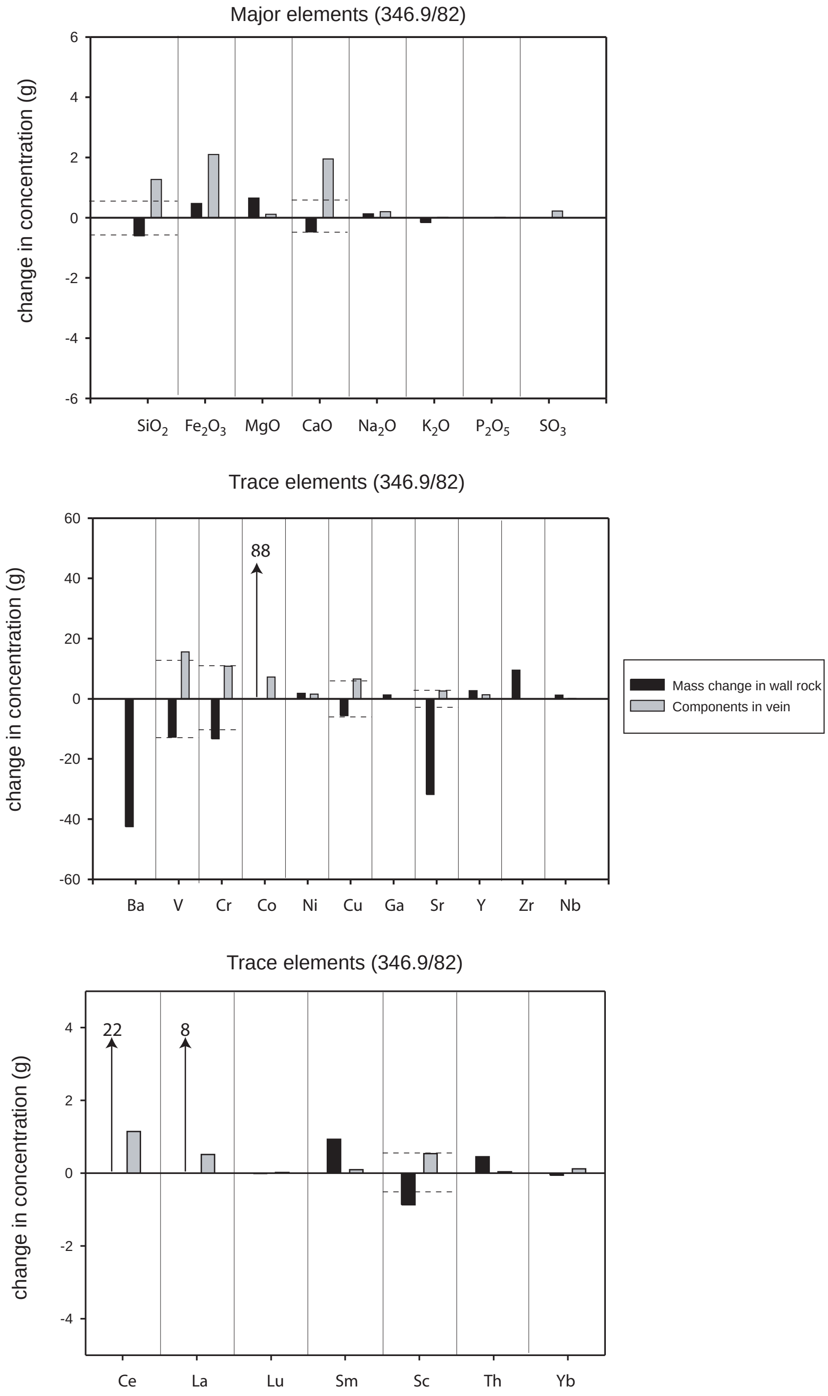

Figure 3.8: Graphical plots of sample 346.9/82 from calculations of XRF data, combining the mass transfer between unaltered to altered rock and components within the vein based in the relative densities and the width of each sample zone across a 1 cm^2 section "trench" (section 3.4.4). A) Mass changes of major elements. Note that Ca is depleted in the wall rock, but is considerably enriched in the vein. Na shows a slight gain in the wall rock and vein, while K is lost. B) and C) Mass changes of trace elements. Note Ba and Sr exhibit considerable losses in the wall rock and are minor to absent in the vein. The depletion of Cu in the wall rock is approximately equivalent to the concentration of Cu in the vein suggesting mass transfer by diffusion. The REE (La and Ce) show considerable gain in the wall rock due to the replacement of ilmenite by titanite.

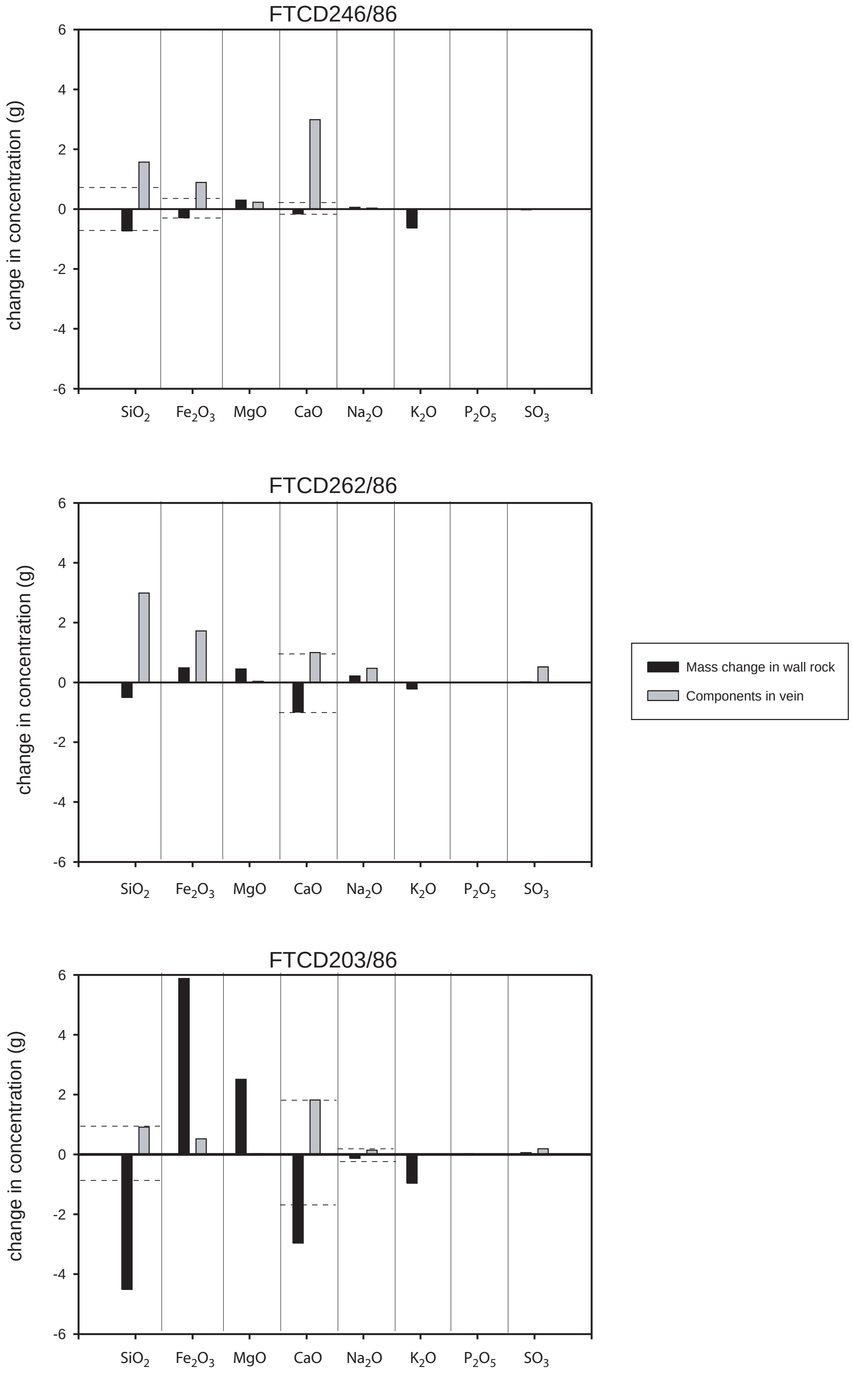

Figure 3.9: Major element graphical plots of samples 246/86, 262.3/86 and 203/86 from calculations of XRF combining the mass transfer between unaltered to altered rock and components within the vein based on the relative densities and the width of each sample zone (section 3.4.4). Composition of the veins were 'back calculated' from a bulk composition of all three veins as described in section 3.4.2. A) Mass changes of major elements for sample 246/86. B) Mass changes of major elements for sample 262.3/86. C) Mass changes of major elements for sample 203/86. Note the loss of K in all three samples. The gains and loss associated with Si, Fe, Mg, Ca and K in 203/86 are larger than those observed for samples 246/86, 262.3/86 and 346.9/82 and are attributed to the larger size of the alteration halo in sample 203/86.

depleted in the altered rock in samples 246/86, 262.3/86 and 346.9/82 (Fig. 3.9a, b, c) relative to the unaltered rock, while Ca in sample 246/86 is relatively immobile (Fig. 3.8a). This may suggest that for samples 262.3/86, 346.9/82 and 203/86 at least some of the Ca in the vein originated from the wall rock via diffusion. Mg is elevated in the host rock due to the replacement of biotite, pyroxene and amphibole by chlorite but is relatively low in the vein (Fig. 3.7, 3.8a, 3.9). Fe is typically immobile from altered to unaltered rock in samples 246/86, 262.3/86 and 346.9/82, although the density calculation results presented in figure 3.8 suggest a slight loss in samples 246/86 and 346.9/82 and a slight gain in sample 262.3/86. S is variable between the unaltered rock and the alteration selvage. The presence of magnetite, pyrite and chalcopyrite in the vein suggests that both S and Fe were introduced externally by the fluid. K is consistently depleted in the alteration selvage compared to the unaltered rock due to the breakdown of primary biotite and muscovite to chlorite and is minor to absent in the veins (Fig. 3.7, 3.8a, 3.9).

As illustrated in the isocon plots described above, Na exhibits a slight increase in the alteration selvage during alteration (except in sample 203/86) (Fig. 3.7, 3.8a, 3.9) and is also present as albite in the veins. Only trace elements from sample 346.9/82 can be studied via the vein / wall rock profiles and mass balance calculations, because the trace element concentrations for the other samples could not be ‘back calculated’ in the same way as for the major elements (section 3.4.2) (Fig. 3.7c, 3.8b, c). Cu shows a slight depletion in the alteration selvage, while it is comparatively rich in the vein (Fig. 3.8b). This is supported by thin section investigations that show primary chalcopyrite being broken down during alteration. This pattern for Cu is interesting, as it suggests that Cu concentrations in the vein, at least in part, may be the result of diffusion of pre-existing Cu from the host rock (Fig. 3.8b). Unfortunately, sample 346.9/82 is not representative of typical mineralised Na-Ca veins at FC12, as the vein only contains 89 ppm Cu (Table 3.3). In contrast, the bulk chemical composition of the veins from samples 246/86, 262.3/86 and 203/86 contain 1.2 wt % Cu and chalcopyrite is clearly present in all thin sections (Table 3.3). For these veins, the high Cu content was most likely derived from outside the scale of observed alteration.

Figures 3.7c and 3.8b show that V and Cr are mobile only over diffusive scales, as the depletion of these elements in the alteration selvage is proportional to their concentration in the vein. Both Ba and Sr exhibit similar patterns whereby both are depleted in the alteration selvage and show low concentrations in the vein. This agrees with the pattern described above for K because both Ba and Sr readily substitute for K in potassic minerals (Goldschmidt, 1958). Figures 3.7 and 3.8b show that the Co concentration in the wall rock is high (516 ppm) with respect to the other transition elements. The repository for the elevated Co is not clear, but Co was most likely introduced via the infiltrating fluid and subsequently partitioned into magnetite or pyrite in the wall rock.

3.6. COMPARISONS WITH OTHER Na (±Ca) ALTERATION SYSTEMS IN THE CLONCURRY DISTRICT

Na-Ca alteration and veins observed at the FC12 prospect are similar to many other Na-Ca assemblages throughout the EFB (Oliver et al., 2004; Oliver and Bons, 2001). Oliver et al (2004) presented evidence supporting the hypothesis by Williams (1994) that mass transfer associated with Na-Ca alteration may be an important mechanism for the liberation of Fe, K and other components that form both Fe oxide-rich rocks and IOCG deposits (discussed further in chapter 5). In their study, a variety of rock types were covered and showed that at constant Al, Si, Ga, Zr, and Ti, Na was consistently enriched while Fe, K, Ba ± Ca, Sr, Co, V, Mn, Pb and Zn were all lost during Na-Ca alteration. Their study also found the mobility of Cu to be variable between different rock types.

A comparison between the results of Oliver et al (2004) and those from this study show a number of similarities but also distinct differences. K, Ba and Sr are all depleted in the alteration selvage at FC12, consistent with the depletion of the same components noted by Oliver et al (2004) in other Na-Ca systems. In addition, Oliver and Bons (2001) observed in Na-Ca veins at Mary Kathleen that K is depleted in the wall rock and essentially absent in Na-Ca veins, suggesting K was moved outside the scale of the alteration. Oliver et al (2004) also noted the relative mobility of Ca coincided with the overall mass balance between the unaltered and altered rock. They observed that Ca was found to be added during alteration when the isocons showed an overall mass increase, while the opposite occurred when alteration coincided with mass depletions. Oliver and Bons (2001) also found Ca to be immobile to slightly depleted in the alteration selvage and consistently enriched in veins from Mary Kathleen. These observations were attributed to the presence or absence of Ca-bearing minerals in micro-veinlets sampled by the geochemical analysis (Oliver et al., 2004). A similar correlation is found at FC12, where the alteration selvage around the veins exhibit Ca depletion and little to no mass gain, while the veins themselves contain abundant Ca in the form of calcite and actinolite (Fig. 3.3, 3.4). These observations support the suggestion made in section 3.5.2 that Ca in the vein probably formed from a combination of local diffusional processes and infiltration by an externally-derived fluid.

One important difference is the relative mobility of Cu at FC12 compared to other Na-Ca assemblages described by Oliver et al (2004) in the EFB. While Oliver et al (2004) found Cu to be variable, Cu is consistently depleted in alteration selvages at FC12. This depletion suggests that some of the Cu in the veins may be a product of local diffusion. However, many of the veins contain considerably higher concentrations (1.2 wt% Cu for samples 246/86, 262.3/86 and 203/86) that cannot be accounted for by diffusional processes alone. A significant proportion of the Cu in Na-Ca veins at FC12 must have been introduced by an external fluid. In contrast to Cu, S is variable during alteration but is also consistently added in the veins, implying that the S was introduced by the fluid (Fig. 3.7, 3.8).

Oliver et al (2004) found that Fe was stripped from a variety of different rock types during Na alteration. Elemental profiles presented by Oliver and Bons (2001) showing Mg and Fe also indicate outward advection, or fluid cycling between different veins, where both Mg and Fe appear to be depleted in the alteration selvage and subsequently added in the vein. These patterns may indicate diffusional processes, however, Oliver and Bons (2001) showed that the Mg and Fe depleted in the wall rock does not equate with the same components added in the vein. Therefore diffusion was not the only processes acting on these particular components. Instead, they suggested that high pressure saline fluids interacted with Mg and Fe-bearing rocks, removed these components and precipitated them in an open fracture as a consequence of a pressure drop. At FC12, Fe was found to be immobile or slightly gained during alteration. Combined with the presence of magnetite, pyrite and chalcopyrite in the veins at FC12, these relationships suggest that no redistribution of Fe occurred. Similarly, the addition of Mg in the wall rock due to the replacement of clinopyroxene, orthopyroxene and biotite by chlorite also rules out any potential for diffusional processes controlling these components. At FC12, these components were clearly introduced by an externally derived fluid.

One interesting observation is the relative mobility of Na at FC12 compared to other alteration systems described by Oliver et al (2004); Rubenach and Lewthwaite (2002) and Oliver and Bons (2001). Although Na is enriched at FC12, the isocons and elemental profiles show that this enrichment is minor compared to other elements in the system. Taking into account the relative densities of the veins, alteration and wall rocks, these gains are even less significant (Fig. 3.8, 3.9). This differs from Na alteration described by the above authors where Na is highly enriched due to intense albite alteration. Instead, at FC12 most of the Na is contained within the veins themselves in the form of albite, while alteration is dominated by Mg enrichment in the wallrock. The lack of significant Na alteration around veins at FC12 may be an indication of host rock control, although this is doubtful considering albitisation of many different rock types (e.g. metapelites at the Snake Creek anticline and diorites at Ernest Henry) have been documented by numerous authors (Oliver et al., 2004; Rubenach and Lewthwaite, 2002). It is also unlikely that the chlorite is associated with a later alteration event as observation of the drill core clearly shows that chlorite is most intense immediately adjacent to the veins and does not appear to replace biotite.

3.7. DISCUSSION AND CONCLUSIONS

The mineral and chemical profiles of Na-Ca veins at FC12 clearly represent open system behaviour. The minerals in these veins are typically large and the fractures are wide (up to 1 m) and abundant in drill core, suggesting that the fractures were open for a sufficient amount of time and that the fluid flow rate was reduced enough for large crystals to nucleate from the vein walls. The alteration halos surrounding these veins reflect chemical disequilibrium of the fluid with respect to the surrounding wall rock, suggesting the fluid and much of the mass was derived from an external source.

These veins show similar chemical and mineralogical characteristics with other Na-Ca systems described by de Jong and Williams (1995), Mark (1998), Mark et al (2001), Rubenach and Lewthwaite (2002) and Oliver et al (2004). Williams (1994) and Oliver et al (2004) demonstrated that regional Na-Ca alteration consistently strips Fe, Ba, Sr and K from country rock, reflecting components which are enriched during Fe-K alteration peripheral to many of the IOCG deposits in the district (discussed further in chapter 5). Patterns of Cu, however, were found to be variable suggesting that Cu associated with Cu-Au mineralisation was not derived from fluid rock interaction, but derived directly from a magmatic source such as the Williams Batholith. A number of differences are apparent when comparing Na-Ca alteration at FC12 with regional Na±Ca assemblages. These differences include:

1) Cu is consistently depleted in the alteration selvage, but added in the vein.
2) S and Fe are variable in the alteration selvage but consistently added in the vein
3) Mg and REE are consistently enriched in the alteration selvage due to chloritisation and the breakdown of ilmenite to titanite, respectively
4) Na enrichment in veins at FC12 is minor compared to similar Na-Ca assemblages described by Oliver et al (2004) and others.

Figure 3.10 summarises the interpreted metasomatic processes associated with Na-Ca veining and alteration within the FC12 prospect. While K, Ba and Sr are all depleted during alteration at FC12, Fe is relatively immobile during wallrock alteration. The presence of magnetite, pyrite and chalcopyrite in the vein, however, suggests that overall, Fe was enriched during veining and must has originated from an external source. The patterns for Cu and S are also different to other Na-Ca systems documented by Oliver et al (2004), where Cu is consistently depleted in the alteration selvage due to the breakdown of chalcopyrite in the gabbro while S appears immobile. However, the high concentration of S and Cu in the veins at FC12 indicates that a significant proportion of both were introduced from outside the scale of the local alteration. The consistent depletion of Cu in wallrock alteration and high Cu concentrations in the veins at FC12 is testimony to the possible role of diffusion and small scale advection during Cu-Au mineralisation.

The above geochemical characteristics for Na-Ca veining and alteration at FC12 compared to regional Na-Ca assemblages described by Oliver et al., (2004) are interesting, especially considering the proximity of FC12 to the Ernest Henry deposit (~20 km). The relative mass transfer of elements such as Cu and Fe at FC12 compared

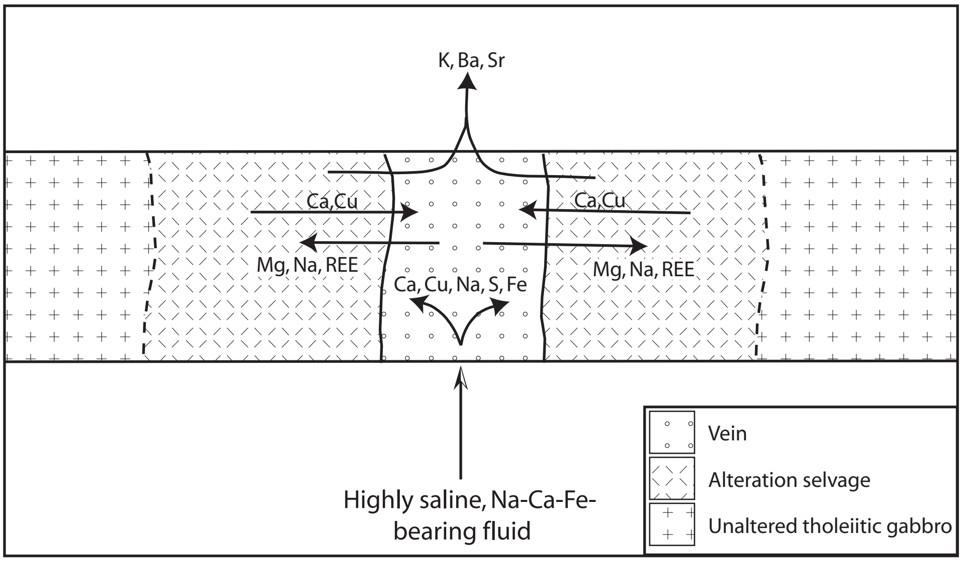

Figure 3.10: Model for the formation of Na-Ca veining and alteration within gabbroic rocks of the FC12 prospect. It is suggested here that an externally-derived fluid penetrated fractures possibly formed from high fluid pressures and interacted with the wall rock. These veins are highly symmetrical and vary in width from a couple of centimetres to 1 metre. The alteration selvage formed from the penetration of Mg and Na into the wall rocks to form chlorite and albite, respectively. K was released from the breakdown of biotite and muscovite and passed through the system. Ca, Fe, Cu and Na precipitated in the vein in calcite + actinolite + magnetite + pyrite + chalcopyrite + albite. Depletion of Ca and Cu in the wall rocks may indicate that these components moved via diffusion and contributed to the concentration of these components in the vein.

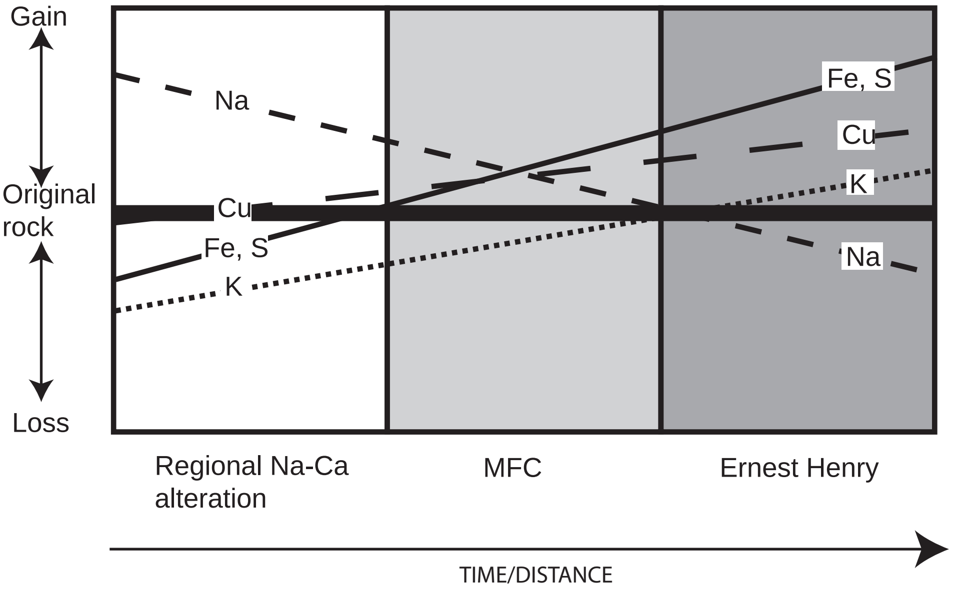

Figure 3.11: Cartoon representing the possible relationships between mass-transfer associated with regional-scale Na-Ca alteration, Na-Ca alteration at FC12 and Fe oxide (Cu-Au) mineralisation at and peripheral to the Ernest Henry deposit. Na is consistently added to the rocks while Fe and K are consistently released to the fluid. At FC12, Na enrichment is comparatively minor while Fe is enriched within Na-Ca veins. Fe oxide (Cu-Au) mineralisation at Ernest Henry is consistent with Fe and K enrichment and Na depletion from the wallrock. These relationships suggest that the FC12 prospect may represent a halfway region between the regional Na-Ca alteration and Fe oxide (Cu-Au) mineralisation endmembers.

to regional Na-Ca systems may reflect a number of different factors including host rock geochemistry, fluid chemistry and / or pressure-temperature conditions. These differences are highlighted by the preference for chlorite over albite in the alteration selvage, showing significant gain in Mg and only a small gain in Na compared to regional Na-Ca systems. It is unlikely that the host rock geochemistry alone was responsible for the different chemical patterns at FC12, as mass transfer associated with regional Na-Ca alteration is consistent regardless of rock type (Oliver et al., 1994). Another interpretation for these contrasting patterns is that Na-Ca alteration and veining at FC12 may represent the start of a depositional phase for Fe, S and Cu associated with Fe oxide (±Cu-Au) mineralisation peripheral to the Ernest Henry deposit (Fig. 3.11). Fluids responsible for Na-Ca alteration at FC12 may have interacted with enough wallrock, stripping Fe and K and releasing Na in the process that they no longer behaved like the more primitive Na-Ca fluids released straight from an intrusion (i.e. regional Na-Ca fluids). This hypothesis reflects the apparent genetic relationship between fluids responsible for Na-Ca alteration and Cu-Au mineralisation inferred by Pollard et al (1997). If Na-Ca alteration at FC12 is part of this depositional phase, this suggests two possible outcomes:

1) The temperature of the fluid has decreased over time; and / or
2) The fluid composition has changed due to earlier leaching of components associated with fluid-rock interaction.

As mentioned in chapter 2, the transition from clinopyroxene-rich to actinolite-rich Na-Ca alteration at the FC4NW prospect implies a down-temperature gradient over time. The presence of chlorite over albite as the dominant mineral in wallrock alteration at FC12 further supports this interpretation, suggesting the Na-Ca fluids being migrated over a significant period of time and cooled to temperatures where chlorite was stable instead of albite. In turn, a more ‘evolved’ fluid would also suggest that it had interacted with enough host rock to significantly change its chemistry through fluid-rock interaction and no longer had the physicochemical characteristics to strip Fe and K and precipitate Na at FC12.

So why wasn’t sufficient Fe oxide (±Cu-Au) mineralisation precipitated at FC12? Mark et al (1999) inferred the interaction of two distinct fluids at Ernest Henry, due in part to the complex mineral assemblage and chemistry associated with Cu-Au mineralisation. One possibility is that the Na-Ca-Fe fluids responsible for sulphide mineralisation at FC12 may only represent one fluid type containing the Fe and Cu but insufficient S to precipitate abundant Cu-bearing minerals, similar to the scenario portrayed by Perring et al (2000) for the Lightning Creek Cu-Au occurrence. Whether there was enough Cu in the fluids responsible for Na-Ca alteration at FC12 to produce significant Cu-Au mineralisation like at Ernest Henry is debatable. However, the geochemical patterns associated with these Na-Ca veins and alteration are clearly distinct from other regional Na-Ca assemblages. Thus, Na-Ca alteration at FC12 may represent one of the fluids responsible transporting and precipitating the Cu and Fe components at Ernest Henry. This possibility is tested further in the next chapters.

CHAPTER 4:

PHYSICOCHEMICAL CHARACTERISTICS OF FLUIDS AT THE MOUNT FORT CONSTANTINE EXPLORATION LEASE, NW QUEENSLAND, AUSTRALIA

PHYSICOCHEMICAL CHARACTERISTICS OF FLUIDS AT THE MOUNT FORT CONSTANTINE EXPLORATION LEASE, NW QUEENSLAND, AUSTRALIA

4.1. INTRODUCTION

Fluid inclusion analysis represents an important tool for investigating the temperature, pressure and composition of fluids associated with hydrothermal mineralisation. The proximity between the MFC exploration lease and the Ernest Henry (Cu-Au) deposit (Fig. 4.1) suggests that fluids associated with hydrothermal mineralisation at both areas may be genetically linked. In particular, the relationship between sulphide mineralisation and Fe oxide metasomatism at MFC and Fe oxide (±Cu-Au) mineralisation at Ernest Henry is not yet understood.

To date, detailed fluid inclusion studies in the Eastern Fold Belt (EFB) have predominantly concentrated on infill assemblages associated with IOCG deposits (e.g. Osborne, Eloise, and Ernest Henry) plus sub-economic Cu-Au occurrences such as Brumby and Lightning Creek (Adshead, 1995; Foster, 1995; Baker, 1998; Rotherham, 1997; Mark et al., 1999; Perring et al., 2000). In addition, Pollard et al (1997) and Blake et al (1997) studied fluid inclusions from various Na-Ca assemblages at Muramungee Creek and peripheral to the Ernest Henry deposit. In the present study, the physicochemical characteristics of fluid inclusions from weakly mineralised Na-Ca assemblages and barren Fe oxide-rich rocks from the MFC exploration lease will be compared to similar Na-Ca assemblages as well as the major IOCG deposits within the EFB. This study will provide valuable insight into the relationship between fluids responsible for Cu-Au mineralisation and spatially related Na-Ca alteration, and help determine whether the two are genetically linked.

4.2. FLUID INCLUSION PARAGENESIS AND SAMPLE SELECTION

Overall, six distinct types of fluid inclusions have been recognised from the analysis of five polished thin sections from the FC4NW prospect and Fe oxide-rich rock in outcrop. Sample numbers and descriptions are presented in table 4.1 while a more rigorous description of Na-Ca alteration at FC4NW and Fe oxide-rich rocks in outcrop at MFC is described in chapter 2. Unfortunately, no workable samples containing quartz and/or large enough fluid inclusions were found within the FC12 prospect.

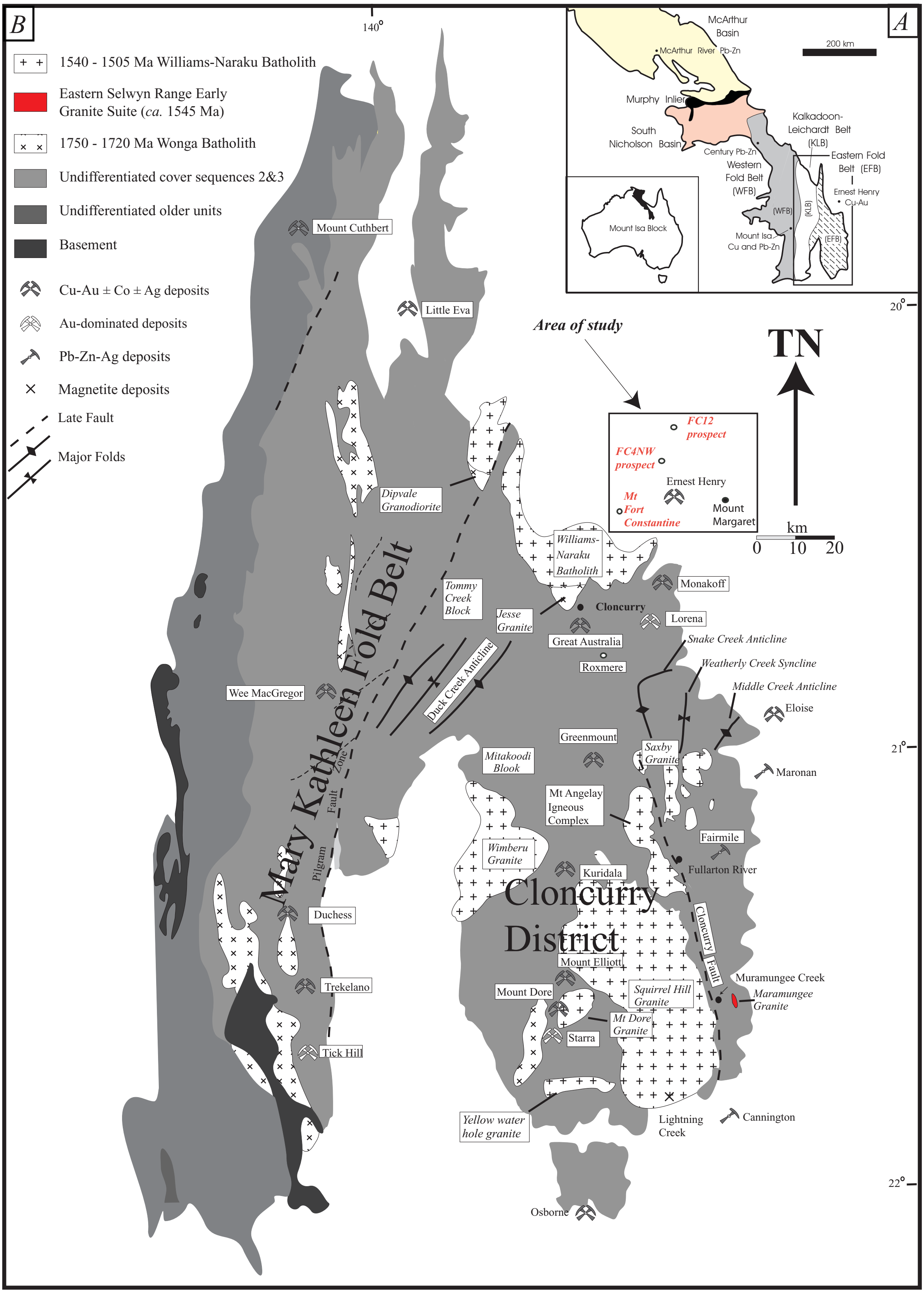

Figure 4.1. A. Tectonostratigraphic divisions of the Mount Isa Inlier, Queensland. B. Enlargement and simplified geology of the Eastern Fold Belt with localities of mineral deposits. Compiled from published AGSO maps and modified by Williams (1998). Includes locations of areas relevant to this study.

Sample	Location	Rock type	Mineralogy	Host mineral
MFC125/27	Hole No: MFC97027 125 m depth	Na-rich granite	Clinopyroxene-albite-quartz-pyrite vein cut by hematite-stained albite alteration	Quartz
MFC002	Magnetite pit south of the MFC hill (outcrop)	Fe oxide-rich rock (ironstone)	Massive fine-grained hematite with minor apatite and actinolite	Apatite
MFC108/27	Hole No: MFC97027 108 m depth	Fine-grained meta-sedimentary rock	Clinopyroxene-titanite-quartz-albite-pyrite-chalcopyrite vein cut by actinolite-magnetite-calcite-quartz-pyrite vein. Both veins cut by hematite-stained albite alteration.	Quartz
MFC259.7/52	Hole No: MFC98052 259.7 m depth	Fine-grained meta-sedimentary rock	Clinopyroxene (altering to actinolite)-quartz-titanite-albite-pyrite vein. Cut by later hematite-stained albite alteration	Quartz
MFC202.2/91	Hole No: MFC99091D 202.2 m depth	Fine-grained meta-sedimentary rock	Clinopyroxene-quartz-titanite-pyrite-calcite-albite cut by later actinolite-magnetite vein. Both veins cut by hematite-stained albite alteration	Quartz

Table 4.1. Description and location of the fluid inclusion samples studied from FC4NW

A classification scheme for the different types of fluid inclusions observed at FC4NW and outcrop was developed based on mineral paragenesis criteria outlined by Reodder (1984):

Primary: Inclusions formed synchronous with the growth of the host mineral. These occur randomly throughout the host mineral either as isolated groups or along growth planes. Type 1 and most type 2 fluid inclusions in this study are primary.

Secondary: Inclusions incorporated into the host by a later process. These inclusions commonly occur as inclusion trails that cut grain boundaries. Type 4a and 4b and most type 3a inclusions in this study are interpreted as secondary.

Pseudosecondary: Inclusions that are trapped during fracturing before the host mineral have stopped growing. These inclusions commonly form inclusion trails but do not cross grain boundaries (Shepherd et al., 1985). Examples of both type 2 and 3a fluid inclusions in this study are interpreted as pseudosecondary.

4.2.1. Na-Ca alteration

Four of the thin sections (MFC125/27, MFC108/27, MFC259.7/52, and MFC202.2/91) represent clinopyroxene-rich Na-Ca alteration that has been variably replaced by later actinolite (Fig. 4.2). In all samples, quartz appears to be associated with the clinopyroxene-rich Na-Ca alteration phase and is the host for all fluid inclusions analysed from the FC4NW prospect. No samples containing significant sulphide mineralisation associated with amphibole-rich Na-Ca alteration could be analysed as none contained any quartz with usable fluid inclusions. As described in chapter 2, however, both clinopyroxene- and actinolite-dominant Na-Ca alteration are most likely related to the same fluid but reflect a down temperature gradient. Hence, it is interpreted here that fluid inclusions in these samples are at least partly representative of fluids associated with the main sulphide mineralisation event at FC4NW. Four fluid inclusion types were observed in Na-Ca alteration assemblages:

Type 1: Multi-solid fluid inclusions are found in samples MFC259.7/52, MFC125/27, MFC202.7/91 and MFC108/27, although examples in the latter three samples were rarely observed (Fig. 4.3). According to the paragenetic criteria of Roedder (1984), type 1 fluid inclusions are probably primary and therefore contain fluids that were trapped during the main growth phase of clinopyroxene-rich Na-Ca alteration. They consist of liquid, a vapour bubble and up to 4 daughter phases (Fig. 4.4a. b). A halite cube is always present and exhibits a large cubic habit (Fig. 4.4a, b), and commonly occupies up to 50% of the total volume of the inclusion. Other daughter phases were identified in some inclusions only and include sylvite identified by its disappearance upon heating the inclusion between 90 and 150ºC (discussed later). Hematite and hedenbergite were each identified via laser Raman spectrometry. Another mineral was analysed by laser Raman and exhibited a spectrum similar to garnet. In the multi-solid inclusions, the 3-4 daughter phases commonly occupy up to 80% of the total volume of the inclusion. Representative spectra of each of these daughter phases are shown in figure 4.5. No other gaseous phases were identified via laser Raman suggesting the liquid was pure H_2O.

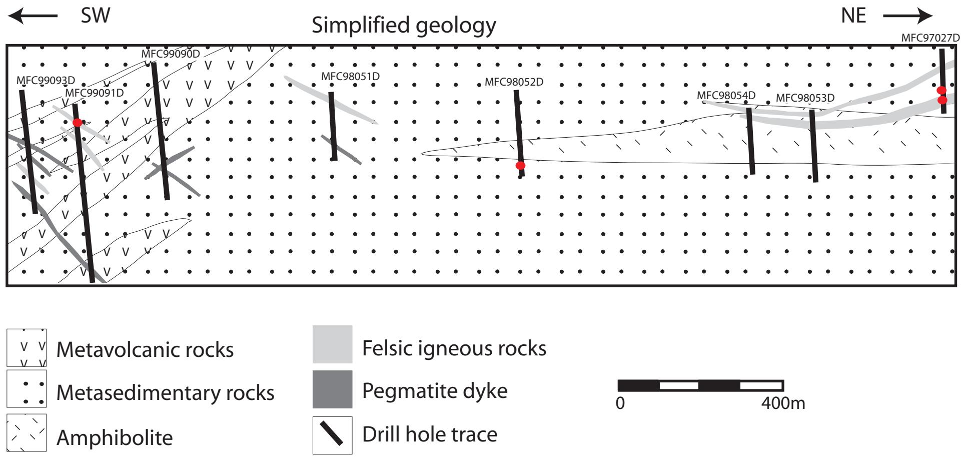

Figure 4.2. Cross-section of the FC4NW prospect showing the major rock types and the location of the samples used for fluid inclusion experiments in this study.

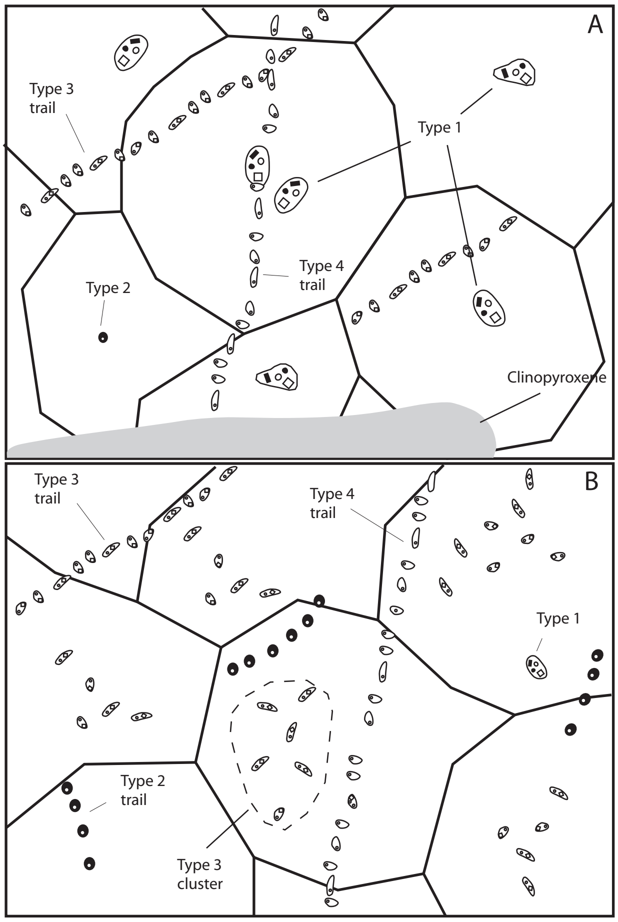

Figure 4.3. A. A schematic representation of the spatial association of type 1, 2, 3a and 4a inclusions based on sample MFC259.7/52. Type 1 inclusions occur in clusters of up to 5 inclusions, while type 2 inclusions are rarely observed. Type 3a inclusions occur as trails which occasionally cross grain boundaries. Type 4a inclusions form trails that commonly cross grain boundaries. B. A schematic representation of the spatial association of type 1, 2, 3a and 4a inclusions based on samples MFC125/27, MFC108/27 and MFC202.9/91. Type 1 inclusions are rarely observed and form small clusters of 1 to 2 inclusions. Type 2 inclusions occur as clusters and inclusion trails that rarely cross grain boundaries. Type 3a inclusions form large clusters of ~50 inclusions as well as inclusion trails that rarely cross grain boundaries. Type 4a inclusions form inclusions trails that commonly cross grain boundaries.

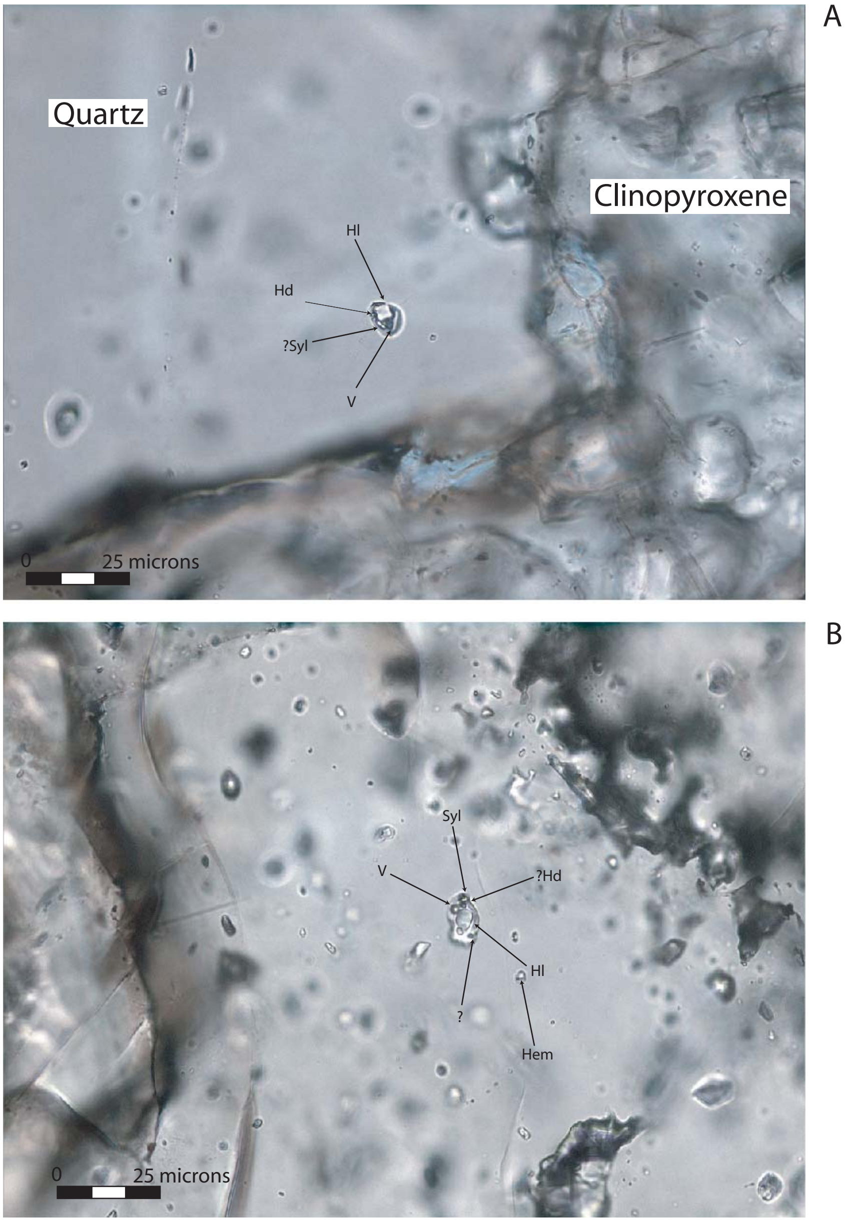

Figure 4.4. Photomicrographs of multi-solid (type 1) fluid inclusions from the FC4NW prospect. All photos were taken from sample MFC259.7/52.

A) One type 1 multi-solid fluid inclusion located near the boundary between a quartz and a clinopyroxene grain. Inclusion is approximately 15 µm in size and contains a hedenbergite crystal identified by laser Raman spectrometry as well as a large halite crystal, a vapour bubble and sylvite (?) crystal (Plane-polarised light: PPL).

B) Large (~20 µm) type 1 multi-solid fluid inclusion with halite crystal, vapour bubble as well as a sylvite and a hedenbergite crystal. Small dark-green coloured daughter phase is unknown but may be another hedenbergite crystal. Small inclusion to the lower right contains a small hematite crystal identified by laser Raman (PPL).

Abbreviations: Hl=halite, Hd=hedenbergite, Syl=sylvite, V=vapour bubble, Hem=hematite. Abbreviations after Kretz (1983).

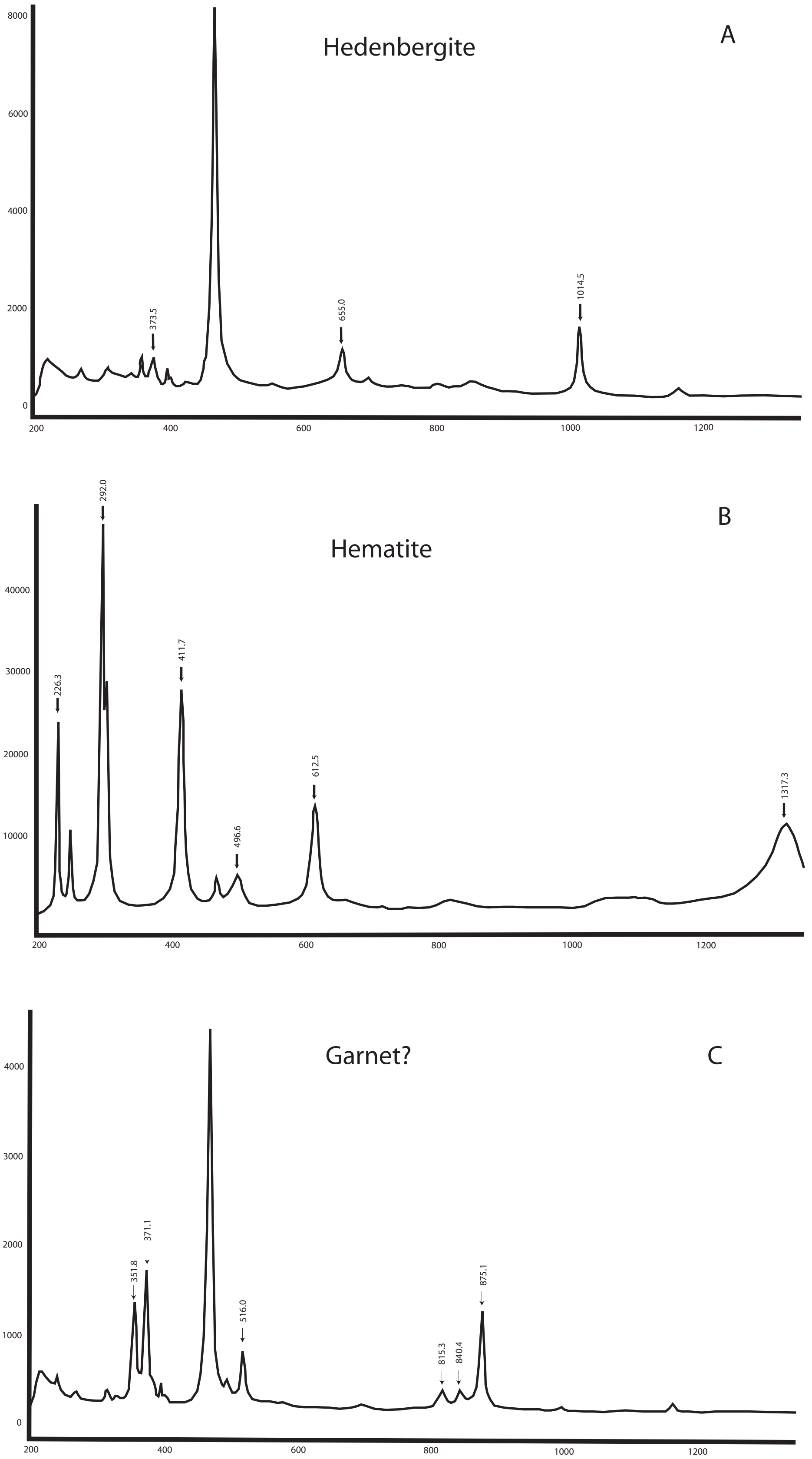

Figure 4.5. Laser Raman spectra of hedenbergite and hematite crystals identified in type 1 multi-solid inclusions (see figure 3). Figure C exhibits a spectra that may represent garnet. All spectra were taken from sample MFC259.7/52.

Type 2: CO_2-rich fluid inclusions range in size from 5 to 15 μm. They occur as both isolated clusters and small inclusions trails (Fig. 4.6) suggesting that some inclusions may be pseudosecondary and formed before the quartz host stopped growing. These inclusions were rarely observed in sample 259.7/52 (Fig 4.3b), but were commonly found in samples MFC125/27, MFC202.7/91 and MFC108/27 (Fig, 4.3a). Laser Raman spectrometry showed these inclusions to be pure CO_2, with no other gaseous phases present.

Type 3a: halite-bearing fluid inclusions represent the most numerous of the four types identified in Na-Ca assemblages at FC4NW and are found in all four samples. They commonly occur as massive clusters as well as inclusion trails that occasionally cross grain boundaries (Fig. 4.3a, 4.7b). Halite crystals commonly occupy up to 50% of the total volume of the inclusion and range in size from <5 to 25 μm (Fig. 4.7a). The timing of type 3 inclusions relative to the mineral paragenesis is uncertain, although they may have formed during the replacement of clinopyroxene by actinolite. No gaseous phases were identified via laser Raman spectrometry suggesting pure H_2O.

Type 4a: Two-phase fluid inclusions are typically very small (<10 μm) but are occasionally up to 25 μm (Fig. 4.8a, b). Larger examples of type 4 inclusions exhibit an irregular and angular shape. These inclusions are clearly secondary and cut all the previous inclusion types (Fig. 4.3a). No gaseous phases were identified by laser Raman spectrometry suggesting these inclusions are pure H_2O.

4.2.2. Fe oxide metasomatism

Sample MFC002 represents a hematite + magnetite + actinolite + apatite Fe oxide-rich rock from outcrop south of the Mount Fort Constantine hill (~15 km southwest of Ernest Henry) (Fig. 4.9). Only two fluid inclusions types were identified within small apatite grains from this sample and include halite-bearing and 2 phase inclusions. Fe oxide metasomatism in outcrop at MFC is mineralogically similar to Na-Ca alteration observed elsewhere in the MFC exploration lease suggesting they may be related. Due to the small size of most of the apatite hosts, determining the paragenesis of these inclusions proved difficult. No type 1 or 2 inclusions were observed in this sample. However, the two fluid inclusion types that were observed appear similar to the type 3a

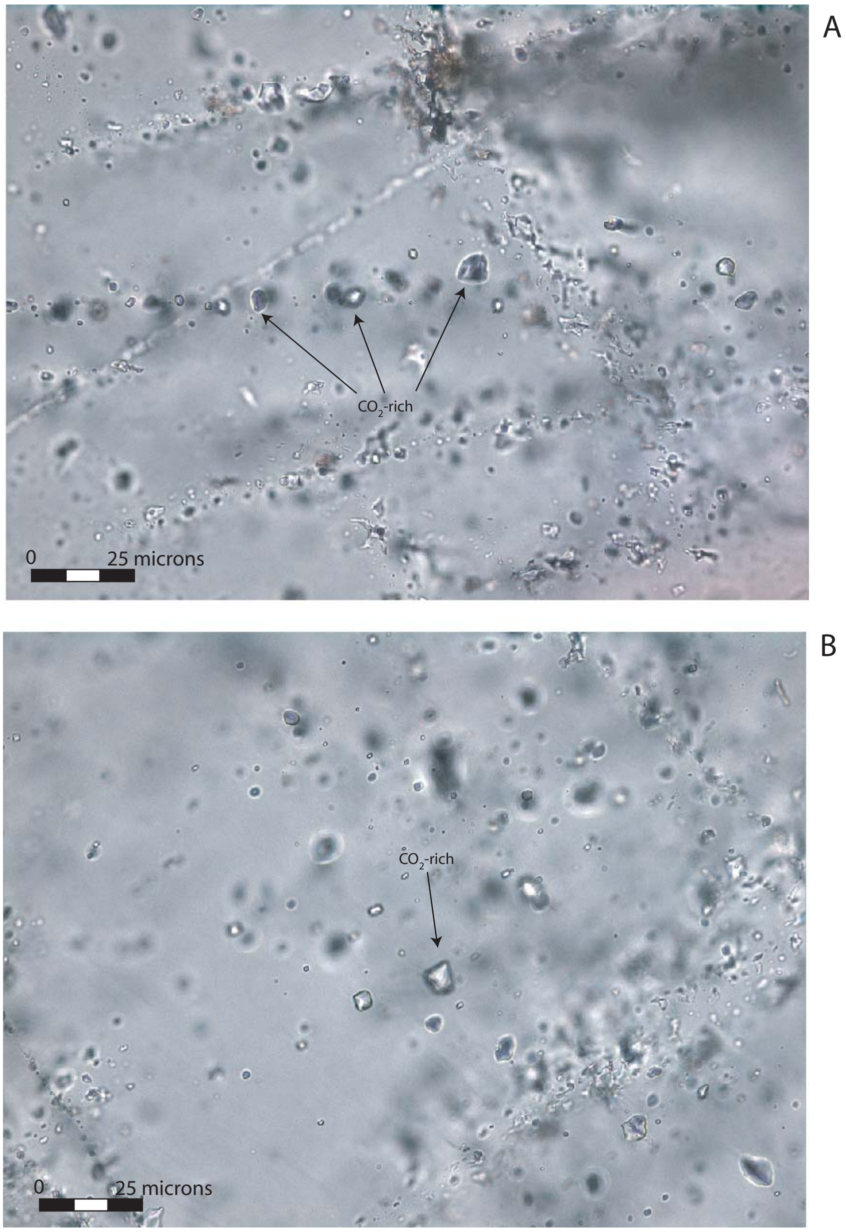

Figure 4.6. Photomicrographs of CO_2-rich (type 2) fluid inclusions from the FC4NW prospect. Both photos were taken from sample MFC180/27.
A) A small trail of CO_2-rich fluid inclusions. These inclusion types typically do not cross grain boundaries (Plane polarised light: PPL).
B) Small cluster of CO_2-rich fluid inclusions (PPL).

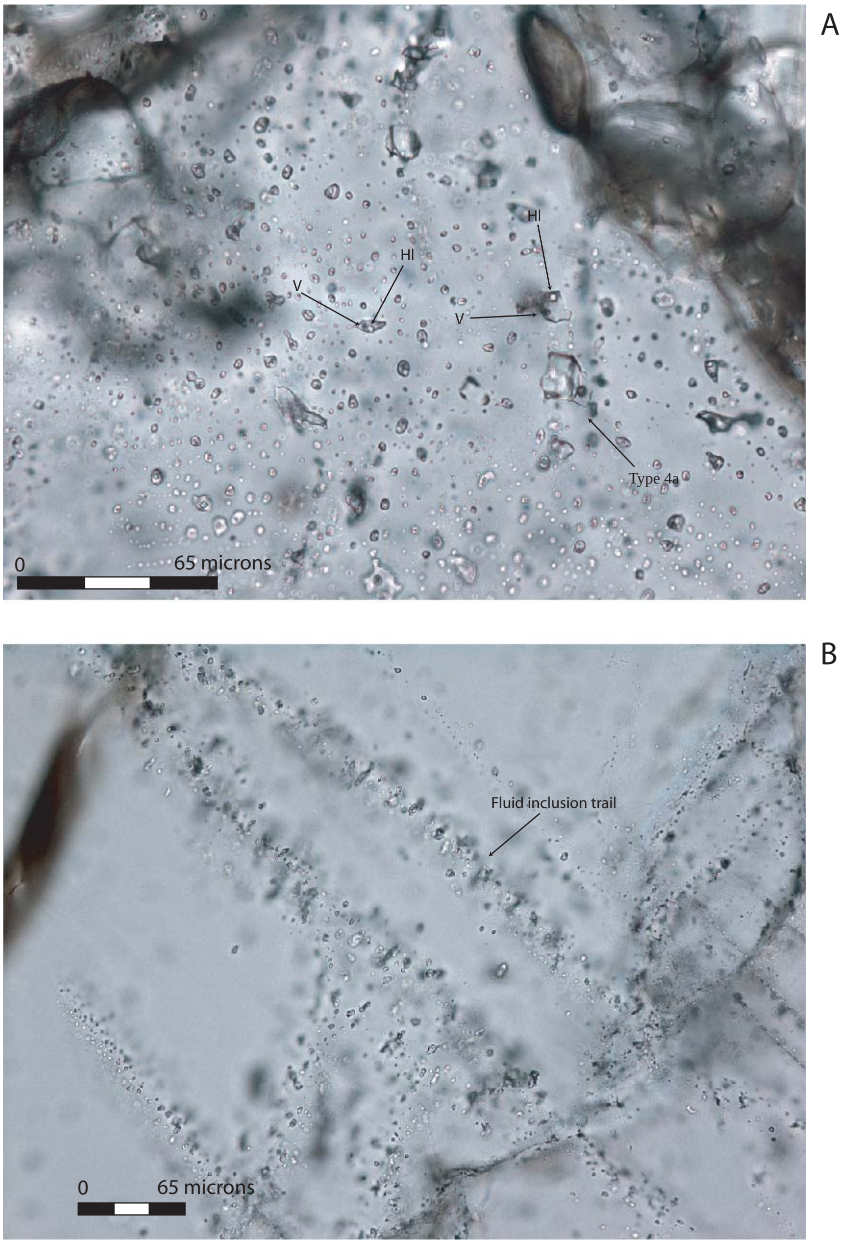

Figure 4.7. Photomicrographs of halite-bearing (type 3a) fluid inclusions from the FC4NW prospect.

A) Sample MFC108/27. Large cluster of type 3 halite-bearing fluid inclusions along with a larger irregular shaped 2-phase (type 4) fluid inclusion (Plane-polarised light: PPL).

B) Sample 259.7/52. Several prominent type 3 inclusion trails, where one clearly crosses a quartz grain boundary (PPL).

Abbreviations: Hl=halite, V=vapour bubble. Abbreviations after Kretz (1983).

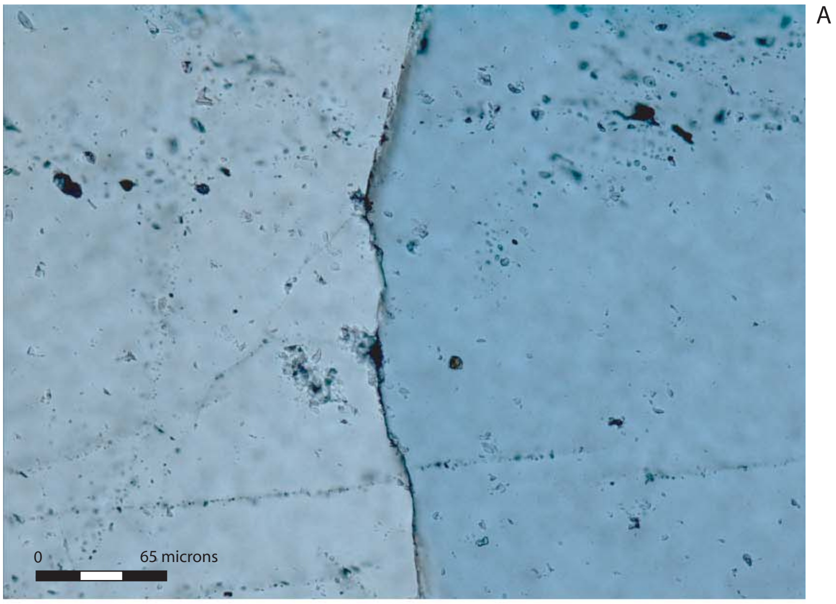

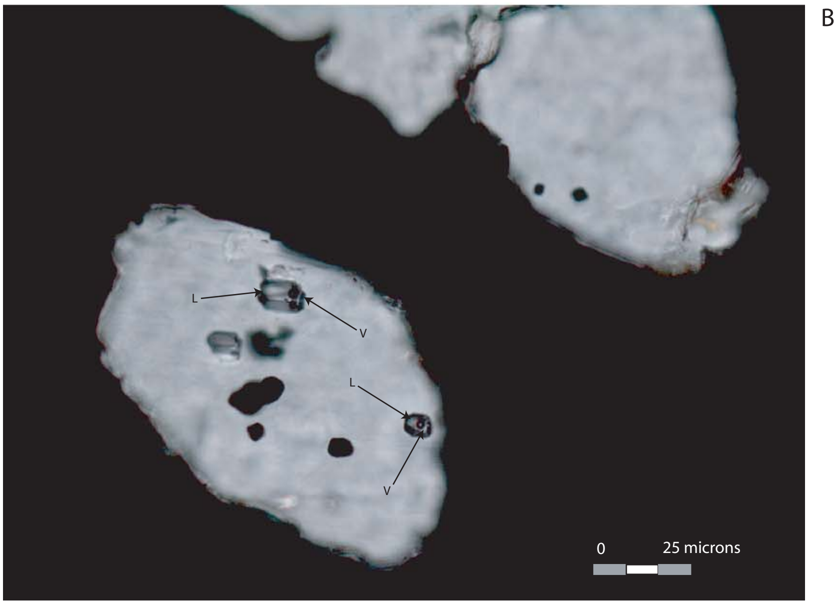

Figure 4.8. Photomicrographs of type 4a and 4b 2-phase fluid inclusions from the FC4NW prosect and an Fe oxide-rich rock from MFC outcrop.
A) Sample 202.2/91. Small inclusion trail composed of type 4 fluid inclusions clearly crossing quartz grain boundary Cross-polarised light: XPL).
B) Sample MFC002. Two 2-phase fluid inclusions within an apatite crystal from an Fe oxide-rich rock (Plane-polarised light: PPL).
Abbreviations: L=liquid, V=vapour bubble. Abbreviations after Kretz (1983).

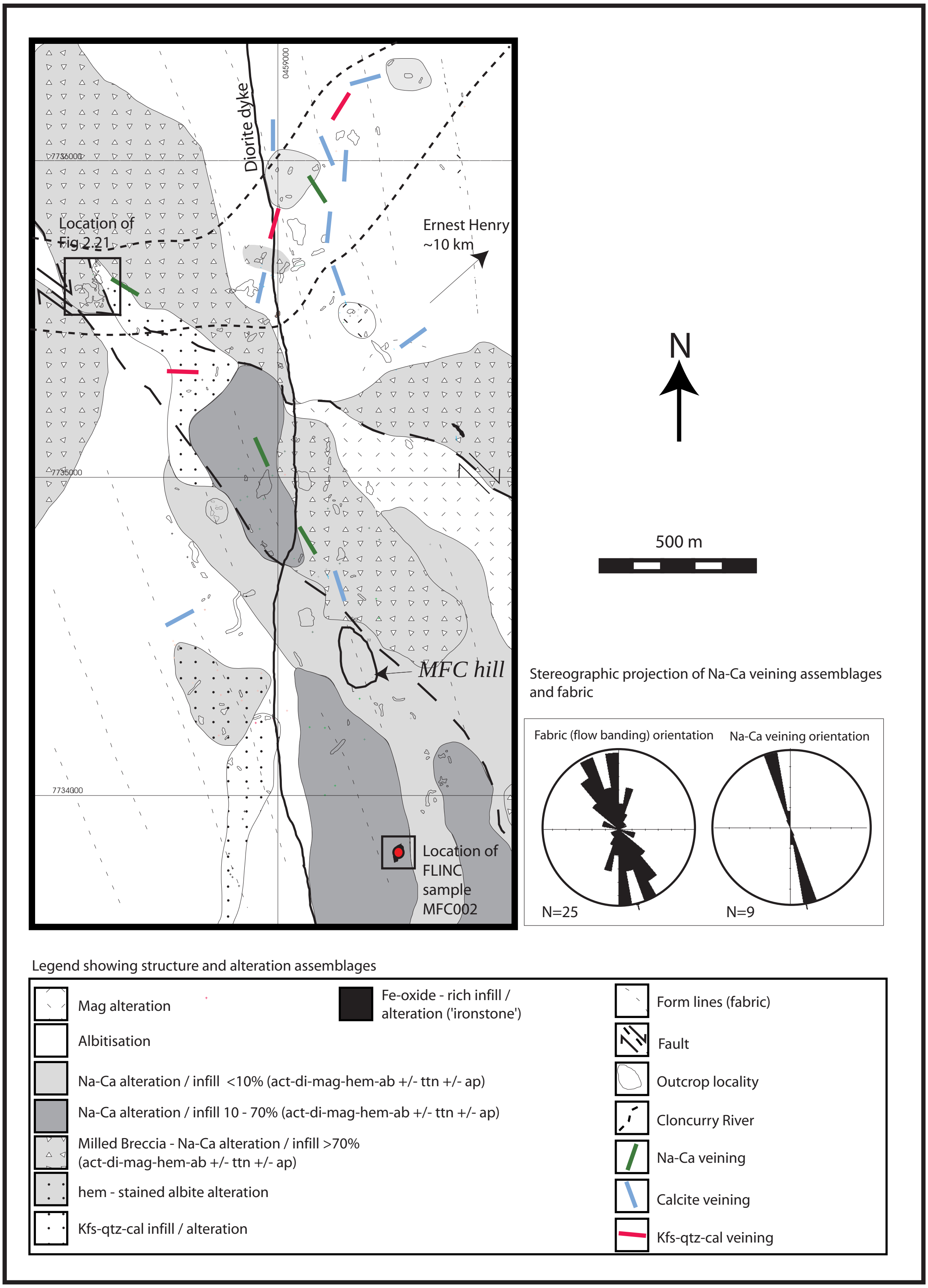

Figure 4.9. Interpreted geological map showing the distribution of alteration in outcrop at MFC. The total exposed outcrop = <5 %, and a combination of geological mapping and geophysical interpretation were used to construct interpreted boundaries. Note two SE-NW trending faults that may have acted as conduits for fluids associated with Na-Ca and K alteration. Red dot shows the location of sample MFC002 used for fluid inclusion experiments in this study. act=actinolite, di=diopside, mt=magnetite, hem=hematite, ab=albite, ttn=titanite, ap=apatite, cal=calcite, qtz=quartz, Kfs=K feldspar, mag=magnetite. Abbreviations after Kretz (1983).

and 4a inclusions described above. Fluid inclusion types found in the Fe oxide-rich rock from outcrop at MFC include:

Type 3b: only four halite-bearing fluid inclusions were observed in sample MFC002 and measured 5 to 7 µm. Halite crystals occupy approximately 40 to 50% of the total volume of the inclusions and range in size from 5 to 7 µm. These inclusions were found in separate apatite grains so their apparent paragenetic timing with respect to Fe oxide metasomatism is uncertain.

Type 4b: Twelve 2-phase fluid inclusions were found in sample MFC002 and were typically very small (<5 µm) (Fig 4.8b). No indication of their paragenesis with respect to the alteration assemblage is apparent; however, they are most likely to be later than the period of mineral precipitation.

4.3. MICROTHERMOMETRIC ANALYSIS AND SALINITY ESTIMATES OF FLUID INCLUSIONS

Microthermometric measurements of fluid inclusions were made on doubly polished sections using a Linkam MDS600 heating/freezing stage and a Linkam TS1500 high-temperature stage at the School of Earth Sciences, James Cook University. The Linkam MDS heating/freezing stage is coupled to a BX51 Olympus polarizing microscope, with liquid nitrogen as the cooling agent (minimum temperature of -195ºC). A PC performs all stage operations with Linksys software connected to an XY-motor control. The stage was calibrated with pure H_2O and mixed CO_2-H_2O in synthetic fluid inclusions. Reproducibility of the melting temperatures for both pure H_2O (0ºC) and pure CO_2 (-56.6ºC) was within ±0.3ºC. In total, heating and freezing experiments were performed on 159 fluid inclusions of type 1 2, 3 and 4 in both quartz and apatite from thin section wafers. Data are tabulated in appendix 5.

4.3.1. Type 1: multi-solid fluid inclusions

17 of the 22 type 1 fluid inclusions were measured from sample MFC 259.7/52. The other 5 were measured from samples MFC125/27 (4) and MFC202/91 (1). To avoid decrepitation problems, freezing experiments were performed first on all inclusions, and then heating was performed on the same inclusions. Unfortunately, most of these inclusions decrepitated when heated (between +150 to +300ºC), probably as a result of

overpressuring due to fluid expansion. Inclusions were initially frozen down to -150ºC, where temperatures of complete freezing were observed for 6 inclusions between –91.5 to –77.4ºC. Upon heating, initial melting (Tm) was difficult to observe but was accompanied by a brown colour indicating the presence of $CaCl_2$ in the fluid (confirmed by PIXE, see below) and ranged from –75 to -50ºC. Ice melted between –43.9 to –20.5ºC (Fig. 4.10), while hydrohalite melted between +1.7 to +14.5ºC (Fig. 4.11). Dissolution of sylvite was observed in two inclusions at +94.6ºC and +148.4ºC (Fig. 4.12). Homogenisation of the vapour bubble occurred prior to the dissolution of the halite crystal. Vapour homogenisation occurred between +73.4 and +293ºC (Fig. 4.12), while halite dissolution occurred between +260.6 and +452.3ºC (Fig. 4.12). An approximation of the salinity of the fluid can be determined by plotting halite dissolution temperatures on a solubility curve for NaCl (Shepherd et al., 1985) giving a range of salinities between 35 and 50 wt% NaCl. Other daughter phases (hematite, hedenbergite, garnet?) did not dissolve below +500ºC and may represent accidentally trapped minerals.

4.3.2. Type 2: CO_2-rich fluid inclusions

Type 2 fluid inclusions were measured from samples MFC202.2/91 (16) and MFC108/27 (31) (appendix 5). No CO_2-rich inclusions were large enough for microthermometric analysis from sample MFC259.7/52. Type 2 inclusions were cooled down to -100ºC and upon heating, the inclusions melted between –56.7 and –56.9ºC (all within error of 56.6ºC) indicating they mostly consisted of pure CO_2. Homogenisation of the vapour bubble occurred between –12.2 and +21.5ºC (Fig. 4.13). No other phase changes were observed upon further heating. Despite the large range in temperatures, there was no observable difference between CO_2-rich inclusions that occurred within clusters or as small inclusion trails. Similar homogenisation temperature ranges of CO_2-rich inclusions have been documented in other alteration systems in the EFB (Adshead, 1995; Rotherham et al., 1998; Mark et al, 1999) suggesting this is a common occurrence (see below).

4.3.3. Type 3a: Single-solid (halite-bearing) fluid inclusions

Type 3a fluid inclusions were measured from samples MFC 259.7/52 (8), MFC202.2/91 (7), MFC108/27 (6) and MFC125/27 (30) (appendix 5). These inclusions were initially frozen to -150ºC and upon heating, a brown colouration appeared at the

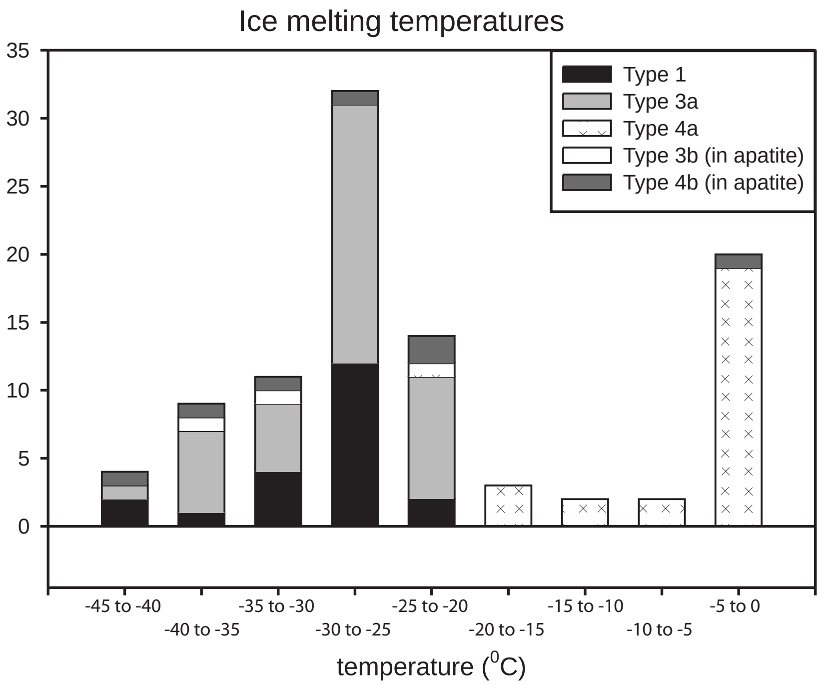

Figure 4.10. Histogram of ice melting temperature ranges for all fluid inclusion types in this study.

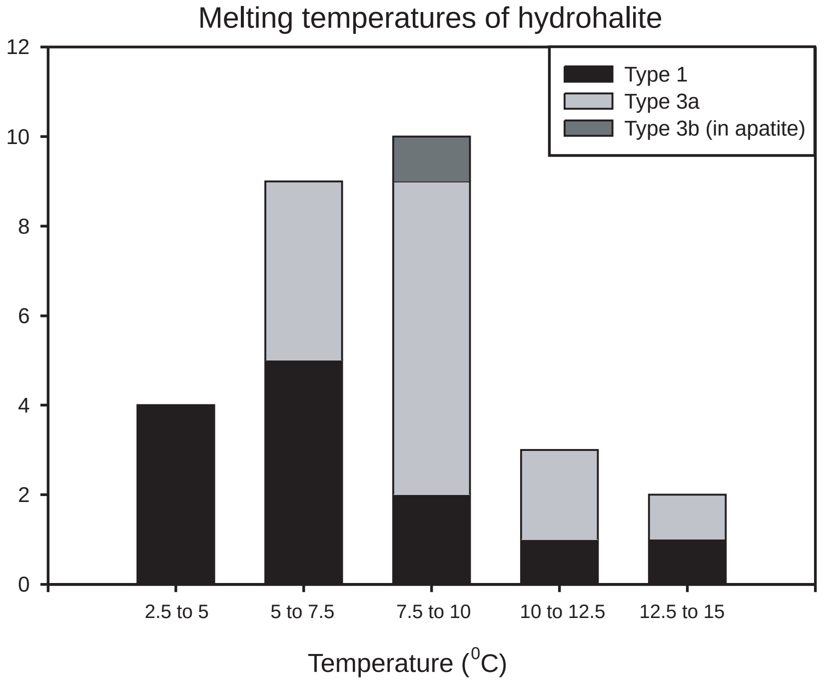

Figure 4.11. Histogram of melting temperatures of hydrohalite (Thh) from type 1, 3a and 3b fluid inclusions.

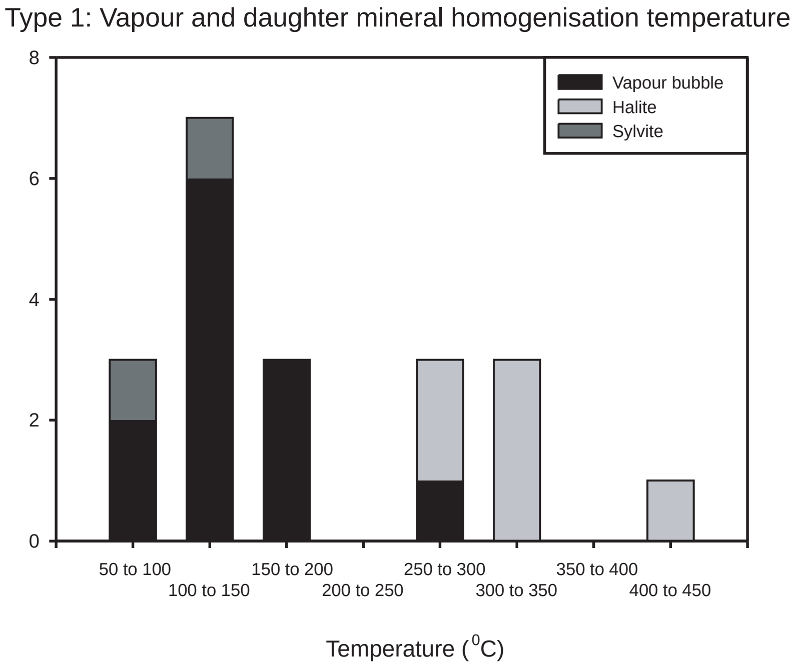

Figure 4.12. Histogram of vapour and daughter mineral homogenisation temperatures for type 1 fluid inclusions. Most type 1 fluid inclusions decrepitated between +150 to 300ºC. Note that hematite and hedenbergite did not homogenise under 500ºC and may represent accidently trapped minerals. Only two sylvite crystals homogenised upon heating. Halite dissolution (Ths) is regarded as the homogenisation temperature. See appendix 5 for fluid inclusion data tables.

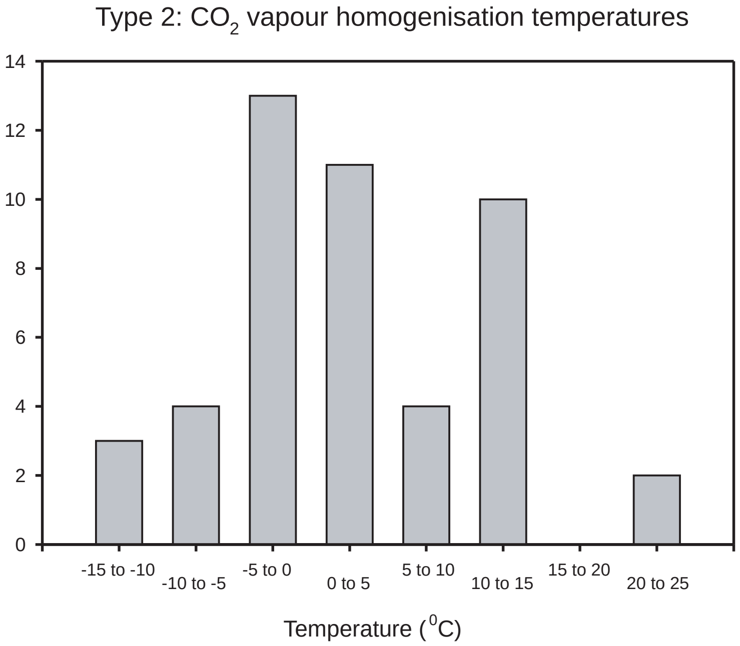

Figure 4.13. Histogram of vapour homogenisation (Th) for CO_2-rich type 2 fluid inclusions. A wide range exists between -12.2 to +21.5ºC. See Appendix 5 for fluid inclusion data tables.

time of initial melting (between –76.6 to -45ºC), indicating the presence of $CaCl_2$ in the fluid. These temperatures are mostly approximate as the exact point of initial melting was commonly difficult to distinguish. Ice melted between –43.7 to –20.4ºC (Fig. 4.10), while hydrohalite melted between +5.7 to +12.1ºC (Fig. 4.11). Further heating of these inclusions commonly resulted in decrepitation (between +150 to +300ºC), perhaps due to overpressuring caused by fluid expansion. As a result, less than half of all the inclusions homogenised completely. As was the case with the type 1 inclusions, vapour homogenisation always occurred before halite dissolution, with vapour homogenisation occurring between +104.5 to +249.3ºC and the disappearance of halite occurring between +210 to +278.9ºC (Fig. 4.14). The solubility of NaCl curve by Shepherd et al (1985) suggests salinities for type 3a inclusions within Na-Ca assemblages range between 32 and 37 wt % $NaCl_{equiv}$.

4.3.4. Type 4a: 2 phase (liquid + vapour) fluid inclusions

Type 4a inclusions were analysed mostly from samples MFC125/27, MFC202.2/91, MFC259.7/52 and MFC108/27. All inclusions were cooled to -150ºC and upon heating exhibited first ice melting temperatures of between –50ºC to –30ºC. Final ice melting of type 4a inclusions occurred at temperatures between –19.6 to –1.1 (Fig. 4.10). Vapour homogenisation ranged from 125 to 384.5ºC although most temperatures were between 125 and 198ºC (Fig. 4.15). Using equations by Potter et al (1978) to calculate salinities from final melting temperatures, these inclusions contain between 2 to 22 wt % NaCl.

4.3.5. Type 3b: Single-solid (halite-bearing) fluid inclusions

The only type 3b fluid inclusion measured in apatite from MFC002 that didn’t decrepitate recorded a vapour homogenisation temperature of +114°C (Fig. 4.14). Halite failed to homogenise in this inclusion suggesting metastable behaviour.

4.3.6. Type 4b: Two-phase (liquid + vapour) fluid inclusions

The small size of type 4b fluid inclusions in sample MFC002, in addition to the host mineral being apatite, meant phase changes during heating and cooling was difficult to observe. Nevertheless, some differences with respect to type 4a inclusions described above were noted. Type 4b fluid inclusions exhibited initial melting temperatures that were significantly lower (~-70ºC) compared to the type 4a inclusions. These low

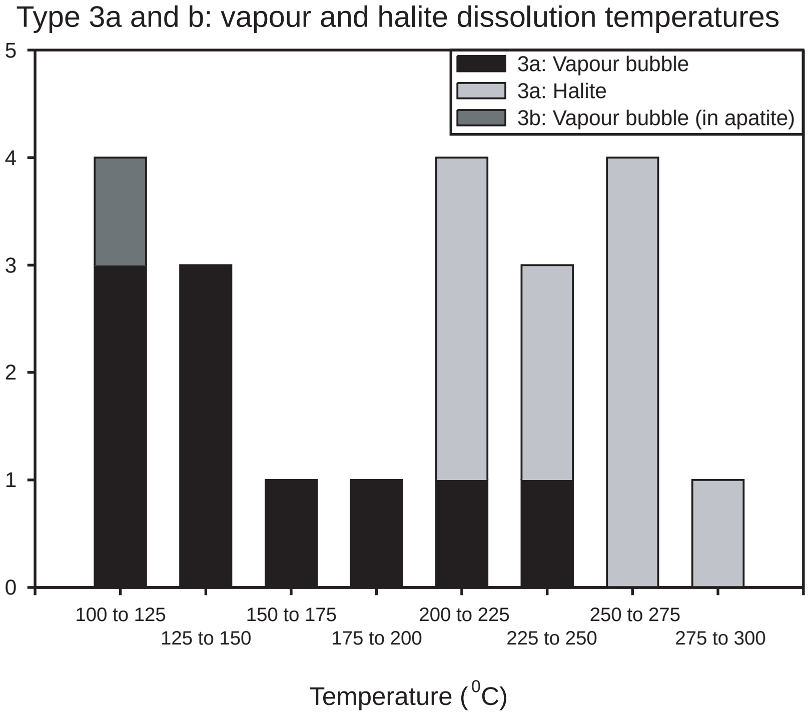

Figure 4.14. Histogram of vapour and halite homogenisation temperatures of halite-bearing type 3a and 3b fluid inclusions. Most type 3a fluid inclusions decrepitated between +150 to 300ºC. Halite dissolution is regarded as the maximum homogenisation temperature for these inclusions. See appendix 5 for fluid inclusion data tables.

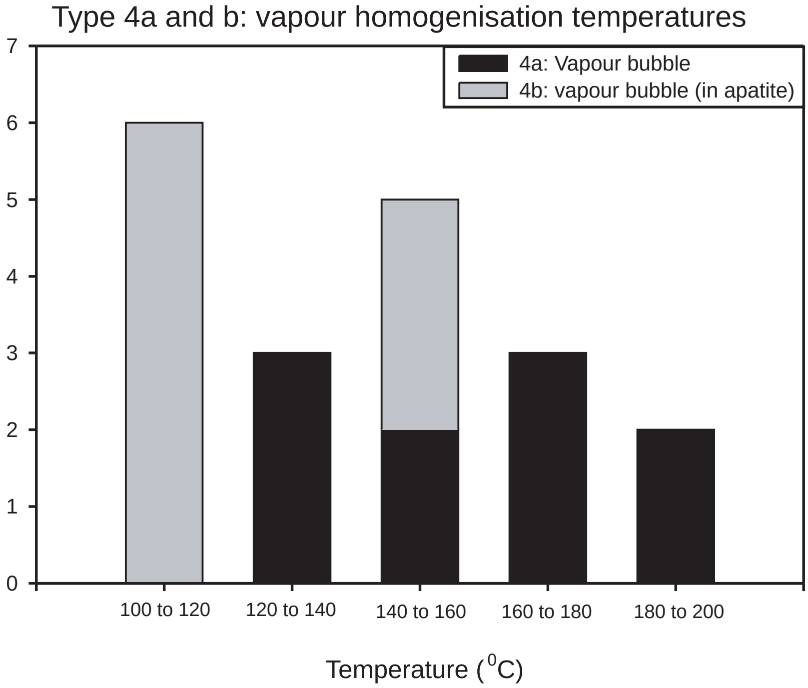

Figure 4.15. Histogram of vapour homogenisation temperatures for type 4a and 4b fluid inclusions. Note vapour homogenisation temperatures are lower for 4b than the 4a fluid inclusions from the FC4NW prospect. See appendix 5 for fluid inclusion data tables.

temperatures may suggest that $CaCl_2$ is present in the fluid, although none appeared to exhibit a brown colour during heating. The melting temperature of ice also differed between type 4a and 4b fluid inclusions. Final melting temperatures of type 4b inclusions varied considerably (between –53.1 to –2.1ºC) (Fig. 4.10), while vapour homogenisation temperatures ranged between 110.2 and 147.2ºC (Fig. 4.15). Calculated salinities using the equation by Potter et al (1978) yielded a wide range (3.5 to 54 wt% NaCl), although these values may also be affected by visibility problems as discussed above.

4.3.7. Estimation of pressure

Pressures associated with fluid inclusions at the time of formation can be estimated by constructing isochores on a pressure-temperature diagram. Isochores are defined by homogenisation and/or melting temperatures, depending on the type of fluid inclusion in question. For type 2 inclusions, isochores were calculated from the Holloway (1981) equation of state and the CO_2 chemical system using the MacFlincor computer program from minimum, maximum and average homogenisation temperatures presented in appendix 5 (Fig. 4.16). Isochores calculated for type 1 and 3a fluid inclusions were calculated using the Zhang and Frantz (1989) equation of state and the H_2O-NaCl chemical system from the average halite dissolution and vapour homogenisation temperatures from appendix 5 (Fig. 4.16). Isochores for type 4a fluid inclusions were also calculated using the Zhang and Frantz (1989) equation of state and the H_2O-NaCl chemical system from the average final melt temperature and vapour homogenisation temperature from the dataset in appendix 5. These must be considered only approximates for the multi-solid inclusions.

In order to estimate the pressure conditions defined by the isochores, an independent geothermometer is needed (e.g. stable isotope pairs or mineral assemblages). Alternatively, the trapping pressure can also be constrained from the intersection of isochores of two fluid inclusion types from the same sample that are interpreted to have originated from the same fluid. In other fluid inclusion studies within the EFB, authors have interpreted the co-existence of both CO_2-rich and hyper-saline fluid inclusions to be a product of fluid un-mixing of an H_2O-CO_2-salt fluid, which can occur if the fluid density is high (Zhang and Frantz, 1989; Adshead, 1995; Baker, 1998; Rotherham et al., 1998; Mark et al., 1999). This relationship was observed in Na-Ca

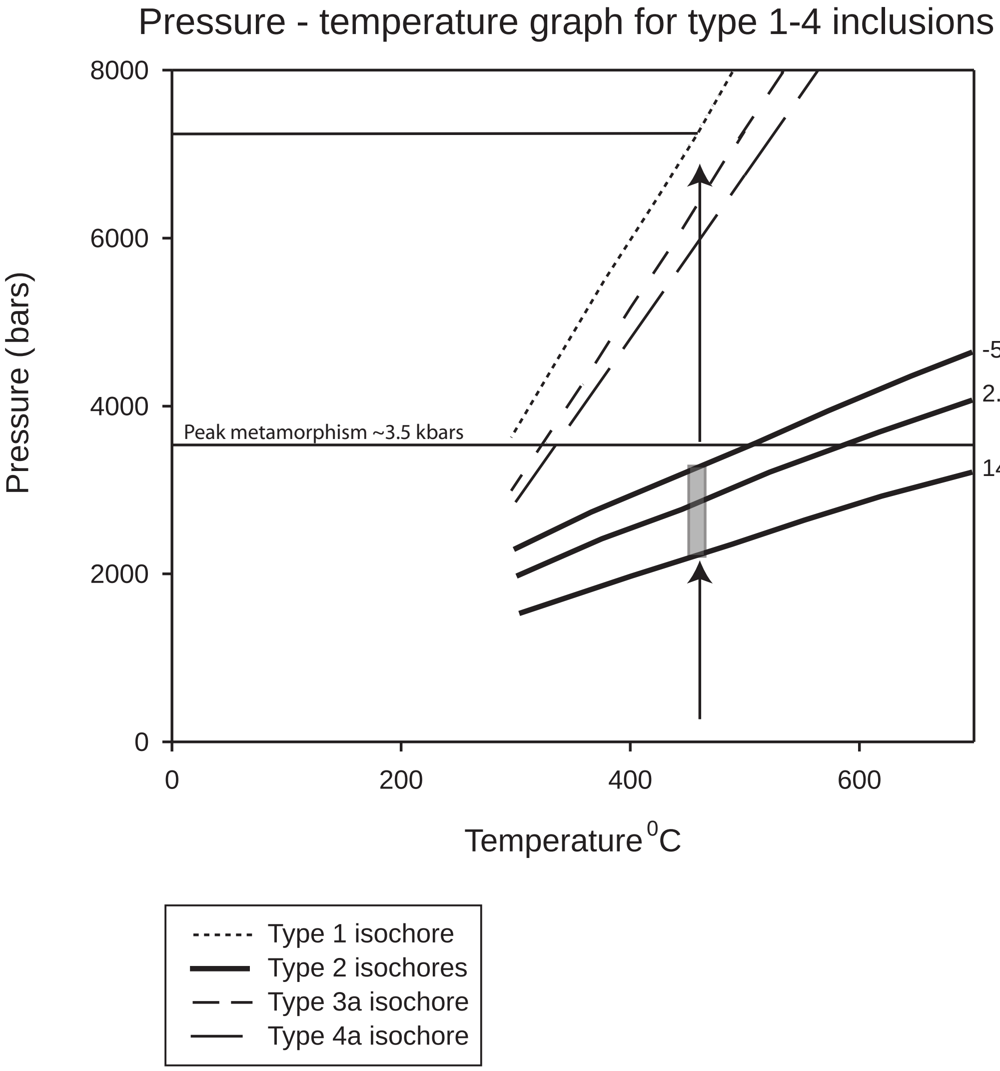

Figure 4.16. Pressure-temperature graph for type 1, 2, 3a and 4a fluid inclusions. For type 2 inclusions, maximum (14°C), minimum (-5°C) and average (2.4°C) homogenisation temperatures were used to construct three isochores. Type 1, 3 and 4 isochores were calculated from their average homogenisation temperatures only. A temperature of 500°C (see text for further information) gives pressures of between 2.4 to 3.24 kbar from the CO_2 isochores (grey box). The slopes of the isochores were constructed using CO_2 homogenisation temperatures for CO_2 isochores, vapour and halite homogenisation temperatures for type 1 and 3a isochores and final melting temperatures for type 4a isochores using the MacFlincor (Brown and Hageman, 1995) computer program. Note the type 1 and 2 isochores do not intersect at any reasonable pressure or temperature suggesting they are not the result of fluid immiscibility.

assemblages from Maramungee Creek and Fullarton River which are mineralogically similar to this study, as well as at some of the major IOCG deposits in the district (Baker, 1998; Rotherham et al, 1998; Mark et al., 1999). However, both type 1 and 2 fluid inclusions were rarely observed in the same sample at FC4NW. In addition, the homogenisation of type 1 inclusions was characterised by dissolution of the vapour bubble prior to the halite cube. This suggests that the type 1 and 2 fluid inclusions at FC4NW cannot have been derived from un-mixing of a H_2O-CO_2-salt fluid in this case. Although no stable isotope data is available for Na-Ca assemblages at FC4NW, oxygen isotope data from similar mineral assemblages nearby can instead be used as an approximation of temperature to constrain the trapping pressure. Blake et al (1997) calculated temperatures of 370ºC to 540ºC from Na-Ca alteration peripheral to the Ernest Henry deposit. In addition, Mark et al (1999) estimated temperatures of 500ºC for pre-mineralisation Na-Ca alteration assemblages within the Ernest Henry deposit. These temperatures correlate well with the mineral assemblages associated with Na-Ca alteration at FC4NW, where occurrences of both actinolite and clinopyroxene and of titanite rather than rutile and calcite probably represent temperatures of 400-500ºC (*cf.* Pollard et al., 1997).

Figure 4.16 shows the isochores for type 1 and 2 fluid inclusions do not cross at any point on the diagram. In addition, at 500°C, there is a significant difference between pressures defined by the type 1 and 2 isochores (type 1 = >7 kbars; type 2 = 2.4 to 3.4 kbars). Pressures obtained for type 1 fluid inclusions may not represent an accurate indication of the true trapping pressures as the presence of $CaCl_2$ in the fluid can greatly influence pressure estimates (Zhang and Frantz, 1989). Due to problems associated with $CaCl_2$ in hypersaline fluid inclusions, pressures of 2.4 to 3.4 kbars defined by type 2 inclusions represent a more accurate estimate of the true trapping pressure associated with clinopyroxene-rich Na-Ca alteration at FC4NW.

4.4. CHEMISTRY OF FLUIDS AT MFC

4.4.1. Procedure and samples used

Proton-induced X-ray emission (PIXE) analysis was carried out on type 1, 3a and 4a fluid inclusions in collaboration with Chris Ryan of CSIRO. Samples used in this study represent the same samples that were used for the heating and freezing experiments described above (MFC108/27, MFC125/27, MFC202.2/91 and MFC259.7/52) and all represent clinopyroxene-rich Na-Ca assemblages from FC4NW. Sample MFC002 was not analysed by PIXE, as the host mineral in this case is apatite which cannot be analysed because of its P and Ca content. PIXE analyses of inclusions were performed prior to heating and freezing experiments to avoid decrepitation problems within the samples. Unfortunately, most inclusions used for PIXE decrepitated during later heating experiments. Similar inclusions within the same samples were analysed instead (as described above) and the average density of each fluid inclusion type was calculated via the average homogenisation temperatures using the computer program MacFlinor 0.9 (Brown and Hagemann, 1995).

PIXE analyses were conducted at the Heavy Ion Analytical Facility (HIAF) of CSIRO at North Ryde, Sydney. A micro-focussed beam of 3MeV was used under experimental conditions similar to that documented by Ryan et al (1991). The incorporation of beam-scanning techniques and the PIXE yield modelling resulted in a quantitative measure of the composition of individual fluid inclusions leading to significantly improved reproducibility and quantification (Ryan et al., 1991, 1995). Analyses of synthetic euhedral fluid inclusions free of daughter phases produced an accuracy of ~10-15% (Ryan et al., 1995). However, analytical uncertainty associated with natural fluid inclusions is larger due to errors in estimating inclusion depth and thickness, deviations of the geometry of the inclusion from ellipsoidal model and geometry, and the internal structure of the inclusion. Modelling also suggests that errors may be up to 30 % for light elements such as Cl in analyses of inclusions that contain solid phases. Typically, only elements with atomic numbers >17 (Cl) are detectable, so important elements such as Na and S cannot be determined.

In this study, an uncertainty of 30 % in element concentrations is estimated for PIXE data from inclusions containing daughter crystals, although inter-element ratios are expected to be more accurate than the absolute concentration values (Mark et al., 1999; Williams et al., 2001). This is due to the errors described above having similar effects on different elements, particularly elements of similar size. These errors are particularly important because Cl, K_α and K_β radiation are absorbed by the host mineral at shallow depths. Therefore, only fluid inclusions close to the surface of the host mineral can be analysed for Cl and K. For this study, depth estimates of individual fluid inclusions were made via focussing positions using a petrological microscope, although errors associated with depth and geometry estimates via a microscope may exceed 20 % (Heinrich et al., 1993).

4.4.2. Results

Problems with the interpretation of PIXE data

Results of the PIXE analysis are presented in table 4.2. First inspection of table 4.2 shows that for many of the fluid inclusions analysed, Cl levels are low (down to 1 wt %). This does not agree with either the homogenisation temperatures or visual estimates which show that 21 of the 22 fluid inclusions analysed by PIXE contain halite. A pure H_2O-NaCl fluid inclusion containing a halite crystal will typically contain at least 26 wt% NaCl (Shepherd et al., 1985), which is equivalent to 16 wt % Cl. The most likely explanation for the low Cl in some of the type 1 and 3a inclusions is they were too deep within the host mineral to accurately detect Cl.

It has been widely recognised that the presence of solutes other than NaCl can strongly influence the melting temperatures of daughter crystals and, hence, also influence the estimates of bulk salinity in fluid inclusions (e.g. Oakes et al., 1990). It is also possible that the amount of NaCl required to form halite in a fluid inclusion may also be affected by the concentration of other cations (e.g. K, Ca) competing for available anions (Cl) in the fluid (Roedder, 1984). Although Na cannot be measured by PIXE analysis, the relative concentration of Na can be estimated by firstly converting the measured cations and Cl values to chloride species assuming chlorides are the predominant anions (e.g. KCl, $CaCl_2$). The Cl concentration associated with each chloride species can be calculated using the equation below:

$$Cl_{sp} = Cl_{mass} \frac{y_{conc}}{y_{mass}} \quad \text{…………...equation 4.1.}$$

Where:
Cl_{sp} = Concentration of Cl for each chloride species
Cl_{mass} = atomic weight of Cl
y_{conc} = concentration of cation
y_{mass} = atomic weight of cation

Sample No	Inclusion type	FLINC No	Na (calc)	Na (calc) error	Cl	MDL	K	MDL	Ca	MDL	Ti	MDL	Mn	MDL	Fe	MDL	Cu	MDL
MFC125/27	Type 3a	mfc15	50845	15253	167408	1755	21354	579	23309	412	2713	293	224	190	19752	183	381	221
MFC125/27	Type 3a	mfc16	76086	22826	241440	2434	37503	861	26789	604	3658	418	bd	-	30474	259	723	294
MFC125/27	Type 3a	mfc20	-5530	-1659	51225	1079	9111	434	15596	339	2536	267	310	193	16879	167	603	174
MFC125/27	Type 3a	mfc23	-16154	-4846	15436	558	7673	190	9417	142	1882	108	347	76	11448	73	253	90
MFC125/27	Type 3a	mfc25	75287	22586	198726	2050	19034	529	27276	334	1527	202	bd	-	12088	96	225	115
MFC125/27	Type 3a	mfc49	-87997	-26399	57593	3854	90442	589	31167	353	2572	198	bd	-	41148	109	1747	147
MFC125/27	Type 3a	mfc51	46864	14059	114448	1545	14614	512	13484	373	922	274	bd	-	1901	170	238	171
MFC125/27	Type 3a	mfc54	95552	28666	283770	1175	132028	374	6195	230	733	135	bd	-	2897	75	222	81
MFC125/27	Type 3a	mfc56	38981	11694	120320	742	16485	365	21770	281	493	220	293	166	3406	146	bd	-
MFC108/27	Type 3a	mfc35	223859	67158	415049	639	34033	326	20944	225	bd	-	bd	-	98	83	124	84
MFC108/27	Type 3a	mfc37	132437	39731	240658	3201	24157	995	5618	645	bd	-	bd	-	1076	210	292	216
MFC202.2/91	Type 3a	mfc58	33691	10107	75390	1946	7838	539	7001	366	571	248	bd	-	1419	141	bd	-
MFC202.2/91	Type 3a	mfc60	185451	55635	335712	9004	20759	1694	15346	1061	1062	592	bd	-	677	261	301	253
MFC202.2/91	Type 3a	mfc70	182755	54827	331417	1803	15074	640	18639	432	bd	-	bd	-	1341	149	bd	-
MFC259.7/52	Type 3a	mfc95	34667	10400	101140	1226	14621	404	16662	274	437	180	629	116	2013	95	bd	-
MFC259.7/52	Type 3a	mfc106	37629	11289	156070	1193	9290	384	47952	263	bd	-	221	115	1177	98	bd	-
MFC259.7/52	Type 1	mfc87	105890	31767	267753	622	19149	207	47355	139	331	88	374	55	424	46	65	51
MFC259.7/52	Type 1	mfc85a	1902	571	37724	131	5867	63	15282	51	52	40	318	30	620	25	46	30
MFC259.7/52	Type 1	mfc83	140568	42170	337405	317	1367	124	12135	84	bd	-	4306	45	71254	45	311	59
MFC259.7/52	Type 1	mfc91	17452	5236	99379	650	8134	218	28313	153	401	106	3738	73	5296	62	106	68
MFC259.7/52	Type 1	mfc96	5804	1741	76387	323	6814	125	24987	91	bd	-	4774	47	6288	40	bd	-
MFC259.7/52	Type 1	mfc99	68806	20642	304743	1380	23842	460	85374	313	bd	-	6762	138	9206	118	bd	-
MFC259.7/52	Type 4a	mfc84	-2560	-768	10186	210	666	110	7152	90	bd	-	bd	-	54	48	bd	-

Sample No	Inclusion type	FLINC No	Zn	MDL	Ge	MDL	As	MDL	Br	MDL	Rb	MDL	Sr	MDL	Ba L	MDL	Pb L	MDL
MFC125/27	Type 3a	mfc15	bd	-	bd	-	334	138	bd	-	bd	-	bd	-	4396	1229	bd	-
MFC125/27	Type 3a	mfc16	450	267	403	193	474	231	530	450	bd	-	bd	-	4899	1757	bd	-
MFC125/27	Type 3a	mfc20	350	137	bd	-	347	178	bd	-	bd	-	bd	-	1774	1117	bd	-
MFC125/27	Type 3a	mfc23	168	80	105	69	77	65	217	86	bd	-	408	192	1934	451	bd	-
MFC125/27	Type 3a	mfc25	185	99	bd	-	118	95	bd	-	bd	-	491	389	1554	856	bd	-
MFC125/27	Type 3a	mfc49	bd	-	bd	-	173	95	139	117	bd	-	bd	-	4575	842	474	214
MFC125/27	Type 3a	mfc51	415	151	301	137	bd	-	bd	-	bd	-	bd	-	3386	1140	bd	-
MFC125/27	Type 3a	mfc54	120	71	120	46	192	53	bd	-	bd	-	bd	-	2680	569	bd	-
MFC125/27	Type 3a	mfc56	262	162	141	116	412	133	bd	-	bd	-	bd	-	2299	918	bd	-
MFC108/27	Type 3a	mfc35	158	72	157	57	134	73	bd	-	bd	-	bd	-	2399	617	bd	-
MFC108/27	Type 3a	mfc37	528	192	466	189	bd	-	bd	-	bd	-	bd	-	4102	1732	bd	-
MFC202.2/91	Type 3a	mfc58	479	120	242	106	bd	-	bd	-	bd	-	bd	-	2496	1046	bd	-
MFC202.2/91	Type 3a	mfc60	576	219	690	234	357	298	bd	-	bd	-	bd	-	2963	2517	bd	-
MFC202.2/91	Type 3a	mfc70	333	137	327	126	bd	-	bd	-	bd	-	bd	-	bd	-	bd	-
MFC259.7/52	Type 3a	mfc95	242	98	233	86	bd	-	bd	-	bd	-	bd	-	2114	759	bd	-
MFC259.7/52	Type 3a	mfc106	324	105	288	83	98	66	278	136	bd	-	690	290	3853	744	bd	-
MFC259.7/52	Type 1	mfc87	234	49	109	41	bd	-	273	49	378	215	834	120	2176	371	bd	-
MFC259.7/52	Type 1	mfc85a	177	27	bd	-	bd	-	158	39	227	148	514	89	878	168	bd	-
MFC259.7/52	Type 1	mfc83	241	53	bd	-	bd	-	bd	-	282	83	144	65	2007	236	274	143
MFC259.7/52	Type 1	mfc91	717	62	67	48	154	44	188	89	443	252	641	192	3037	447	305	139
MFC259.7/52	Type 1	mfc96	573	42	bd	-	bd	-	188	46	318	167	619	108	2792	276	490	104
MFC259.7/52	Type 1	mfc99	1161	121	193	91	bd	-	455	189	bd	-	911	412	6234	858	1207	308
MFC259.7/52	Type 4a	mfc84	66	57	68	53	bd	-	476	75	bd	-	298	154	1134	319	114	119

Table 4.2. PIXE analysis (ppm) of type 1, 3a and 4a fluid inclusions from the FC4NW prospect. Na values were calculated using equations 4.1 and 4.2 (see text). Also included are the minimum detection limits (MDL) for each analysis. Where concentrations were below detection, the values have been replaced with '-'. Cl, K and Na values were not used in the interpretation of the dataset because of depth issues associated with the analysed inclusions (see text). These values are highlighted by the grey boxes in the table above.

The difference between the sum of these chloride values (Cl_{sp}) and the Cl concentration determined by PIXE gives the excess amount of Cl in the fluid (Cl_{excess}). The Na concentration (Na_{calc}) is then calculated by the following equation below:

$$Na_{calc} = Na_{mass} \frac{Cl_{excess}}{Cl_{mass}}$$

…………equation 4.2

Where:

Na_{calc} = calculated Na
Na_{mass} = atomic weight of Na
Cl_{excess} = excess Cl
Cl_{mass} = atomic weight of Cl

Calculated Na values are given in table 4.2. One major consideration is the amount of Mg in the fluid, which also cannot be measured by PIXE. The presence of Mg-bearing minerals, including actinolite and clinopyroxene in the alteration assemblages, suggests that the fluid may have contained some Mg. However, concentrations of Mg in natural waters from other studies (e.g. Audetat et al., 2000; McCaig et al., 2001) show that Mg is typically low in most systems. In addition, laser ablation ICP MS work by Fu (unpublished data) on fluid inclusions from regional Na±Ca alteration assemblages in the EFB also indicate low Mg concentrations. Anions other than Cl in the fluid may potentially affect the calculated concentration of Na (e.g. $Ca(HCO_3)_2$), and some metals have multiple valence states (e.g. Mn) making determination of Cl balance uncertain. Therefore, the calculated Na from the analysed cations and anions determined by PIXE represents an approximation only.

A plot of calculated Na versus the total concentration of other cations (except Na) determined by PIXE is shown in figure 4.17. As was the case for Cl, it is clear from the graph that many of the PIXE analyses contain Na values that are too low to account for the presence of halite. Inclusions that appear to contain reasonable Na concentrations have been outlined in figure 4.17. For inclusions that plot just below the minimum Na line in figure 4.17, the analyses were also assumed to be reasonable considering the effect of other cations on the concentration of Na required to form halite as discussed

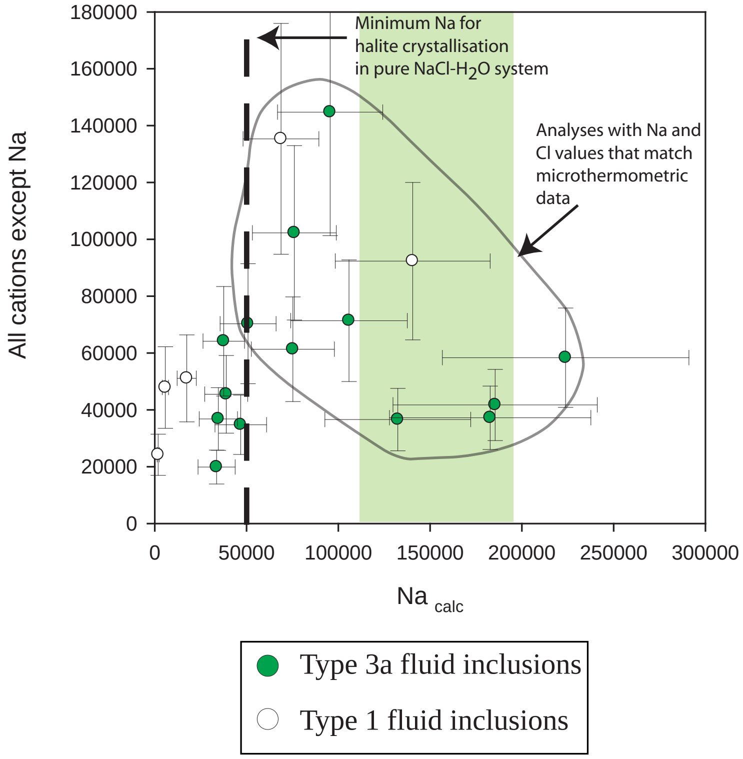

Figure 4.17. Plot of the sum of all cations, except Na_{calc}, vs Na_{calc} for type 1 and type 3a fluid inclusions from FC4NW. Na values were calculated by converting cations (e.g. K, Fe) and Cl values to chloride species (e.g. KCl). The difference between the sum of these chloride species and the Cl concentration determined by PIXE gives the relative concentration of Na in the fluid. Also plotted is the approximate amount of Na required to form halite in a pure H_2O-NaCl-K_2O fluid (Roedder, 1984), represented by the black dashed line. The shading represents the minimum and maximum salinity values for type 1 and 3 inclusions from this study. All analyses interpreted to contain reasonable Na concentrations are indicated by the outlined area

above. For all analyses, depth estimates were measured again using the petrographic microscope. For fluid inclusions that were found to be deeper than originally thought, and taking into consideration the errors and uncertainties involved, Cl and K values were ignored. Elements with higher atomic weights (e.g. Fe, Zn, Cu. Ba), however, were retained, as the depth of the fluid inclusions within the quartz host is unlikely to affect the analysis of these elements (Ryan et al., 1995).

In figure 4.17, it is interesting to note that some of the type 3a halite-bearing inclusions appear to contain higher concentrations of overall cations compared to some of the type 1 inclusions. Considering that the type 3a inclusions contain only halite daughter crystals, one would expect the type 1 inclusions to contain higher concentrations of most cations, especially K and Fe due to the presence of sylvite and hematite as solid phases. Table 4.2 shows that Fe concentrations vary significantly within type 3a fluid inclusions, ranging from 97 to 30000 ppm (± 30%). Inspection of the elemental maps generated from PIXE analysis, however, shows that many of the high Fe concentrations may coincide with a high Fe background content (Fig. 4.18) possibly from the host mineral itself (quartz). These high background values may be a function of proton scatter from nearby Fe-bearing minerals (e.g. magnetite, pyrite) during analysis or reflect Fe contained within the quartz host (Williams, *pers comm*). In contrast, the type 1 inclusions exhibit distinct Fe anomalies in the elemental maps and represent the presence of hematite and/or hedenbergite in the inclusions (Fig. 4.5, 4.19). Therefore, Fe values for type 3a fluid inclusions were ignored.

Table 4.2 shows that Cu, Zn and Ba are present in most fluid inclusions in this study. However, some discrepancy is apparent when table 4.2 and the elemental maps are compared (Fig. 4.18 and 4.19). In many cases where concentrations of Cu, Zn and Ba are apparently above the detection limit in type 3a inclusions (table 4.2), no distinct anomaly is present in the elemental maps (e.g. Fig. 4.18). In contrast, distinct anomalies are observed for these elements in the elemental maps for type 1 fluid inclusions (Fig. 4.19). It is unlikely that absorption problems discussed for Cl and K above will affect these heavier elements, therefore the Ba, Cu and Zn values have been tentatively included.

Chemical composition of fluids

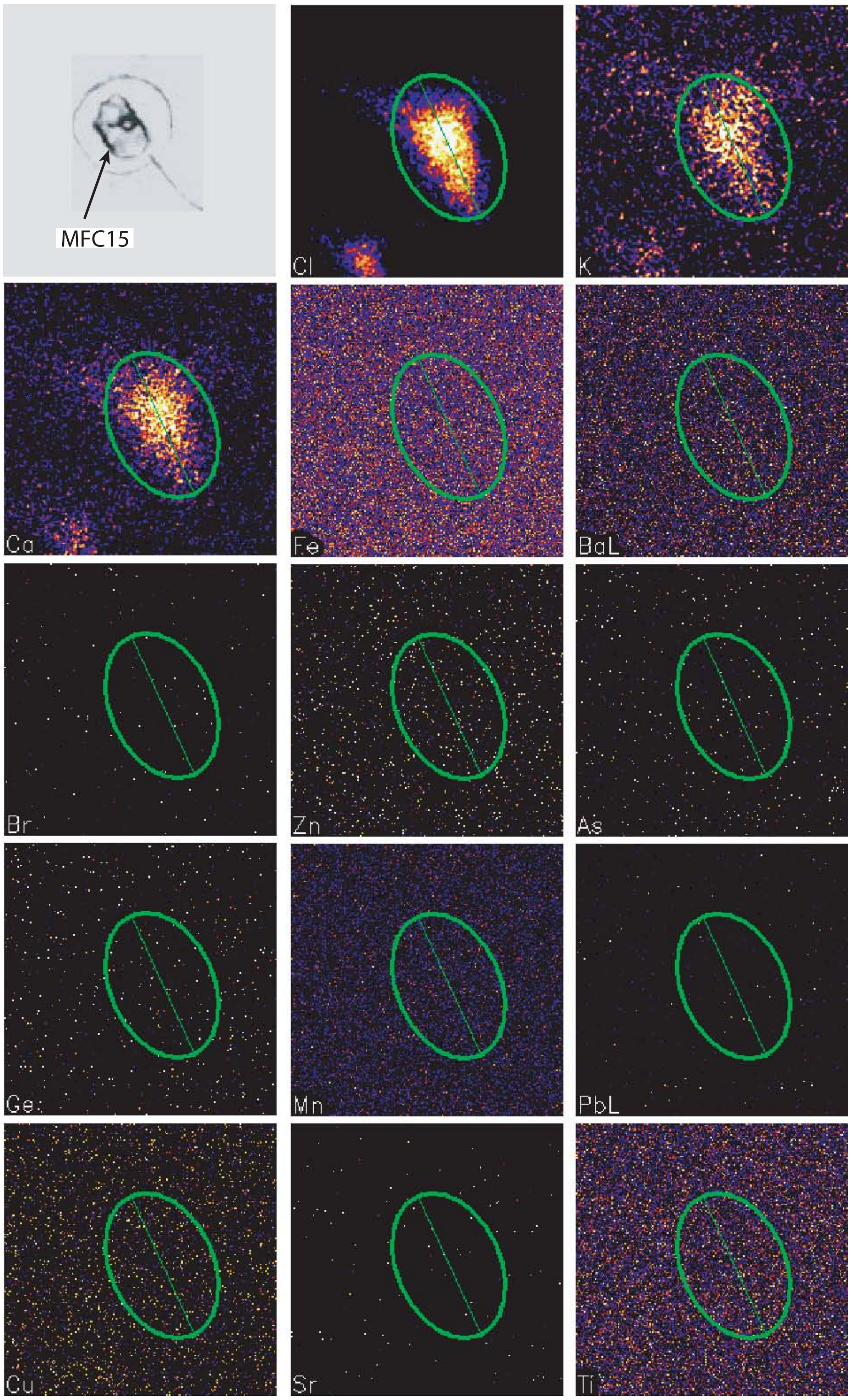

Figure 4.18. PIXE X-ray maps of a type 3a halite-bearing inclusion from sample MFC125/27 showing the distribution of different phases of fluid inclusion number MFC15 (first image) under proton radiation. Image brightness is proportional to element abundance. The green circle for each element represents the outline of the inclusion. Notice only Cl, Ca and K are visible in the elemental maps. Fe, Ba and Ti all exhibit high background levels, which is likely to affect the overall concentration of these elements measured by the proton probe. This inclusion is also quite small (12 µm) which probably affected the apparent distribution of Cl which does not match with the location of the halite crystal in the inclusion photo.

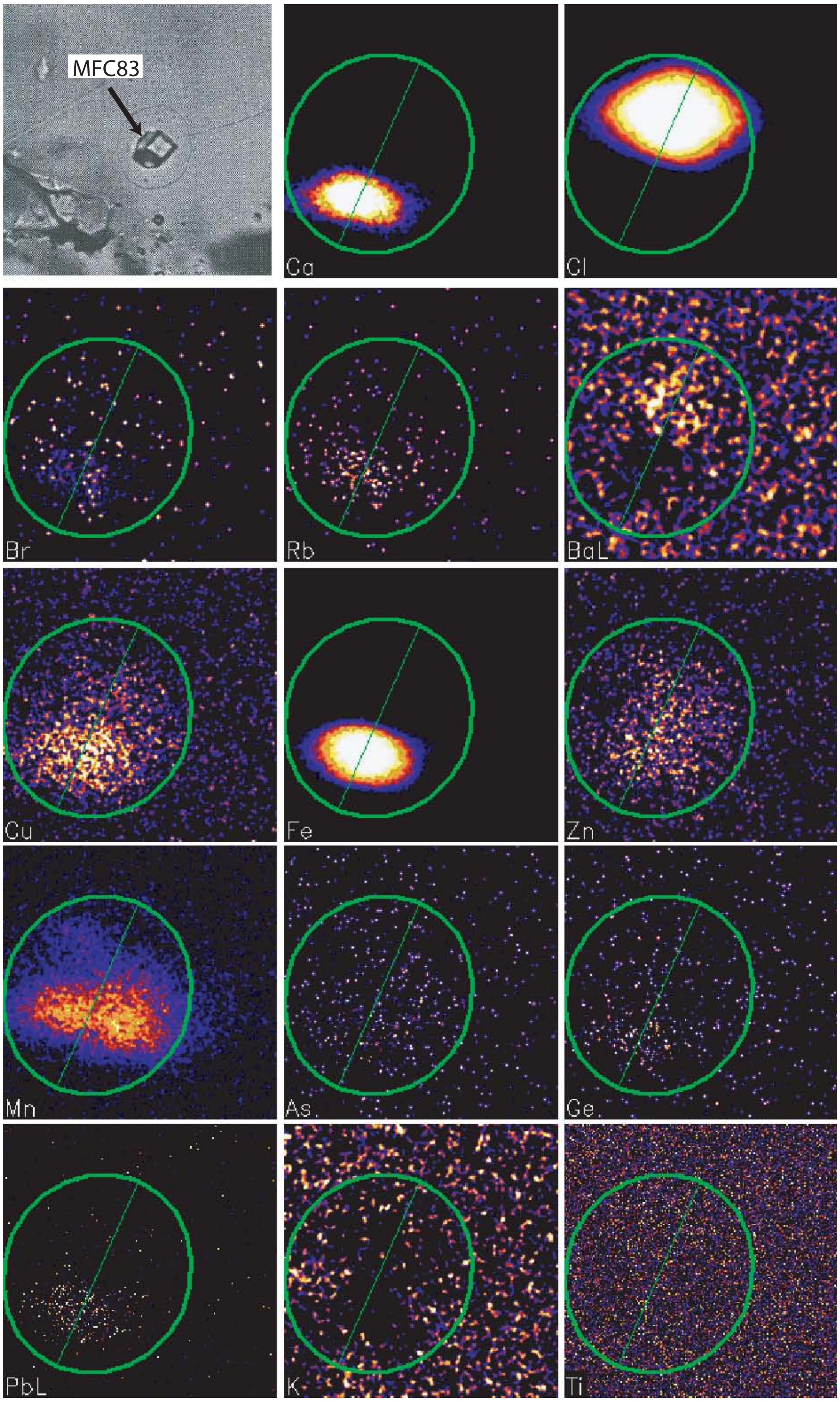

Figure 4.19. PIXE X-ray maps of a type 1 multi-solid inclusion from sample 259.7/52 showing the distribution of different phases of fluid inclusion number MFC83 (first image) under proton radiation. Image brightness is proportional to element abundance. The green circle for each element represents the outline of the inclusion. Ca and Fe are concentrated in the same part of the inclusion and represent hedenbergite. The high Cl concentration represents the halite crystal. Br, Cu, Mn and Zn appear to be part of the fluid. Notice the high background levels in Ba and, to a lesser extent, K.

The PIXE analyses show a considerable variation in Ca (8000 ppm to 10 wt%) and K (800 ppm to 10 wt%) both between and within the different types of fluid inclusions detected in this study (Fig. 4.20). No differentiation can be made between type 1 and 3a inclusions with respect to the Ca values, although one of the type 1 inclusions analysed contains higher Ca than any of the type 3a inclusions. For K, the type 4a inclusion exhibited the lowest values, while one type 1 inclusion also exhibits considerably low K (800 ppm). Mn values are typically much higher in type 1 fluid inclusions (300 to 4000 ppm) compared to type 3a inclusions (200 to 600 ppm). Interestingly, Type 3a inclusions typically contain higher Cu values (up to 1747 ppm) than the primary type 1 fluid inclusions (up to 311 ppm) (table 4.2 and Fig. 4.20), and may be related to the later amphibole-rich Na-Ca alteration phase at FC4NW. No distinction between type 1 and 3a inclusions are apparent for Zn (100 to 600 ppm and Ba (1000 to 8000 ppm).

Despite the small number of inclusions in the dataset, some trends are still apparent (Fig. 4.20 and 4.21). In particular, Ba and K values for type 3a inclusions exhibit a positive trend. While both K and Ba will readily substitute for each other in K-bearing minerals (Goldschmidt, 1958), Ba is also considered to be insoluble in aqueous solution (cf. Rotherham et al, 1998) (discussed below). Cu and Fe exhibit what appears to be a positive trend (100 to 70 wt% Fe and 50 to 2000 ppm Cu), probably reflecting the presence of magnetite and chalcopyrite associated with Na-Ca alteration at FC4NW. A positive trend is also apparent for Mn and Fe (1000 to 1 wt% Fe and 500 to 0.6 wt% Mn) and Pb and Ba (1000 to 0.5 wt% Ba and 100 to 1000 ppm Pb). Clearly more analyses are needed to confirm whether these trends are real.

Figure 4.21a compares Br/Cl ratio of fluid inclusions in this study with fluid inclusions from Mount Isa (Heinrich et al., 1993) and juvenile magmatic values from modern volcanoes (Bohlke and Irwin, 1992). The type 1 and type 3a fluid inclusions each plot in the magmatic field, while the type 4 inclusion contains a high Br/Cl ratio (0.014) and plots closer to the Mount Isa field. Since the type 4a inclusions are interpreted to be of a late secondary phase, the high Br/Cl ratio suggests the fluids associated with type 4 may be of meteoric origin.

4.5 COMPARISONS WITH OTHER STUDIES

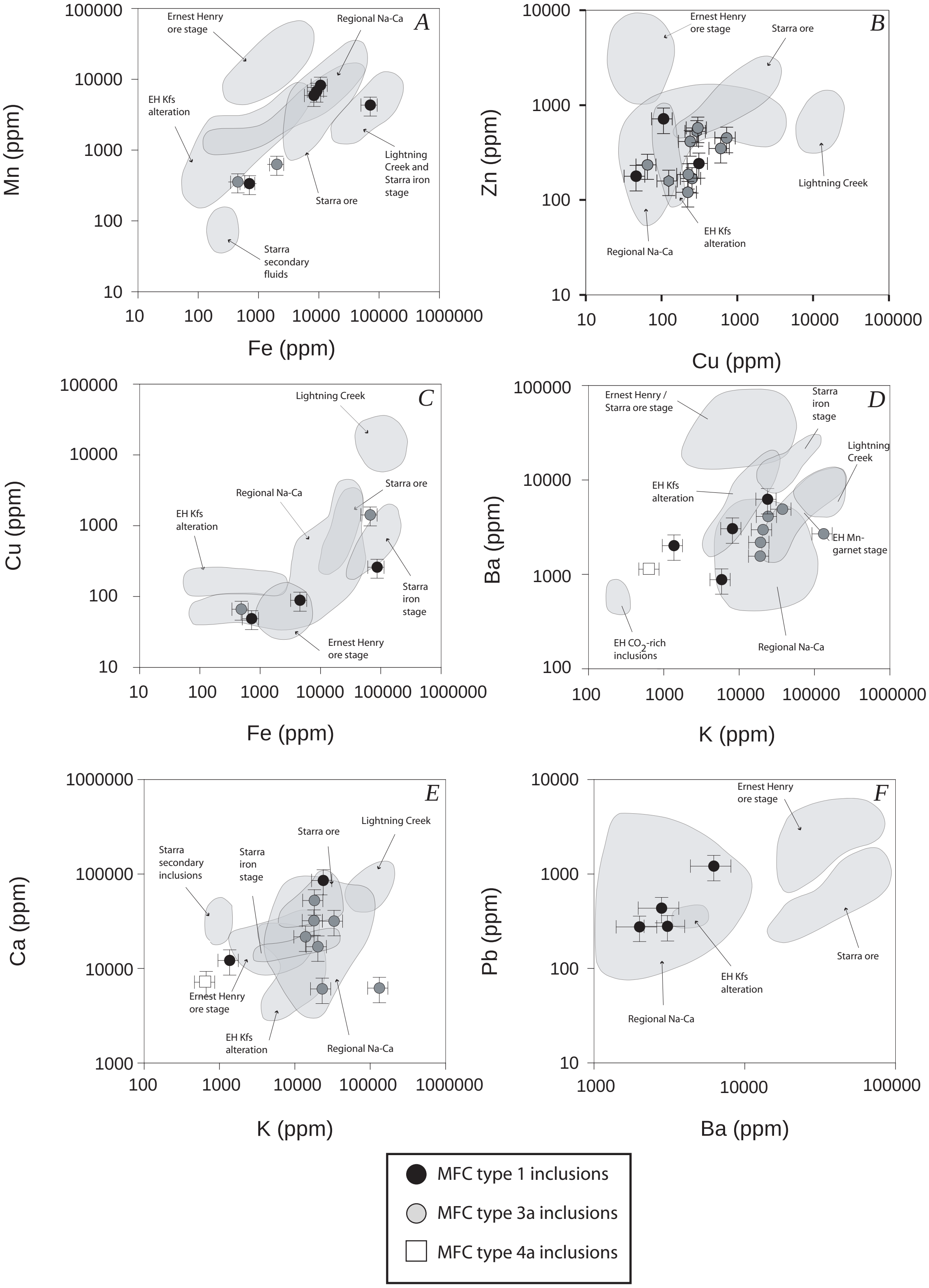

Figure 4.20. Bi-plots from PIXE of type 1, 3a, and 4a fluid inclusions from weakly mineralised Na-Ca alteration assemblages at the FC4NW prospect compared to PIXE data from Starra (Williams et al, 2001), Ernest Henry (Mark et al, 1999), Lightning Creek (Perring et al, 2000) and regional Na-Ca alteration (Fu et al. unpublished data). Note the similar Fe and Cu values between type 1 and 3a inclusions from FC4NW and fluid inclusions associated with Cu-Au mineralisation from Ernest Henry . Error bars shown are 30 percent of the coordinate value. Abbreviations: Kfs=K-feldspar, EH=Ernest Henry.

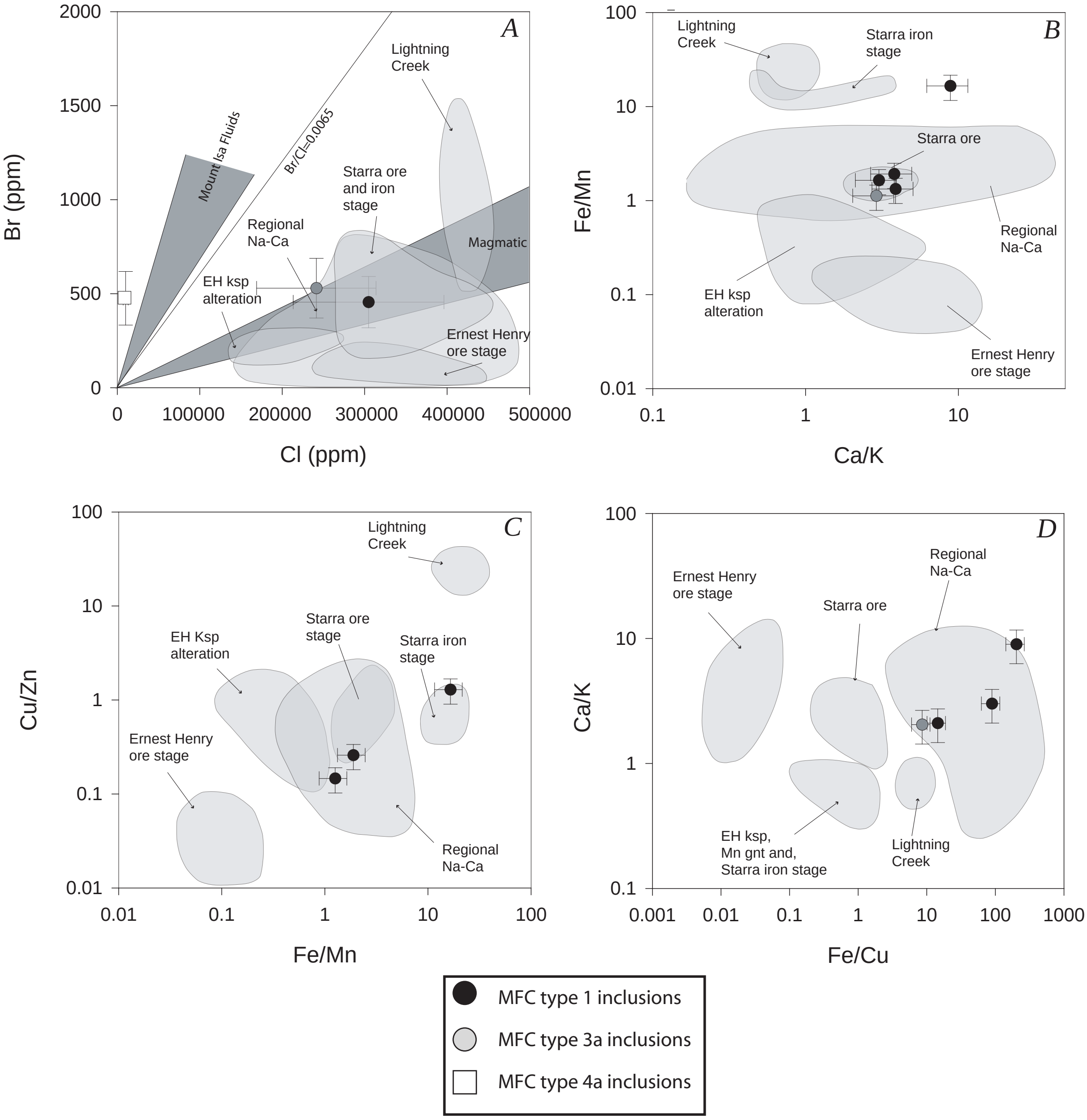

Figure 4.21. Inter-element ratio plots from PIXE of type 1, 3a and 4a inclusions from weakly mineralised Na-Ca alteration assemblages at the FC4NW prospect compared to PIXE data from Starra (Williams et al, 2001), Ernest Henry (Mark et al, 1999), Lightning Creek (Perring et al, 2000) and regional Na-Ca assemblages (Fu et al., unpublished data. Note the relatively high Cu/Zn ratio of fluid inclusion from Lighting Creek compared to FC4NW, Starra and Ernest Henry. Error bars shown are 30 percent of the coordinate value. Abbreviations: Kfs=K-feldspar, EH=Ernest Henry.

A vast body of fluid inclusion data from various mineral assemblages in the EFB is available. These studies have mostly concentrated on mineral assemblages directly related to, or adjacent to Cu-Au mineralisation within many of the major deposits. This section compares the characteristics of fluid inclusions from clinopyroxene-rich Na-Ca alteration and Fe oxide metasomatism within the MFC area with fluid inclusions from Cu-Au mineralisation assemblages and regional Na-Ca assemblages from the EFB. PIXE results are also compared to other related deposits including Olympic Dam and Tennant Creek. Published data from Starra (Williams et al., 2001), Ernest Henry (Mark et al., 1999) and Lightning Creek (Perring et al., 2000) are presented in figures 4.20 and 4.21. Also included are representative analyses of regional Na-Ca alteration from the Mount Angelay igneous complex (Fu, unpublished data).

4.5.1. Eastern Fold Belt

Na-Ca alteration is pervasive throughout most parts of the EFB (Oliver, 1995). Work by de Jong and Williams (1995), Oliver (1995), Blake et al. (1997) and Pollard et al. (1997) on regional Na-Ca assemblages all show similar fluid inclusion characteristics as those from FC4NW. They typically range from highly saline (>30 wt % $NaCl_{equiv}$), multi-solid inclusions (sylvite and pyrosmalite-bearing) to secondary two-phase inclusions that exhibit a high range of homogenisation temperatures (250 to 600°C) and fluid compositions ($NaCl-H_2O$, $NaCl-CaCl_2-H_2O$, CO_2). In contrast, multisolid fluid inclusions associated with ore and pre- and post-mineralisation events at the deposits typically are chemically more complex than fluid inclusions from regional Na-Ca assemblages, and contain a variety of daughter phases including halite, sylvite, pyrosmalite, kutnahorite (Ernest Henry only), calcite, Mn-Fe chlorides, chalcopyrite, amphibole and magnetite (Adshead, 1995; Rotherham et al., 1998; Mark et al., 1999). These multisolid fluid inclusions are Ca-rich and exhibit homogenisation temperatures ranging from 200º to 615ºC (Adshead, 1995; Baker, 1998; Rotherham et al., 1998; Mark et al., 1999; Williams et al., 2001). In addition, PIXE analysis of multisolid fluid inclusions from Ernest Henry, Starra and Lightning Creek show that these Cu-Au occurrences are associated with an extraordinary range of Mn, Ba, Cu and Fe concentrations. The Ba values at Ernest Henry, Starra and Lightning Creek typically are much higher than regional Na-Ca alteration assemblages from Mount Angelay (Fig. 4.20 and 4.21).

One common theme associated with both regional Na-Ca assemblages and alteration within and peripheral to the major deposits in the district is the co-existence of CO_2-rich and multiphase inclusions as discrete populations, which prompted many authors to suggest these inclusions were derived from immiscible fluid separation from complex NaCl-$CaCl_2$-KCl-H_2O-CO_2-rich brines (Oliver, 1995; de Jong and Williams, 1995; Blake et al., 1997, Pollard et al., 1997). At FC4NW, the co-existence of hypersaline (type 1) and CO_2-rich (type 2) fluid inclusions was rarely observed in clinopyroxene-rich Na-Ca assemblages. This suggests that the CO_2-rich and hypersaline fluid inclusions were unlikely to have formed from immiscible fluid separation of a CO_2-H_2O-salts brine and are probably related to different fluids.

Pollard et al (1997) recorded a wide range of salinities and temperatures associated with different fluid inclusion generations at Maramungee Creek (Fig. 4.1), and implicated fluid mixing with a lower-temperature, low-salinity fluid. Types 1, 3a and 4a inclusions from clinopyroxene-rich Na-Ca alteration at FC4NW also show a wide range of temperatures and salinities. Type 1 fluid inclusions are of high temperature (260 to 442ºC), highly saline (35 to 50 wt% $NaCl_{equiv}$) and contain low Cu. In comparison, type 3a inclusions are of lower temperature (210 to 280ºC) and less saline (32 to 37 wt% $NaCl_{equiv}$), but contain higher Cu than type 1 inclusions. Type 4a inclusions exhibit even lower temperatures (125 to 198ºC) and lower salinities but over a wider range (2 to 22 wt% $NaCl_{equiv}$) (Fig. 4.22). This temperature decrease is consistent with progressive cooling of a homogenous fluid with time, and is in agreement with the mineral paragenesis at FC4NW where the early clinopyroxene-rich Na-Ca alteration is overprinted by the later actinolite-rich Na-Ca alteration and K-feldspar and hematite-stained albite alteration as discussed in chapter 2. In addition, while type 1 fluid inclusions are associated with the early clinopyroxene-rich Na-Ca phase at FC4NW, the type 3a inclusions may be related to the later amphibole-rich phase, consistent with the presence of sulphide in the alteration assemblage and higher Cu values in the fluids.

Br/Cl ratios for type 1 and 3a inclusions from FC4NW are similar to regional Na-Ca alteration, Lightning Creek, Starra and Ernest Henry, and are all considerably different to sedimentary-hosted copper mineralisation at Mount Isa (Fig. 4.21a) suggesting a magmatic origin for these fluids. Interestingly, one type 4 inclusion measured contains Br/Cl ratios that plot close to the Mount Isa fluid field. This correlates well

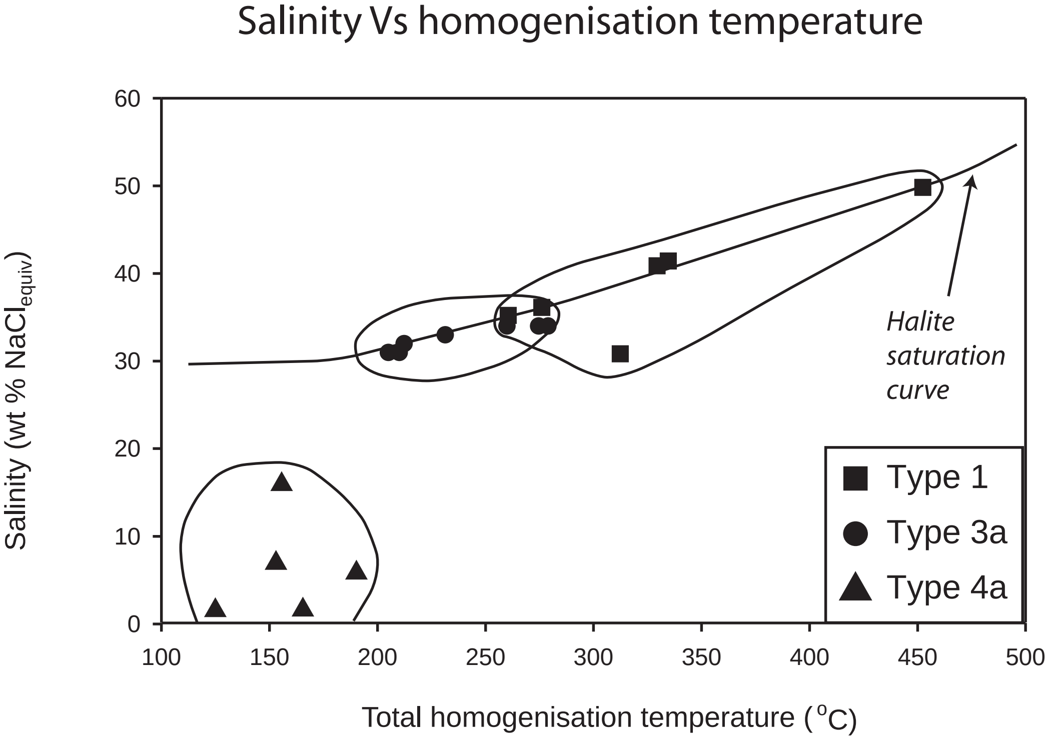

Figure 4.22. Scatter plot of salinity versus homogenisation temperature for type 1, 3a and 4a fluid inclusions. The graph shows a decrease in salinity with decreasing temperature. The halite saturation curve is defined by the homogenisation data because type 1 and 3a inclusions homogenised by halite dissolution (Shepherd et al., 1985). The type 1 and 3a fluid inclusions which in the area of overlap of the two fields may represent an intermediate subtype. The type 4 inclusions exhibit a wide range of salinity values and a narrow temperature range which may imply mixing with an externally-derived meteoric fluid.

with the wide range of salinities recorded for type 4a inclusions at FC4NW, and implicates the interaction of another low salinity fluid, possibly of meteoric origin.

Ca and K concentrations at FC4NW exhibit a large range of values that do not separate FC4NW from the rest of the data (Fig. 4.21d, 4.20e). For Mn, multiphase inclusions from the Cu-Au mineralisation phase at Ernest Henry and Starra (5000 to 100000 ppm ±30%) contain the highest values, while FC4NW, regional Na-Ca alteration, Lightning Creek, the iron stage at Starra and Mn-garnet alteration at Ernest Henry also contain considerable amounts (500 to 10000 ppm ±30%) (Fig. 4.20a). Interestingly, Fe/Mn ratios of some type 1 inclusions from FC4NW appear to correlate with the multiphase inclusions from Starra (Fig. 4.21b, c, 4.20a). Type 1 and 3a fluid inclusions from clinopyroxene-rich Na-Ca alteration at FC4NW also contain considerably lower concentrations of Ba and Zn compared to all fluid inclusion types from Starra, Ernest Henry and Lightning Creek (except the CO_2-rich inclusions) (Fig. 4.20b, f). Instead, Ba and Zn values at FC4NW are more akin to regional Na-Ca alteration and pre-mineralisation events at Ernest Henry (4.20b, d). Williams et al (2001) noted that Ba concentrations in fluid inclusions at Starra clearly correlate with the elemental maps and that Ba is present in a solid phase. It is unclear from the elemental maps whether the Ba is present as a solid phase or within the fluid at FC4NW because no Ba-bearing solid phases were observed under the microscope.

Cu and Fe concentrations of type 1 and 3a inclusions in this study are similar to fluid inclusions associated with Cu-Au mineralisation at Ernest Henry and regional Na-Ca alteration from Mount Angelay (80 to 120 ppm Cu; 1000 to 10000 ppm Fe), although Mark et al (1999) interpreted the low Cu values at Ernest Henry to represent spent fluids. In contrast, the Lightning Creek prospect contains the highest Cu values in fluid inclusions in the district (1-5 wt % Cu), despite sulphide mineralisation at Lightning Creek being relatively minor. Perring et al (2000) suggested that the high Cu values in fluid inclusions from Lightning Creek meant the fluids had the capacity to precipitate significant chalcopyrite, but were prevented from doing so by the lack of S in the fluid and/or host rock. It is unclear whether a similar scenario influenced the degree of sulphide mineralisation at FC4NW. Nevertheless, this result shows the ability of fluids associated with Na-Ca alteration at FC4NW to transport both Cu and Fe, and further strengthens the argument by Pollard et al (1997) that fluids responsible for Na-Ca alteration and Cu-Au mineralisation were possibly related.

4.5.2. Other Fe oxide (Cu-Au) deposits

Huston et al (1993) showed that the Tennant Creek ‘ironstones’ were deposited from low to moderate temperature (~250ºC) and moderately saline fluids (15 to 20 wt% NaCl equiv). These Fe oxide-rich rocks predominately contain chlorite and/or quartz. In outcrop at MFC, most of the fluid inclusions within the Fe oxide-rich rocks were type 4b, 2-phase inclusions and exhibited lower homogenisation temperatures (110.2 to 147.2ºC) compared to Tennant Creek. One type 3b inclusion was also measured, however this also exhibited low homogenisation temperatures (~114°C). Subsequent Au-Cu mineralisation at Tennant Creek was deposited from higher temperature (~350ºC) and salinity (~15 to 30 wt %) fluids than the precursor ironstones. However, these temperatures and salinities are significantly lower than Na-Ca alteration and Cu-Au mineralisation in the EFB. Khin Zaw et al (1990) suggested that these fluids may have originated, at least in part, from basinal brines, although the involvement of magmatic fluids, as described by Huston et al (1993), cannot be completely ruled out.

At Olympic Dam, fluid inclusions associated with early magnetite, pyrite and siderite were entrapped at ~280 to 420°C. These inclusions contain complex Fe-bearing daughter salt phases and coexist with CO_2-rich inclusions, similar to fluid inclusions associated with Na-Ca alteration and Cu-Au mineralisation in the EFB. However, fluid inclusions associated with the main phase of Cu-Au mineralisation at Olympic Dam exhibits considerably lower homogenisation temperatures, with most ranging between 170 to 190ºC (Oreskes and Einaudi, 1992). These inclusions are also CO_2-rich, and may be associated with a highly complex chemistry ($KCl-CaCl_2-CaF-BaCl_2-FeCl_2$). Oreskes and Einaudi (1992) noted that the majority of inclusions from the hematite breccias exhibited highly constrained temperatures but broad ranges in salinities. Oreskes and Einaudi (1992) suggested the broad salinity ranges may be a product of boiling, or mixing of high temperature, moderately saline magmatic fluids with low temperature, and highly saline surficial fluids such as seawater or groundwater. These lower-temperature inclusions are clearly quite distinct from the more highly saline, high-temperature inclusions at FC4NW. While salinity ranges are variable at Olympic Dam, primary type 1 inclusions at FC4NW are well constrained, probably reflecting a single fluid source.

4.6. DISCUSSION: FLUID EVOLUTION AT MFC

Na-Ca alteration occurs abundantly throughout the EFB, and is spatially and temporally associated with the intrusion of the Williams and Naraku Batholith (discussed in detail in chapter 2). Na-Ca alteration at FC4NW occurs as two phases, clinopyroxene-rich and amphibole-rich Na-Ca alteration, the latter of which represents the main host for Cu. These are interpreted to be related to the same fluids, whereby clinopyroxene was stable at higher temperatures followed by actinolite at lower temperatures. This study has shown that both of the Na-Ca alteration phases at FC4NW probably formed from fluids similar to those responsible for regional Na-Ca alteration (Pollard et al., 1997; de Jong and Williams, 1995), and are distinct from fluids associated with ore and pre- to post- Cu-Au mineralisation stages at Starra, Eloise, Osborne and Ernest Henry (Rotherham et al., 1998; Baker, 1998; Adshead, 1995; Mark et al., 1999).

Although only two type 3b and ten type 4b workable inclusions were analysed from sample MFC002, these results show that fluids associated with Fe oxide metasomatism from outcrop at MFC differ considerably compared to fluids associated with Na-Ca alteration. In particular, type 4b inclusions exhibited lower homogenisation temperatures and varied over a larger range compared to type 4b inclusions from Na-Ca alteration at FC4NW. These broad temperature ranges may suggest the interaction of both a high and low temperature fluid, the latter of which may be of meteoric origin.

Studies of regional Na-Ca alteration and Cu-Au mineralisation in the EFB show hypersaline and CO_2-rich inclusions to co-exist, suggesting unmixing of a CO_2-H_2O brine (de Jong and Williams, 1995; Pollard et al., 1997). In contrast, type 1 and 2 fluid inclusions at FC4NW were rarely observed in the same sample suggesting immiscible fluid separation was not responsible for these inclusions. Pressure estimates for type 1 and 2 inclusions also give vastly different values at FC4NW, however values calculated for type 1 fluid inclusions are almost certainly overestimated due to their $CaCl_2$ content (Zhang and Frantz, 1989). In addition, the type 1 inclusions in this study were homogenised by halite dissolution. This is inconsistent with the separation of an immiscible CO_2-H_2O brine, and suggests that the type 1 and 2 fluid inclusions at FC4NW and are most likely related to different fluids.

Fluid mixing has been invoked at both the Starra and Ernest Henry Cu-Au deposits by Rotherham et al (1998), Williams et al (2001) and Mark et al (1999). In particular, high salinity ranges and well defined temperatures of secondary two-phase and halite-bearing (type 4) inclusions were noted by Rotherham et al (1998) and assumed to be the product of fluid mixing between high- and low- salinity fluids. Mark et al (1999) proposed that fluid mixing may have been a potential trigger for Cu-Au mineralisation at Ernest Henry. At FC4NW, the transition from clinopyroxene-rich to the amphibole-rich sulphide-bearing Na-Ca alteration phase suggests that a down temperature gradient with time may have triggered sulphide precipitation. Type 1 fluid inclusions typically exhibit the highest temperatures and salinities and contain relatively low Cu. In contrast, temperatures and salinities associated with type 3a inclusions are considerably lower and contain relatively high Cu compared to the type 1 inclusions. The type 3a fluid inclusions, therefore, may represent the mineralising fluid responsible for sulphide-bearing amphibole-rich Na-Ca alteration prior to mineral precipitation. Type 4a inclusions were also found to indicate lower temperatures, and also exhibited a broader range of salinities compared to the other fluid inclusion types. Together with the high Br/Cl ratio analysed by PIXE, these broad salinity values suggest the type 4a inclusions were formed from the interaction of an externally derived low-salinity fluid, possibly of meteoric origin.

In general, fluids associated with clinopyroxene-rich and amphibole-rich Na-Ca alteration at FC4NW contain variable amounts of Cl, Br, Ba, Ca, K, Zn, Cu, Fe, Mn, that are more reminiscent of regional Na-Ca assemblages from Mount Angelay as opposed to Cu-Au mineralisation at Ernest Henry, Starra, Mount Elliott and Osborne. This is surprising considering the amphibole-rich Na-Ca phase at FC4NW contains sulphide, which is typically absent in most (but not all) regional Na-Ca assemblages. Perhaps fluids associated with the amphibole-rich Na-Ca phase at FC4NW interacted with another S-bearing fluid to produce sulphide. In contrast, fluids responsible for regional Na-Ca alteration such as at Mount Angelay may not have interacted with a S-bearing fluid inhibiting the precipitation of sulphides.

The presence of sulphides in Na-Ca assemblages at both the FC4NW and FC12 (chapter 3) prospects may correlate with the start of the depositional phase peripheral to the Ernest Henry deposit. At the FC12 prospect situated to the north of FC4NW (chapter 3), mineral assemblages associated with Na-Ca alteration (chlorite and carbonate) reflect lower-temperature conditions, and geochemical mass transfer patterns associated with alteration differ considerably from other regional Na-Ca assemblages in the EFB (cf. Rubenach and Lewthwaite, 2002; Oliver et al., 2004). This is attributed to fluids at FC12 undergoing significant fluid-rock interaction and may thus represent a more evolved fluid that cooled over time. In contrast, the mineral assemblages associated with clinopyroxene-rich and amphibole-rich Na-Ca alteration at FC4NW require much higher temperatures compared to FC12. These assemblages are also similar to those found around weakly mineralised hanging wall Fe oxide-rich rocks and Na-Ca alteration at Ernest Henry. The presence of sulphides associated with Na-Ca alteration at FC4NW, FC12 and the Ernest Henry hanging wall is testimony to the potential for these fluids to precipitate Cu over a range of temperatures. One possibility is that certain physicochemical conditions (P, T, f_{O2}, f_{s}) combined with a down-temperature gradient favoured the precipitation of sulphides at and around the Ernest Henry system. Another possibility is that fluids associated with both Na-Ca alteration stages at FC4NW may have interacted with, or were overprinted by, another externally-derived fluid containing additional Cu, Fe and/or S. This latter suggestion is supported by the presence of low-temperature carbonate + hematite + chalcopyrite + pyrite veins overprinting Na-Ca alteration within the FC4 and FC4 south prospects of the MFC exploration lease (Mark, G, *pers comm*). If this is the case, then the fluids responsible for Na-Ca alteration may not be the main source of Cu at FC4NW.

In contrast to FC4NW and Mount Angelay, fluids associated with ore and pre- to post-mineralisation events at Starra and Ernest Henry contain a distinctly different fluid chemistry, with Mn, Cu, Fe, Zn and Ba commonly in higher concentrations in the Cu-Au deposits. In particular, Lightning Creek fluid inclusions contain Cu values that are two orders of magnitude higher, probably representing a lack of significant S in the fluid and/or host rocks (Perring et al., 2000). One exception are the Cu values at Ernest Henry, which are significantly lower than both at Lightning Creek and Starra but similar to Cu values associated with FC4NW and regional Na-Ca assemblages. However, these low values were attributed to these fluids representing ‘spent’ equivalents after the main Cu-Au mineralisation phase. Nevertheless, the presence of both Cu and Fe at FC4NW and Mount Angelay suggests these fluids had the ability to transport both of these components in the fluid phase (Mark et al., 1999). The complex chemistry associated with Cu-Au mineralisation at Ernest Henry (Mark et al., 1999) implicates the interaction of two or more fluids that vary significantly in their chemical composition (as mentioned above). Economic Cu-Au mineralisation may not have occurred at FC4NW due to either the absence of a second (S-bearing) fluid, and/or the fluids simply did not contain enough Cu to produce significant Cu-Au mineralisation.

CHAPTER 5:

THE GEOCHEMISTRY OF FE OXIDE-RICH ROCKS IN THE PROTEROZOIC EASTERN FOLD BELT, NW QUEENSLAND: IMPLICATIONS FOR EXPLORATION

THE GEOCHEMISTRY OF FE OXIDE-RICH ROCKS IN THE PROTEROZOIC EASTERN FOLD BELT, NW QUEENSLAND: IMPLICATIONS FOR EXPLORATION

5.1. INTRODUCTION

The Eastern Fold Belt (EFB) of the Mount Isa Inlier is one of the most significant Proterozoic base metal provinces in the world. Many of the IOCG deposits in the EFB are spatially associated with Fe oxide-rich rocks, commonly termed ‘ironstones’. There has been much debate amongst workers regarding the source of fluids responsible for the formation of Fe oxide-rich rocks and Cu-Au mineralisation (e.g. Barton and Johnson, 2000; Pollard, 2000). The effective discrimination between barren and mineralised Fe oxide-rich rocks could prove invaluable for the future exploration of IOCG deposits in the EFB and elsewhere.

A unified mechanism for the formation of Fe oxide-rich rocks in the EFB remains unresolved. Their monomineralic nature and lack of distinct textures make it difficult to determine whether primary (e.g. magmatic or sedimentary) or secondary (e.g. hydrothermal) processes are responsible for their formation (Davidson et al., 1989; Williams, 1994). The poor preservation of contact relations between Fe oxide-rich rocks and the adjacent rocks compound satisfactory resolution of the likely genetic mechanisms. In this chapter, the mass and volume changes associated with Fe oxide metasomatism within the MFC exploration lease and at Roxmere (Fig. 5.1) are examined to more precisely understand the chemical processes involved in their formation. The results will be employed to better assess the ore-forming mechanisms associated with IOCG deposits in the EFB and elsewhere.

5.2. PROCESSES INVOLVED IN THE FORMATION OF FE OXIDE-RICH ROCKS

The term ‘ironstone’ has been used extensively in the literature and commonly refers to any rocks consisting of a high Fe oxide content. It has been used mostly as a generic term that is of indiscriminate origin, and lacks a precise definition of chemical or mineralogical composition. Boggs (1995) defined ironstones as thin, massive, or poorly banded sequences a few meters to a few tens of meters thick. However, this classification refers to Fe-bearing rocks produced by sedimentary processes only. Consequently, those rocks formed by other processes (e.g. banded iron formations

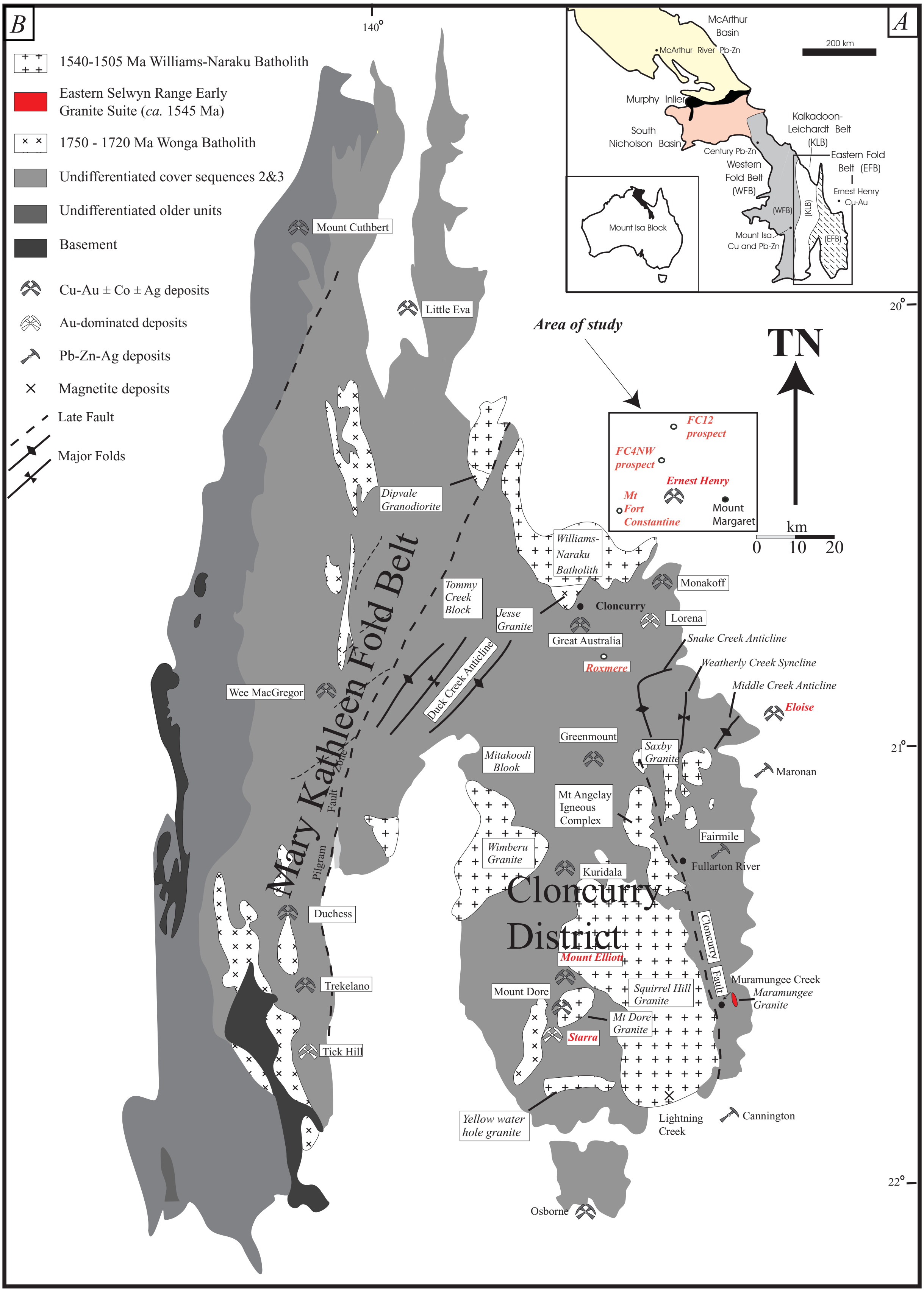

Figure 5.1. A. Tectonostratigraphic divisions of the Mount Isa Inlier, Queensland. B. Enlargement and simplified geology of the Eastern Fold Belt with locations of areas relevant to this study including Roxmere, MFC outcrop, FC12 and FC4NW prospects. Also shown are the major Fe oxide Cu-Au deposits. Compiled from published AGSO maps and modified by Williams (1998).

(BIF), laterites, orthomagmatic Fe oxide-rich rocks, apatite (Kiruna) type iron ores and hydrothermal Fe oxide-rich rocks), described in more detail below, require characterization. Therefore, for the purpose of this study, a non-genetic approach is initially employed to define all rocks with >20 wt % Fe_2O_3 (T) as 'Fe oxide-rich rocks'.

5.2.1. Banded Iron Formations (BIF)

By far the most volumetrically significant of all Fe oxide-rich rocks globally are Banded Iron Formations (BIF), which are typically between 3000 and 1500 Ma in age. BIFs occur in stratigraphic units up to 100's m thick, and can extend for 100's to 1000's km in lateral extent (Evans, 1993). It is generally agreed that BIFs are formed via chemical (Holland, 1973; Anbar and Holland, 1992; Alibert and McCulloch, 1993; Canfield, 1998) and/or biological processes (LaBerge, 1973; Walker, 1984) however, the source of Fe and the exact processes that form BIFs are still controversial. Many scientists have argued that BIFs originated in an upwelling continental shelf setting while others have argued that BIFs are deep water deposits (Beukes and Klein, 1990). Geochemically, BIFs exhibit REE patterns with pronounced positive Eu anomalies, negative Ce anomalies and depletion in the light REE interpreted to represent chemical precipitation from solutions that represent mixtures of seawater and hydrothermal input (Beukes and Klein, 1990). The Hamersley Province of Western Australia hosts one of the best examples of BIFs in the world, and contains several economic deposits of iron ore derived from these BIFs (see below) (e.g. Mt Whaleback, Mt Tom Price and Paraburdoo) (Morris, 1985; Harmsworth et al., 1990; Webb et al., 2003).

5.2.2. Laterites and iron ores derived from BIFs

Iron-rich laterites are residual deposits that form as a product of intense chemical weathering, and may be as much as 20 m thick, but are usually < 6 m. They typically consist of nodular red, yellow or brown hematite and goethite and contain up to 20 % alumina (Evans, 1993). The process of laterisation to produce ore-grade Fe-bearing rocks has been linked to the weathering of BIFs (e.g. Hamersley Province) (Morris, 1985; Hamsworth et al., 1990). This involves the uplift of BIF layers and the weathering and oxidation of magnetite to martite along with the replacement of chert by goethite. Subsequent burial and metamorphism then upgrades the goethite to form fine-grained hematite (Morris, 1985). More recent research, however, has identified problems with these supergene models including the timing of metamorphism and deformation with respect to the formation of some orebodies (Oliver and Dickens, 1999; Powell et al., 1999; Taylor et al., 2001). Models for the formation of some of these iron ores propose Si dissolution and Fe oxidation associated with high temperature fluids (Oliver and Dickens, 1999; Powell et al., 1999; Taylor et al., 2001). Webb (2003) also demonstrated that iron ore enrichment might be obtained by mass loss via the removal of gangue minerals (i.e. quartz, carbonates and silicates) rather than the addition of iron.

5.2.3. Orthomagmatic Fe oxide-rich rocks

Fe oxide-rich rocks can form when particular minerals are concentrated by magmatic accumulation. Fractional crystallisation within a magma chamber is believed to be the major process involved in the formation of cumulate Fe oxide-rich rocks that predominately form in layered gabbros as well as in some syenitic and granitic intrusions (Phillpots, 1990). The layering exhibited in most cumulates range in thickness from millimetre- to metre-scale and results from variation in the modal abundance of cumulus minerals, grain size, texture and mineral composition (Phillpotts, 1990).

Wager et al (1960) and Phillpotts (1990) defined accumulation as the enrichment of early crystallising minerals in magma. Cumulates have a characteristic texture formed by two contrasting types of mineral grains, which are distinguished by the relative timing of their crystallisation. Cumulus grains are the earliest and most abundant, and tend to be euhedral and rest against each other. The interstitial minerals then grow during a postcumulus period from an intercumulus liquid. Common cumulus minerals include olivine, pyroxene, plagioclase, chromite and magnetite, and the postcumulus minerals typically include pyroxene, plagioclase, magnetite, ilmenite, hornblende and granophyric intergrowths of quartz and alkali feldspar (Phillpotts, 1990).

Almost all large layered gabbroic complexes of this type are of Precambrian age, which may reflect higher heat production early in the Earths history (Phillpots, 1990). Two examples of large igneous complexes containing layers of near-pure cumulate magnetite include the Skaergaard Intrusion of East Greenland and the Bushveld Complex of South Africa. The exact mechanism by which Fe oxide-rich layers form is still largely uncertain, and is likely to differ according to the composition of the fractionating magma (Evans, 1993). The Bushveld Complex hosts one layer within the upper zone of the igneous complex that forms a prominent stratigraphic marker consisting of ferrodiorites continuing for up to 1500 m in lateral extent (Reynolds, 1985). More recent studies on magnetite-rich gabbro in layered tholeiitic sequences shows that high f_{O2} favours the crystallisation of Fe-Ti oxides during early fractional crystallisation (Reynolds, 1985; Jiren et al., 1988; Kariyanna et al., 1996; Karkkainen, 1999; Vinayaka et al., 1999).

5.2.4. Apatite (Kiruna) type iron ores

Kiruna type iron ores are associated with volcanic rocks or high-level intrusions and occur in many parts of the world including Sweden (Nystrom and Henriquez, 1994), Chile and the Anvik region of southeastern Turkey (Helvaci, 1994). The ores are typically composed of magnetite with varying amounts of apatite and actinolite and occur as large massive bodies as well as small dykes and veinlets (Nystrom and Henriquez, 1994). The age of Kiruna-type deposits varies significantly from the late Proterozoic Kiirunavaara deposit (1880 ± 3 Ma; Cliff et al., 1990) to much younger Cretaceous deposits within the Chilean Iron Belt (Nystrom and Henriquez, 1994). One factor that links all the deposits, however, is their spatial association with intermediate to acid intrusives and volcanics (Hildebrand, 1986 and Nystrom and Henriquez, 1994). In addition, Na-Ca alteration is also prevalent in and around many of these deposits. Both magmatic, hydrothermal and exhalative-sedimentary origins have been invoked for the origins of these iron ores. Early models proposed that the Kiruna-type ores were exhalative-sedimentary in origin and precipitated as chemical sediment in a volcanic-marine environment (Parak, 1975). Later models have appealed to transitional magmatic – hydrothermal processes (Rhodes et al., 1999) as well as magmatic differentiation, liquid immiscibility and leaching of cooling plutons by late magmatic (deuteric) fluids as possible sources (Nystrom and Henriquez, 1994 and references therein).

Nystrom and Henriquez (1994) investigated the trace element geochemistry of iron ores from Sweden and Chile and compared these to limestone-hosted stratiform ores from Bandurrias in the Chilean iron belt. The most important chemical difference between the Kiruna-type iron ores and the exhalative-sedimentary ore from the Bandurrias deposit is the relatively low V content in the latter. Nystrom and Henriquez (1994) suggest that V contents of up to 4000 ppm in magnetite derived from Kiruna-type ores are much too high to have occurred from a sedimentary-exhalative origin. This interpretation is supported by the ore breccias and tabular morphologies of these magnetite bodies, proposed to be consistent with a magmatic origin. Frietsch and Perdahl (1995) investigated the content and distribution of REE in apatite and magnetite in iron ores from Kiruna and the Anvik region of South Turkey. Their work showed that the REE patterns of magnetite and apatite from each of these deposits suggest a close affinity with alkaline and subalkaline magmas, indicating a rifting environment. Cliff et al (1990) presented isotopic evidence that indicated the iron ore at Kiruna formed at *ca.* 600^{o}C, and speculated that the iron ores, at least in part, may have formed by both high temperature hydrothermal and magmatic processes. Bookstrom (1995) and Rhodes et al (1999) also suggested that textures inferred by Nystrom and Henriquez (1994) to be magmatic in origin could have been produced by hydrothermal replacement of original volcanic textures in the igneous host.

5.2.5. Fe oxide-rich rocks formed via hydrothermal processes

Fe oxide-rich rocks produced by metasomatic processes typically occur as massive hematite and/or magnetite, with minor apatite ± amphibole ± clinopyroxene ± biotite ± albite and carbonates. Many Fe oxide-rich rocks derived from hydrothermal processes are associated with Cu-Au mineralisation (e.g. Ernest Henry). Fe oxide-rich rocks are produced by both infill and replacement processes (Williams, 1994). However, distinguishing between these two processes is commonly difficult due to their monomineralic nature and lack of distinctive textures. Experimental work has shown that Fe solubility in supercritical fluids can be controlled by a number of factors including salinity, pressure, temperature, pH/a_{HCl}, f_{O2} and f_S (e.g. Hemley et al., 1992). Eugster and Chou (1979) noted that at high temperatures, high-salinity solutions would react with micas to produce feldspar. In turn, the acidity of the fluid will increase and iron will become more soluble. As these fluids cooled and reacted with suitable host rocks, magnetite precipitated. Williams (1994) and Oliver et al (2004) proposed that the mobilisation of Fe in the EFB via albitisation was an important mechanism forproducing both barren and (Cu-Au) mineralised Fe oxide-rich rocks.

The EFB contains numerous examples of Fe oxide-rich rocks, many of which are associated with Cu-Au mineralisation. However, the genetic relationship between the two has been controversial. Carbon and oxygen isotope data is available from a variety of IOCG deposits in the EFB. For the Starra Cu-Au deposit, Davidson et al (1989) and Rotherham et al (1998) provided conflicting interpretations for $\delta^{13}C$ and $\delta^{18}O$ isotopic signatures of calcites associated with the Cu-Au mineralisation stage and with earlier Fe oxide-rich rocks. The isotopic signatures show a decrease in $\delta^{13}C$ and an increase in $\delta^{18}O$ for calcite. The original interpretation by Davidson et al (1989) was that the trend reflected equilibrium between a light $\delta^{13}C$, heavy $\delta^{18}O$ fluid and carbonates in the host metasedimentary sequence. Limited $\delta^{13}C$ and $\delta^{18}O$ isotopic signatures from Fe oxide-rich rocks at Osborne also showed similar results. Williams (1994) volunteered an alternative hypothesis invoking their derivation during syn-tectonic hydrothermal alteration. This hypothesis was supported by Rotherham et al (1998) who found quartz-magnetite stable isotope pairs (early Fe oxide phase) and hematite-calcite stable isotope pairs (Cu-Au mineralisation) reflecting a decreasing temperature gradient, thus suggesting that both Fe oxide-rich stages formed from a cooling magmatic fluid. Further $\delta^{13}C$ and $\delta^{18}O$ work by Marshall (2003), however, showed that isotopic signatures from Osborne and Starra Fe oxide-rich rocks away from ore differ markedly with respect to $\delta^{13}C$ and $\delta^{18}O$ signatures compared to regional Na-Ca alteration and other examples of iron oxide and Cu-Au mineralisation (e.g. Eloise, Mount Elliott). This led Marshall (2003) to suggest that at least some of the Fe oxide-rich rocks hosting Cu-Au mineralisation at Osborne and Starra may have originated from sedimentary or metamorphogenic processes, supporting part of Davidson's et al (1989) model.

5.3. Fe OXIDE-RICH 'IRONSTONE' OCCURENCES IN THE CLONCURRY DISTRICT – RELATIONSHIPS TO Cu-Au MINERALISATION

The origin of Fe oxide-rich rocks in the EFB is one of considerable interest due to the apparent spatial and temporal association with Cu-Au mineralisation, raising the possibility that both may be genetically linked. Figure 5.2 shows the various relationships between Cu-Au mineralisation and Fe oxide-rich rocks in the EFB. Four main groups of Fe oxide-rich rocks were delineated in the EFB. The four groups are:

1) Category 1-type Fe oxide (Cu-Au) mineralisation: Fe oxide-rich rocks where sulphides are minor to absent;

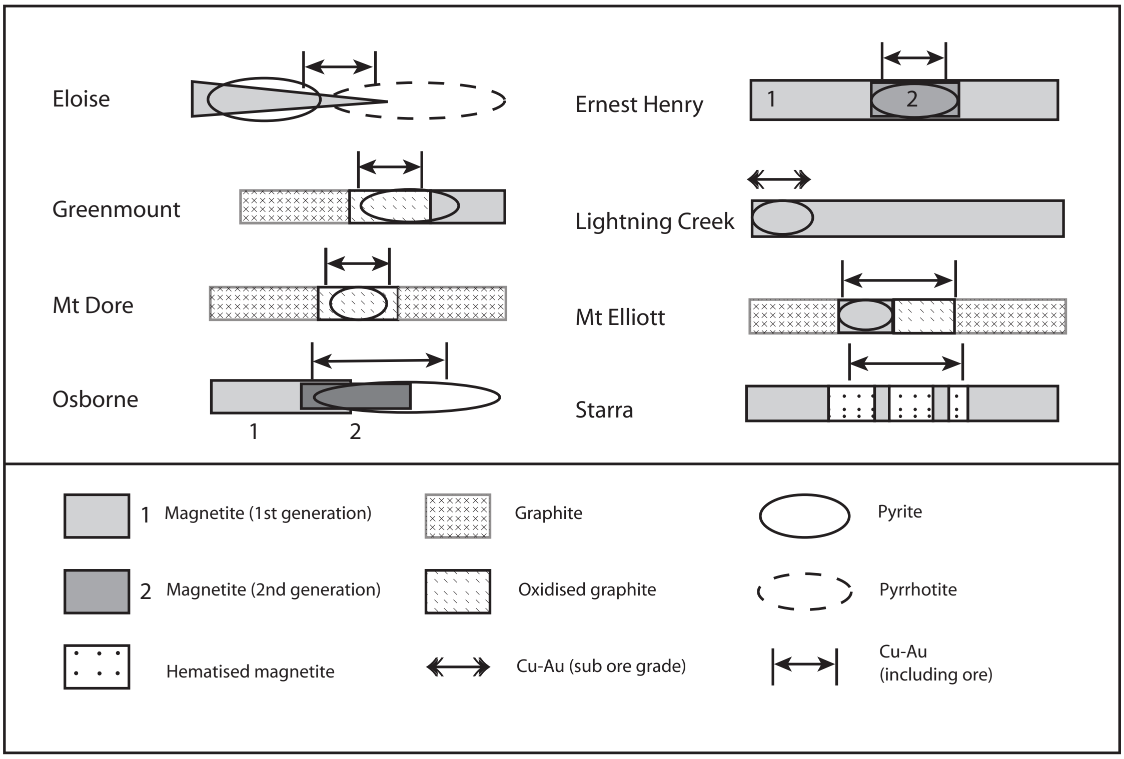

Figure 5.2: Schematic illustration showing the spatial relationships of Cu-Au ore with magnetite, iron sulphides, and graphite in several IOCG deposits in the EFB. Each deposit is drawn according to the relative abundance and overlap of certain components within an individual system (i.e. magnetite at Eloise). The relationships between these individual components are discussed in more detail in the text (Williams and Pollard, 2001 and references therein).

2) Category 2-type Fe oxide (Cu-Au) mineralisation: Cu-Au mineralisation overprints earlier Fe oxide-rich rocks;
3) Category 3-type Fe oxide (Cu-Au) mineralisation: Cu-Au mineralisation and Fe oxide formation are synchronous; and
4) Category 4-type Fe oxide (Cu-Au) mineralisation: Cu-Au mineralisation is not spatially or temporally associated with significant Fe oxide.

5.3.1. Category 1-type Fe oxide (Cu-Au) mineralisation

Fe oxide-rich rocks devoid of Cu-Au mineralisation are common throughout the EFB. Examples of sedimentary Fe oxide-rich rocks do occur (e.g. Monakoff and Fairmile; *c.f.* Davidson and Davis, 1997; Davidson, 1998) (Fig. 5.3a), although some examples are controversial (e.g. Starra in the Selwyn District). Most Fe oxide-rich rocks in the EFB occur as massive, monomineralic rocks, with little to no defining textural characteristics and are commonly interpreted to be metasomatic (Hitzman et al., 1992; Williams, 1994; Oliver et al., 2004). They occur as lenticular or vertical bodies associated with dilation within, or at intersections between fault/shear zones (Hitzman et al., 1992). Barren Fe oxide-rich occurrences are hosted in a range of rock types including calc-silicate, metasedimentary and mafic and felsic igneous rocks (Fig. 5.3b, c, d).

5.3.2. Category 2-type Fe oxide (Cu-Au) mineralisation

This category refers to pre-existing Fe oxide-rich rock overprinted by a later, not necessarily related, Cu-Au mineralising event. Deposits in this category include Starra and Osborne in the EFB (Rotherham, 1997; Adshead, 1995). The other significant IOCG deposits of Australia not located in the EFB also appear to fall into this category. These include the Olympic Dam and Emmie Bluff deposits of the Gawler Craton (Oreskes and Einaudi, 1992; Gow et al., 1994) and various IOCG deposits within the Tommy Creek Block of the EFB (Wedekind et al., 1989).

Starra Au-Cu

One of the most significant reported examples of this style of mineralisation in the EFB is the Starra Au-Cu deposit. The Starra deposit is unique in the EFB in that

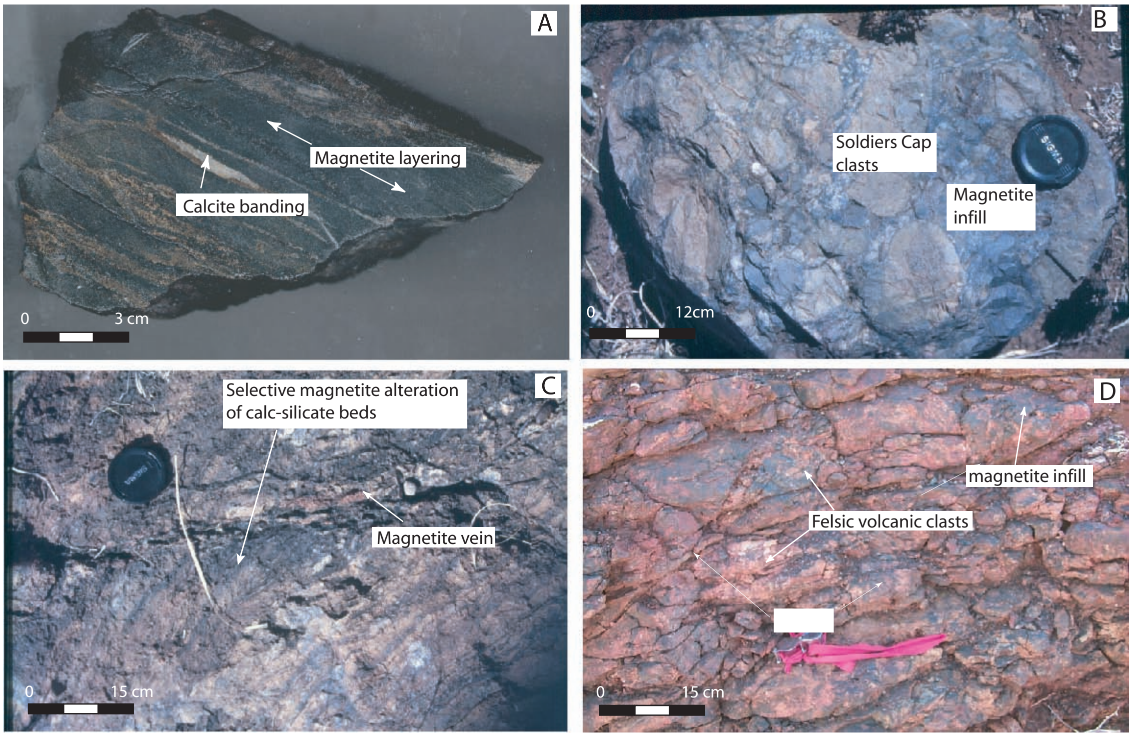

Figure 5.3: Field photographs of Fe oxide-rich rocks from the EFB.
A) Fine-grained magnetite-bearing biotite-muscovite schist, located adjacent to the Monakoff workings (Fig 5.1). Sample Monakoff W.
B) Brecciated Fe oxide-rich rock containing clasts of fine-grained metapelite of the Soldiers Cap Group, within the Gilded Rose area (Fig. 5.1). In this case, Fe oxide metasomatism (hematite and magnetite) predominately occurs as infill.
C) Magnetite vein cutting calc-silicate rock from the Corella Formation within the Gilded Rose area (Fig. 5.1). Note thin (<1 cm wide) magnetite alteration bands emanating from the magnetite vein and selectively replacing relict bedding within the calc-silicate rock.
D) Fe oxide-rich breccia from south of MFC (approximately 10 km southwest of the Ernest Henry mine) containing albitised felsic volcanic clasts (Fig. 5.1).

it has significantly higher Au:Cu ratios than the other deposits. Fe oxide-rich rocks at Starra form two prominent ridges that are situated in a major N-S striking and steeply dipping shear active late in the deformational history of the region (Adshead-Bell, 1998). Economic Cu-Au mineralisation is confined to only one of these ridges and is referred to as the Western Ironstone. However, Au-only and Cu-only equivalents also exist and in some cases are totally devoid of Fe oxides (Rotherham, 1997).

Two paragenetic stages pre-dating Cu-Au mineralisation are recognised and include: early widespread Na-Ca alteration (albite, quartz, scapolite, actinolite); and localised K-Fe alteration (biotite, magnetite, hematite, quartz, pyrite), with the latter responsible for the formation of the Western Ironstones. Typical mineral assemblages associated with Au-Cu mineralisation include pyrite, gold, chalcopyrite, barite, hematite, calcite, anhydrite and magnetite (Rotherham, 1997). The Au-Cu mineralisation is interpreted to have formed via the brecciation and subsequent hematisation of previous magnetite-rich rocks by their interaction with oxidised fluids (Rotherham et al, 1998). It is these oxidised fluids, unique to the Starra deposit, which may be responsible for the high Au:Cu ratios at Starra (Rotherham et al, 1998). The source of Cu, Au and S remains uncertain, although Williams et al (2001) identified highly complex fluid inclusions associated with Cu-Au mineralisation at Starra and speculated that fluid mixing may have contributed to ore genesis, rather than fluid-rock interaction alone.

Osborne Cu-Au

Osborne represents the other major deposit of this type in the EFB. The deposit is hosted by Mesoproterozoic metamorphic and igneous rocks. The host rocks are dominated by Na-rich feldspathic psammites with lesser amphibolites, early Fe oxide-rich rocks and a 30 m thick metaperidotite, a rock type that is not observed anywhere else in the EFB. These host rocks are cut by pegmatite and calc-alkaline lamprophyre dykes that post-date regional metasomatism (Adshead, 1995). Regional-scale faults are thought to have acted as conduits for the fluids responsible for economic Cu-Au mineralisation, while reverse movement on biotite shears are believed to have provided structural traps for the ore-bearing fluids (Harris, 1997).

Mineralisation at Osborne is divided into two discrete domains: the western domain containing two substantial Fe oxide-rich units, and the eastern domain, which is largely devoid of Fe oxide-rich rocks (Adshead, 1995). The ore mineral assemblage at Osborne comprises of massive silica flooding, chalcopyrite, hematite, magnetite and pyrrhotite as well as quartz, apatite, chlorite, talc, magnetite, chalcopyrite and pyrite within magnetite-rich breccia. The assemblages differ between domains and highlight the possible role played by previous Fe oxide-rich rocks in the precipitation of the Cu-Au mineralisation. In particular, Cu-Au mineralisation in the eastern domain contains more reduced associations of pyrrhotite-magnetite ± pyrite compared to the more oxidised hematite-magnetite-pyrite altered Fe oxide-rich rocks of the western domain (Adshead, 1995).

5.3.3. Category 3-type Fe oxide (Cu-Au) mineralisation:

This category refers to deposits in which Cu-Au and Fe oxides appear to have co-precipitated. Deposits of this type include Ernest Henry, the largest Cu-Au deposit in the Mount Isa Block (Ryan, 1998) and the Mt Elliott deposit (Little, 1997; Drabsch, 1998). Details of Fe oxide metasomatism associated with Cu-Au mineralisation at Ernest Henry are discussed in chapter 2.

Mount Elliott Cu-Au

Cu-Au mineralisation at Mount Elliott is hosted within multiply deformed and extensively skarn altered metasedimentary rocks and amphibolite of Paleoproterozoic age (Little, 1997, Wang and Williams, 2001). Importantly, Mt Elliott represents the only significant deposit in the district where intra-ore intrusions have been identified (Drabsch, 1998; Wang and Williams, 2001). The development of skarn and Cu-Au mineralisation occurred synchronously with movement along NE-dipping brittle reverse faults (Little, 1997, Wang and Williams, 2001). Cu-Au mineralisation is associated with a large component of infill and very large ore and gangue mineral grain sizes (up to 5 mm).

Economically significant Cu-Au mineralisation occurs in three distinct zones referred to as the upper, lower and Corbould zones. Fe oxides occur as magnetite associated with pyrrhotite + chalcopyrite within the amphibolites in the lower zone. In contrast, Cu-Au mineralisation hosted in metasedimentary rocks is variable in the upper zone but typically magnetite poor (Little, 1997; Wang and Williams, 2001). The Corbould zone has pyrite + minor pyrrhotite with low magnetite content. This lack of Fe oxide metasomatism directly associated with Cu-Au mineralisation within metasedimentary rocks also places part of Mount Elliott in the sulphide-dominant Cu-Au mineralisation category described below.

5.3.4 Category 4-type Fe oxide (Cu-Au) mineralisation

This category refers to deposits where Cu-Au mineralisation is not spatially associated with significant Fe oxide, or where Fe oxide phases are not a major constituent in the Cu-Au mineralisation assemblage. Instead these deposits are associated with a dominant sulphide association. This style of deposit includes the Eloise Cu-Au deposit (Baker, 1998) as well as the Mount Dore and Greenmount IOCG deposits (Krcamrov and Stewart, 1998; Laing, 1998). Some Cu-Au mineralisation hosted in metasedimentary rocks at the Mount Elliott deposit also falls into this category.

Eloise Cu-Au

The Eloise Cu-Au deposit is hosted in meta-arkoses, quartz-biotite schist and amphibolite within a dilational structural setting known as the Levuka Jog (Baker, 1998). The Levuka Jog is interpreted as the major conduit for Cu-Au-bearing fluids, in which alteration and mineralisation was synchronous with ductile-brittle deformation. Baker and Laing (1998) suggested that Cu-Au mineralisation was synchronous with the waning stages of the Isan orogeny and emplacement of the Williams and Naraku Batholith. Radiogenic ($^{40}Ar/^{39}Ar$) and stable (O, H and S) isotope analyses of biotite, muscovite and quartz indicates that the age of the Cu-Au mineralisation is likely to be ca. 1530 Ma (Baker et al., 2001).

While parts of the structural features associated with the Levuka Jog coincide with aeromagnetic highs, Cu-Au mineralisation is spatially unrelated to these magnetite-rich zones. The majority of the deposit is contained within the Elrose and Levuka lodes. These lodes are associated with highly strained and altered rocks that form part of the Eloise Shear Zone and are largely composed of chalcopyrite + pyrrhotite + minor magnetite and pyrite (Baker, 1998). The paragenesis of alteration and mineralisation at Eloise can be divided into three distinct alteration packages:

Stage 1: comprises extensive alteration reminiscent of regional albitisation observed throughout the EFB;

Stage 2: associated with hornblende + biotite + quartz-bearing veins, wall-rock alteration and shear zones; and,
Stage 3: vein-controlled Cu-Au mineralization associated with gangue minerals that include quartz ± calcite ± chlorite ± muscovite ± actinolite (Baker and Laing, 1998).

The deposition of pyrrhotite at Eloise instead of iron oxide observed at many of the other IOCG deposits in the district (Starra, Osborne and Ernest Henry) may be a reflection of the composition and redox state of the host rock, where carbonaceous shale and other metasedimentary rocks at Eloise may have inhibited the deposition of iron oxides.

5.4. PROPOSED MODELS FOR THE FORMATION OF Fe OXIDE (Cu-Au) DEPOSITS

Several models pertaining to the origin of both mineralised and barren Fe oxide-rich rocks have been proposed, with the most contentious issue being the origin of the fluids responsible for their formation. Three of the more recently proposed models include a magmatic fluid model, non-magmatic fluid model and a magmatic-evaporitic fluid mixing model, each of which are described in more detail below. However, no single model satisfactorily accounts for the diverse mineralogical and chemical characteristics observed in Fe oxide (± Cu-Au) deposits both within the EFB and elsewhere. The main variables that make the development of a single model difficult include: Variations in hematite:magnetite:sulphide and Cu:Au ratios; the variability of spatially associated magmas, and the distribution and volumes of spatially related hydrothermal alteration events.

5.4.1. Magmatic fluid model

Perring et al (2000), Pollard (2000) and Williams and Skirrow (2000) proposed that fluids derived from contemporaneous magmas played a major role in the formation of Na-Ca alteration and Cu-Au mineralisation. This apparent association with contemporaneous magmas has led Pollard (2000) to draw a genetic link between IOCG deposits and the more thoroughly understood porphyry Cu-Au deposits suggesting that both deposit types may be viewed as part of a broad spectrum of intrusion-related Cu-Au deposits (Pollard, 2000). This hypothesis is supported by oxygen and hydrogen isotope analyses of pre-ore and syn-ore hydrothermal minerals from a number of IOCG deposits that exhibit dominantly magmatic signatures, and slight indications of meteoric and/or connate fluids in later stages (Rotherham et al., 1998; Mark and Foster, 2000; Perring et al., 2000; Baker et al., 2001). Furthermore, fluid inclusion studies typically indicate the presence of co-existing hypersaline and CO_2-rich fluid inclusions in both syn- and pre-ore alteration assemblages that may be the product of unmixing of an original H_2O-CO_2-salts fluid (Adshead, 1995; Rotherham et al, 1998; Baker, 1998; Pollard, 2000). Xu and Pollard (1999) suggested that the entrapment of CO_2-rich inclusions evolved progressively from early high-density to late low-density fluids, while aqueous inclusions evolved from early hot to late cooler fluids. These coincide with similar inclusions identified at Lightning Creek that were formed during the crystallisation of granitic sills associated with major magnetite precipitation (Perring et al., 2000). It is possible therefore that both the hypersaline and CO_2-rich fluids were produced from I-type granitoids which are mostly distal to the actual ore zones.

5.4.2. Non-magmatic fluid model

Haynes (2000) proposed that the source of the fluids responsible for sulphide precipitation at Olympic Dam may be brines or saline waters stored in an overlying extensional or trans-tensional basin, with the circulation of these basinal brines driven by thermal events associated with the emplacement of granitic intrusions. Haynes (2000) also draws similarities between both Olympic Dam and EFB IOCG deposits and Fe sulphide Cu (±Au) deposits of the Western Succession of the Mount Isa Block including Mount Isa and Gunpowder. Contrasts in mineralogy of the two ‘end member’ deposit styles is attributed to differences in the gross oxidation state of the respective host rock successions. More specifically, Haynes (2000) proposed that the oxidation state of the host rocks or of another interacting hydrothermal fluid is what governs the mineralogy and precipitation of sulphides, whereby sulphide precipitation at Olympic Dam occurred through the reduction of sulphate and oxidation of ferrous iron from fluid mixing. In contrast, Haynes (2000) proposed the Mount Isa copper system resulted from the reduction of an oxidised hydrothermal fluid, most likely by fluid-rock interaction.

5.4.3. Magmatic – evaporitic fluid mixing model

Barton and Johnson (2000) proposed that a variety of fluid sources may be responsible for the formation of various IOCG deposits, reflected in the diverse mineralogical and chemical characteristics of deposits of this type. Barton and Johnson (2000) used mass and energy balance models to illustrate that magmatic fluid alone cannot produce the Na-Ca alteration spatially associated with numerous IOCG deposits particularly in Nevada. As a consequence, two end-member variants were proposed. High temperature mineralisation and high K/Na and Si/Fe ratios in the alteration, reflecting magmatic fluid sources similar to porphyry Cu-Au and related deposits, typify one group. A second group is characterised by more oxide-rich, sulphide poor mineralisation, low Si/Fe ratios and voluminous alkali-rich alteration. In this case, non-magmatic brines are circulated by thermal convection where ore grade concentrations are less common as metals are less easily trapped. This model provides one explanation for the occurrence of barren Fe oxide-rich rocks, because sulphur-bearing magmatic fluids need to mix with externally derived saline-rich fluids evolved from evaporitic sedimentary country rock to deposit ore (Barton and Johnson, 2000). If this mixing does not occur, Cu-Au mineralisation will not take place and will lead to the formation of barren Fe oxide-rich rocks.

5.4.4. Common characteristics associated with Fe oxide Cu-Au mineralisation

Although the source of fluids responsible for Cu-Au mineralisation is not completely understood, certain aspects are consistently apparent at all deposits that can help define the specific conditions needed for Cu-Au mineralisation to occur. These include:

1. All IOCG deposits in the EFB occur in dilational sites within shear zones (Adshead, 1995; Rotherham, 1997; Adshead-Bell, 1998; Baker and Laing, 1998; Baker, 1998; Mark et al., 1999; Marshall, 2003)
2. Most deposits record an earlier period of Na-Ca alteration followed by later potassic alteration.
3. The result of this alteration is an increase in competency of the host rocks so more open space can develop as a result of deformation (Adshead-Bell, 1998; Baker, 1998; Mark et al., 1999).
4. All deposits are associated with both CO_2 and hypersaline fluid inclusions which may represent unmixing of a H_2O-CO_2 salts fluid (Pollard, 2000), or fluid mixing (Mark et al., 1999, Williams et al., 2001)
5. The Cu-Au systems exhibit overlapping calculated $\delta^{18}O$ (+7 to +11 ‰) and $\delta^{34}S$ (-3 to +3 ‰) fluid compositions, which largely preserve a dominant magmatic

component diluted by external fluid input and/or variable host rock interaction (Davidson and Dixon, 1992; Adshead, 1995; Twyerould, 1997; Rotherham et al., 1998; Mark and Crookes, 1999; Mark et al., 1999; Baker et al., 2001). These data show that the ore-forming fluids for most ore systems were most likely derived from similar source fluids that experienced various fluid-rock interactions over a range of pressure and temperature conditions at the site of ore deposition to produce variations in the mineralogy and geochemistry of the ore system.

Conversely, variations in mineralogical and chemical characteristics between deposits may be due to:

a. A change in the composition or oxidation state of source intrusions;
b. Changes in the conditions of ore formation (T, P, fO_2, fS_2, fluid salinity, and pH); and/or
c. Varying degrees of fluid mixing (Adshead, 1995; Little, 1997; Baker, 1998; Rotherham et al., 1998; Mark et al., 1999; Williams et al., 2001; Oliver et al., 2004)

5.5. PETROGRAPHY OF Fe OXIDE-RICH ROCKS: THIS STUDY

5.5.1. Regional Fe oxide-rich rocks

Roxmere ‘ironstone’

The Roxmere ‘ironstone’ represents one of the few examples in the EFB where contacts between Fe oxide-rich rocks and adjacent rock types crop out. The outcrop forms a hill with an approximate length of 75 m that trends NW-SE, and a maximum height of ~10-30 m. The outcrop was mapped along a NW-SE traverse (Fig. 5.4), and consists of variably albitized calc-silicate rocks. Rarely preserved bedding within the calc-silicate rocks displays a consistent E-W to SE-NW trend (Fig. 5.4, 5.5a). Brecciated calc-silicate rocks occur parallel to bedding, with hematite + carbonate ± magnetite ± apatite dominating the matrix assemblage (Fig. 5.4, 5.5b). These breccias show no evidence of milling, with clasts typically being angular and highly albitised. Towards the northeastern part of the outcrop, the variably albitised calc-silicate rocks exhibit a sharp contact against massive Fe oxide-rich rocks (Fig. 5.4, 5.5c,

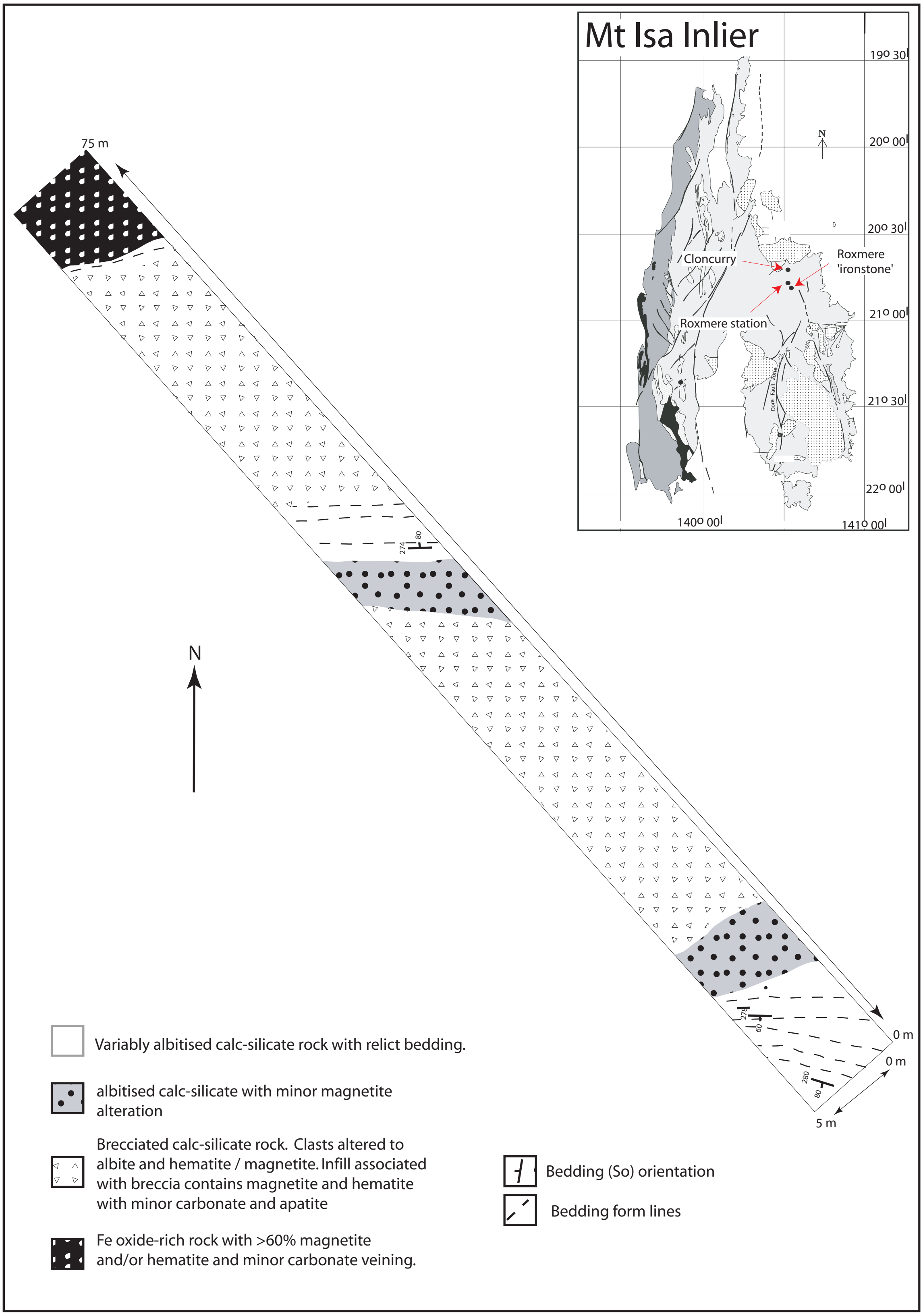

Figure 5.4: Traverse map of the Roxmere ironstone illustrating the distribution of albitised calc-silicate rocks and Fe oxide-rich rocks, as well as the orientation of contacts and bedding. Most of the outcrop is composed of brecciated calc-silicate rock with hematite + magnetite + apatite + carbonate infill. Note the contacts between the albitised calc-silicate rocks, Fe oxide-rich breccias and massive Fe oxide-rich rock are all sharp and parallel to bedding (where present). Inset shows a simplified map of the Mt Isa Inlier (see Fig. 5.1 for detailed version) with the location of the Roxmere ironstone.

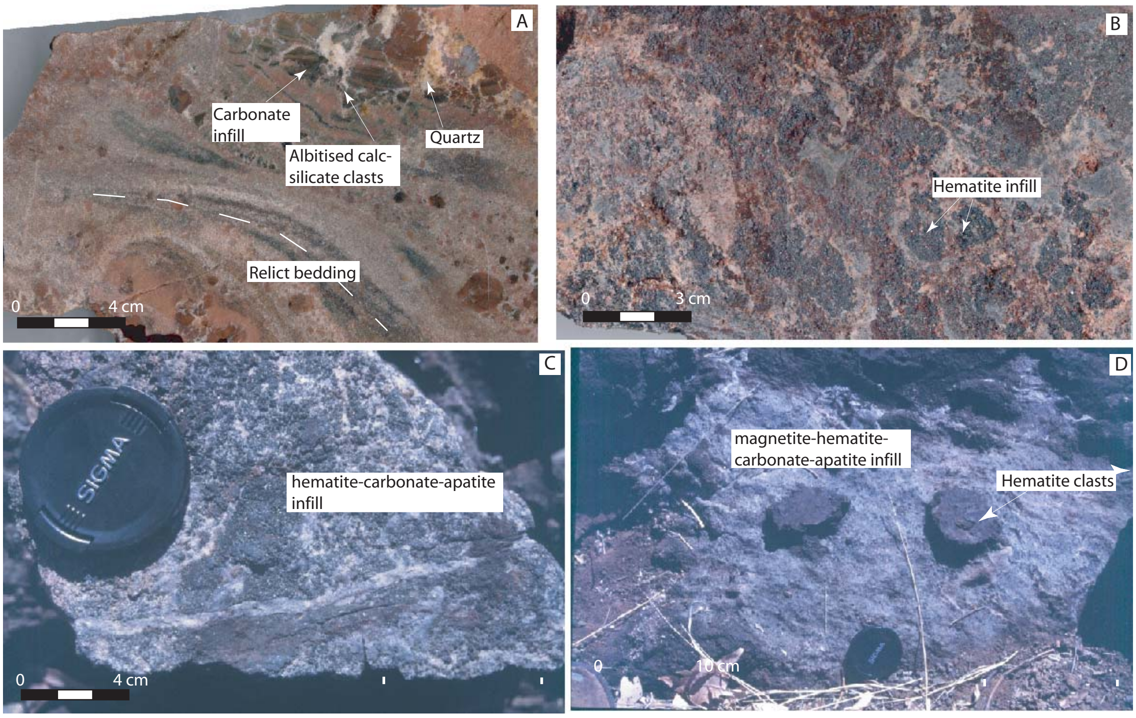

Figure 5.5: Photographs of calc-silicate rocks and Fe oxide-rich rocks from the Roxmere ironstone.

A) Albitised calc-silicate rock with relict bedding affected by later carbonate veining. Note local brecciation associated with carbonate veining.

B) Hydrothermal Fe oxide-rich breccia containing intensely albitised clasts of calc-silicate rock and hematite + magnetite + apatite infill.

C) Hematite + carbonate + apatite Fe oxide-rich rock with overprinting carbonate veining.

D) Hydrothermal Fe oxide-rich breccia with hematite and magnetite clasts cut by later magnetite + hematite + carbonate + apatite infill.

d). These Fe oxide-rich rocks exhibit no discernable banding in hand specimen and given their sharp contact relations with the adjacent calc-silicate rocks, are interpreted to represent hydrothermal veins. Overprinting these massive rocks are fine-grained hematite + carbonate ± magnetite ± apatite veins (Fig 5.5c, d), which are also mineralogically similar to the breccias and massive Fe oxide-rich rocks.

Mount Fort Constantine

Mount Fort Constantine (MFC) is located approximately 10 km southwest of the Ernest Henry Cu-Au deposit (chapter 2). Toward the south of the MFC hill lies a pit of old workings where sharp contacts between Fe oxide-rich rocks composed of hematite + apatite + actinolite ± magnetite and variably albitised felsic volcanic rocks are exposed (Fig. 5.3d). Two rock faces measuring 100 m by 5 m were mapped (Fig. 5.6). Due to its proximity to the Ernest Henry Cu-Au deposit, the genetic relationship between Fe oxide-rich rocks at MFC and similar rocks peripheral to the Ernest Henry ore body is of particular interest.

Monakoff

Monakoff represents the most proximal significant Cu-Au occurrence to the Ernest Henry Cu-Au deposit (~25 km south), and shares many geochemical similarities with its larger neighbour (e.g. the element association F-Mn-Co-As-Ba-REE-U). The Fe oxide-rich rocks which host Cu-Au mineralisation have been previously interpreted as syngenetic (Davidson and Davis, 1997). Monakoff ore exhibits many similarities with Ernest Henry ore including a barite + carbonate + fluorite + magnetite + chalcopyrite-dominant mineral assemblage, and contains economic Cu, Au, Co, U and Ag. However, one distinct difference between the two deposits is the absence of a distinctive K-feldspar alteration halo at Monakoff. Mineralisation at Monakoff occurs as two lenses, termed the western and eastern lenses, and is hosted mainly in meta-pelitic rocks of the Soldiers Cap Group. The deposit itself is positioned within a linear magnetic anomaly expressed by the presence of BIFs and Fe oxide-rich rocks. No granitic intrusions have been identified at Monakoff, however ~2 km north of Monakoff lies minor outcrop of the Naraku Batholith.

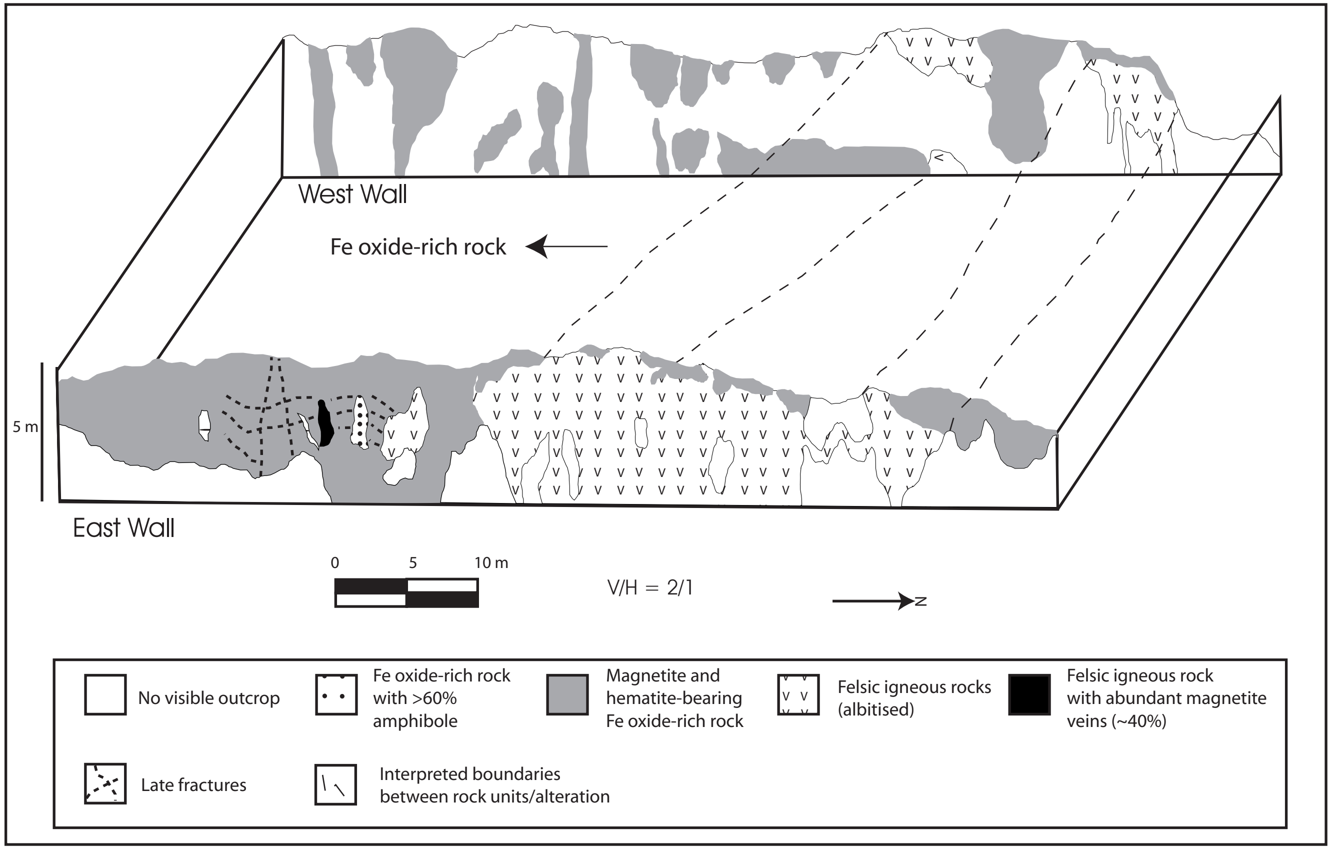

Figure 5.6: Box diagram of variably albitised felsic volcanic rocks and Fe oxide-rich rocks at the MFC outcrop located approximately 10 km southwest of the Ernest Henry mine (see figure 5.1 for location). Note sharp contacts between the massive Fe oxide-rich rocks and felsic volcanic rocks.

One sample of magnetite-bearing biotite-muscovite schist located adjacent to the workings at Monakoff was collected for chemical analysis (Fig. 5.3a). In hand specimen, the sample is very fine grained, exhibits a dark grey colour and is cut by a 2 mm wide calcite vein. In thin section, the schist is composed of magnetite (~20 %) + biotite + muscovite + quartz with minor albite due to alteration. The rock preserves a strong tectonic fabric which is defined by the alignment of muscovite and biotite grains.

5.5.2. FC12 Prospect

Fe oxide-rich rocks are hosted within a tholeiitic gabbroic sequence at the FC12 prospect. The gabbroic rocks are typically medium- to coarse-grained, dark grey to black in colour, and are composed of albitic plagioclase, amphibole, biotite, magnetite, ilmenite, pyrite, orthopyroxene, clinopyroxene and rare chalcopyrite. The petrography of the gabbroic hosts is discussed further in chapter 2. The Fe oxide-rich rocks occur in intervals that range from >3 cm to >5 m and their distribution is shown in figure 5.7. The contacts between the Fe oxide-rich rocks and gabbro vary from sharp to gradual (Fig. 5.8a, 5.9a). In hand specimen, the origin of the Fe oxide-rich rocks is difficult to ascertain. They are typically fine-grained, dark grey to black in colour and exhibit a green colouration where chlorite has replaced biotite (Fig. 5.8a and 5.9b). Many of the Fe oxide-rich rocks appear foliated (Fig. 5.8b), while others contain a distinct layering highlighted by sequential light (plagioclase + apatite + chlorite) and dark coloured bands (magnetite + ilmenite) (Fig. 5.8d).

All Fe oxide-rich intervals at FC12 contain at least 40 modal % of Fe-rich oxide, composed of roughly equal proportions of ilmenite and magnetite (Fig. 5.9e). Other minerals in these intervals include chlorite after biotite, titanite, clinopyroxene, orthopyroxene, albitic plagioclase, quartz, apatite and minor pyrite and chalcopyrite (Fig. 5.9a, b, c, d). In thin section, cumulate-like magnetite and ilmenite are intergrown with clinopyroxene, biotite, titanite, microcline, quartz and plagioclase. The grain size is variable, and appears to coincide with the proportion of Fe oxide minerals in the rock, whereby an increase in silicate content corresponds to a decrease in grain size (Fig. 5.9d). Triple point junctions (120°) between magnetite and ilmenite grains as well as thin silicate films are common, particularly in Fe oxide-rich rocks with a very low

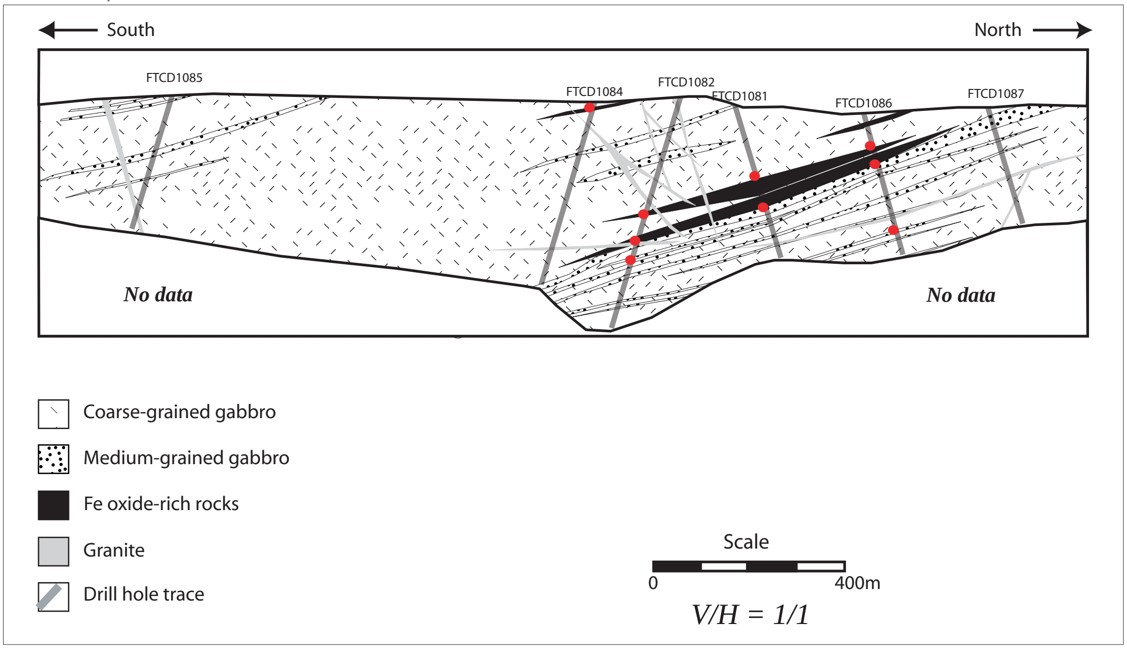

Figure 5.7: Interpreted geological cross-section showing the distribution of rock types from diamond drill core at the FC12 prospect (Fig. 5.1). Coarse-grained gabbroic rocks are the dominant rock type. Thin layers of fine-grained gabbroic rocks and Fe oxide-rich rocks occur within the coarser-grained gabbroic sequence. Cutting these rocks are Na-rich granitic rocks and later coarse-grained pegmatites. Also shown are the diamond drill hole numbers and the locations of samples used for geochemical analysis (indicated by red dots). See chapter 2 for further details on the geology.

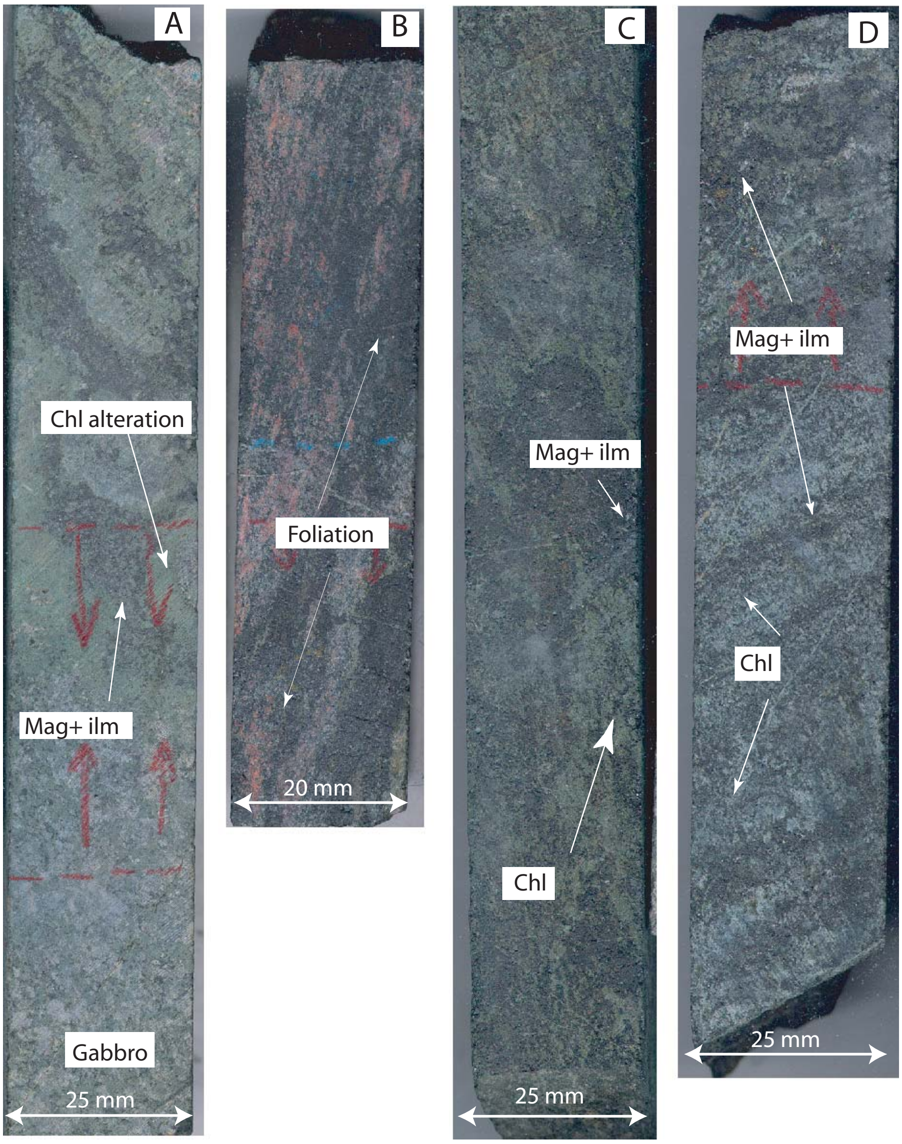

Figure 5.8: Photographs of Fe oxide-rich rocks in drill core from the FC12 prospect.
A) Disseminated contact between an Fe oxide-rich rock and a gabbroic rock. Chlorite is related to a later alteration phase and obstructs the view of the contact. FTCD1087, 192.6m
B) Fe oxide-rich rock affected by a later foliation. Albite within the Fe oxide-rich rock has been overprinted by later hematite-stained albite. FTCD1081, 291m
C) Massive Fe oxide-rich rock with later chlorite alteration. FTCD1086, 303.8m
D) Massive Fe oxide-rich rock overprinted by late chlorite alteration. Note obscure light- and dark- coloured banding. Light banding represents chlorite + minor apatite. The dark banding represents dominantly magnetite + ilmenite. FTCD1081, 266.3m
Abbreviations: Mag=magnetite, Ilm=illmenite, Chl=chlorite. Abbreviations after Kretz (1983).

Figure 5.9 Photomicrographs of Fe oxide-rich rocks from the FC12 prospect.

A) Contact between an Fe oxide-rich rock containing magnetite + ilmenite + biotite + actinolite and a gabbroic host rock. Notice sharp contact between the two rock types (Plane polarised light: PPL). FTCD1082, 338m.
B) Fe oxide-rich rock with muscovite + biotite and later chlorite alteration (PPL). FTCD1084, 120.7m.
C) Fe oxide-rich rock with associated apatite, clinopyroxene and biotite (PPL). Note sharp grain boundaries between opaque Fe oxide minerals and associated silicate minerals. FTCD1086, 428.8.
D) Hematite-stained albitised gabbroic rock with a relict magnetite + ilmenite band (PPL). FTCD1081, 291m.
E) Fe oxide-rich rock containing ilmenite and magnetite. Note common 120° triple point junctions between ilmenite and magnetite grains. Associated sulphides are pyrite and minor chalcopyrite. (reflected light). FTCD1081, 358.9m.
F) Fe oxide-rich rock with coarse-grained magnetite and interstitial pyrite and chalcopyrite. Notice thin silicate films between magnetite and pyrite grains (reflected light). FTCD1082, 390.3m.
G) Fe oxide-rich rock containing magnetite and minor interstitial pyrite. Note common triple point junctions (120º) between magnetite grains (reflected light). FTCD1081, 289.6m.
H) Fe oxide-rich rock containing magnetite and ilmenite grains plus minor pyrite. Note ilmenite laminae within coarse-grained magnetite grains (reflected light). FTCD1081, 360.3m.
Abbreviations: Mag=magnetite, Bt=biotite, Act=actinolite, Ilm=llmenite, Cpx=clinopyroxene, Ap=apatite, Ms=muscovite, Py=pyrite, Chl=chlorite. Ccp=chalcopyrite. Abbreviations after Kretz (1983).

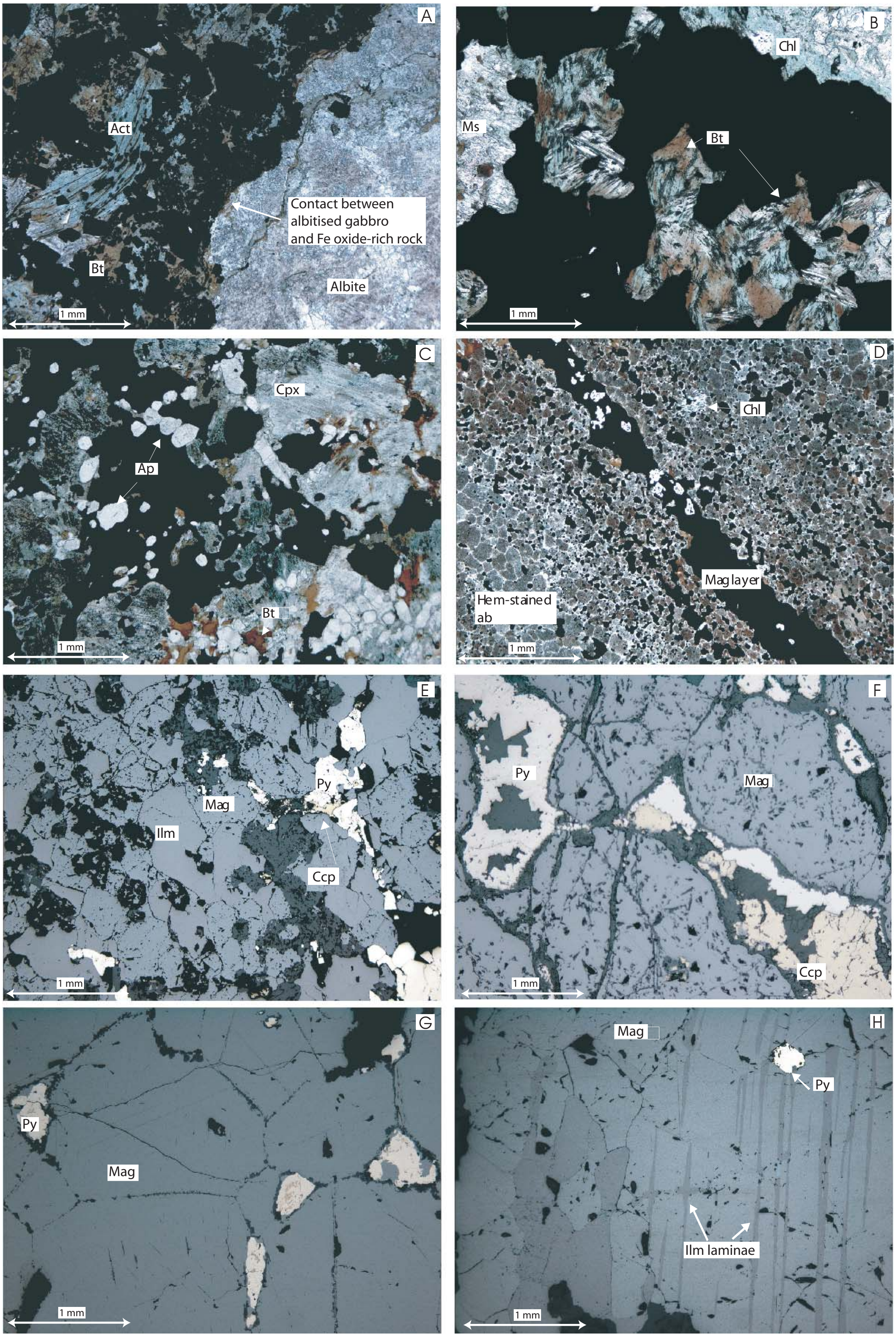
A
Act
Contact between albitised gabbro and Fe oxide-rich rock
Bt
Albite
1 mm
B
Chl
Ms
Bt
1 mm
C
Cpx
Ap
Bt
1 mm
D
Chl
Mag layer
Hem-stained ab
1 mm
E
Py
Mag
Ilm
Ccp
1 mm
F
Py
Mag
Ccp
1 mm
G
Py
Mag
1 mm
H
Mag
Py
Ilm laminae
1 mm

silicate content (Fig. 5.9f, g). Additionally, in cross-polarised light ilmenite laminae in magnetite are commonly observed (Fig. 5.9h).

5.5.3. FC4NW prospect

Several Fe oxide-rich rocks units were observed in drill core at the FC4NW prospect (Fig. 5.10). Samples collected for this study are hosted within biotite-bearing metapelitic rocks, which have been affected by earlier Na alteration and biotite-magnetite alteration. Both samples contain biotite + actinolite (after diopside) + magnetite + quartz + plagioclase. Fe oxide metasomatism at FC4NW is largely associated with type 1 clinopyroxene-rich Na-Ca alteration. These Fe oxide-rich rocks occur in intervals ranging from 1 to >10 m (Fig. 5.10b). Contacts between Fe oxide-rich rocks and the adjacent rock types are typically sharp. In thin section, Fe oxide metasomatism is associated with magnetite + diopside + albite + titanite ± pyrite ± minor chalcopyrite. Most of the Fe oxide-rich rocks are devoid of any significant sulphide mineralisation except for one interval at MFC99090D 252 – 268 m (Fig. 5.10). Here chalcopyrite and pyrite is associated with a later type 2 actinolite-rich Na-Ca alteration. Details of the relationship between Fe oxide metasomatism and sulphide mineralisation at FC4NW is described in detail in chapter 2.

5.6. SAMPLES AND ANALYTICAL TECHNIQUE

Thirty-one samples representing Fe oxide-altered rocks and their unaltered equivalents were analysed from a variety of locations throughout the EFB including the FC12 and FC4NW prospects, Roxmere ironstone, Monakoff and MFC. The FC12 samples were collected from four diamond drill holes (FTCD 1081, FTCD 1082, FTCD 1084 and FTCD 1086), while the FC4NW samples were collected from drill hole MFC97051D (Fig. 5.7 and 5.10). Samples from Roxmere, MFC and Monakoff were collected from outcrop. All samples were analysed for major element (SiO_2, TiO_2, Al_2O_3, Fe_2O_3 (total), MnO, MgO, CaO, Na_2O, K_2O, P_2O_5 and SO_3) and trace element (Ba, V, Cr, Co, Ni, Cu, Zn, Ga, Pb, Rb, Sr, Y, Zr and Nb) concentrations by X-ray fluorescence at the James Cook University Advanced Analytical Centre (AAC) (Appendix 6). Many of the samples (excluding samples from FC4NW) were also analysed by instrumental neutron activation analysis (INAA) for Ce, Eu, La, Lu, Sm, Sc, Tb, Th and Yb at Becqueral Laboratories, Sydney (Appendix 6). The experimental procedure for XRF and INAA analysis is described in chapter 3 (section 4.1).

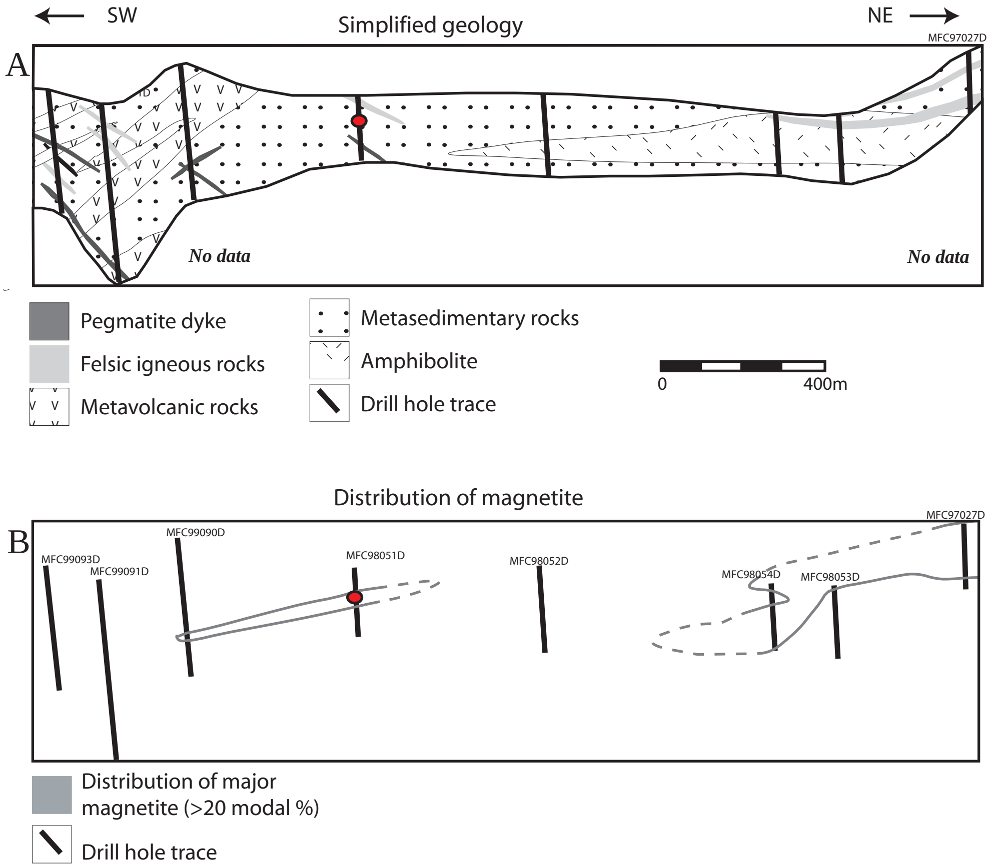

Figure 5.10: Interpreted geological cross-section showing the distribution of rock types and Fe oxide metasomatism in diamond drill core at the FC4NW prospect.
A) The dominant rock type at FC4NW is biotite-bearing metapelite. Towards the northeast, dioritic rocks are present, whereas towards the southwest, felsic volcanic rocks are more common. Cutting each of these rock types are Na-rich granitic rocks and later coarse-grained pegmatites.
B) Fe oxide metasomatism is more common toward the NE. The small Fe oxide-rich interval in hole MFC99090D contains anomalous Cu concentrations of up to 2 wt % (chapter 2). The Fe oxide interval within hole MFC98051 contain very minor chalcopyrite only. Also shown are the diamond drill hole numbers and the location of samples used for geochemical analysis (indicated by red circles). See chapter 2 for further details of the geology.

The isocon method (Grant, 1986) was employed for paired samples from the FC12 and FC4NW prospects, as well as two rock pairs from the Roxmere ironstone and MFC to quantify the geochemical changes during alteration. This method is usually robust in the sense that elements considered to be immobile in hydrothermal systems will usually plot as a linear array on a dimensionless X-Y diagram, reflecting no relative mass gains or losses of these elements during alteration. A detailed procedure for constructing the isocon diagrams is presented in chapter 3 (section 4.3).

5.7. RESULTS: FC12 PROSPECT

5.7.1. Major and trace element variation

Isocon plots comparing the mass and volume changes between four gabbros and Fe oxide-rich rocks are presented in figure 5.11. Upon first inspection, the common characteristic encountered in each of the isocon diagrams is the high degree of scatter of elements that are normally considered to be immobile during alteration such as Ti, Al, Zr, Y and Ga (Goldschmidt, 1958). As a result, an isocon could not be drawn through these elements. The mobility of elements such as Ti, Y and Zr in hydrothermal systems is rarely noted in the literature, although as discussed in chapter 3, Ti mobility might occur in certain environments during alteration albeit over distances no greater than a few metres (Van Baalen, 1993). At FC12, alteration haloes were not observed peripheral to the contacts of the Fe oxide-rich rocks to suggest local diffusion from the gabbroic hosts. It is unlikely; therefore, that the apparent mobility of Ti associated with the Fe oxide-rich rocks is due to Ti solubility in aqueous fluids.

As discussed in chapters 3 and 4, work by Williams (1994) and Oliver et al (2004) has demonstrated that a genetic link may exist between Na ±Ca alteration and the formation of Fe oxide-rich rocks and IOCG deposits. Several studies on mass and volume changes associated with Na-Ca alteration have shown that while Na is enriched, Fe, K, Ba and Rb are consistently depleted, while elements that appear to be immobile during alteration include Si, Al, Ti, Zr, Ga ± Y (This study, chapter 3; Mark, 1998a; Rubenach and Lewthwaite, 2002; Oliver et al., 2004). In contrast, Fe oxide metasomatism of rocks at or adjacent to known IOCG deposits involve the addition of the same elements that are depleted during Na-Ca alteration (Williams, 1994; Mark, 1998a).

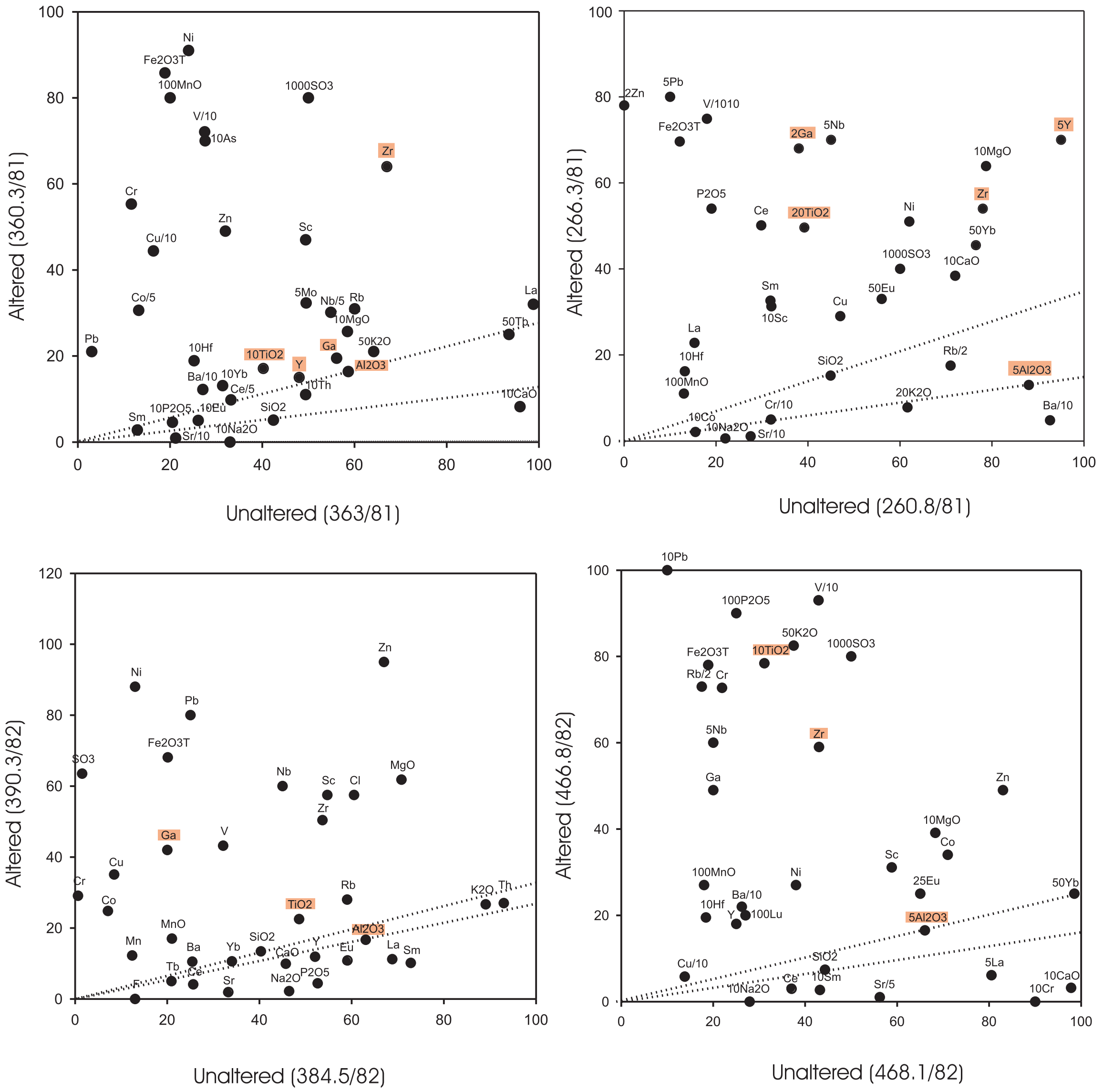

Figure 5.11: Examples of four isocons plots constructed for individual rock pairs of Fe oxide-rich rocks and adjacent gabbroic rocks from the FC12 prospect. Elements normally considered immobile during alteration (Ti, Al, Ga, Zr; Goldschmidt, 1958) show a high degree of scatter with respect to each other. These elements are highlighted in red. Isocons were instead defined by Al and Si, which appear relatively immobile during intense Na-Ca alteration of various rock types in the EFB (Oliver et al., 2004). Note that while the isocon defines a small field of immobility, the slope of the isocon suggests an unrealistic degree of mass gain associated with alteration. Sample numbers of each rock pair are located on the X and Y axis of the isocon plots. Multiplication factors are indicated for each element of the diagram. Where no number is shown, the data are in ppm for trace elements and % oxides for major elements.

This being the case, perhaps Si and Al can be used as an immobile reference frame instead of Ti and Zr. Figure 5.11 shows a line of best fit through Si and Al. However, despite the apparent moderately good fit of the isocons, the slope suggests massive dilation of up to 400 % associated with alteration. This degree of dilation is inconsistent with the apparent lack of infill associated with the Fe oxide-rich rocks and as such does not represent the correct immobile reference frame in this case. An alternative explanation is sought below.

5.7.2. Mass and volume changes

The apparent mass gain between the gabbro and Fe oxide-rich rock can be partially explained by the relative volume change between the unaltered rock (gabbro) and its altered equivalent. An Fe oxide-rich rock containing 100 % magnetite will have a specific gravity of ~ 5.2 g/cm^3. A typical gabbro will have a specific gravity of ~3.2 g/cm^3. By using the Grant (1986) equation below, a volume change of 60% is calculated if no bulk mass change occurred during alteration:

$$Fv = \frac{SG_b}{SG_A} \text{………………Equation 1}$$

Where:
Fv = Volume change correction factor
SG_b = Specific gravity of altered rock
SG_a = Specific gravity of unaltered rock

While a volume change of 60% can explain some of the mass gain interpreted from the isocons, it alone cannot account for mass gains of up to 400% as indicated by the isocon defined by Al and Si in figure 5.11. Additionally, all the Fe oxide-rich rocks in this study are composed of only 90% Fe oxide. Therefore calculated volume changes due to differences in mineralogy will be even less than the 60% calculated via the Grant (1986) equation above.

The isocon method employed above suggests that the Fe oxide-rich rocks were not formed from Fe oxide metasomatism of the gabbroic sequence. This conclusion could mean one of two things: 1. The Fe oxide-rich rocks were precipitated directly as infill; or, 2. The Fe oxide-rich rocks represent primary differences associated with magmatic processes. The second hypothesis is supported by thin section analysis detailed in section 5.5.2. where observed textures within the Fe oxide-rich rocks do not resemble alteration or infill of a previous host. Rather, textures are more reminiscent of a magmatic source, and the differences between the pairs of rocks may thus be related to fractional crystallisation of Fe oxide-rich layers in a magmatic chamber.

5.7.3. Geochemical evidence for an orthomagmatic origin.

To determine whether the Fe oxide-rich rocks at FC12 are a product of magmatic or hydrothermal processes, X-Y Harker diagrams of major and trace elements were constructed for all samples to identify any possible fractionation trends that should be present if they are magmatically derived (Fig. 5.12). Additionally, REE compositions of Fe oxide-rich rocks and gabbroic rocks are compared to assess similarities in relative geochemical trends (Fig. 5.13).

Major element geochemistry

The geochemistry of these rocks shows a strong positive linear correlation between TiO_2 and Fe_2O_3 for most samples (Fig. 5.12a). However, four samples reside outside this association and exhibit significantly lower Ti:Fe ratios and contain particularly high Fe_2O_3 (50-90 wt %), but relatively less TiO_2 (2-8 wt %). This change in geochemistry correlates well with a proportionately lower relative abundance of ilmenite to magnetite in the four samples relative to the rest of the sample suite. SiO_2 (5-30 wt %), CaO (0-8 wt %), K_2O (0-1 wt %), Al_2O_3 (1-7 wt %), and Na_2O (0-1 wt %) are all depleted in the Fe oxide-rich rocks compared to their gabbroic hosts (35-50 wt %, 7-11 wt %, 0.5-2 wt % and 2-3.5 wt % respectively). This is largely attributed to dilution affects associated with the low modal % of silicate minerals in the Fe oxide-rich rocks. MgO is relatively high in four of the Fe oxide-rich samples (10-14 wt %) compared to the gabbroic rocks (4-8 wt %). The P_2O_5 and SO_3 show no distinct variation between rock types, where both rock types contain up to 3.5 wt % P_2O_5, predominantly as apatite, and up to 0.3 wt % SO_3 (Fig. 5.9c).

Trace element geochemistry

In general, V (100-1800 ppm), Ni (25-100 ppm), Ga (5-50 ppm) and Pb (10-25 ppm) are more abundant in the Fe oxide-rich rocks than the gabbros (100-500 ppm V, 20-30 ppm Ga, 10-60 ppm Ni, and 0-10 ppm Pb; Fig 5.12). The high V and

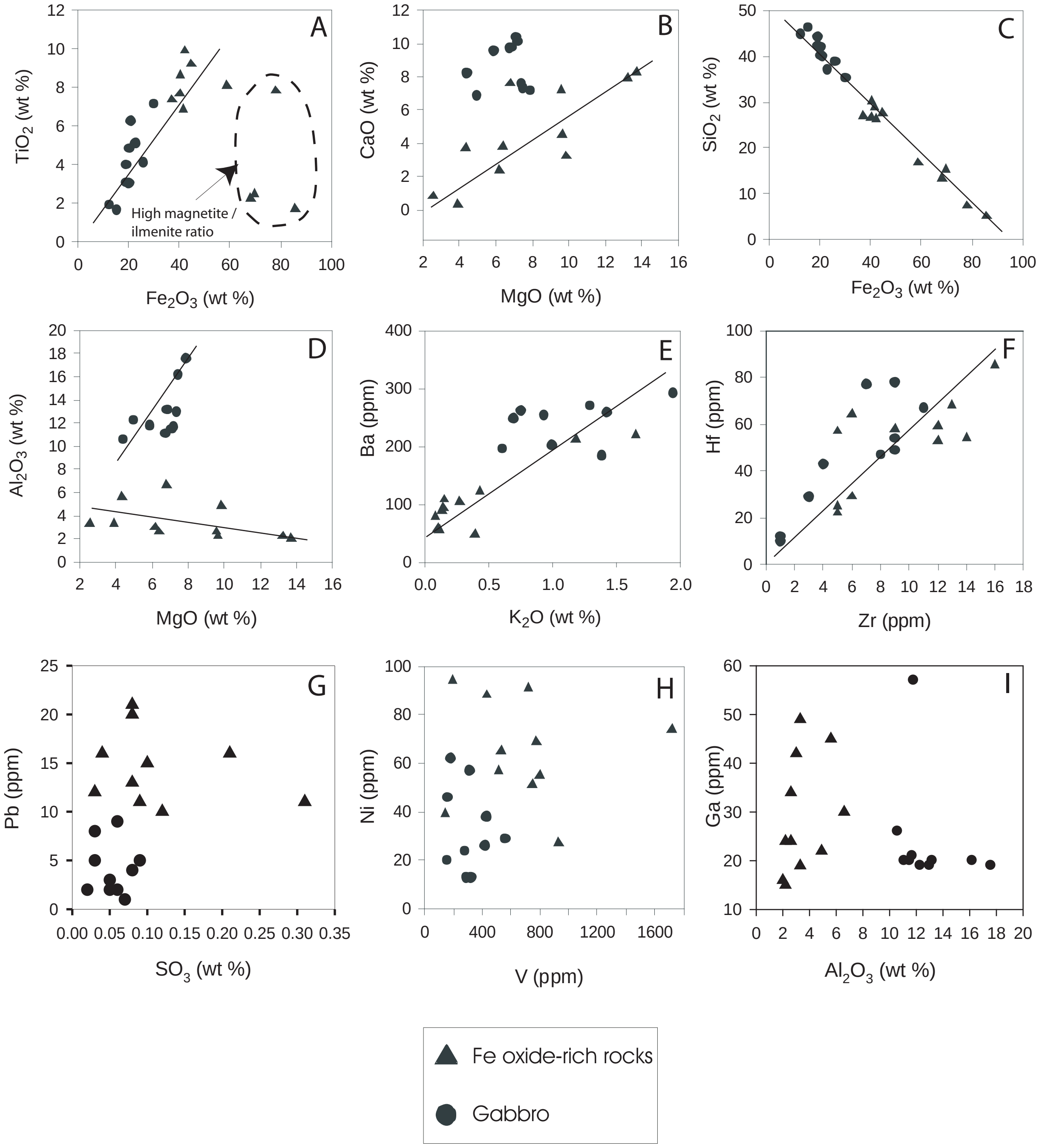

Figure 5.12: X-Y plots comparing the major and trace element geochemistry of Fe oxide-rich rocks and gabbroic rocks from the FC12 prospect. Note linear trends associated with Hf/Zr and TiO_2 vs Fe_2O_3. Also note the Fe oxide-rich rocks containing high Fe concentrationds (>60 wt %) are associated with a higher Fe_2O_3:TiO_2 ratio. This is reflected in their high magnetite:ilmenite ratio.

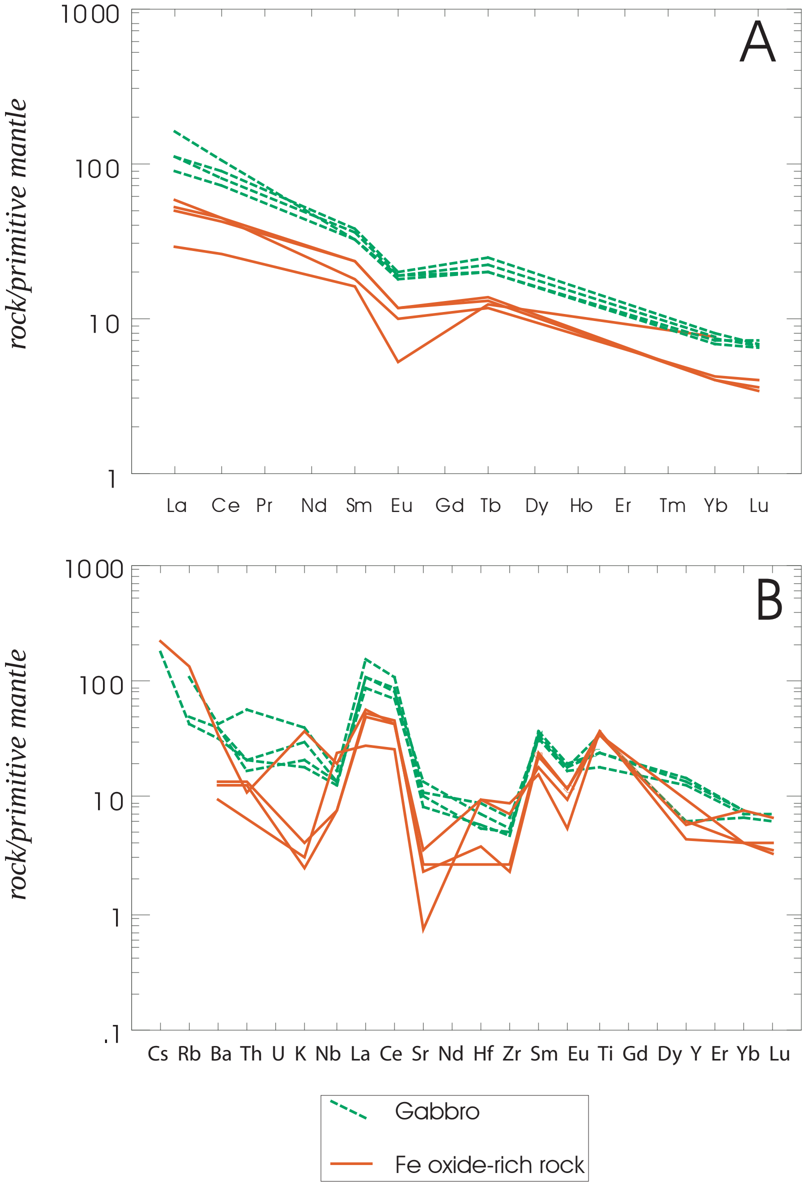

Figure 5.13: REE and multi-element geochemistry of gabbroic rocks and Fe oxide-rich rocks from the FC12 prospect.
A) Primitive mantle-normalised (Sun and McDonough, 1989) rare-earth-element diagram.
B) Primitive mantle-normalised (Sun and McDonough, 1989) multi-element diagram. Note the similar REE and multi-element trends associated with the both the Fe oxide-rich rocks and their gabbroic hosts.

Ni concentrations in the Fe oxide-rich rocks can be explained by their high partitioning coefficients with respect to magnetite (Goldschmidt, 1958). In contrast, Ba (50-200 ppm), Sr (0-100 ppm) and Rb (20-80 ppm) are all depleted in Fe oxide-rich rocks relative to the gabbroic rocks (200-300 ppm Ba, 150-300 ppm Sr and 20-140 ppm Rb) due to the lower proportion of silicate minerals in the Fe oxide-rich rocks.

The relative increase of Ga and Pb in Fe oxide-rich rocks compared to their gabbroic hosts is surprising. Ga is normally intimately associated with Al in magmatic systems (Goldschmidt, 1958). However, the Al in the Fe oxide-rich rocks at FC12 is greatly depleted with respect to the gabbroic rocks. Instead, high Ga coincides with Fe oxide-rich rocks that have a high magnetite/ilmenite ratio (Fig. 5.12a), and as such Ga most likely substitutes into the magnetite structure given its similar ionic radius to Fe^{2+} (0.67 Å). This interpretation is supported by laser ablation ICP MS (chapter 6) data where magnetite from FC12 contains up to 100 ppm Ga. The high Pb content in the Fe oxide-rich rocks does not coincide with Sr, K_2O, Ba or Ca, elements with which Pb is commonly associated due to similar ionic radii (Ringwood, 1955). Pb can also exhibit a close affinity with S in the form of galena (PbS), however figure 5.12 shows only a slight positive correlation but may indicate the presence of galena in the Fe oxide-rich rocks that was not identified in thin section.

Rare earth element geochemistry (REE's)

The normalised multi-element diagram and REE diagram in figure 5.13 shows that Fe oxide-rich rocks and their gabbroic hosts exhibit similar trends. One difference, however, is reflected in the gabbroic rocks which are relatively enriched in lithophile elements (Cs, Ba, Rb, Sr and K) compared to the Fe oxide-rich rocks (Fig. 5.13b), which is consistent with the gabbros being more biotite rich. Additionally, Y is also depleted in the Fe oxide-rich rocks and reflects the lower modal proportion of titanite in the Fe oxide-rich rocks compared to the gabbro. Figure 5.13a shows that the most significant difference between Fe oxide-rich rocks and gabbroic rocks at FC12 is the relative depletion of REE's in the Fe oxide-rich rocks. The depleted Eu, and to a lesser extent Sm, can be attributed to the Fe oxide-rich rocks containing less K feldspar and plagioclase, into which Eu is strongly partitioned. The Fe oxide-rich rocks containing >65 wt% Fe_2O_3 (total) typically exhibit lower concentrations of the HREEs, Tb, Lu and

Eu (in two of the three samples), where these elements are close to instrumental detection limits (Fig. 5.13a). The above geochemical evidence suggests that the Fe oxide-rich layers at FC12 were formed by fractional crystallisation.

5.8. RESULTS: FC4NW PROSPECT

5.8.1. Major and trace element variation

Two rocks affected by Fe oxide metasomatism along with their unaltered equivalents from the FC4NW prospect were compared to determine the mass changes involved during metasomatism. These changes were assessed using the isocon method of Grant (1986) and the results are presented in figure 5.14. Ti, Zr, Si, and Al all appear to be immobile (*cf.* Goldschmidt, 1958) unlike for FC12. Both plots indicate a mass increase in Fe, Pb, Ni, Zn, Mn, Co, S, P and V, whereas K and Ba are depleted. Figure 5.14a shows that sample MFC160.5 exhibits an increase in Mg, while Na and As are relatively immobile. In contrast, all three of these elements are depleted in sample MFC 160.2 (Fig. 5.14b).

5.8.2. Mass and volume changes

The best-fit isocon for both altered / unaltered rock pairs indicate that a significant component of mass gain was associated with Fe oxide metasomatism at FC4NW (F_m = 64% and 57% respectively). One possibility for at least part of the apparent mass gains associated with alteration is the effect of volume change between unaltered and altered equivalents. An increase in volume may reflect a component of infill associated with Fe oxide metasomatism at FC4NW. Volume changes associated with alteration can be calculated using the methods of Gresens (1967) (see chapter 3). The average density of each unaltered and altered pair is given in appendix 7.

Composition-volume (C-V) diagrams can be used to assess the changes in volume (F_v) between altered and unaltered rocks. This procedure is described in chapter 3. For the purpose of this study, Ti, Al and Si are assumed to be immobile (Fig. 5.14). Figure 5.15 shows the three lines representing changes in concentration of Ti, Al and Si with respect to different values of F_v. All three lines cross the zero line between about 1.3 and 2.25 (Fig. 5.15a) and 1.45 and 2.05 (Fig. 5.15b), giving an average value for F_v of about 1.75 and 1.68 respectively. These Fv values can then be used to determine the

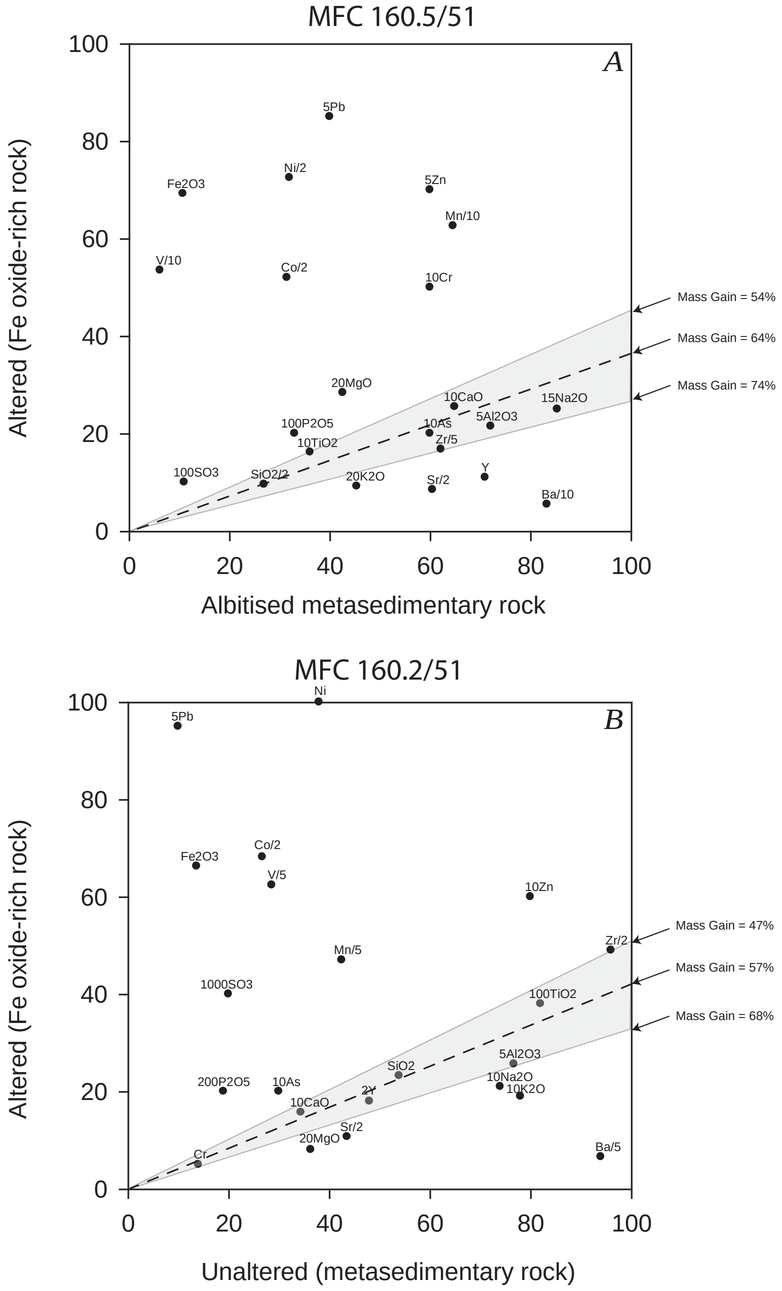

Figure 5.14: Isocon plots (after Grant, 1986) constructed for individual pairs of altered and unaltered rocks, comparing rocks affected by Fe oxide metasomatism and their unaltered equivalents from the FC4NW prospect.
A) Compares an actinolite (replacing diopside) + magnetite + albite + pyrite + muscovite-bearing Fe oxide-rich rock with an albitised metapelite .
B) Compares an actinolite (replacing diopside) + magnetite + albite + pyrite - bearing Fe oxide-rich rock with a biotite-bearing metapelite.
The isocon (grey area) is defined by the best fit between TiO2, Al2O3 and Zr and assumes that these elements have remained immobile during alteration. Major elements are plotted as wt %, trace elements are plotted as ppm. Multiplication factors are shown for each element. Note the low-angle slope of the isocon suggesting dilation associated with Fe oxide metasomatism. The location of these samples is shown in Figure 5.10.

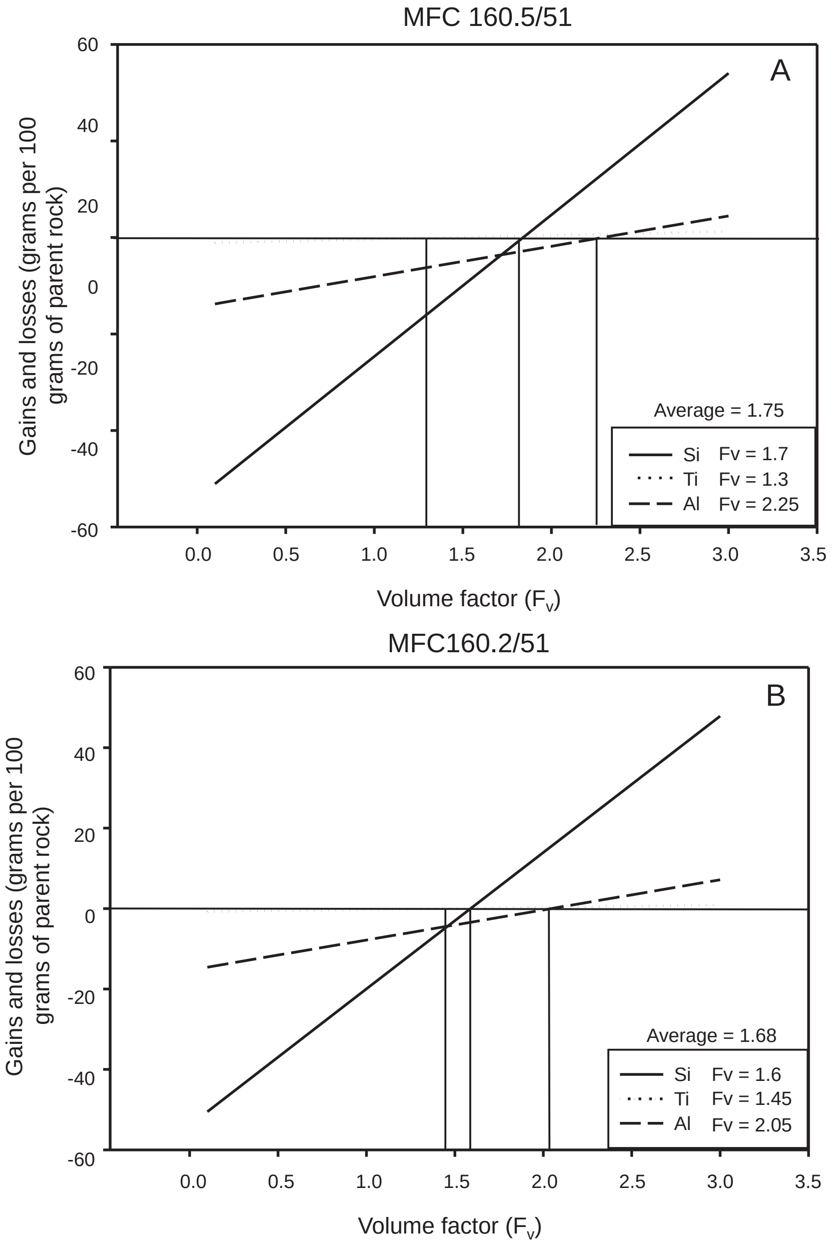

Figure 5.15: Composition - volume diagrams showing the change in elemental gains and losses (Y-axis) associated with arbitrary values of Fv (X-axis).

SAMPLE	Change in concentration (Xm)	Change in concentration (Xm)
	MFC 160.5	MFC160.2
SiO_2	-2.66	0.37
TiO_2	0.20	0.07
Al_2O_3	-3.42	-3.35
Fe_2O_3	168.78	141.22
MgO	1.55	-1.76
CaO	0.13	0.23
Na_2O	-1.22	-2.49
K_2O	-1.08	-0.34
P_2O_5	0.19	0.28
Ba	-690.3	-392.9
Sr	-76.9	-37.3
Rb	-96.1	42.4
Pb	36.1	37.0
Zr	-93.1	-5.3
Y	-42.5	-3.0
Mn	978.1	673.1
V	1326.0	585.9
Co	206.8	395.6
Ni	312.2	198.0
Zn	24.3	6.0

Table 5.1: Elemental mass changes as a function of volume for Fe oxide metasomatism at FC4NW. Notes: mass changes in grams and 10 $^{-5}$ grams per 100 grams of parent rock for major element oxides and trace elements respectively; Xm = elemental mass change.

change in concentration of the remaining elements associated with Fe oxide metasomatism. Using the calculated volume gains and bulk rock density, changes in the major elements during the transformation from unaltered to altered rock are shown in table 5.1 and figures 5.16a and b. As expected, Fe_2O_3 shows the largest change in concentration (up to 168 g/100g). Changes in concentration in the other major elements is relatively small compared to Fe_2O_3, with SiO_2, CaO, Al_2O_3, Na_2O and MgO all exhibiting changes of up to 3g/100g for both rock pairs. The trace element chemistry is similar between samples, with Ni (up to 312 ppm/100g), Mn (978 ppm/100g), V (1326 ppm/100g) and Co (395 ppm/100g) exhibiting the highest increases associated with metasomatism (Fig. 5.17). Ba is depleted (down to -690 ppm/100g) in both rock pairs. Other trace elements represented in figures 5.16 a and b are all comparatively immobile.

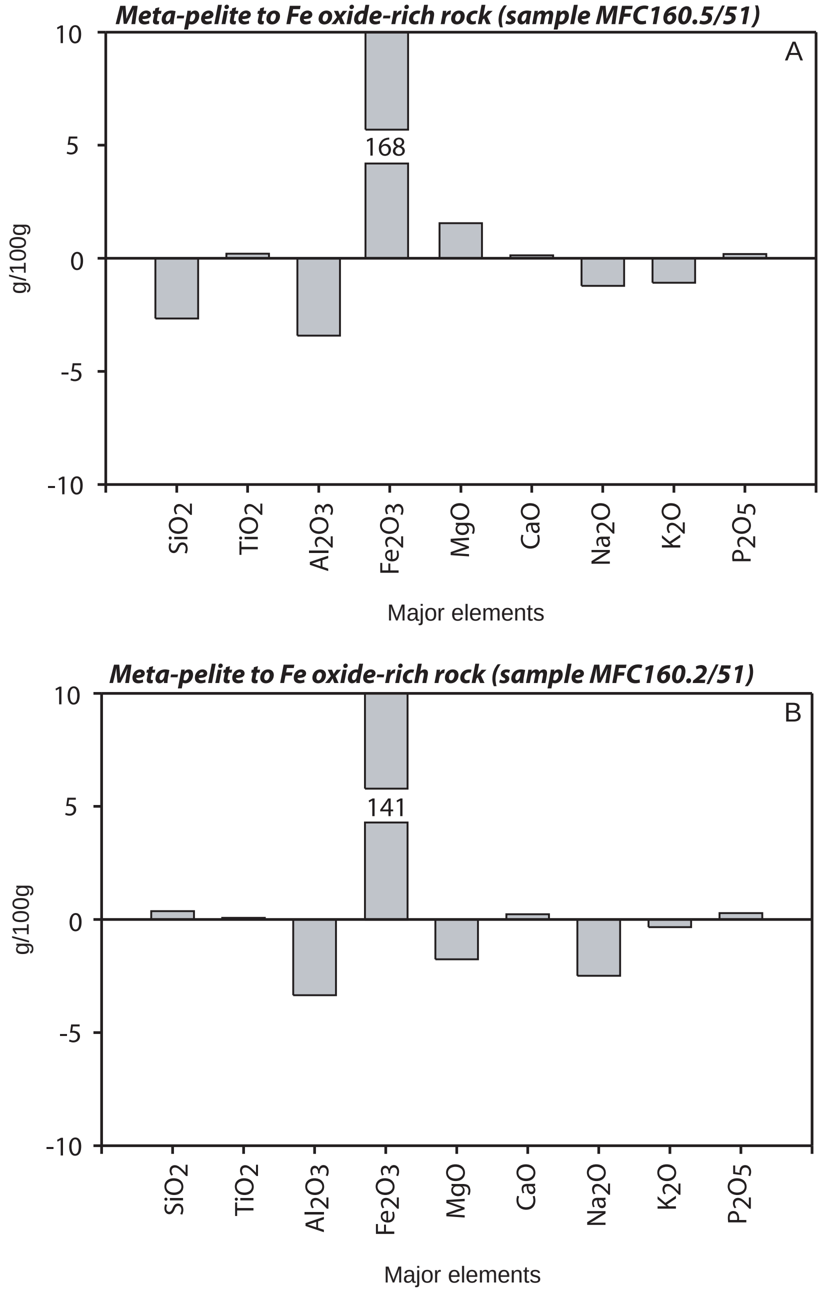

Figure 5.16: Major element oxide mass changes related to volume gains associated with Fe oxide metasomatism within the FC4NW prospect using the Gresens equation (1967). Horizontal line indicates a position of zero concentration change. Elemental mass changes are in grams per 100 grams of parent rock.
A). Compares a metapelitic rock affected by early albite alteration with a magnetite + albite + actinolite + pyrite + muscovite-bearing Fe oxide-rich rock.
B). Compares a biotite-bearing metapelitic rock containing minor actinolite due to an early alteration phase with a magnetite + albite + actinolite + pyrite-bearing Fe oxide-rich rock.

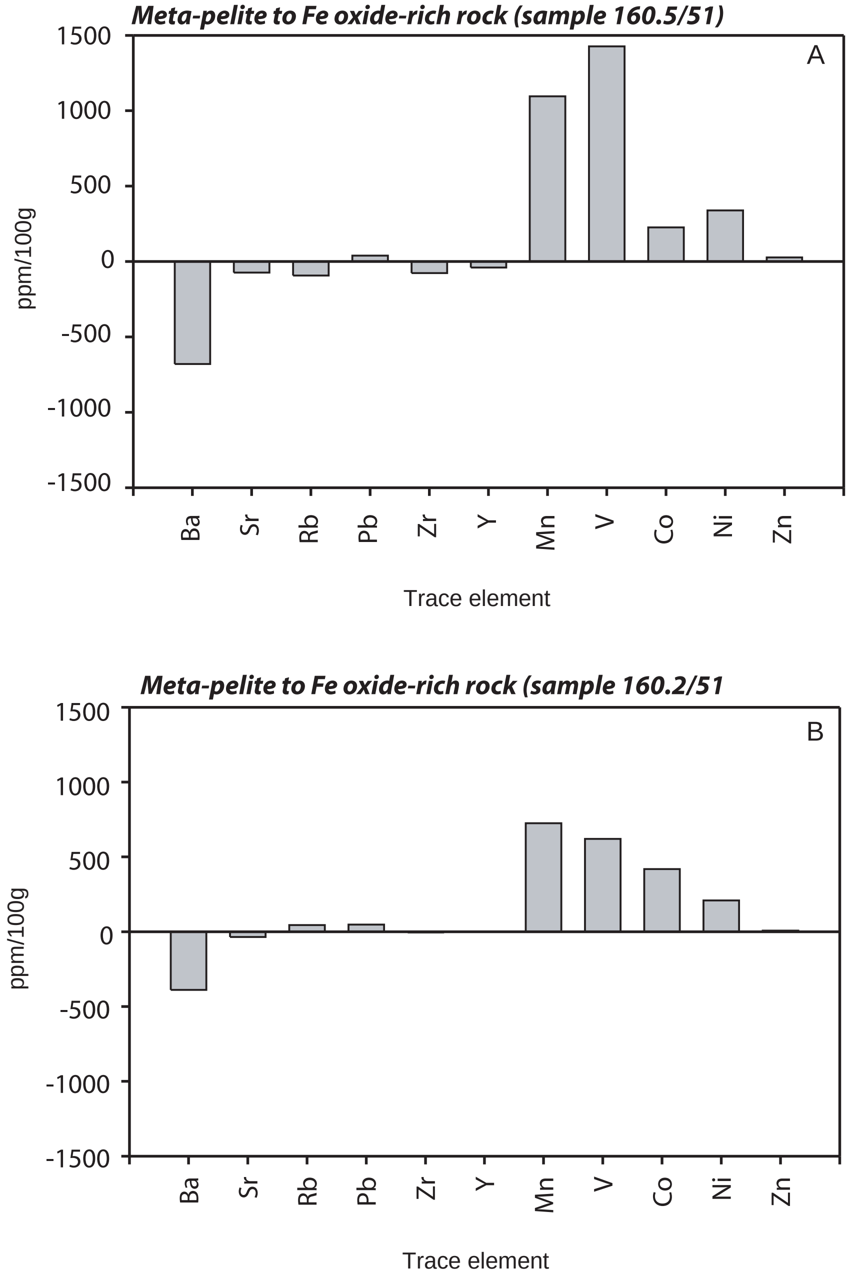

Figure 5.17: Trace element mass changes related to volume gains associated with Fe oxide metasomatism within the FC4NW prospect using the Gresens equation (1967). Horizontal line indicates a position of zero concentration change. Elemental mass changes are in ppm per 100 grams of parent rock.

A). Compares a metapelitic rock affected by early albite alteration with a magnetite + albite + actinolite + pyrite + muscovite-bearing Fe oxide-rich rock.

B). Compares a biotite-bearing metapelitic rock containing minor actinolite due to an early alteration phase with a magnetite + albite + actinolite + pyrite-bearing Fe oxide-rich rock.

5.9. RESULTS: REGIONAL FE OXIDE-RICH ROCKS

5.9.1. Major and trace element variation

The isocon method of Grant (1986) was employed to determine mass transfer between two regionally occurring Fe oxide-rich rocks and their unaltered equivalents from Roxmere and MFC (see section 3.5.1). Figure 5.18 shows that elements normally considered to be immobile during alteration (e.g. Ti, Al, Ga, Zr) have a high degree of scatter; therefore an isocon could not be constructed. There are three possible interpretations for the scatter associated with 'immobile' elements in this case, namely: 1) An incorrect rock type was assigned as the unaltered equivalent to the Fe oxide-rich rocks, 2) the Fe oxide-rich rocks formed as BIFs, or 3) the Fe oxide-rich rocks are a product of massive dilation. Each of these possibilities is discussed below:

- <u>An incorrect rock type was assigned as the unaltered equivalent to the Fe oxide-rich rocks</u>:

  Contact relations between Fe oxide-rich rocks and adjacent rock types are rarely observed in the EFB. However, samples from Roxmere and MFC chosen for geochemical analysis in this study are two examples where contacts were observed. In both cases, contacts between the Fe oxide-rich rocks and their interpreted unaltered equivalents are sharp. These contact relations suggest that if the Fe oxide-rich rocks are a product of replacement, then the correct precursor rock was sampled both at Roxmere and MFC.

- <u>The Fe oxide-rich rocks formed as BIF*s*</u>:

  Several factors suggest that the Fe oxide-rich rocks at Roxmere and MFC are not likely to have formed from sedimentary processes. Most importantly, sedimentary banding commonly attributed to BIF (e.g. Hamersley Province, section 5.3.2) is absent at Roxmere and MFC. Also the Fe oxide-rich rocks at MFC are hosted in felsic volcanic rocks and occur as vertical features (Fig. 5.6) more akin to hydrothermal alteration than sedimentary accumulation. The contacts between the Fe oxide-rich and felsic volcanic rocks also exhibit small veins of magnetite and hematite emanating from the Fe oxide-rich units. At Roxmere, Fe oxide is commonly observed as infill within brecciated calc-silicate rocks, and contains a similar mineralogy to the massive Fe oxide-rich rocks sampled for this study (Fig.

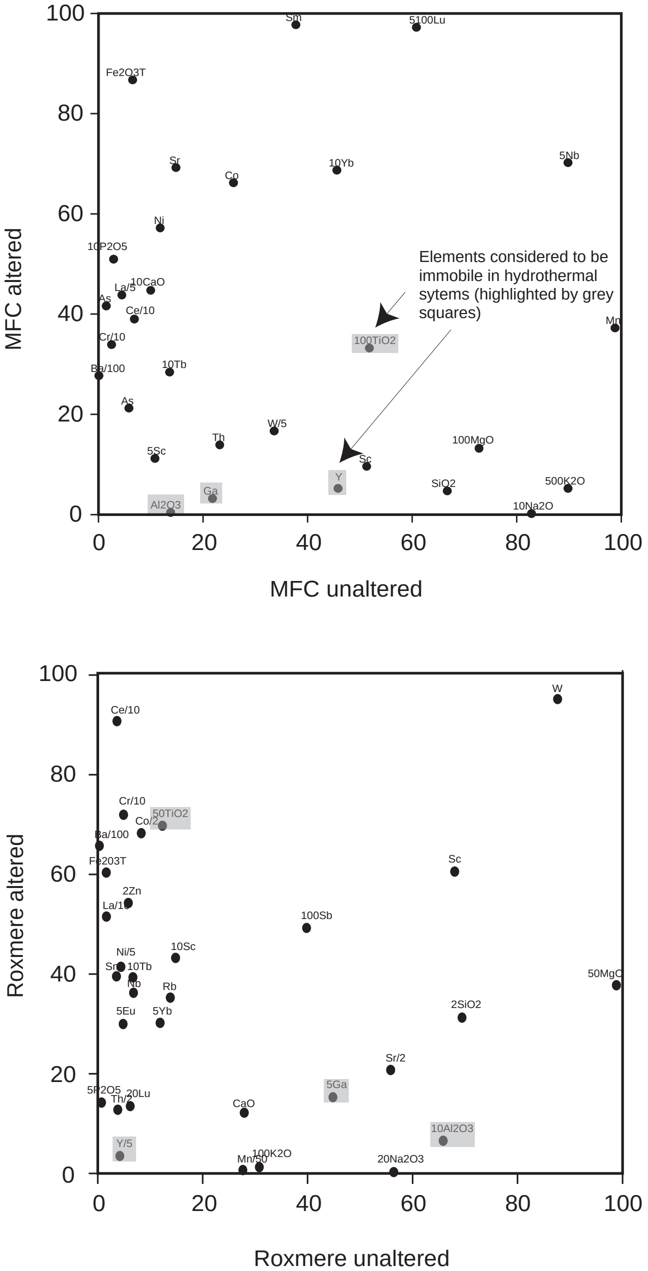
Elements considered to be immobile in hydrothermal sytems (highlighted by grey squares)

Figure 5.18: Two isocons constructed for individual pairs of altered and unaltered rocks, comparing 'regional' Fe oxide-rich rocks (Roxmere and MFC) and interpreted unaltered precursors. Elements considered immobile in hydrothermal systems are highlighted in grey. Note that no line of best fit can be constructed through elements that are normally considered to be immobile in hydrothermal systems

5.4). It is unlikely; therefore, that Fe oxide-rich rocks at MFC and Roxmere are BIFs.

- The Fe oxide is a product of massive dilation:
  The most plausible explanation for the apparent poor geochemical correlation is that the Fe oxide-rich rocks at Roxmere and MFC are both products of hydrothermal infill. This is supported by the observed sharp contacts with adjacent rock types in addition to the lack of discernable textures that would indicate replacement or sedimentary accumulation. Below the immobile element geochemistry of the Fe oxide-rich rocks and other rock types collected throughout the EFB and elsewhere will be compared to investigate this hypothesis.

5.9.2. Geochemical comparison between Fe oxide-rich rocks and other rock types in the EFB

Immobile element geochemistry

A geochemical dataset of rock types, including Fe oxide-rich rocks in the EFB, as well as examples of Fe oxide-rich rocks from elsewhere (see figure 5.19 for references) have been collected to test the feasibility of various mechanisms for the formation of Fe oxide-rich rocks. Wang and Williams (2001) used immobile trace element geochemistry (Ti, Zr, Nb) to demonstrate that the Mount Elliott Skarns (hosts to mineralisation) formed in both metasedimentary and mafic metavolcanic rocks. In a similar fashion, the relative concentration of immobile elements of Fe oxide-rich rocks and other rock types should give an indication as to the possible processes that may have formed Fe oxide-rich rocks at Roxmere and MFC. For example, if the ‘regional’ Fe oxide-rich rocks were formed by the replacement of a previous rock type, then the immobile elements should reflect similar ratios to its precursor. In contrast, Fe oxide-rich rocks formed by chemical sedimentation or by infill are likely to exhibit relatively low immobile element concentrations, because of the low solubility of such elements in seawater and hydrothermal fluids.

On the basis of work by Mark (1998) and Oliver et al (2004), Ti, Al, Zr and Y may be considered potentially immobile in Fe oxide-rich rock producing systems. Figure 5.19 shows several plots of these elements, which for the most part discriminate the Fe oxide-rich rocks from other rocks in the EFB. All of the Fe oxide-rich rocks contain

Figure 5.19: X-Y plots comparing the immobile element geochemistry of Fe oxide-rich rocks from various affinities both within the EFB and elsewhere with other rock types of the EFB. These other rock types include felsic volcanic rocks and diorite from Ernest Henry, Pelitic rocks from Fullarton River, Quartz Monzonite, calc-silicate rocks and quartz diorite from Mount Angelay and calc-silicate rocks from Knobby Creek. Elements chosen are those that appear immobile during magnetite alteration at FC4NW (see Fig. 5.13). Note infill-dominant Fe oxide-rich rocks and BIFs contain comparatively lower immobile element concentrations than replacement-dominant (FC4NW), orthomagmatic (FC12 and Lightning Creek) and other rock types of the EFB. Geochemical data collected from: This study, Parak (1975), Gross and Mcleod (1980), Davidson et al (1989), Williams (1994), Adshead (1995), Baker (1998), Rubenach and Barker (1998), Mark (1998), Mark et al (1999), Mark and Foster (2000), Perring et al (2000), Rubenach and Lewthwaite (2002), Oliver et al (2004), Webb (2003).

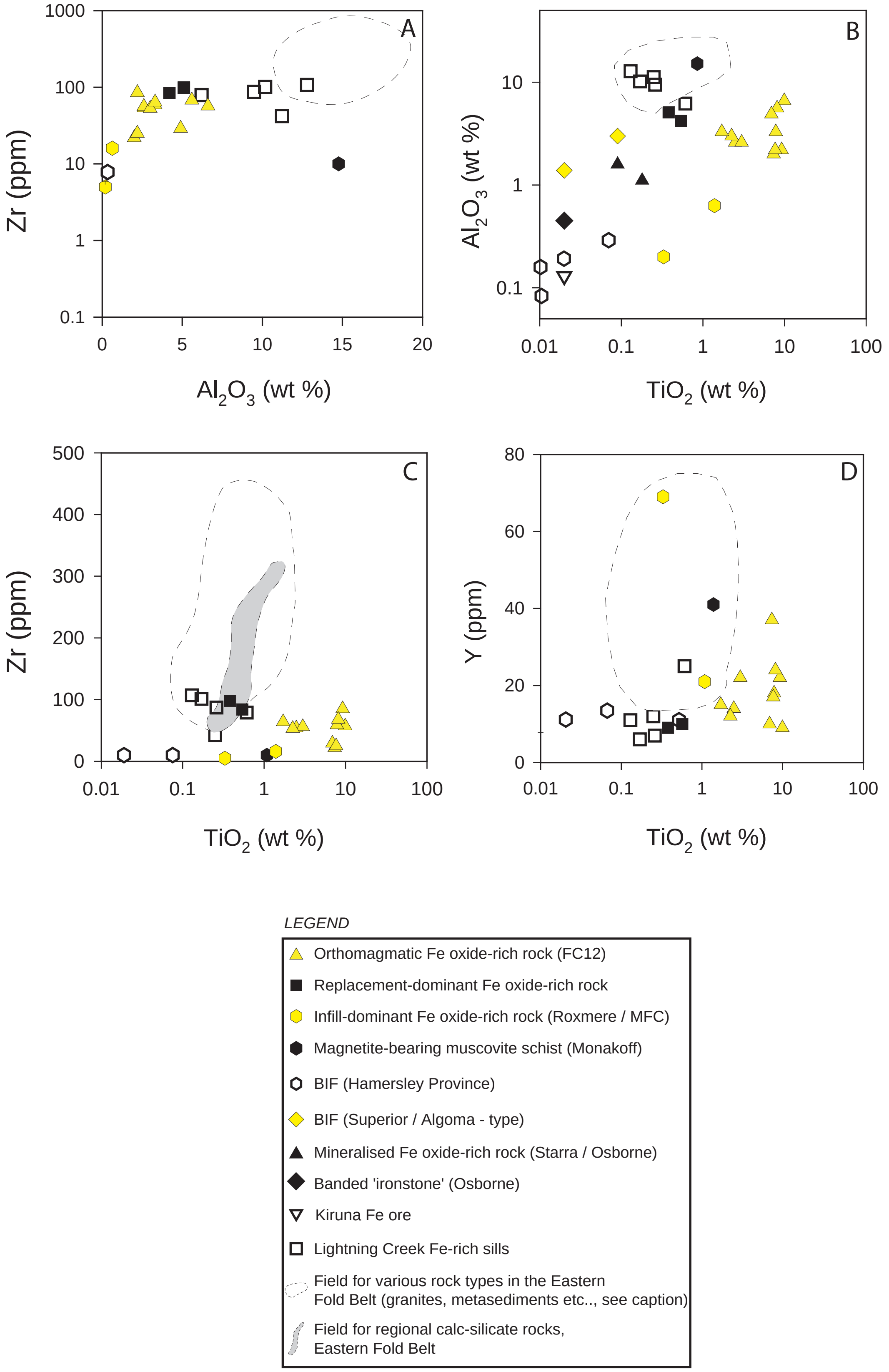
A
Zr (ppm)
1000
100
10
1
0.1
0
5
10
15
20
Al₂O₃ (wt %)
B
Al₂O₃ (wt %)
10
1
0.1
0.01
0.1
1
10
100
TiO₂ (wt %)
C
Zr (ppm)
500
400
300
200
100
0
0.01
0.1
1
10
100
TiO₂ (wt %)
D
Y (ppm)
80
60
40
20
0
0.01
0.1
1
10
100
TiO₂ (wt %)
LEGEND
△ Orthomagmatic Fe oxide-rich rock (FC12)
■ Replacement-dominant Fe oxide-rich rock
⬢ Infill-dominant Fe oxide-rich rock (Roxmere / MFC)
⬢ Magnetite-bearing muscovite schist (Monakoff)
⬡ BIF (Hamersley Province)
◇ BIF (Superior / Algoma - type)
▲ Mineralised Fe oxide-rich rock (Starra / Osborne)
◆ Banded 'ironstone' (Osborne)
▽ Kiruna Fe ore
□ Lightning Creek Fe-rich sills
Field for various rock types in the Eastern Fold Belt (granites, metasediments etc.., see caption)
Field for regional calc-silicate rocks, Eastern Fold Belt

between 5-150 ppm Zr, 0.01-10 wt % TiO_2, 0.1-10 wt % Al_2O_3, and 5-40 ppm Y. In contrast, other rock in the EFB contain between 100-1000 ppm Zr, 0.1-2 wt % TiO_2, 10-20 wt % Al_2O_3 and 18-70 ppm Y. Fe oxide-rich rocks from FC4NW and FC12 contain relatively higher Al_2O_3 concentrations (5-10 wt % - FC4NW, and 3-10 wt % - FC12) and Zr (70-150 ppm – FC4NW, and 20-100 ppm – FC12) compared to similar rocks from other affinities (Zr: 5-20 ppm and Al_2O_3: 0.1-5 wt %), whereas the elevated Y in Fe oxide-rich rocks from Roxmere and MFC can be attributed to the presence of apatite, as supported by the high P_2O_5 content in these samples. Interestingly, TiO_2/Zr and TiO_2/Al_2O_3 plots show Fe oxide-rich rocks from FC4NW plotting similarly to regional calc-silicate rocks, whereas the 'regional' Fe oxide-rich rocks do not correlate with any other rock type. The associations highlighted by these plots support the interpretations from the isocon data above, and are used to suggest that some 'regional' Fe oxide-rich rocks are not a product of replacement. Rather, the Fe oxide-rich rocks contain immobile element concentrations similar to the Hamersley BIFs in WA and Kiruna Fe ore in Sweden. While this data supports the interpretation that the Fe oxide-rich rocks were not formed by the replacement of a pre-existing rock type, it does not distinguish between Fe oxides precipitated as infill and as BIFs.

REE geochemistry

Another method that may be used to discriminate Fe oxide-rich rocks of different origins is the comparison of chondrite-normalised REE and multi-element spider diagrams. Rhodes et al (1999) used REE signatures to determine the origin of Fe oxide-rich rocks from the El Laco magnetite deposit in Chile, and found that all forms of magnetite in the deposit exhibited similar trends (section 5.2.4). That study suggested that all the Fe oxide-rich rocks at El Laco formed from magmatic-hydrothermal processes, predominately as a replacement of the andesitic hosts.

For this study, REE concentrations may help distinguish Fe oxide-rich rocks that form from chemical sedimentation from Fe oxide-rich rocks formed by other processes. Webb et al (2003) demonstrated that BIFs from the Hamersley Province in Western Australia exhibit REE trends similar to seawater (Webb et al., 2003). Seawater in general contains relatively low concentrations of REE, where there is a relative increase in LREE compared to HREE (Rollinson, 1993). Therefore, if any of the Fe oxide-rich rocks analysed here are the product of syn-sedimentary processes, this should be reflected in their REE distribution.

Figure 5.20 presents REE and multi-element trends for several Fe oxide-rich rocks, which include the ‘regional’ Fe oxide-rich rocks (Roxmere and MFC), magnetite-bearing biotite-muscovite schists from Monakoff, BIFs from the Hamersley Province (Webb, 2003), and banded Fe oxide-rich rocks at Osborne (Adshead, 1995). Figure 5.20a shows that the MFC and Roxmere Fe oxide-rich rocks contain REE concentrations an order of magnitude higher than BIFs from the Hamersley Province, magnetite-rich metasedimentary rocks from Monakoff, or banded Fe oxide-rich rocks from Osborne. The ‘regional’ Fe oxide-rich rocks also exhibit a significant negative Eu anomaly and a steeper LREE to HREE trend. This is also reflected in the multi-element diagram in figure 5.20b. Interestingly, the banded Fe oxide-rich rocks from Osborne exhibit a relatively flat trend in figure 5.20a, similar to the Hamersley BIFs. A similar trend is also apparent in the multi-element diagram in figure 5.20b. The high REE content of the Fe oxide-rich rocks from MFC and Roxmere is attributed to the presence of apatite, which strongly partitions these elements. The positive Eu anomaly associated with the banded Fe oxide-rich rocks may be caused by another REE-bearing phase, or other Fe oxide-forming process not considered by previous workers.

5.10. COMPARISONS WITH OTHER Fe OXIDE-RICH OCCURRENCES IN THE EASTERN FOLD BELT AND ELSEWHERE

This study has demonstrated that the geochemistry of Fe oxide-rich rocks provides useful information regarding the processes involved in their formation, and more importantly helps to distinguish between these different depositional processes. Four categories of Fe oxide-rich rocks have been described here and include: orthomagmatic, infill-dominant, replacement-dominant and BIF. All four are discussed below, with particular emphasis on their spatial and temporal relationship to IOCG deposits. In addition, new findings discussed in this chapter will be compared to recent theories on the relationship between albitisation and Fe oxide metasomatism in the EFB (e.g. Oliver et al., 2004). A summary of the important defining characteristics between different Fe oxide-rich rock types is presented in table 5.2.

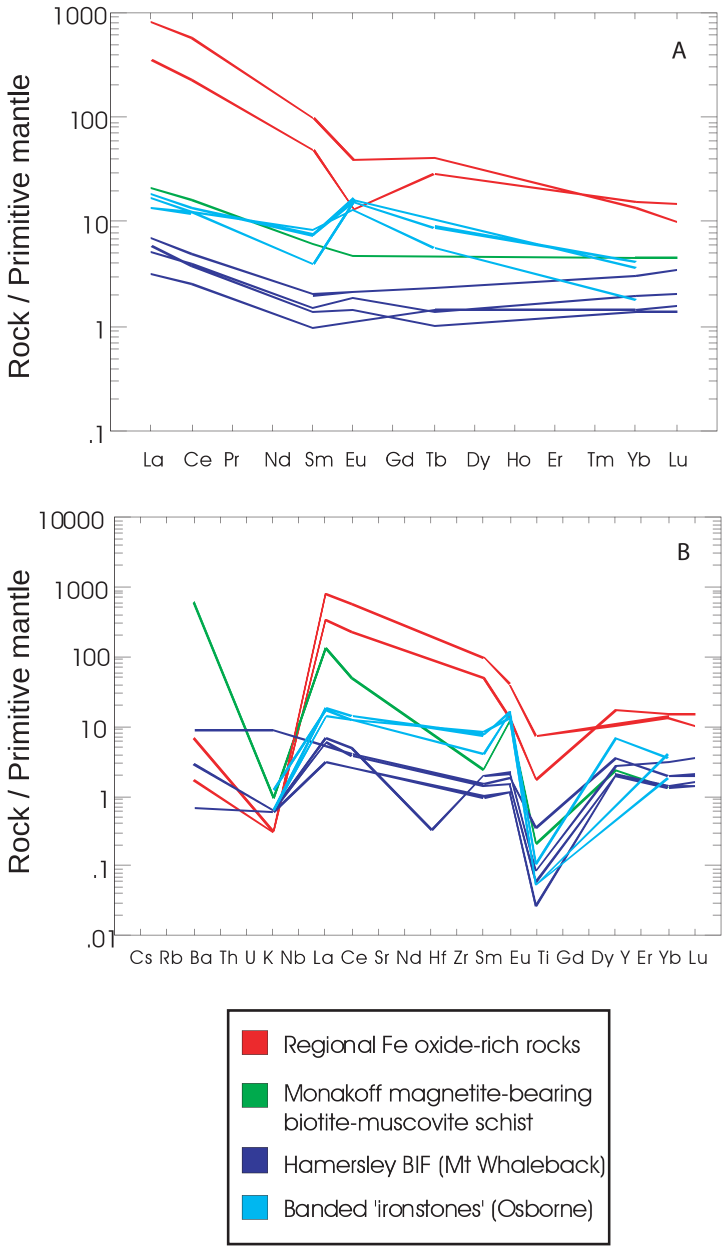

Figure 5.20: Normalised REE and multi-element geochemistry of Fe oxide-rich rocks formed via different processes including 'regional' Fe oxide-rich rocks (Roxmere and MFC), banded Fe oxide-rich rocks from Osborne (Adshead, 1995) and Monakoff and BIFs from the Hamersley Province (Webb, 2003).

A). Primitive mantle-normalised (Sun and McDonough, 1989) REE diagram (rock/primitive mantle).

B). Primitive mantle-normalised (Sun and McDonough, 1989) multi-element diagram (rock/primitive mantle). Note the discrimination between Fe oxide-rich rocks of different affinities reflected in the REE and multi-element trends.

Type of Fe oxide-rich rock	Chemistry	Textures / other minerals	Host Rock types	Presence / type of sulphides	Spatial assoc with Cu-Au deposits
Orthomagnatic e.g. FC12 magnetite layers	FC12: *Whole-rock geochem:* high REE, Y *-Mineral chem.:* high Al, V, Cr	FC12: - Common 120° triple junctions between oxides - Silicate-rich string textures between oxides.	FC12: -Coarse-grained gabbro	FC12: -Minor pyrite and chalcopyrite (sub-economic)	FC12: -Distal from other Cu-Au deposits.
Transitional magmatic hydrothermal: e.g. Lightning Creek magnetite-rich sills	Lightning Creek sills -High concentration of immobile elements (Al, Zr, Ti) *-Mineral chem.:* high Al, V, Cr	Lightning Creek sills - Globular / spherulitic texture	Lightning Creek sills: -Granite	Lightning Creek sills: None	Lightning Creek sills: -Associated with C-Au-bearing magnetite veins
Infill dominant e.g. Regional Fe oxide-rich rocks - Roxmere and MFC,	Regional Fe oxide-rich rock *Whole-rock geochem:* -low concentration of immobile elements (Al, Ti, Zr, Ga) *Mineral chem.:* -low V, Ti, Al, Mg	Regional Fe oxide-rich rock -Commonly contains simple mineralogy	All infill dominant types: *Numerous rock types*: -Calc-silicate (Roxmere) -Felsic volcanics (MFC, EH) -Soldiers Cap Group (Starra, Osborne, Mt Elliott)	Regional Fe oxide -rich rocks -(none)	All infill dominant types: Occur as lenticular / vertical bodies associated with dilation
Cu-Au mineralisation Ernest Henry, Starra, Osborne Cu-Au.		-Generally massive ironstone and/or hydrothermal breccia		Cu-Au deposits: -Chalcopyrite, pyrite, pyrrhotite, arsenopyrite, molybdenite etc&	Cu-Au deposits: -Large Cu-Au deposits associated with syn-Fe oxide infill.
Replacement dominant. e.g. FC4NW, K-Fe alteration (Ernest Henry, Starra), Fe-Ca alteration (Lightning Creek)	All replacement-dominant types: *Whole-rock geochem:* Immobile element signature reflects precursor. Typically higher than infill/BIF Fe oxide-rich rocks FC4NW *Mass balance:* Enriched elements: *Fe+Mn+Co+Zn+Ni ± Pb, P* Depleted elements: Na ± K ± As	FC4NW: -Associated with cpx-rich Na-Ca alteration (see chapter 2). K-Fe alteration: -Fine-grained biotite + magnetite	All replacement-dominant types: Numerous rock types: -Metasedimentary rocks (e.g. FC4NW) -Felsic volcanic rocks (e.g. K-Fe alt: Ernest Henry)	FC4NW: Minor cpy/py alteration K-Fe alteration: Minor cpy/py alteration	FC4NW: Distal to Ernest Henry (~10 km) K-Fe alteration: Peripheral to Ernest Henry/Starra Fe-Ca alteration: Peripheral to Lightning Creek
Syn-sedimentary BIFs Hammersley, Banded Fe oxide-rich rock. Osborne(?) Monakoff: magnetite-bearing metasediment	All BIFs -Whole-rock geochem: Low concentrations of immobile elements (Al, Ti, Zr), low REE trends. Banded Fe oxide-rich rock (?) Low Ti, Al (banded ironstone Osborne)	All BIFs -Commonly long, banded bodies. -associated with chert and minor silica	All BIFs Hosted in Sedimentary rocks	All BIFs None to minor	Banded Fe oxide-rich rocks Precursor to Cu-Au mineralisation (?): (Osborne, Starra)

Table 5.2: Summary of Fe oxide-forming processes observed in the EFB and defining characteristics that can be used to discriminate between different processes. Data taken from this study, Davidson et al (1989), Adshead (1995), Rotherham (1997), Mark et al (1999) and Perring et al (2000).

5.10.1 Orthomagmatic Fe oxide-rich rocks

Few examples of Fe oxide-rich rocks produced from orthomagmatic processes have been documented in the EFB. Moreover, Fe oxide-rich rocks within the FC12 prospect represent the first to be attributed to magmatic accumulation. From a geochemical perspective, there are three features that suggest the Fe oxide-rich rocks at FC12 are not related to hydrothermal processes, but rather late fractional crystallization from a magmatic intrusion. These three features are listed below:

- The immobile elements (e.g. Ti, Al, Ga and Zr) all exhibit a high degree of scatter in the isocon plots, suggesting that the Fe oxide-rich rocks were not formed by hydrothermal replacement of gabbroic rocks
- Linear trends between TiO_2/Fe_2O_3 and Hf/Zr suggest that both the Fe oxide-rich rocks and gabbroic rocks are a product of crystal fractionation. In addition, Fe oxide-rich rocks containing >60 wt % Fe_2O_3 correlate with a higher Fe_2O_3/TiO_2 ratio compared to Fe oxide-rich rocks with lower overall Fe_2O_3 content (Fig. 5.12a).
- Both the Fe oxide-rich rocks and their gabbroic hosts exhibit very similar REE and multi-element trends.

To support this interpretation, characteristics observed at FC12 are compared to features described at the Bushveld Complex in South Africa (c.f. Reynolds, 1985), with both sharing a range of mineralogical and textural similarities. These are listed below:

1. 120° triple-point junctions between magnetite and ilmenite are commonly observed in rocks from both regions. These are produced by the annealing of magnetite and ilmenite grains at the time of crystallisation (although later recrystallisation may also produce this texture) (Fig. 5.9e, g).
2. Thin silicate films at 120° triple junction points and along grain boundaries between magnetite, pyrite and ilmenite grains are commonly observed (Fig. 5.9f). These are interpreted to be the product of the crystallization of an intercumulus liquid trapped during the growth of adcumulate minerals.
3. A greater modal abundance of silicate minerals correlates with a significant decrease in the grain size of magnetite and ilmenite (Fig. 5.9d).
4. Magnetite grains commonly contain ilmenite laminae (Fig. 5.9h). These are interpreted to reflect variations in fO_2 at various stages during subsolidus cooling

where Ti originally contained in magnetite was exsolved to form ilmenite (Reynolds, 1985)

5. Disseminated sulphides, particularly pyrite and chalcopyrite, are occasionally identified in magnetite-rich layers from both the Bushveld Complex (Liebenberg, 1970) and the FC12 prospect, and are generally present as small grains interstitial to larger magnetite grains. In both cases, however, the sulphide content is too low to be of economic interest (cf. chapter 2)

Recent models on the formation of Fe oxide-rich layers in mafic and ultramafic intrusive rocks appeal to mechanisms whereby episodic increases in fO_2 trigger the crystallization of Ti-rich magnetite and subsequent development of cumulate layers (Reynolds, 1985 and references therein). Other variables that can potentially affect the precipitation of Fe oxide include magma temperature and water content. Experimental work by Carmichael and Nicolls (1967) showed that relatively high levels of Fe_2O_3 (1.2-3.5 wt %) and TiO_2 (0.9-1.2 wt %) must be present in a tholeiitic liquid before Ti magnetite and ilmenite will co-precipitate as primary phases. In order for rapid increases in fO_2 to occur, an increase in the amount of oxygen in the system is required, which is perhaps introduced below in the base of the magma column (Klemm et al., 1982).

The process of accumulation starts with the fractional crystallization of silicate minerals including plagioclase, which concentrates Fe, Ti and V and the residual magma density. This is followed by the accumulation of oxide minerals as a stagnant layer on the floor of the magma chamber. This dense, immiscible layer will not mix with the overlying magma and thus provides a suitable environment for the deposition and concentration of Ti-rich magnetite. With continuing crystallization of Ti magnetite, the residual magma evolves to progressively lower densities where it ultimately mixes with the overlying magma when they reach a comparable density. Gradual contacts commonly observed between Fe oxide-rich rocks and gabbroic rocks at FC12 may represent examples of this mixing phase during magmatic accumulation (Reynolds, 1985).

Transitional magmatic-hydrothermal Fe oxide-rich rocks

Fe-rich sills from the Brumby and Lightning Creek Cu-Au occurrences are unique in the EFB as they exhibit textures reminiscent of both magmatic and hydrothermal processes (Foster, 1995; Perring et al., 2000). As such they have tentatively been included in this category, although they are texturally and geochemically quite distinct from Fe oxide-rich rocks at FC12. Perring et al (2000) noted that these rocks display considerable textural and compositional variation, and are mineralogically similar to the magnetite-rich veins that host Cu-Au mineralisation. These observations led Perring et al (2000) to argue that the sills reflect magmatic crystallisation under different degrees of melt saturation, and may provide evidence for the transition from magmatic to hydrothermal conditions associated with the Williams-Naraku Batholith (Perring et al., 2000).

Both Fe oxide-rich rocks from the FC12 prospect and Fe-rich sills from Lightning Creek exhibit textures that distinguish them from other Fe oxide-forming processes. In the case of FC12, thin section analysis shows textures that are similar to those documented in magnetite-rich layers from other tholeiitic gabbroic sequences (e.g. the Bushveld Complex, South Africa; Reynolds, 1985) (Fig. 5.9e, f, g, h). In contrast, Lightning Creek Fe-rich sills display distinct macroscopic globular and spherulitic textures which are attributed to a high degree of undercooling during crystal fractionation due to the enrichment of H_2O in the crystallising melt (Perring et al., 2000). These balloon-textured Fe-rich sills are characterised by thin trains of fine-grained magnetite, separating spherulitic albite-rich domains from polygonal quartz-rich domains (Perring et al., 2000), while the surfaces of these domains are cuspate to ovoid in shape and may indicate fluid immiscibility. The magnetite is interpreted to have crystallised early with respect to the albite and quartz domains (Perring et al., 2000).

Finally, both the Fe oxide-rich rocks from FC12 and Fe-rich sills from Lightning Creek are chemically distinct from other Fe oxide-rich rocks (Fig. 5.19). In particular, both rock types exhibit elevated concentrations of Al_2O_3 and Zr (Fig. 5.19), whereas Fe oxide-rich rocks produced from sedimentary processes or infill contain significantly lower concentrations of Al_2O_3 and Zr. These concentration differences reflect the low solubility of Al_2O_3 and Zr in aqueous solutions.

5.10.2. Replacement-style Fe oxide-rich rocks

Fe oxide-rich rocks at FC4NW, K-Fe alteration at Ernest Henry and Starra, and Fe-Ca alteration at Lightning Creek represent the major documented examples of Fe oxide formed via replacement of a previous rock (Table 5.2). At FC4NW, the relative immobility of Ti, Al, Y and Zr defines an isocon for two altered/unaltered pairs indicating variable changes in mass. However, mass gains are quite extreme during Fe oxide metasomatism and most likely represent significant dilation associated with alteration, although the relative density of the altered rock compared to the unaltered equivalent may also be a significant factor. Fe oxide metasomatism at FC4NW is associated with the enrichment of Fe, Mn, Co, V, Zn, Ni, P, Pb and S, whereas Ba, Sr K and Na are invariably depleted.

Pre-ore Fe, Mn, K and Ba veining and alteration at Ernest Henry extends for approximately 1.5 km from the orebody (Mark et al., 2000). It is associated with the formation of K-feldspar, biotite, amphibole, magnetite, garnet and carbonate and is reminiscent of similar styles of alteration peripheral to other IOCG deposits (e.g. Osborne and Starra). Isocons constructed from their geochemistry indicate the addition of Fe_2O_3 (total), K_2O, MnO, MgO, Ba, Zn, Rb, Cl and loss of Na_2O, SiO_2, Pb, Cu and LREE (Mark et al., 1999; Oliver et al., 2004). Differences in mass transfer between magnetite alteration of metasedimentary rocks at FC4NW and fine-grained magnetite-biotite alteration at Ernest Henry include the loss of K_2O, Ba and Sr and the addition of Pb in metasedimentary rocks at FC4NW. The gain in K_2O and Ba at Ernest Henry can be attributed to the addition of biotite and K-feldspar associated with magnetite alteration. In contrast, biotite in the metasedimentary rocks at FC4NW is typically destroyed during Fe oxide alteration resulting in the depletion of K_2O.

Fe-Ca alteration of quartz-feldspar sills at Lightning Creek (Perring et al., 2000) is mineralogically similar to Fe oxide metasomatism at FC4NW. Magnetite alteration is accompanied by the addition of Fe_2O_3 (T), CaO, Ga and Na_2O along with a depletion of K_2O. In comparison, Na_2O is depleted in one sample (MFC 160.2/51) and undepleted in the other sample (MFC 160.5/51) at FC4NW. The addition of Na_2O during magnetite alteration at Lightning Creek is associated with albitisation during Fe oxide metasomatism (Perring et al., 2000) and may represent a similar Fe oxide-metasomatic event to that described for FC4NW in this study.

5.10.3. Infill-dominated Fe oxide-rich rocks

Fe oxide-rich rocks formed by infill possibly represent the most common type in the EFB. Fe oxide associated with Cu-Au mineralisation at Ernest Henry and Mount Elliott occur predominately as veins and breccia similar to many barren Fe oxide-rich rocks throughout the EFB (Adshead, 1995; Little, 1997; Rotherham, 1997; Mark et al., 1999). Infill-dominated Fe oxide-rich rocks typically occur as lenticular and vertical bodies associated with dilation, or intersections between fault and shear zones, and are spatially associated with numerous rock types (section 4.4; see also Williams, 1994; Mark et al., 1999).

Two techniques were employed in this study to test whether geochemistry could be used to distinguish between the processes by which barren Fe oxide-rich rocks formed (e.g. infill, alteration or sedimentary-exhalative processes). Figure 5.19 shows that barren Fe oxide-rich rocks (Roxmere, MFC, BIFs) contain comparatively low concentrations of immobile elements (Al_2O_3, Zr and to a lesser extent, TiO_2), compared to Fe oxide-rich rocks formed (at least in part) by alteration (FC4NW) and magmatic processes (FC12, Lightning Creek). As mentioned above, if the Fe oxide-rich rocks are a product of alteration, then the altered equivalent should contain ratios of immobile elements that reflect the composition of the original rock. The geochemical data presented in figure 5.19 shows that the immobile element content of regional Fe oxide-rich rocks from Roxmere and MFC do not reflect any other rock type in the dataset, suggesting that these rocks formed via hydrothermal infill processes.

This differentiation between Fe oxide-rich rocks formed from different processes is also apparent in figures 5.20a and b, where BIF and the regional Fe oxide-rich rocks have distinctly different REE and multi-element trends. The infill-dominant Fe oxide-rich rocks from MFC and Roxmere clearly contain higher concentrations of all the major REE and also exhibit a prominent negative Eu anomaly, and can be attributed to the presence of apatite. Studies on REE partitioning in apatites within various I-type and S-type granites (Sha and Chappell, 1999) show that REE patterns are largely controlled by the presence of additional REE-bearing minerals. For example, the presence of monazite in I-type and felsic S-type granites will greatly affect the concentration of REE in apatite, as opposed to I-type mafic granites which contain titanite, apatite, zircon and allanite as the dominant REE-bearing minerals. The Eu^{2+}:Eu^{3+} ratio in a silicate melt is a critical factor in controlling the degree of Eu depletion in apatite, as apatite has a strong preference for Eu^{3+} in its crystal lattice due to it having a similar ionic radius to Ca^{2+} (Goldschmidt, 1958). Despite this, it is uncertain whether infill-dominant Fe oxide-rich rocks containing no apatite will still exhibit similar REE and multi-element trends to those from MFC and Roxmere. More geochemical data of regional Fe oxide-rich rocks from other parts of the EFB is needed to explore this further.

5.10.4. Banded Iron Formations (BIFs)

This study combined with recent work by Marshall (2003) shows that the origin of early Fe oxide-rich rocks at Osborne, and perhaps at Starra is different, to most others in the district. Marshall (2003) proposed that $\delta^{13}C$ and $\delta^{18}O$ isotope signatures of the early banded Fe oxide-rich rocks at Starra and Osborne exhibit signatures reminiscent of marine meta-carbonates, in contrast to the interpretation of Rotherham et al (1998) who suggested that the C and O isotope trends for banded Fe oxide-rich rocks reflected a cooling magmatic fluid. The REE trends presented differ considerably between Fe oxide-rich rocks formed by infill (Roxmere and MFC) and by sedimentary exhalative processes (BIF). In particular, the REE patterns for banded Fe oxide-rich rocks at Starra exhibit a flatter trend more akin to the BIF from the Hamersley Province.

Hatton and Davidson (2004) studied the major and trace element geochemistry of iron formation within the Mt Norna quartzite and Weatherly Creek formation situated within the Soldiers Cap Group of the Eastern Succession, approximately 25 and 30 km south of Monakoff, respectively (Fig. 5.1). In both cases, REE patterns exhibited LREE enrichment, strong positive Eu anomaly and a weak negative Ce anomaly. Hatton and Davidson (2004) noted that the REE patterns are similar to those of modern metalliferous sea-floor sediments and display anomalies controlled by high temperature hydrothermal fluids, seawater and detrital minerals. They proposed that the iron-formations were products of the mixing of hydrothermal fluids and seawater. In addition, major element data and the LREE enrichment trends suggest that the iron-formation formed at or near a sediment-water interface via chemical sedimentation of mafic-derived clays and detritus.

Comparisons with Fe oxide-rich rocks discussed in this study (Fig. 5.20) show that the Mt Norna and Weatherly Creek iron-formations are similar to the REE patterns of the banded ironstones from Osborne, although the iron-formations described by Hatton and Davidson (2004) also exhibit a distinct positive Ce anomaly, not present in the banded Fe oxide-rich rocks from Osborne. Regardless, the similar REE patterns between banded Fe oxide-rich rocks at Osborne, BIFs from the Hamersley Province and iron-formation in the Eastern Succession suggest that the early Fe oxide-rich rocks from Osborne and Starra may be syn-sedimentary as originally interpreted by Davidson et al (1989).

5.11. Fe OXIDE-RICH ROCKS AND ALBITISATION IN THE EASTERN FOLD BELT

This study, with several earlier ones (Williams, 1994; Davidson and Davis, 1997), has shown that numerous different processes are responsible for the formation of Fe oxide-rich rocks in the EFB. Regardless of the contentious origin of some of these Fe oxide-rich rocks, it appears likely that Fe oxide metasomatism is responsible for most, but not all Fe oxide-rich occurrences in the EFB. The occurrence of both Cu-Au-bearing and barren Fe oxide-rich rocks close to each other (e.g. Ernest Henry) has led numerous authors to suggest that both are intimately related. One current model addressing the sources of Fe responsible for Fe oxide ±Cu-Au mineralisation in the EFB involves the liberation of Fe and K by widespread post-metamorphic albitisation of country rocks, as summarised in chapter 3 (Williams, 1994; Rubenach and Lewthwaite, 2001; Oliver et al., 2004). Figure 5.21 illustrates the possible mechanisms and sources of fluids responsible for the formation of Fe oxide-rich rocks both enriched and barren of significant Cu-Au mineralisation. It is suggested that the fluids responsible for albitisation are likely to have been derived from the crystallisation of the Williams Batholith. This is supported by the fluid immiscibility model prefered by Pollard (2000) which suggests that hypersaline and CO_2-rich gas are separated from a complex NaCl-H_2O-CO_2±$CaCl_2$ fluid, with stable isotope values indicating a magmatic-hydrothermal origin as discussed in section 5.4.1.

Oliver et al (2004) noted that most of the deposits within the EFB are hosted in meta-pelitic rocks of the Soldiers Cap Group, although there are examples that occur in siliclastic schists or volcanic rocks of the Mary Kathleen Group (e.g. Ernest Henry).

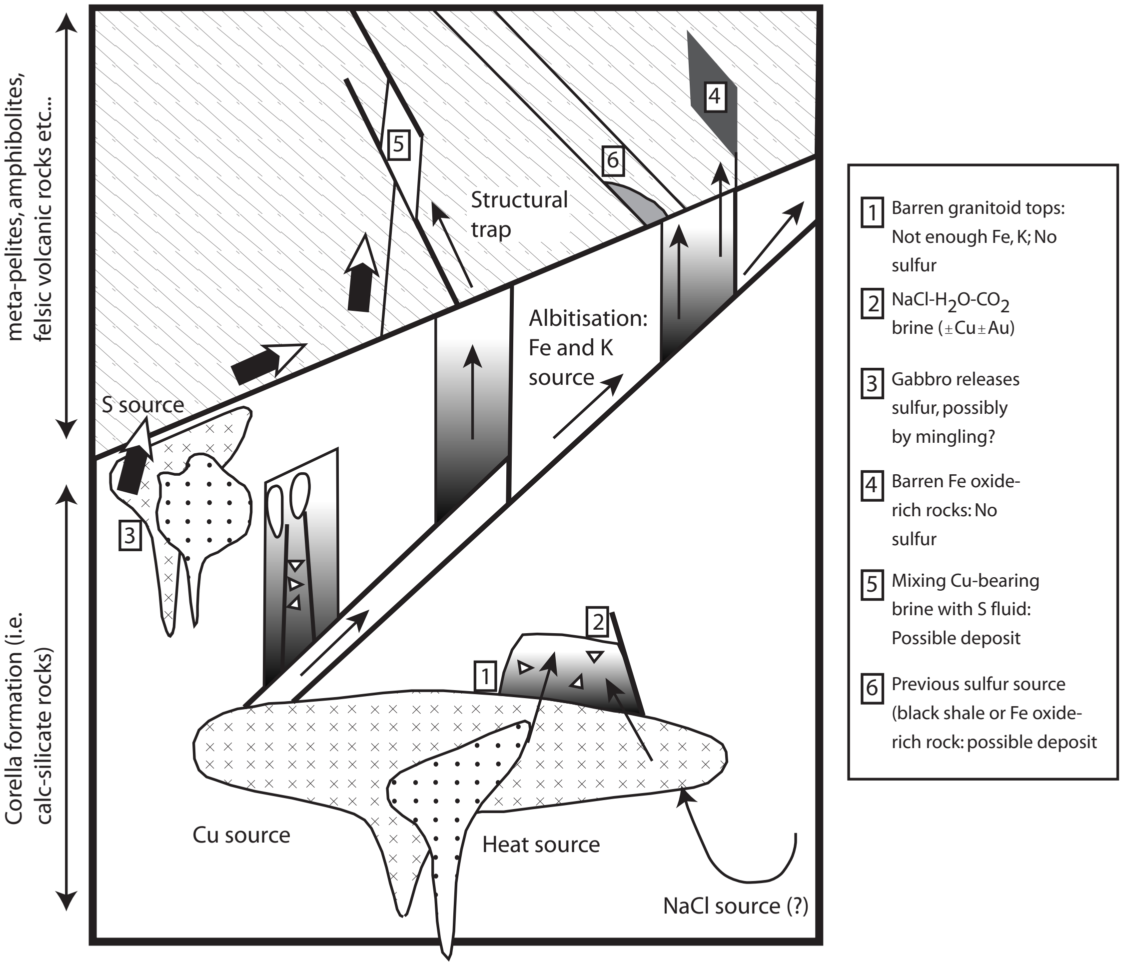

Figure 5.21: Schematic diagram explaining the distribution and generation of albitites and the relationship between their formation and Fe oxide-rich rocks in the EFB. Various conditions and processes suitable for ore genesis are shown including fluid modification via albitisation, a structural trap, a reactive host rock in overlying schists (or calc-silicate rocks of the Mary Kathleen Group), and a sulphur source. Barren Fe oxide-rich rocks produced via metasomatic processes may be produced via albitisation but lack sulphur. The mixing of a similar fluid that also contains Cu, with an external S-bearing fluid, may produce Cu-Au mineralisation (modified from Oliver et al., 2004).

They suggest saline-rich fluids derived from temporally-related intrusions initially flow through and albite calc-silicate rocks. The resulting re-equilibrated fluids then interact with the overlying pelitic rocks of the Soldiers Cap Group (Oliver et al., 2004) thus releasing into the fluid both Fe and K and other components responsible for Fe oxide metasomatism. The origin of the Cu, however, is contentious, although geochemical data presented by Oliver et al (2004) suggests that the Cu could be derived from the fluid source i.e. the intrusions. If this is the case, barren Fe oxide-rich rocks may form from fluids that contain little or no Cu and/or S. Alternatively, mineralisation may occur from the interaction of a Cu-bearing fluid enriched in Fe (due to earlier albitisation), with either another S-rich fluid or S-rich host rock (Oliver et al., 2004).

Whole rock geochemistry of albitised rocks and their unaltered equivalents have shown that Na addition is accompanied by the loss of Fe, K, Ba, Rb ± Ca Sr, Co, V, Mn, Pb and Zn (Rubenach and Lewthwaite, 2002; Oliver et al., 2004). Consequently, the depleted elements appear to be added to the fluid at the time of albitisation and ultimately re-precipitate as K- and Fe-bearing metasomatic rock. This study has shown that Fe oxide metasomatism at FC4NW is associated with chemical changes that only partly resemble that of regional albitisation. In particular, whereas Na is consistently added during albitisation and depleted during Fe oxide metasomatism, as noted by Oliver et al (2004), this study has shown that Na is immobile to slightly depleted in Fe oxide-rich rocks at FC4NW (Fig. 5.14). Fe oxide metasomatism at FC4NW is also associated with losses in Sr, K and Ba. This does not coincide with the model proposed by Oliver et al (2004) as these components should be relatively enriched as a result of their liberation from country rock during albitisation. The Fe oxide-rich rocks at FC4NW are devoid of K-Fe minerals such as biotite and K-feldspar found in many Fe oxide-rich rocks peripheral to IOCG deposits. On the other hand, Fe, Mn, V, Pb and Zn are clearly gained during Fe oxide metasomatism at FC4NW and relate to the same components consistently depleted during albitisation.

The relationship between Fe oxide metasomatism and early clinopyroxene-rich Na-Ca alteration at FC4NW is discussed in detail in chapter 2, with evidence suggesting that they are genetically linked as has also been inferred for pre-ore Fe oxide-rich rock and Na-Ca alteration in the Ernest Henry hanging wall (Mark et al., in prep). The precipitation of magnetite at FC4NW is associated with diopside + titanite + albite ± pyrite ± carbonate. The K-Fe alteration at Ernest Henry, meanwhile, overprints regional Na-Ca alteration and is associated with K-feldspar + biotite + amphibole + magnetite ± garnet ± carbonate. The relative timing of Fe oxide metasomatism with respect to Na-Ca alteration, as well as the different mineral assemblages and geochemistry at FC4NW and Ernest Henry, suggests that perhaps Fe oxide metasomatism is either strongly influenced by the host rock and/or may be a result of different fluid chemistry. The generation of Fe oxide-rich rocks at FC4NW most likely predated ore-stage Fe oxide metasomatism at Ernest Henry because the former is clearly related to Na-Ca alteration, which predates ore-related K-Fe alteration at Ernest Henry (Mark et al, 1999).

5.12. DISCUSSION AND CONCLUSIONS

The discrimination between Fe oxide-rich rocks that form from various processes may provide a greater understanding of the important mechanisms involved in the formation of Fe oxide-rich rocks and IOCG deposits as well as provide potential targets for exploration. The current understanding is that the relations between Fe oxide-rich rocks and Cu-Au mineralisation range from Fe oxide-rich rocks that predate Cu-Au mineralisation (e.g. Starra, Osborne), synchronous Fe oxide and Cu-Au precipitation (e.g. Ernest Henry) and Cu-Au mineralisation associated with little or no Fe oxide (e.g. Eloise). Importantly, there are many Fe oxide-rich rocks scattered throughout the EFB that are devoid of Cu-Au mineralisation. The origin of many of these Fe oxide-rich rocks has been controversial, particularly where Cu-Au mineralisation is spatially and/or temporally related. This study has described four main categories of Fe oxide-rich rocks formed by different geological processes, each of which can be distinguished by their texture, mineralogy and/or geochemistry. These categories include:

1) Orthomagmatic
2) BIF
3) Replacement deposits
4) Infill deposits

5.12.1 Fe oxide-rich rocks formed from primary processes

Fe oxide-rich rocks formed from orthomagmatic and chemical sedimentary (BIF) processes represent categories which are genetically unrelated to Fe oxide-Cu-Au mineralisation, although it is possible that these rocks may act as a reactive host to Cu-bearing fluids, similar to pre-ore Fe oxide-rich rocks hosting the Starra and Osborne ore bodies. In particular, interpreted origins of the banded Fe oxide-rich rocks from Starra and Osborne include both syn-sedimentary and metasomatic processes. REE geochemistry of these rocks reflect signatures similar to typical BIFs both from the Hamersley Province in WA and the Selwyn Range District in the EFB, supporting the original interpretation by Davidson et al (1989) who inferred a syn-sedimentary origin.

Orthomagmatic Fe oxide-rich rocks have not been described previously in the EFB, although other layered gabbroic sequences have been documented including the Tee Tree complex (Brown, 1998). These rocks typically contain cumulate-like textures defined by intergrown magnetite, ilmenite and other silicate minerals as well as minor pyrite and chalcopyrite. The presence of thin silicate films along magnetite and ilmenite grain boundaries and ilmenite laminae within individual magnetite grains also reflect orthomagmatic processes, the latter of which is caused by the exsolution of ilmenite from Ti-rich magnetite (Reynolds, 1985). The Fe_2O_3 (total)/TiO_2 and Hf/Zr plots of the Fe oxide-rich rocks and their gabbroic hosts at FC12 exhibit strong positive correlations while REE patterns for both are almost identical, suggesting that the Fe oxide-rich rocks are related to similar orthomagmatic processes to that which formed the gabbroic hosts. Episodic increases in fO_2 and alternating fractional crytallisation of silicate and oxide minerals has been attributed to the formation of these rocks (Reynolds, 1985 and references therin).

5.12.2 Fe oxide-rich rocks formed by secondary (hydrothermal) processes

Fe oxide-rich rocks that are most likely to be genetically related to the formation of Fe oxide (Cu-Au) mineralisation are those related to hydrothermal processes. Although hydrothermal Fe oxide-rich rocks commonly lack textures that reflect their origin, this study has shown that geochemistry may aid in their discrimination from other Fe oxide-forming processes. In the case of Fe oxide-rich rocks formed from replacement, such as those at FC4NW and surrounding the Ernest Henry deposit, ratios of elements that are immobile in aqueous solution should be similar between altered and unaltered equivalents, provided the unaltered rock represents the correct precursor. Isocons comparing the Fe oxide-rich rocks from FC4NW with their unaltered equivalents show that these relationships hold even if a significant proportion of the Fe oxide is infill (Fig. 5.14). In contrast, Fe oxide-rich rocks formed predominately from infill will contain very low concentrations of immobile elements compared to other rock types (Fig. 5.19). In cases where other Fe oxide-rich rocks also contain low concentrations of immobile elements (e.g. BIFs), REE geochemistry can help distinguish between these processes because the REE trends of BIFs reflect marine sediments that are distinct from other Fe oxide-forming processes (Fig. 5.20)

5.12.3 Implications for the origin of fluids responsible for Fe oxide (±Cu-Au) mineralisation

The deposition mechanism whereby Fe oxide is precipitated from a fluid (i.e. replacement or infill) will dictate the chemical composition of the Fe oxide-rich rock. Where Fe oxide-rich rocks formed via replacement, the chemistry will be reminiscent of its precursor and the interacting fluid. In contrast, the chemistry of Fe oxide-rich rocks precipitated as infill will be dictated predominantly by the fluid. Mass balance work shows elements gained during Fe oxide metasomatism at FC4NW only partly resemble elements lost during albitisation (cf. Oliver et al., 2004; Rubenach and Lewthwaite, 2002; Williams, 1994). These findings conflict with the hypothesis by Williams (1994) and Oliver et al (2004) who suggested that components released during albitisation into the fluid are later precipitated in Fe oxide (±Cu-Au) mineralisation. In addition, the mineralogical and temporal relationship between Fe oxide metasomatism and clinopyroxene-rich Na-Ca alteration at FC4NW differs from that observed at Ernest Henry, where K-Fe alteration and mineralisation is observed to overprint Na-Ca alteration. The relative timing of Fe oxide metasomatism and Na-Ca alteration at FC4NW compared to Ernest Henry combined with the relative mobility of components during Fe oxide metasomatism implies that different processes may have been involved in the formation of these Fe oxide-rich rocks.

While Williams (1994), Rubenach and Lewthwaite (2001) and Oliver et al (2004) all provided convincing evidence to suggest that components enriched during Fe oxide metasomatism originated from components depleted during albitisation, work by Perring et al (2000) at Lightning Creek showed that Fe may also originate directly from a fractionating magma. In chapter 2, a close spatial and temporal association was noted between felsic igneous intrusions, clinopyroxene-rich Na-Ca alteration and latter pegmatite dykes at FC4NW. One possibility is that the fluids responsible for Na-Ca alteration at FC4NW may have originated from the same intrusion responsible for the granitic and pegmatitic dykes observed in drill core (chapter 2). If the fluids responsible for Fe oxide metasomatism at FC4NW were derived from a nearby magmatic intrusion, the close spatial association between Fe oxide metasomatism and granitic and pegmatitic intrusions would suggest that the resultant fluid flow probably occurred over small distances only (<100 m). Thus, it is debatable whether the fluids could have been enriched with Fe over such short distances by fluid-rock interaction alone. Therefore, a more plausible source for the Fe in the fluid is directly from a crystallising intrusion.

The transition from clinopyroxene-rich to actinolite-rich Na-Ca alteration at FC4NW is similar to alteration assemblages described by de Jong and Williams (1995) at Muramungee Creek and Fullarton River, and was attributed to changes in pressure, temperature, and XCO_2. Work by Hemley et al (1992) and McPhail (1993) have shown that a decrease in temperature at constant pressure can play a major role in the precipitation of large masses of iron from highly saline fluids. It is possible, therefore, that the decreasing temperature inferred by the transition of clinopyroxene-rich to actinolite-rich Na-Ca alteration, may have been an important mechanism for the precipitation of magnetite ± hematite associated with clinopyroxene-rich Na-Ca alteration at FC4NW, and by implication, for the early pre-ore magnetite bodies in the Ernest Henry hanging wall.

Neither of the Fe oxide-rich rocks in outcrop at MFC, within the FC4NW prospect, or in the hanging wall Fe oxide-rich rock at Ernest Henry are directly associated with the precipitation of chalcopyrite. In the case of FC4NW, most of the Fe oxide-rich rocks are devoid of Cu, illustrated by the negative correlation between Fe and Cu described in chapter 2. Where Cu is present within Fe oxide-rich rock, textural evidence shows that the chalcopyrite is associated with a later actinolite-rich Na-Ca event overprinting Fe oxide and clinopyroxene-rich Na-Ca alteration. Instead, most of the chalcopyrite at FC4NW (and FC12) is associated with brittle-style actinolite-rich Na-Ca veins, which contain minor magnetite and hematite only. These observations suggest that the presence of Fe oxide-rich rocks played no major role in the precipitation of chalcopyrite at FC12 or FC4NW, either as a direct precipitant (in contrast to the main mineralisation stage at Ernest Henry) or as a reactive host (i.e. Osborne).

The absence of significant chalcopyrite at the FC12 and FC4NW prospects and in outcrop, however, does not rule out the potential for Cu-Au mineralisation to occur in these systems. It could be argued that if similar fluids to those responsible for Cu-Au mineralisation at Osborne interacted with the Fe oxide-rich rocks at FC4NW, MFC outcrop or Roxmere, then mineralisation may also occur, provided that the fluid and rock differ significantly in redox state. Since the Fe oxide-rich rocks at FC4NW, MFC outcrop and Roxmere all contain magnetite (although the major Fe oxide at Roxmere is hematite) then the Cu-Au-bearing fluid would need to be significantly oxidised (hematite-stable).

Whether Cu-Au mineralisation could occur from mixing between fluids responsible for Fe oxide metasomatism at FC4NW, MFC outcrop and Roxmere and those responsible for Cu-Au mineralisation at Ernest Henry is less clear. The current model for the formation of the Ernest Henry deposit invokes the mixing of a Fe- and Cu-bearing fluids with a S-bearing fluid (Mark et al., 1999). The mechanism whereby chalcopyrite precipitation occurred at FC4NW is most likely related to the transition from clinopyroxene-rich to actinolite-rich Na-Ca alteration resulting from a down-temperature gradient and/or increase in pressure and reduced XCO_2. Although Cu concentrations in fluid inclusions at FC4NW are similar to those at Ernest Henry, the latter most likely represents a ‘spent’ system (Mark et al., 1999) (see chapter 4). Hence, Cu concentrations were most likely higher prior to Cu-Au mineralisation at Ernest Henry (chapter 4). Instead, it appears that Cu-Au mineralisation at FC4NW did not occur due to either a lack of voluminous S in the host rock, and/or the fluids did not contain enough Cu.

CHAPTER 6:

TRACE ELEMENT GEOCHEMISTRY OF SELECTED MAGNETITE, HEMATITE, PYRITE AND CHALCOPYRITE ASSOCIATED WITH VARIOUS FE OXIDE (±CU-AU)-MINERALISED SYSTEMS: INSIGHTS INTO THE GEOCHEMISTRY OF ORE-FORMING FLUIDS

TRACE ELEMENT GEOCHEMISTRY OF MAGNETITE, HEMATITE, PYRITE AND CHALCOPYRITE ASSOCIATED WITH VARIOUS FE OXIDE (±CU-AU)-MINERALISED SYSTEMS: INSIGHTS INTO THE GEOCHEMISTRY OF ORE-FORMING FLUIDS

6.1. INTRODUCTION

The primary unresolved issues for the genesis of Fe oxide (Cu-Au) deposits (IOCG) are the fluid source(s), and the relative significance of intrusions as providers of fluid, heat and metals (Barton and Johnson, 2000; Haynes, 2000; Hitzman, 2000; Pollard, 2000). Most IOCG deposits are occurrences where Cu-Au mineralisation overprinted earlier Fe oxide-rich rocks, or where both the Fe oxides and Fe sulphides were precipitated together. Some IOCG deposits are associated with rocks where Fe oxide is a minor component, while barren Fe oxide-rich rocks are also common in regions where IOCG deposits occur. The different spatial and temporal relationships between Cu-Au mineralisation and Fe oxide-rich rocks in the Eastern Fold Belt of the Mount Isa Inlier (EFB) have complicated the issue regarding the genetic relationship between Fe oxide occurrences and Cu-Au mineralisation. As such, a model illustrating the important genetic and temporal relationships between Cu-Au mineralised and barren Fe oxide-rich is yet to be developed.

The trace element geochemistry of magnetite, hematite, pyrite and chalcopyrite within various Fe oxide- and Cu-Au- mineralised systems in the EFB has been investigated using *in situ* laser ablation inductively coupled plasma-mass spectrometry (LA-ICP-MS). This will provide a better understanding regarding the composition of ore fluids and processes responsible for Fe oxide (±Cu-Au) mineralisation. In addition, the geochemistry of different minerals formed in the same vein/breccia association can provide constraints on the nature of elemental partitioning between minerals and aqueous fluids. Samples from IOCG deposits, barren Fe oxide-rich rocks, and weakly Cu-mineralized occurrences associated with Fe oxides mostly in the Mount Fort Constantine (MFC) and Ernest Henry district were selected to ascertain whether the trace element geochemistry of magnetite, hematite, chalcopyrite and pyrite can be used to distinguish the different ore forming processes. Some of the factors that may have influenced the trace element composition of these minerals include:

1. Mineral assemblage (e.g. diversity of minerals in the suite);

2. Host rock composition;
3. Magma petrogenesis:
4. Degree of fluid-rock interaction (e.g. hydrothermal replacement versus infill); and,
5. Physicochemical parameters during deposition (e.g. P, T, pH, f_{O2}, f_{S2}, X_{CO2} conditions).

The aim is to develop: 1) A more robust generic model describing the sources and chemical makeup of fluids associated with Fe oxide-rich rocks and Fe oxide (Cu-Au) mineralisation; and 2) A geochemical '*fingerprinting*' tool for discriminating between barren and Cu-Au mineralised Fe oxide-rich systems.

6.2. Fe OXIDE (±Cu-Au) MINERALISATION IN THE EASTERN FOLD BELT

The EFB represents one of the most significant Proterozoic base metal provinces in the world. The Cloncurry District in the east of the EFB contains many IOCG deposits including Ernest Henry, Starra, Osborne, Mount Elliott and Eloise (Fig. 6.1). In addition to these ore deposits, numerous magnetite- and hematite-bearing rocks and Na-Ca-bearing alteration assemblages are common throughout the district. In this part of the study, the ore mineral associations in the region are divided into three categories, including Cu-Au mineralisation, weakly mineralised sulphide-bearing systems, and barren Fe oxide systems.

6.2.1. Sample Selection

Cu-Au mineralised systems

Occurrences that reside in this category are represented by the Ernest Henry, Starra, Osborne and Mt Elliott Cu-Au deposits (Fig. 6.1). Appendix 8 shows the main mineral constituents and rock types associated with Cu-Au mineralisation for each deposit.

Weakly mineralised sulphide-bearing systems

Many of the samples collected in this category are associated with pre-ore and post-ore hydrothermal phases at the Ernest Henry (Cu-Au) deposit (Appendix 8). The sample suite also includes material from the FC4NW and FC12 prospects in the Mount Fort Constantine (MFC) exploration lease (Fig. 6.1), as well as the Lightning Creek (Cu-Au) occurrence (cf. Perring et al., 2000) and sulphide-bearing Na-Ca veins from the Gilded Rose area (cf. Marshall, 2003).

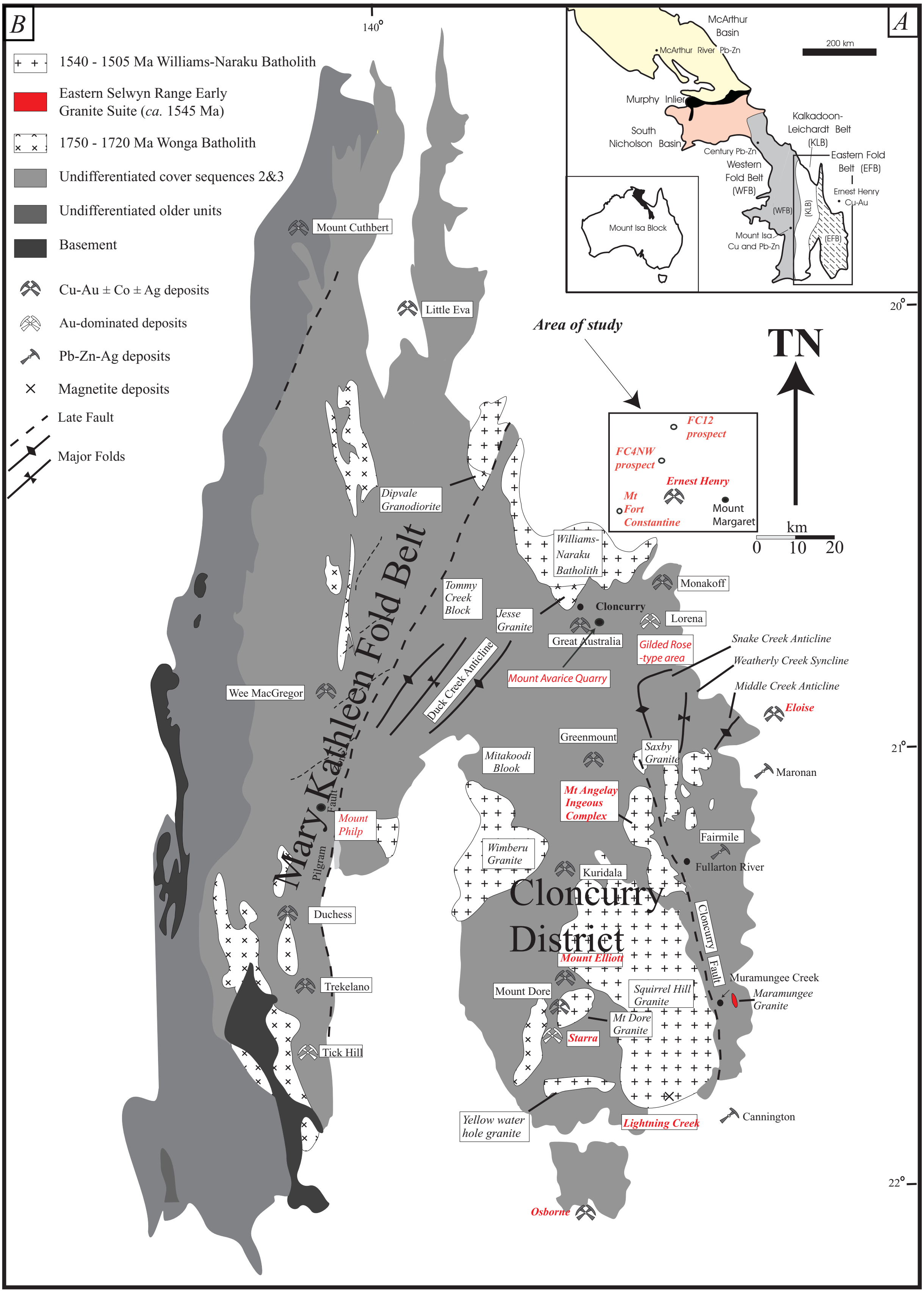

Figure 6.1. A. Tectonostratigraphic divisions of the Mount Isa Inlier, Queensland. B. Enlargement and simplified geology of the Eastern Fold Belt with locations of samples analysed for trace element geochemistry using LA-ICP-MS (highlighted in red). Compiled from published AGSO maps and modified by Williams (1998).

Barren Fe oxide systems

Fe oxide-bearing and sulphide-deficient samples were collected from various locations in the EFB (Appendix 8, cf. Marshall, 2003) and include Na-Ca assemblages from the Gilded Rose area, Mount Avarice quarry and the Mount Angelay igneous complex. This suite of samples contains both hematite and magnetite-bearing rocks, which include samples of the banded Fe oxide-rich rocks hosting Cu-Au mineralisation at the Starra and Osborne Cu-Au deposits. Magnetite in igneous rocks from the Lightning Creek Fe oxide deposit and Slaughter Yard Creek, and metamorphic magnetite in Corella formation calc-silicate rocks were also collected.

6.3. FUNDAMENTALS OF TRACE ELEMENT SUBSTITUTION

6.3.1. Element substitution mechanisms in minerals

There is an abundance of literature addressing the behaviour of trace element partitioning in minerals (Ringwood, 1955; Goldschmidt, 1958). However, most studies detail the relations on partitioning between crystals and melt, rather than between minerals and aqueous fluids (cf. Blundy and Wood, 2003). Despite this, the nature and controls on trace element partitioning between crystals and melt provide useful information on the likely partitioning relations between fluids and mineral precipitates. The properties governing partitioning between different elements can be attributed to work by Pauling (1948), Ringwood (1955) and Goldschmidt (1958), amongst others, but are generally referred to today as ‘Goldschmidt’s rules of substitution’ (Faure, 1998), and include:

1. Ions of one element can substitute for another element if their ionic radii differ by less than 15%.
2. Ions whose charges differ by one unit substitute readily provided that the electrical neutrality of the crystal is maintained. If the difference in charge is > 1 unit, substitution is generally slight.
3. Two different ions that can potentially occupy the same position in a particular mineral will be sorted by the ion with the higher ionic potential, which will form a bond with surrounding anions within the crystal site.
4. Even if size and charge are similar, substitution may be limited by different electro-negativities, which represents the ability of an atom in a molecule to attract electrons to itself.

These rules have been critically reviewed by many geochemists over the years. Many exceptions can arise, as substitution is generally site specific (Faure, 1998). Despite this, Goldschmidt's rules serve as a useful tool for considering the possible replacement of ions in crystals forming in a cooling magma or aqueous solution.

6.3.2. Crystal chemistry

Crystal chemistry is a combination of the rules of crystallography and solid state physics and chemistry, allowing interpretations, rationalisations and predictions of atomic arrangements of crystals (e.g. Waychunas, 1991). The crystal chemistry of individual minerals is fundamental in understanding trace element substitution. For example, inter-site partitioning of large ions will tend to favour the larger and more distorted sites within a crystal lattice (Waychunas, 1991), whereas the small ions (e.g. Si^{4+}, Ti^{4+}) will preferentially partition into smaller sites. This section discusses the crystal structures of each of the minerals applicable to this study.

Magnetite

Magnetite is a member of the spinel group, which is characterised by a unit cell containing 32 oxygen ions and 24 cations (Deer et al., 1992). The spinel structure is organised in a Cubic Close Packing (CCP) arrangement for oxygen ions (Fig. 6.2) and forms a cubic symmetry (Waychunas, 1991). The stoichiometry of the spinel group is represented by AB_2O_4, and contains cations of two different valence states in the ratio of 2:1. In the case of magnetite, iron represents cations of both valence states. The spinel group can be divided into two structural types according to cation site occupancy (e.g. tetrahedral or octahedral sites) within the crystal structure. These two structural types are termed normal and inverse depending on where the more abundant of the two cations reside within the general formula $R_8^{2+}R_{16}^{3+}O_{32}$ (Deer et al., 1992). If cations are located within the octahedral sites, the spinel is normal (i.e. $8R^{3+}$ in A, $16R^{3+}$ in B). Alternatively, if the dominant cation is split evenly between the octahedral and tetrahedral sites then the spinel is inverse (i.e. $8R^{3+}$ in A, $8R^{2+} + 8R^{3+}$ in B). Magnetite has an inverse structure, therefore its theoretical end member can be written as $Fe^{3+}(Fe^{2+}Fe^{3+})O_4$. It is important to note that magnetite will rarely, if ever, occur as its theoretical end member in natural systems. Hence, solid solutions between magnetite

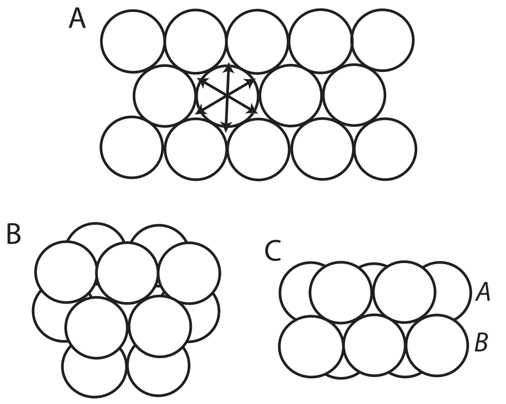

Figure 6.2: A. Example of a typical spinel structure for magnetite showing close packed layer of anions. The arrows indicate the directions and displacement necessary for an over layer to sit within the interstices. B. A piece of such a double layer created by a displacement of the second layer toward the top of the page. C. Side view of the bilayer with the planes designated A and B. After Clark (1972) and Waychunas (1991).

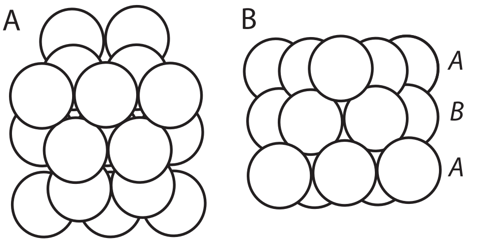

Figure 6.3: A. Example of a typical hematite structure showing hexagonal close packing created by adding a third layer with identical positioning to the first, creating an ABA sequence. Top view. B. Side view. After Waychunas (1991).

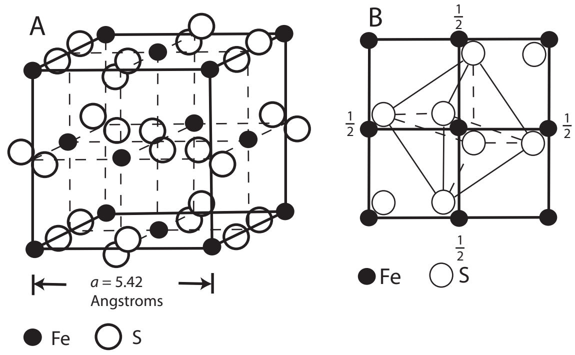

Figure 6.4: A. Structure of pyrite showing Fe atoms at the corners and face centres of the cube while S atoms are centred at the mid-points of the cube edges and at the cubes body centre. B. The projection of the pyrite structure on the (001) plane shows the octahedral coordination of Fe and S. Note each of the Fe atoms are surrounded by six S atoms. After Deer et al (1992)

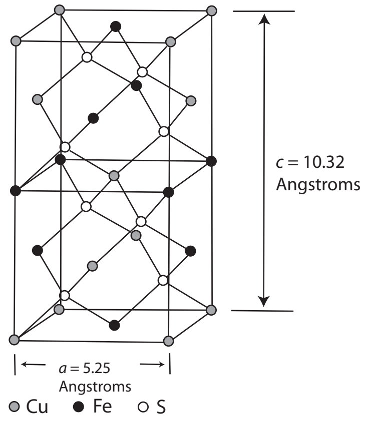

Figure 6.5: The crystal structure of chalcopyrite. Cu atoms are located on the face corners of the crystal structure, while four Fe atoms are located at the centre corners of the stacked cubic close packing structure. The open array of S atoms in chalcopyrite allows the accommodation of additional metal ions (e.g. $Cu_9Fe_8S_{16}$, $Cu_9Fe_9S_{16}$, $Cu_8Fe_{10}S_{16}$*). After Deer et al (1992).*

and other spinel or Fe oxide phases (e.g. hematite) will affect the partitioning of various trace elements into its crystal structure (Deer et al., 1992).

Hematite

'Pure' hematite has a trigonal (rhombohedral) oxide structure based on the HCP (Hexagonal Close Packing) oxygen-packing scheme (Fig. 6.3) (Deer et al., 1992). Trivalent cations occupy 2/3 of the octahedral interstices to produce A_2O_3-type stoichiometry. As a consequence, Fe in 'pure' hematite occurs predominantly in the trivalent state (cf. Frost, 1991; Waychunas, 1991). However, as described for magnetite, 'pure' hematite is a theoretical end member only, and solid solutions of magnetite-hematite and hematite-maghemite will greatly influence the partitioning of various trace elements into its crystal structure (Deer et al., 1992).

Pyrite

Pyrite (FeS_2) typically has a cubic crystal structure, where each iron atom is surrounded by six sulphur atoms in octahedral coordination, while each sulphur atom is of equal distance from three iron atoms which form a triangular planar group to the side (Fig. 6.4) (Deer et al., 1992). Elements other than Fe and S have been reported in pyrite including Cu, Pb, As and Zn; however, these reported cases commonly involve impurities within the pyrite crystal (e.g. Cu in chalcopyrite and Zn in sphalerite) (Deer et al., 1992; Huston et al., 1995). Other elements that may replace Fe in the crystal lattice include Mn, Co and Ni, while Se and Te will partition for S (Deer et al., 1992; Huston et al., 1995). Brodie (2001) also found As-Co-Ni- bearing pyrite grains associated with Cu-Au mineralisation at Ernest Henry (see below).

Chalcopyrite

Layers stacked in CCP arrangements as illustrated in figure 6.5 dominate the structure of chalcopyrite. Each metal atom occurs in a metal-sulphur tetrahedral coordination (Fig. 6.5), while each sulphur atom shares a similar coordination with metal cations (2Fe and 2Cu; Deer et al., 1992). Like pyrite, natural chalcopyrite deviates very little from its ideal composition $CuFeS_2$, where solid solution between chalcopyrite and sphalerite (containing a similar crystal structure) is rare. However, unlike pyrite, an abundance of minor and trace elements have been recorded in chalcopyrite and include Co, Ni, Mn, Zn and Sn substitution for Cu and Fe, and As and Se for S (Deer et al., 1992; Huston et al., 1995). In addition, Ag, Au, Pt, Pb, V, Cr, In, Al, Sb and Bi are also reported, but may occur as finely intergrown mineral inclusions rather than lattice-bound elements (Deer et al., 1992; Huston et al., 1995; Butler and Nesbit, 1999).

6.4. ANALYTICAL TECHNIQUES

6.4.1. Laser ablation ICP-MS

In total, approximately 500 single-grain trace element analyses of magnetite, hematite, pyrite and chalcopyrite were performed using a 266 μm quadrapole UV laser ablation microprobe coupled to an Agilent 7500s ICPMS at GEMOC, Macquarie University. Detailed descriptions of instrumentation and analytical and calibration procedures are given by Norman et al (1996). Operating conditions involved a pulse rate of 5 Hz and beam energy of ~0.5 mJ per pulse for magnetite, hematite, pyrite and chalcopyrite, producing a spatial resolution of ~30 μm.

A NIST 610 glass was used as the external calibration standard to obtain quantitative results of 33 trace elements for hematite and magnetite. The NIST 610 glass and a PGE-A (a doped quenched NiS bead) standard were used to calibrate for pyrite and chalcopyrite, with 41 trace elements (^{24}Mg, ^{27}Al, ^{29}Si, ^{45}Sc, ^{49}Ti, ^{51}V, ^{53}Cr, ^{55}Mn, ^{59}Co, ^{60}Ni, ^{65}Cu, ^{66}Zn, ^{71}Ga, ^{75}As, ^{82}Se, ^{89}Y, ^{90}Zr, ^{93}Nb, ^{95}Mo, ^{103}Rh, ^{107}Ag, ^{108}Pd, ^{111}Cd, ^{115}In, ^{118}Sn, ^{121}Sb, ^{139}La, ^{140}Ce, ^{146}Nd, ^{178}Hf, ^{182}W, ^{185}Re, ^{195}Pt, ^{197}Au, ^{208}Pb, ^{209}Bi, ^{232}Th and ^{238}U) measured in total. In similar studies, electron microprobe analyses of major and minor elements are commonly employed for calibration for LA-ICP-MS analyses. For magnetite, hematite, chalcopyrite and pyrite Fe and S were employed as internal standards as these elements exhibit very little solid solution relative to mineral counterparts (cf. Fleet et al., 1989; Deer et al., 1992). Fe values were used to normalise the NIST 610 external standard, while S was used to normalise the PGE-A external standard. Detection limits are typically *ca*. 0.1-1 ppm for most trace elements, but may reach up to hundreds of ppm for elements including V, As, Mg and Fe (Norman et al., 1996). Some elements including Ni, As, Se and Bi were analysed using both the NIST 610 and PGE-A external standards and gave similar results when compared. Elemental concentrations from the external standards remained consistent for all analyses in the dataset, with precision and accuracy of ±10% for Fe, Mn, V, Mn, As and Pb, and ±2 to 5 % for all remaining elements.

The NIST 610 standard and PGE-A standards (for chalcopyrite and pyrite) were analysed as an unknown at least once for each 15 mineral analyses. Each analysis takes approximately 3-4 minutes, and can be traced in real time using the Glitter program (van Achterburgh et al., 2001) and is separated into three parts. The first part typically consists of 40-60 seconds where the background is measured on pure Ar-He gas. The laser is then turned on and ablation starts, where the signal rapidly builds up and reaches a steady state. This portion of the signal is the one integrated, but if the sample shows zonation or impurities several parts can be selected and processed independently. Data was processed using the Glitter^{TM} program to eliminate contamination (e.g. inclusions of other phases) encountered across the depth profile of each laser-ablated area.

6.4.2. Discriminant analysis

The multivariate technique of stepwise discriminant analysis was used to statistically identify the main trace element associations within various Fe oxide-bearing systems in the EFB. Discriminant analysis is a powerful tool useful for classifying samples into pre-defined groups on the basis of multiple variables (Davis, 1986). Essentially, the aim is to identify which variables are most useful in discriminating between the groups. Concentrations of each element, grouped according to the associated mineral assemblage, are tested by one-way analysis of variance to determine whether the mean concentrations are different between mineral associations. This technique is particularly useful for large datasets with multiple independent variables (e.g. trace elements), where categorical dependant variables can be chosen to determine patterns and clusters in the dataset by producing new variables, called discriminant functions (Francis, 2001). Raw data transformations and a discriminant analysis were performed using the statistical package SPSS Version 11 (SPSS Inc, 2001).

In the discriminant models, a combination of linear variables (trace elements) is used to form a function for assigning cases to pre-defined groups. These groups (mineral associations) are shown in table 6.1, and are each allocated a representative number for the discriminant analysis. Each discriminant function is defined by a linear description that can be expressed as:

$$D = B_0 + B_1 X_1 + B_2 X_2 + \dots\dots B_n X_n \quad \text{................equation 1}$$

Groupings employed for discriminant analysis

Mineral associations			
Magnetite	*Pyrite*	*Hematite*	*Chalcopyrite*
1: Cu-Au mineralisation	1: Cu-Au mineralisation	1: Cu-Au mineralisation (EH only)	1: Cu-Au mineralisation
2: Na-Ca alteration	2: Na-Ca alteration	2: Barren Fe oxide-rich rocks	2: Na-Ca alteration
3: K-Fe alteration	3: Pre- / post- mineralisation (Ernest Henry)	3: Na-Ca alteration	3: cumulate magnetite (FC12)
4. Marble matrix breccia	4: Fe oxide rich rocks (FC12 and FC4NW)		4: Lightning Creek Cu-Au
5: Lightning Creek Cu-Au	5: Lightning creek Cu-Au		
6: Cumulate magnetite (FC12)			
7: Fe oxide-rich rock (metasomatic)			
8: metamorphic magnetite			
9: Slaughter Yard / Lightning Creek sills/granite			
10: Banded Fe oxide-rich rock (Starra, Osborne)			

Table 6.1: Table showing the pre-defined groups used in the discriminant analysis. Each group represent a different mineral association pre-defined from the dataset. The numbers beside each group are those used in the SPSS program and represent their respective group in the output tables (Tables 6.4, 6.7, 6.9, 6.11).

Where X_1, X_2….., X_p are the independent variables (trace elements) and B_0, B_1, B_2…, B_p are coefficients, chosen so that the value of the discriminant function, D, differs as much as possible between groups (cf. Grevenitz et al., 2003). A discriminant diagram can be constructed using the discriminant functions as axes, and the average of each group, called group centroids, are plotted as a representation of the group. The stepwise method was employed during the discriminant analysis, where all variables are used in order of discriminatory power to distinguish between groups. As such, the variables that contribute the least discriminatory power are sequentially removed from the dataset after each step of the analysis (SPSS Inc, 2001). For this study, all elements that were either below detection and/or exhibited highly erratic concentrations were discarded prior to the discriminant analysis.

6.5. MAGNETITE, HEMATITE, PYRITE AND CHALCOPYRITE TRACE ELEMENT GEOCHEMISTRY: BACKGROUND

For the purpose of this study, there are eight major factors that may control the partitioning of trace elements in minerals, and these include:

- Major element chemistry
- Mineral assemblage
- Degree of fluid-rock interaction
- Rock and fluid geochemistry
- Magma petrogenesis
- Redox
- Temperature
- Pressure

The significance of the first five factors on trace element partitioning can be largely characterized by petrochemical analysis of the minerals and host rocks. However, constraining the effects of the aforementioned intensive variables (fo_2, T and P) relies primarily on results of previously published work integrated with petrological data to fixed conditions of deposition (cf. Huston et al., 1995; Toplis and Corgne, 2002). The following section summarises previous work concerning the trace element chemistry of magnetite, hematite, pyrite and chalcopyrite.

6.5.1 Fe oxides (magnetite and hematite)

The trace element concentration of magnetite and hematite has been investigated using a variety of analytical techniques. Work during the 1960's analysed separate mineral grains using X-ray emission spectroscopy, although the sensitivity of these early techniques was stymied by detection limits several orders of magnitude higher (i.e. >1 ppm) than the more advanced analytical techniques of today (James and Dennen, 1962; Dasgupta, 1967 and Kisvarsanyi and Procter, 1967). This earlier work concentrated on various iron ore deposits, particularly in the U.S.A (e.g. Missouri) but despite the high detection limits associated with these analytical techniques, the workers still identified variations in some trace elements, especially V, Mg, Cu, Co, and Ti. Banvill (1998) and Nystrom and Henriquez (1994) used ICP-MS technology to investigate the trace element content of magnetite from the Osborne (Cu-Au) deposit, and Kiruna-type iron ores of Sweden and Chile, respectively. These instruments involved greater precision during analysis (±0.3 to 2 %) and allowed for a greater suite of elements to be analysed (e.g. V, Cr, Ti, Al, Mg, Mn, Ni, Co, Zn and Cu) than before. Very little work using LA-ICP-MS on hydrothermal magnetite or hematite is available in the literature, although more recent work by Muller et al (2003) provide preliminary data on magnetite geochemistry for the Kiirunavaara deposit using LA-ICP-MS. Due to the very low detection limits (0.001-1 ppm) provided by LA-ICP-MS, the nature and distribution of a greater suite of elements (e.g. Rb, Sr, Mo, Ag, Cd, Ba, Ce, Tl, Bi, Th and U) within minerals can be assessed.

Despite the various analytical techniques used in the aforementioned studies, certain patterns emerge which are consistent with the properties of major element substitution described above. For instance, many of these studies document variable concentrations of V and Cr, both of which substitute readily for Fe. Variations in V and Cr have been described by Banvill (1998) for different paragenetic stages of magnetite at the Osborne (Cu-Au) deposit, while Nystrom and Henriquez (1994) noted variations in V and Cr between Kiruna-type iron ore deposits in Chile and Sweden and the Bandurrias deposit in the Chilean iron belt (Chapter 5). Nystrom and Henriquez (1994) interpreted this variation to represent different depositional processes. Magnetite associated with the Kiruna iron ores in Sweden and Chile was thought to be magmatic, whereas magnetite from the Bandurrias deposit apparently formed from sedimentary-exhalative processes.

Other elements which appear to reside within the crystal lattice of both magnetite and hematite are Ti, Al, Mg, Mn, Ni, Co, Zn. Rb, Sr, Mo, Ag, Cd, Cu, Ba, Ce, Tl, Bi, Th and U. However, these elements were found to exhibit concentrations below detection using LA-ICP-MS. Other elements detected in magnetite and hematite had highly erratic concentrations that may correspond to their inability to substitute into the magnetite and hematite crystal lattice. Where the latter elements were identified, the studies suggest that they most likely are present as inclusions of other phases in magnetite and hematite (cf. Nystrom and Henriquez, 1994; Banvill, 1998; Muller et al., 2003).

6.5.2. Fe sulphides (pyrite and chalcopyrite)

The trace element concentrations of pyrite and chalcopyrite have also been investigated using a variety of analytical techniques. Roberts (1982) presents some of the earliest work found in the literature investigating the trace element chemistry of pyrite. That study used XRF analysis of pyrite separates from the Kangiara Region, eastern Australia and detected anomalous concentrations of Ti, Co and Ni. One of the more comprehensive studies on the trace element composition of pyrite and chalcopyrite was by Huston et al (1995) on various VHMS deposits from eastern Australia including Mount Chambers, Waterloo, Agincourt, Balcooma and Dry River South in Queensland, and Rosebery in Tasmania. Huston's work involved the application of the CSIRO-GEMOC Nuclear Proton Microprobe, which produced analyses with high spatial resolution and significantly lower detection limits (3-30 ppm) for a range of elements (e.g. Cu, Zn, Pb, Ba, Bi, Ag, Sb, As, Tl, Au, Mo, Co, In, Ni, Se and Te). Huston et al (1995) described 3 categories of trace elements, depending on how and where they reside within the pyrite and chalcopyrite crystal lattice. For example, they found that the elements which substituted into the crystal lattice of pyrite include Se and Te (for S), and Co and Ni (for Fe), while elements that substituted into chalcopyrite include Ag (for Cu), In, Sn and Zn (for Fe), and Se (for S). Huston et al (1995) define a second category that involved elements which occur mainly as inclusions representing other mineral phases. These elements include Cu, V, Zn (pyrite only), Pb, Ba, Bi, Ag (pyrite only) and Sb. The third category described by Huston et al (1995) represents elements detected in individual grains, but do not readily substitute into the crystal lattice (As, Tl, Au and Mo in pyrite) and are not associated with any other mineral.

However, as was the case for magnetite and hematite, very little other published work is currently available on the trace element composition of pyrite and chalcopyrite using LA-ICP-MS. Brodie (2001) analysed pyrite and chalcopyrite associated with Cu-Au mineralisation at the Ernest Henry deposit, and found Co, As, Se, Ag, Te and Cu in pyrite remained constant, while Au, Mo, Cd, Sb and Bi all exhibited spiking during ablation indicating either the presence of other inclusion phases bearing these phases or elemental zoning. Ulrich et al (2002) undertook ICP-OES solution analysis at the Mount Morgan Au-Cu deposit, Queensland and found high variations in As, V, Mo and Ni in pyrite and attributed this to different fluid composition and/or depositional processes. Butler and Nesbit (1999) also investigated the trace element content of chalcopyrite from deep-sea black smoker chimneys finding variable concentrations of V, Ag, In, Te, Ba, Au, Pb and U. Butler and Nesbit (1999) found consistent increases in Te, Ag and In adjacent to the chimney tip and suggested elevated temperature may increase the partitioning of these elements into chalcopyrite.

6.6. RESULTS

The diversity in hydrothermal mineral associations around the Ernest Henry (Cu-Au) deposit affords investigation of the affects of variation in mineral chemistry between Cu-Au mineralised and weakly mineralised / barren systems. Magnetite and pyrite are particularly useful as they occur in numerous alteration phases that formed pre-, syn- and post Cu-Au mineralisation. This section describes the trace element concentrations of magnetite, pyrite, chalcopyrite and hematite from various mineral assemblages throughout the EFB, with particular emphasis on alteration within and peripheral to the Ernest Henry (Cu-Au) system.

6.6.1. Magnetite

Trace element content and variation

Ernest Henry

The most abundant trace elements in magnetite at Ernest Henry are Ti, Si, Al, Mg, V, Cr, Mn, Co, Ni, Cu, Zn, Ga, Sn and Pb. Less commonly detected elements were As, Zr, Y, U, Hf, La, Ce, Bi, Sb, In, Mo, W and Sn; these were either close to or below the detection limit or exhibited considerable variation in content between analyses (cf. appendix 9). Mean, minimum and maximum values for each sample analysed are shown in table 6.2, and the spatial distribution of selected trace elements at the Ernest Henry ore-body is presented in figure 6.6. Zn, Mg, Si, Ti, Cr, Sn, V and Mn show considerable variation between magnetite from Cu-Au mineralisation and other pre- and post-mineralisation hydrothermal events (Fig. 6.6, 6.7). In general, Sn and Mn exhibit a stronger affinity for magnetite associated with Cu-Au mineralisation, while Cr, V, Ti, Mg, Si and Zn are typically higher in pre-ore magnetite. Al, Cu, Ga, Pb, Ni and Co show no significant difference in composition between Cu-Au mineralisation and pre-ore magnetite at Ernest Henry (Fig. 6.6, 6.7).

Other Fe oxide-rich systems

With the exception of Sc, all elements detected in magnetite from Ernest Henry are also present in the other Fe oxide systems investigated. Mean, minimum and maximum values from all analyses are shown in tables 6.3 and 6.4, and all LA-ICP-MS analyses are presented in appendix 9. Magnetite associated with ore also contains higher Mo, W and U. In comparison, these elements are relatively low or absent in magnetite derived from the most barren and some weakly mineralised mineral assemblages. Exceptions include magnetite derived from igneous processes (e.g. Fe oxide-rich rocks at FC12), weakly mineralised Na-Ca assemblages from FC4NW, FC12 and Ernest Henry and the barren Fe oxide-rich rocks from Starra and Osborne.

Magnetite associated with Cu-Au mineralisation typically contains lower concentrations of Ti, V and Cr compared to their weakly mineralised and barren counterparts. V exhibits the most significant separation in the dataset, where the deposits contain <1000 ppm (Fig. 6.8a, b) but the most weakly mineralised and barren mineral assemblages contain >1000 ppm. The barren Fe oxide-rich rocks hosting Cu-Au mineralisation at Osborne and Starra and the marble matrix breccia stage in the footwall at Ernest Henry also exhibit low V. Similar signatures are also observed at the Lightning Creek Cu-Au occurrence where Cu-Au bearing veins contain significantly lower V compared to magnetite within the Fe-rich sills and granites. Mt Elliott magnetite contains significantly lower Ga (<10 ppm) and higher Ti compared to the other deposits (Fig. 6.8a, d). Osborne magnetite contains higher Ti and lower Cr compared to the other deposits (Fig. 6.8b). Elements that are distinctly higher in magnetite from Cu-Au mineralised systems include Sc and Mn (Fig. 6.8f, h). In particular, magnetite in Cu-Au mineralisation at Ernest Henry is defined by two distinct Mn populations. One

Table 6.2: Mean, minimum and maximum values of the trace element content of magnetite from the Ernest Henry Cu-Au deposit (in ppm). Sample location numbers are presented in appendix 9. Sample type refers to whether the rock is Cu-Au mineralised (M) or weakly mineralised (W). Also shown is the number of analyses taken for each sample. The hyphen represents analyses that are below the detection limit..

Sample No	Sample Type	No of Analyses		Mg	Al	Si	Sc	Ti	V	Cr	Mn	Co	Ni	Cu	Zn	Ga
FT8C	M	5	Min	33.83	153.03	431.78	-	44.47	93.55	-	1185.07	0.903	47.03	2.75	6.64	25.5
			Mean	***138.12***	***260.58***	***676.56***	***-***	***74.77***	***192.27***	***-***	***1970.99***	***1.92***	***62.30***	***7.46***	***12.52***	***29.28***
			Max	495.37	655.4	1332.51	-	181.07	240.84	-	2481.05	5.59	101.65	13.77	19.83	32.47
EH201B	M	6	Min	35.74	173.15	396.98	1.414	131.3	176.61	-	2777.16	1.184	29.82	2.14	13.51	21.22
			Mean	***672.44***	***783.60***	***1727.91***	***2.40***	***208.71***	***219.67***	***-***	***3884.69***	***20.57***	***49.62***	***6.16***	***18.88***	***26.47***
			Max	2291.59	2257.29	4953.65	3.5	271.1	281.91	-	5026.12	34.88	77.14	16.6	28.88	32.03
FT8A	M	5	Min	27.28	206.55	248.36	3.15	124.17	570.31	2.81	450.75	129.53	87.66	5.03	15.7	32.67
			Mean	***42.18***	***216.12***	***759.86***	***6.03***	***243.77***	***607.73***	***10.30***	***729.99***	***163.61***	***91.35***	***23.63***	***29.03***	***37.89***
			Max	59.82	227.17	1343.76	7.61	316.5	655.34	16.42	845.46	197.32	97.98	47.05	71.3	45.64
EH201C	M	6	Min	27.85	208.02	407.96	1.57	289.02	62.79	0.87	257.09	1.85	6.58	0.55	6.92	25.28
			Mean	***168.97***	***364.33***	***760.22***	***1.81***	***409.09***	***64.57***	***1.55***	***434.42***	***7.47***	***9.87***	***6.71***	***14.69***	***30.37***
			Max	507.37	672.85	1350.25	2.13	654.28	66.82	2.69	642.12	17.99	12.27	15.93	20.21	33.27
EH184D	M	5	Min	21.11	223.76	403.4	2.27	85.63	191.19	2.63	231.72	63.14	80.68	11.12	8.75	17.23
			Mean	***32.66***	***286.78***	***1069.15***	***2.55***	***135.30***	***199.67***	***4.15***	***336.36***	***77.42***	***88.13***	***26.99***	***11.24***	***18.80***
			Max	65.87	456.75	2457.85	2.76	255.94	218.96	6.53	422.73	97.53	95.27	45.97	13.96	21.05
EH09	M	10	Min	26.69	244.19	513.61	1.83	233.63	452.72	1.26	3033.33	1.08	98.16	0.151	28.51	20.07
			Mean	***47.25***	***649.51***	***1272.14***	***2.25***	***306.27***	***504.97***	***7.20***	***4496.50***	***4.87***	***155.84***	***2.40***	***34.13***	***25.94***
			Max	100.09	4009.48	6327.72	3.04	425.3	552.86	28.42	6065.34	7.78	204.56	6.09	49.78	30.05
EH10	M	8	Min	153.01	266.19	509.62	0.38	262.83	294.65	5.62	807.13	8.22	11.48	0.41	17.53	10.34
			Mean	***1620.47***	***1232.47***	***3941.52***	***0.73***	***453.55***	***463.52***	***43.26***	***1401.39***	***13.79***	***22.76***	***104.85***	***30.30***	***13.07***
			Max	6383.24	5395.04	13500.88	1.76	646.41	676.66	149.31	2853.57	27.35	62.37	567.8	45.39	15.99
EH235	W	7	Min	89.51	482.81	1887.94	1.77	448.49	3561.99	42.11	503.17	111.05	285.02	3.02	40.07	50.23
			Mean	***480.70***	***812.61***	***4456.26***	***3.36***	***1947.17***	***3944.96***	***117.64***	***579.33***	***128.10***	***330.25***	***731.07***	***454.78***	***62.66***
			Max	1266.01	1308.34	7084.02	7.85	6826.71	4753.06	209.67	690.97	145.25	365.59	3956.74	1127.48	86.02
FT021A	W	7	Min	153.01	266.19	509.62	0.38	262.83	294.65	5.62	807.13	8.22	11.48	0.41	17.53	10.34
			Mean	***37.70***	***426.55***	***532.45***	***3.28***	***285.02***	***474.44***	***5.15***	***1183.50***	***6.47***	***51.49***	***1.74***	***84.70***	***47.68***
			Max	6383.24	5395.04	13500.88	1.76	646.41	676.66	149.31	2853.57	27.35	62.37	567.8	45.39	15.99
FT94C	W	6	Min	46.02	265.11	584.37	0.261	106.78	2027.14	8.92	495.04	11.89	130.75	0.94	71.66	26.95
			Mean	***86.80***	***507.54***	***2242.27***	***0.54***	***2749.71***	***2153.29***	***23.45***	***876.72***	***38.86***	***144.17***	***2.53***	***88.13***	***30.79***
			Max	148.8	790.89	6361.83	1.04	9015.15	2309.84	50.52	1995.53	54.2	157.61	5.34	107.01	34.02
EH223B	W	6	Min	64.95	1436.53	430.3	2.69	1121.73	2075.09	37.98	383.21	39.34	83.8	0.166	35.29	41.86
			Mean	***139.44***	***1576.65***	***685.11***	***3.58***	***1712.78***	***2139.36***	***56.99***	***463.63***	***51.32***	***89.15***	***0.60***	***54.33***	***44.66***
			Max	218.48	1901.6	978.98	4.89	2175.31	2232.17	93.67	549.81	60.3	93.64	1.99	67.9	48.41
FT94B	W	4	Min	47.04	120.72	504.9	0.678	136.14	1728.18	33.16	101.18	30.05	84.28	0.86	6.86	16.92
			Mean	***553.27***	***526.18***	***1491.18***	***1.19***	***263.91***	***1791.19***	***34.10***	***129.24***	***34.69***	***91.33***	***1.72***	***9.17***	***18.51***
			Max	1975.7	1646.15	4090.13	2.41	547.83	1905.4	35.38	144.26	38.13	97.07	3.3	13.82	22.07
EH223A	W	5	Min	77.93	1035.57	480.06	1.95	335.94	1350.24	3.48	520.58	33	61.67	1.52	52.87	26.39
			Mean	***182.90***	***1199.91***	***889.42***	***3.34***	***458.58***	***1562.23***	***21.99***	***742.27***	***38.57***	***78.12***	***2.07***	***68.04***	***30.25***
			Max	344.19	1458.11	1631.4	5.87	532.08	1751.03	40.49	938.28	44.15	87.15	2.79	90.02	32.83
FT4A	W	6	Min	43.82	316.75	505.5	1.18	295.09	331.67	2.75	1406.03	0.563	35.62	0.22	26.86	28.16
			Mean	***57.14***	***404.68***	***1235.62***	***1.44***	***418.24***	***424.11***	***4.58***	***1633.11***	***3.09***	***46.31***	***1.83***	***32.91***	***29.30***
			Max	66.6	479.09	4141.33	1.76	563.77	593.8	9.08	1838.24	8.75	55.49	7.62	36.32	31.77
EH201A	W	6	Min	63.27	476.75	348.46	1.27	445.24	550.76	4.32	517.9	4.18	31.03	0.54	38.96	37.85
			Mean	***85.89***	***697.97***	***935.74***	***1.62***	***543.34***	***635.69***	***9.86***	***796.64***	***9.11***	***41.61***	***14.64***	***112.07***	***39.23***
			Max	122.75	1084	2037.8	2.63	643.3	773.99	20.76	1058.48	18.59	62.68	73.58	369.47	41.45
EH184B	W	5	Min	58.72	212.8	692.82	2.43	71.33	572.13	2.27	419.43	20.72	130.76	1.09	24.37	30.76
			Mean	***253.51***	***519.17***	***1864.54***	***4.07***	***235.76***	***639.83***	***5.91***	***584.63***	***22.89***	***143.98***	***11.00***	***36.29***	***32.00***
			Max	586.53	777.94	2925.51	6.61	778.41	752.98	14.89	786.86	24.69	167.08	34.03	46.44	34.71
FT8B	W	5	Min	74.87	189.58	472.66	0.075	286.21	288.73	1.24	1040.45	0.64	27.08	4.3	32.05	20.64
			Mean	***183.53***	***259.37***	***625.51***	***0.11***	***342.51***	***389.96***	***9.54***	***1249.48***	***1.29***	***71.25***	***109.87***	***50.39***	***28.68***
			Max	517.66	413.87	1004.64	0.171	415.65	522.22	31.05	1449.1	2.39	136.82	310.74	81.07	33.12

Sample No	Sample Type	No of Analyses		As	Y	Zr	Mo	In	Sn	Sb	La	Ce	Hf	W	Pb	Bi	Th	U
FT8C	M	5	Min	2.78	0.01	0.02	0.41	0.02	0.71	2.57	0.03	0.02	0.03	0.05	0.33	0.06	0.02	0.03
			Mean	***3.19***	***0.05***	***0.19***	***4.35***	***0.02***	***1.55***	***2.83***	***1.87***	***1.16***	***0.03***	***1.29***	***1.29***	***0.17***	***0.03***	***0.53***
			Max	3.59	0.14	0.45	19.41	0.02	3.96	3.09	6.06	4.73	0.04	5.33	3.44	0.28	0.04	1.27
EH201B	M	6	Min	2.41	0.03	0.08	0.66	0.01	1.11	0.35	0.20	0.12	0.04	7.10	0.55	0.05	0.03	0.55
			Mean	***4.72***	***0.26***	***0.65***	***1.06***	***0.09***	***8.84***	***4.79***	***1.27***	***0.88***	***0.06***	***20.35***	***2.18***	***0.06***	***0.11***	***2.63***
			Max	8.49	0.49	1.71	2.18	0.25	24.12	11.69	2.90	1.71	0.09	36.87	4.43	0.06	0.29	5.36
FT8A	M	5	Min	4.10	0.01	0.20	0.13	0.02	0.72	0.16	0.04	0.02	-	0.10	1.27	0.48	0.03	0.07
			Mean	***76.73***	***0.58***	***4.36***	***23.81***	***0.61***	***1.52***	***0.64***	***0.10***	***0.11***	-	***7.76***	***5.42***	***0.48***	***0.05***	***1.64***
			Max	330.27	1.68	8.52	115.59	1.20	2.48	1.55	0.15	0.26	-	15.43	9.94	0.48	0.07	7.03
EH201C	M	6	Min	3.83	0.01	0.06	0.07	0.02	1.54	0.18	0.05	0.06	0.03	0.44	0.32	0.05	0.06	0.05
			Mean	***20.23***	***0.40***	***4.47***	***0.28***	***0.05***	***2.79***	***1.70***	***1.90***	***1.47***	***0.20***	***14.30***	***1.15***	***0.42***	***0.70***	***0.98***
			Max	64.78	1.17	15.01	0.63	0.11	4.72	4.45	6.79	4.73	0.38	60.52	2.89	1.56	1.85	3.06
EH184D	M	5	Min	1.51	0.04	0.29	0.60	0.02	0.45	0.31	0.94	0.92	0.07	1.52	0.10	0.03	0.06	0.25
			Mean	***2.82***	***0.16***	***5.35***	***7.59***	***1.56***	***2.35***	***0.90***	***1.63***	***1.69***	***0.25***	***11.89***	***0.49***	***0.05***	***0.28***	***4.45***
			Max	4.64	0.29	20.03	30.97	4.64	6.14	2.39	2.85	2.80	0.47	23.33	1.31	0.09	0.74	16.48
EH09	M	10	Min	2.09	0.01	0.02	0.71	0.01	2.42	0.40	0.01	0.01	0.00	0.03	0.80	0.01	0.00	0.01
			Mean	***2.61***	***1.34***	***0.20***	***0.89***	***0.04***	***3.77***	***1.53***	***2.07***	***1.75***	***0.06***	***9.72***	***10.58***	***0.02***	***0.03***	***0.24***
			Max	3.13	7.06	0.52	1.09	0.08	7.54	4.37	11.99	10.95	0.20	81.15	30.77	0.03	0.10	1.08
EH10	M	8	Min	1.12	0.10	0.08	0.05	0.02	1.44	0.27	0.01	0.07	0.00	0.02	2.10	0.02	0.01	0.02
			Mean	***10.22***	***0.89***	***1.18***	***18.31***	***0.05***	***2.75***	***2.82***	***0.93***	***0.95***	***0.09***	***6.50***	***28.04***	***3.50***	***0.27***	***0.28***
			Max	45.08	4.91	4.01	133.68	0.15	4.67	5.99	5.98	4.54	0.28	43.71	77.51	16.10	1.09	0.60
EH235	W	7	Min	9.28	0.25	0.11	2.60	0.63	1.32	0.42	0.13	0.97	0.19	0.88	2.23	0.37	0.22	0.07
			Mean	***11.12***	***3.15***	***7.80***	***2.80***	***1.63***	***3.09***	***4.42***	***0.82***	***2.62***	***1.01***	***4.16***	***3.73***	***2.19***	***0.44***	***2.04***
			Max	12.95	12.81	25.78	3.00	3.25	3.84	11.25	1.94	3.79	1.75	13.15	6.12	8.00	0.97	4.60
FT021A	W	7	Min	1.12	0.10	0.08	0.05	0.02	1.44	0.27	0.01	0.07	0.00	0.02	2.10	0.02	0.01	0.02
			Mean	***2.82***	***0.06***	***2.69***	***0.39***	***0.31***	***1.68***	***1.30***	***2.26***	***0.05***	***0.69***	***0.94***	***3.48***	***0.46***	***0.19***	***0.64***
			Max	45.08	4.91	4.01	133.68	0.15	4.67	5.99	5.98	4.54	0.28	43.71	77.51	16.10	1.09	0.60
FT94C	W	6	Min	2.15	0.05	0.04	0.12	0.03	0.15	0.12	0.04	0.01	0.03	0.19	0.38	0.03	0.03	0.02
			Mean	***4.05***	***6.21***	***0.36***	***0.24***	***0.05***	***1.45***	***0.32***	***0.18***	***0.75***	***0.09***	***1.16***	***0.88***	***0.10***	***0.11***	***1.34***
			Max	5.51	25.50	0.94	0.43	0.08	3.30	0.58	0.32	1.31	0.16	2.85	2.67	0.18	0.17	6.43
EH223B	W	6	Min	2.58	0.02	0.02	0.09	0.01	1.38	0.13	0.04	0.01	0.04	0.26	0.10	0.05	0.03	0.02
			Mean	***3.63***	***0.05***	***1.64***	***0.16***	***0.03***	***1.63***	***0.62***	***0.08***	***0.05***	***0.16***	***0.43***	***0.44***	***0.34***	***0.19***	***0.21***
			Max	4.93	0.09	6.26	0.33	0.05	2.15	1.78	0.16	0.10	0.29	0.93	1.28	1.10	0.50	0.67
FT94B	W	4	Min	4.88	0.03	0.04	0.05	0.03	0.32	0.13	0.07	0.02	0.02	0.08	0.49	0.04	0.09	0.21
			Mean	***4.88***	***0.09***	***0.26***	***0.05***	***0.17***	***0.40***	***0.13***	***0.07***	***0.11***	***0.03***	***0.16***	***0.86***	***0.04***	***0.09***	***0.62***
			Max	4.88	0.26	0.69	0.05	0.30	0.54	0.13	0.07	0.19	0.04	0.31	1.31	0.04	0.09	1.15
EH223A	W	5	Min	3.46	0.06	0.02	0.16	0.01	0.67	0.17	0.02	0.06	-	0.11	0.11	0.09	0.02	0.02
			Mean	***3.95***	***0.18***	***0.03***	***0.23***	***0.07***	***0.79***	***0.23***	***0.23***	***0.27***	-	***0.36***	***0.27***	***0.15***	***0.03***	***0.03***
			Max	4.44	0.37	0.03	0.35	0.15	0.86	0.33	0.70	0.71	-	0.62	0.43	0.31	0.04	0.03
FT4A	W	6	Min	1.62	0.01	0.02	0.18	0.02	0.87	2.09	0.07	0.02	0.43	5.93	0.09	0.05	0.03	0.05
			Mean	***1.62***	***0.12***	***8.05***	***4.62***	***0.15***	***1.11***	***2.09***	***0.20***	***0.12***	***0.43***	***5.93***	***0.31***	***0.05***	***0.03***	***0.12***
			Max	1.62	0.20	16.07	26.02	0.54	1.26	2.09	0.28	0.30	0.43	5.93	0.65	0.05	0.03	0.18
EH201A	W	6	Min	3.98	0.02	1.55	0.08	0.03	0.76	0.23	0.01	0.02	0.05	0.16	0.22	0.07	0.02	0.01
			Mean	***7.27***	***0.07***	***3.44***	***0.84***	***1.45***	***1.19***	***1.68***	***0.24***	***0.25***	***0.06***	***1.61***	***1.84***	***0.84***	***0.06***	***0.05***
			Max	10.99	0.16	5.33	2.74	6.05	1.81	5.55	0.62	0.72	0.06	5.07	4.84	3.13	0.16	0.10
EH184B	W	5	Min	3.06	0.07	0.04	0.09	0.01	0.22	0.18	0.05	0.01	-	-	0.18	0.07	0.04	0.05
			Mean	***4.14***	***1.93***	***0.14***	***0.18***	***0.02***	***0.84***	***0.46***	***0.42***	***0.50***	-	-	***0.78***	***0.18***	***0.04***	***0.46***
			Max	5.21	6.91	0.33	0.37	0.02	2.18	0.84	1.41	2.07	-	-	1.61	0.37	0.04	1.20
FT8B	W	5	Min	2.37	0.01	0.07	0.16	0.03	0.59	0.15	0.01	0.03	0.01	0.11	0.05	0.03	0.02	0.15
			Mean	***2.85***	***0.13***	***2.38***	***0.21***	***0.36***	***0.61***	***0.44***	***0.11***	***0.21***	***0.09***	***2.05***	***0.16***	***0.04***	***0.19***	***0.39***
			Max	3.81	0.43	9.21	0.25	1.08	0.64	1.00	0.42	0.57	0.19	5.14	0.30	0.04	0.47	0.63

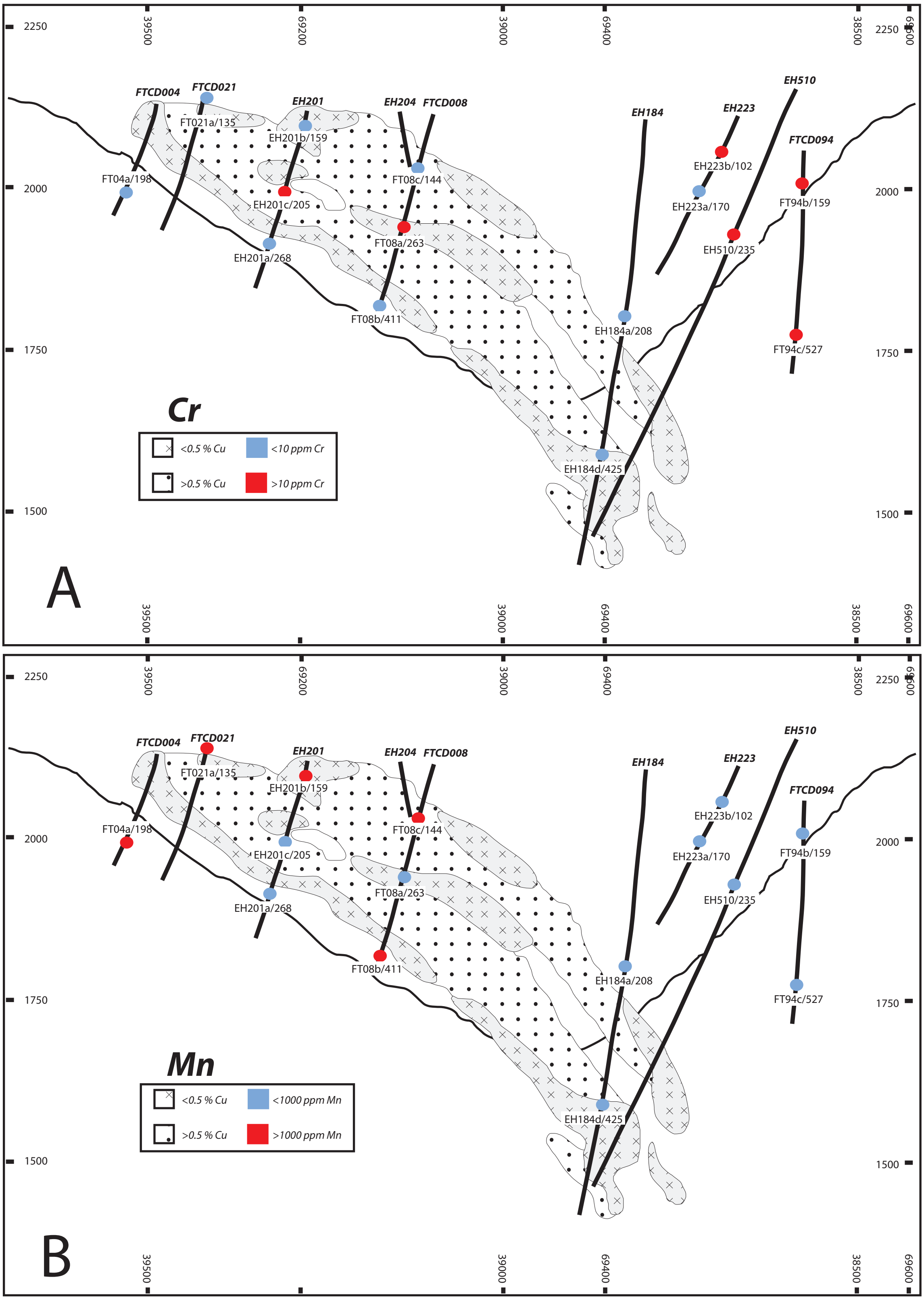

Figure 6.6a and b: Cr and Mn content of magnetite annotated on a crossection of the Ernest Henry ore body looking north, with drill hole traces and location of samples used for this study. Trace element values of magnetite are averaged equivalents of individual analyses from each sample. Standard deviations of these values are given in Appendix 9. The values are divided into categories of low and high, represented as coloured circles (blue=low and red=high).

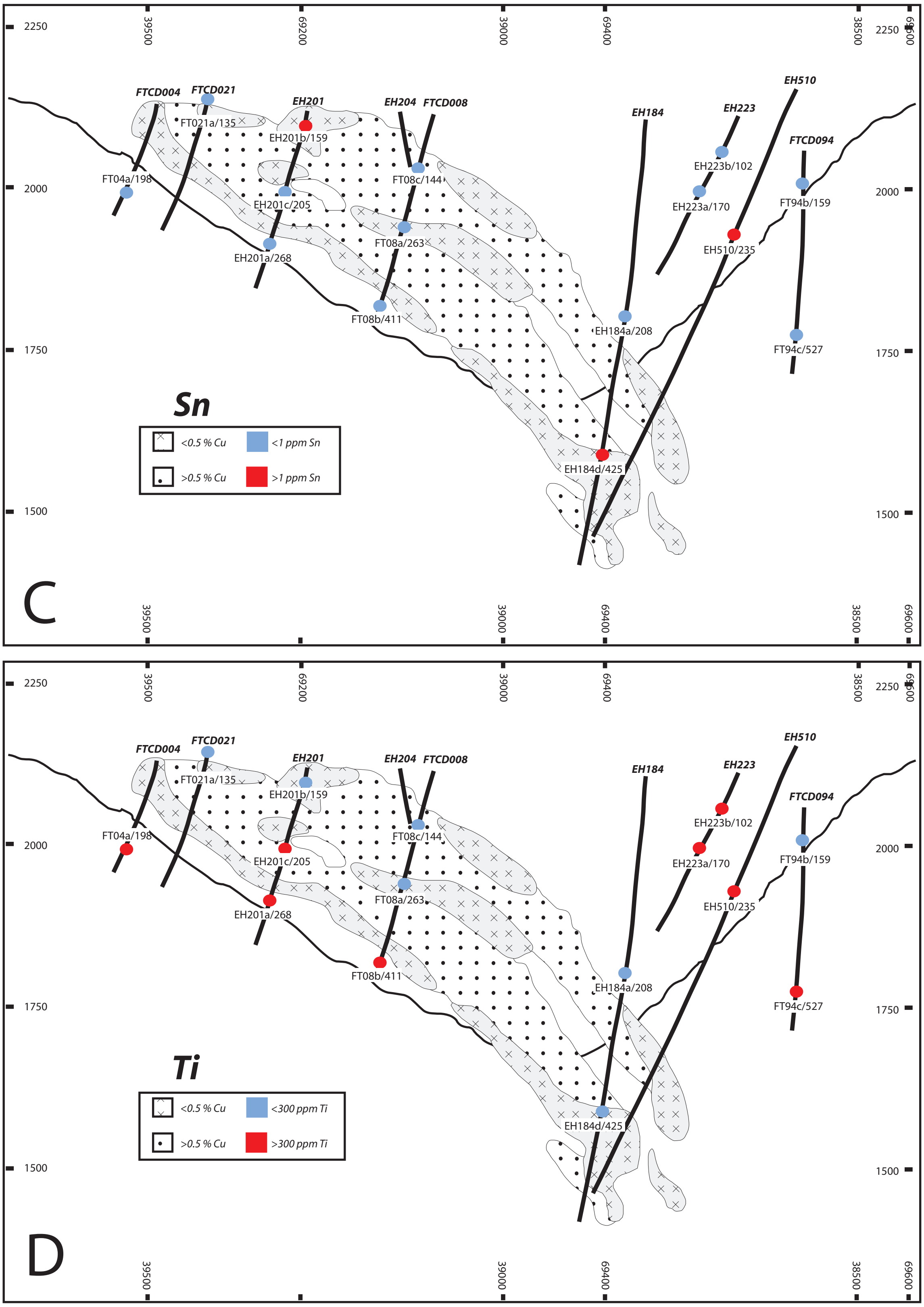

Figure 6.6c and d: Sn and Ti content of magnetite annotated on a crossection of the Ernest Henry ore body looking north, with drill hole traces and location of samples used for this study. Trace element values of magnetite are averaged equivalents of individual analyses from each sample. Standard deviations of these values are given in Appendix 9. The values are divided into categories of low and high, represented as coloured circles (blue=low and red=high).

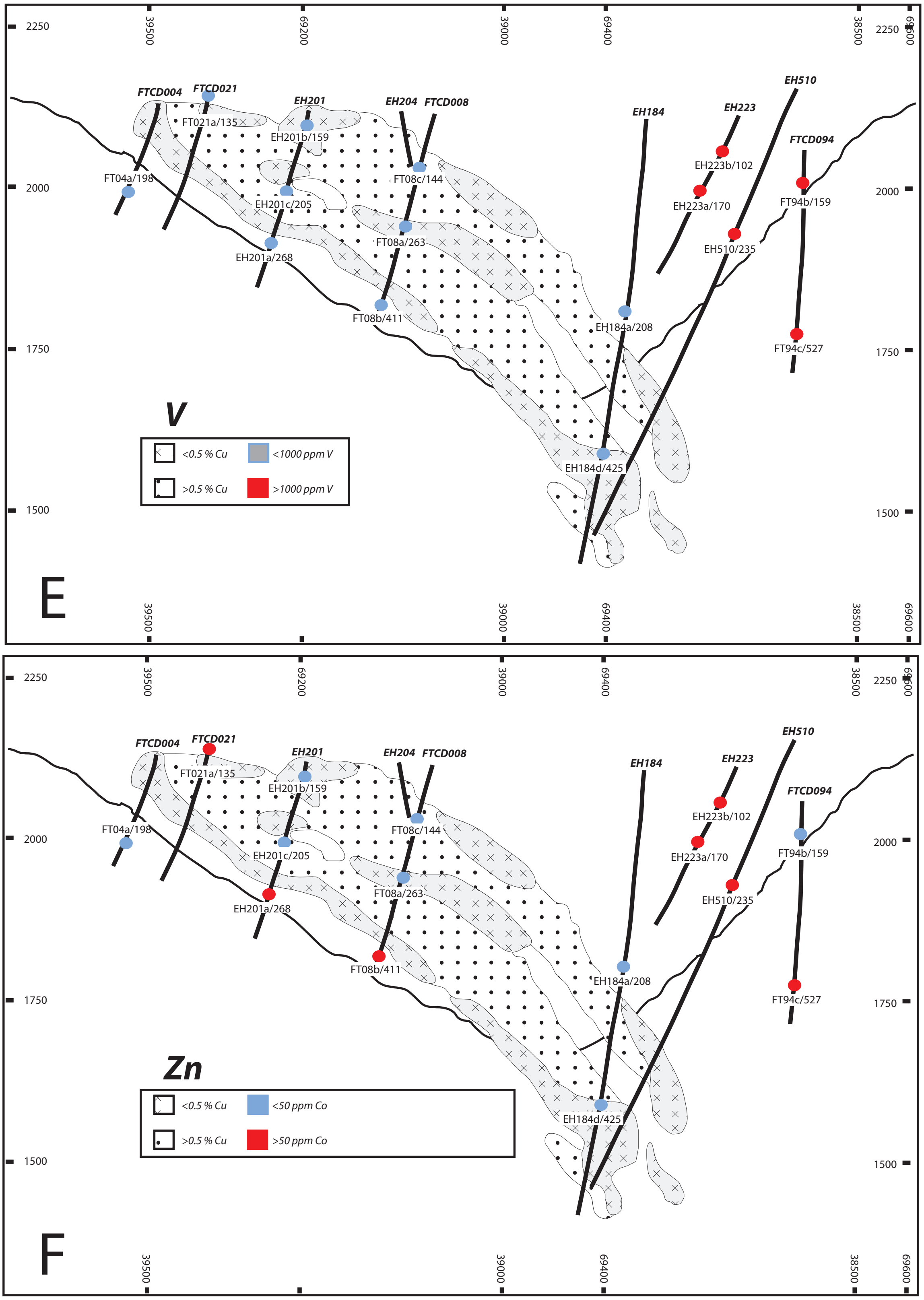

Figure 6.6e and f: V and Zn content of magnetite annotated on a crossection of the Ernest Henry ore body looking north, with drill hole traces and location of samples used for this study. Trace element values of magnetite are averaged equivalents of individual analyses from each sample. Standard deviations of these values are given in Appendix 9. The values are divided into categories of low and high, represented as coloured circles (blue=low and red=high).

Figure 6.7: Bi-plots of trace elements identified in magnetite from the Ernest Henry (Cu-Au) system. Various alteration phases include: Cu-Au mineralisation (yellow), Na-Ca alteration (green), K-Fe alteration (blue) and marble matrix breccia (grey).

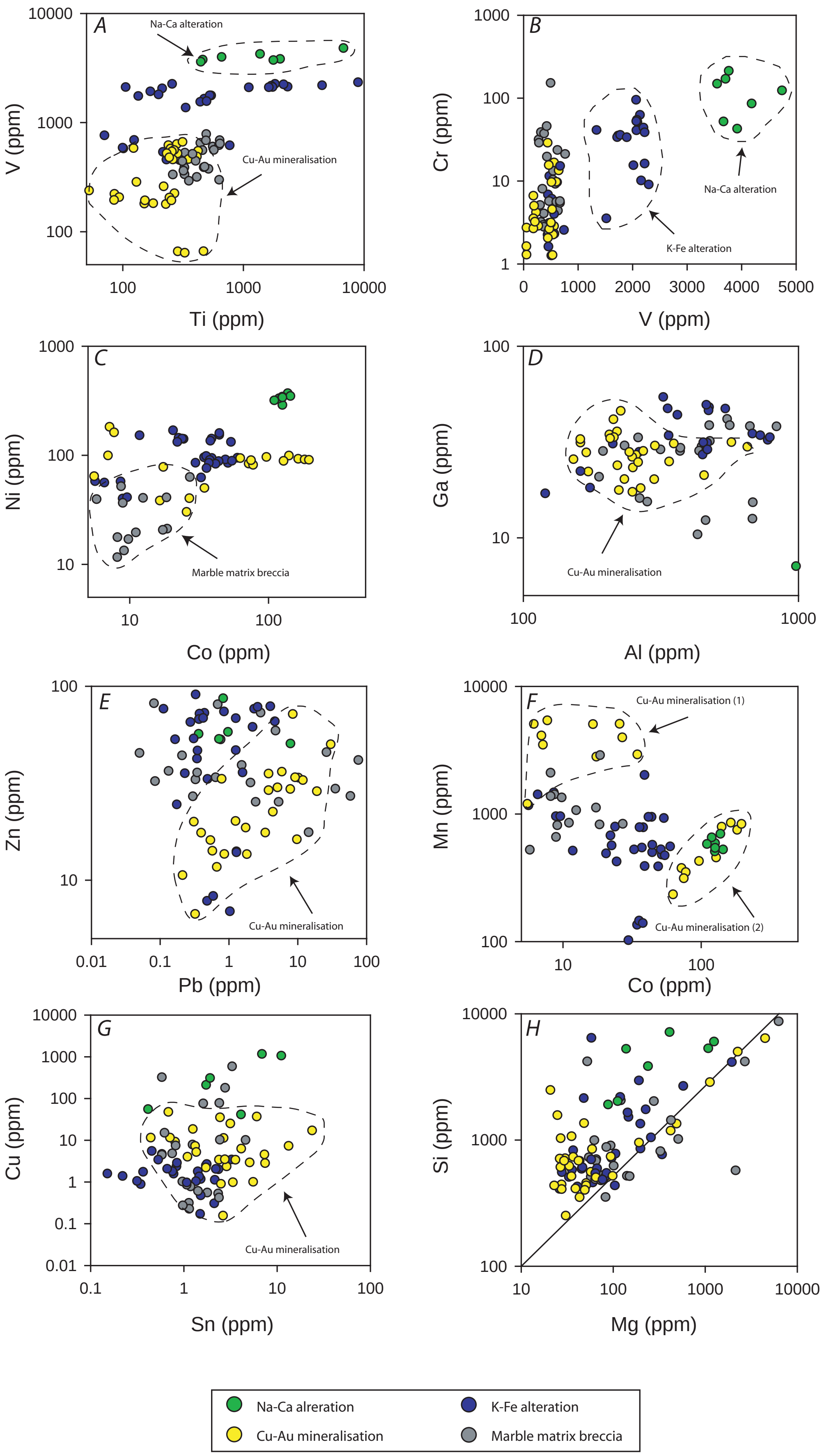
A
Na-Ca alteration
Cu-Au mineralisation
V (ppm)
Ti (ppm)
10000
1000
100
100
1000
10000
B
Na-Ca alteration
K-Fe alteration
Cr (ppm)
V (ppm)
1000
100
10
1
0
1000
2000
3000
4000
5000
C
Marble matrix breccia
Ni (ppm)
Co (ppm)
1000
100
10
10
100
D
Cu-Au mineralisation
Ga (ppm)
Al (ppm)
100
10
100
1000
E
Cu-Au mineralisation
Zn (ppm)
Pb (ppm)
100
10
0.01
0.1
1
10
100
F
Cu-Au mineralisation (1)
Cu-Au mineralisation (2)
Mn (ppm)
Co (ppm)
10000
1000
100
10
100
G
Cu-Au mineralisation
Cu (ppm)
Sn (ppm)
10000
1000
100
10
1
0.1
0.01
0.1
1
10
100
H
Si (ppm)
Mg (ppm)
10000
1000
100
10
100
1000
10000
● Na-Ca alreration
● K-Fe alteration
● Cu-Au mineralisation
● Marble matrix breccia

Table 6.3: Mean, minimum and maximum values of the trace element content of magnetite from various Cu-Au mineralised and weakly mineralised Fe oxide-rich systems in the EFB (in ppm). Sample location numbers are presented in appendix 9. Sample type refers to whether the rock is Cu-Au mineralised (M) or weakly mineralised (W). Also shown is the number of analyses taken for each sample. The hyphen represents analyses that are below the detection limit.

Sample No	Sample Type	No of Analyses		Mg	Al	Si	Sc	Ti	V	Cr	Mn	Co	Ni	Cu	Zn	Ga
ST1	M	3	Min	165.0	844.5	2658.7	6.5	-	86.8	-	146.1	25.5	43.0	118.9	-	32.6
			Mean	***343.61***	***869.68***	***4620.24***	***7.45***	***13.55***	***98.15***	-	***155.44***	***45.93***	***67.72***	***269.93***	-	***48.21***
			Max	198.1	917.6	6581.8	9.0	-	109.5	-	166.8	66.4	101.2	287.4	-	68.1
OS1	M	8	Min	378.9	838.3	1700.7	11.4	13.2	191.0	9.6	229.8	14.4	41.3	14.7	34.1	35.1
			Mean	***303.19***	***2382.42***	***2317.14***	***12.87***	***22.47***	***164.25***	***10.26***	***215.53***	***83.96***	***45.98***	***309.94***	***961.99***	***29.76***
			Max	681.9	4622.8	4872.0	21.2	57.8	359.5	14.3	564.3	190.3	163.0	1609.8	18286.8	67.9
ME	M	7	Min	149.09	151.2	1382.69	0.276	10.4	1.2	1.07	386.96	3.53	31.63	5.65	32.86	6.08
			Mean	***719.07***	***566.73***	***4396.41***	***0.28***	***122.01***	***248.30***	***12.04***	***514.01***	***43.80***	***51.80***	***282.39***	***74.06***	***6.89***
			Max	1746.7	1163.4	6904.4	0.291	231.8	642.48	47.91	689.25	277.19	86.3	815.3	108.69	8.33
291	W	6	Min	217.3	6021.8	1551.0	10.1	1394.3	2262.0	62.4	266.6	16.9	47.1	65.1	114.2	64.9
			Mean	***1570.42***	***7731.54***	***3448.36***	***21.14***	***3773.97***	***2489.12***	***76.41***	***562.36***	***83.25***	***94.64***	***755.32***	***921.00***	***94.65***
			Max	3039.52	9318.9	5982.2	46.8	11370.7	2852.3	92.3	1339.1	212.3	145.8	3254.5	1983.9	152.7
262	W	9	Min	116.75	554.8	2221.3	3.5	32.9	703.2	26.1	238.2	5.5	7.7	26.8	21.7	5.4
			Mean	***630.77***	***2232.48***	***3912.70***	***4.12***	***798.36***	***1093.86***	***35.28***	***274.67***	***37.02***	***29.88***	***1801.66***	***1944.57***	***10.24***
			Max	1527.7	3140.9	6102.2	5.0	5624.5	1536.3	44.5	338.8	94.2	57.0	7125.3	7622.8	15.5
204	W	4	Min	981.76	3201.2	1736.0	2.7	1703.6	1616.8	-	632.6	17.4	134.3	99.1	336.2	73.8
			Mean	***1128.72***	***3554.87***	***4334.22***	***3.40***	***2058.96***	***1924.57***	-	***689.67***	***100.00***	***173.93***	***345.69***	***8182.53***	***86.04***
			Max	1365.02	3975.8	6535.2	4.0	2612.5	2071.2	-	774.3	257.1	207.2	757.1	25457.8	110.6
168	W	5	Min	506.56	3301.0	861.9	-	1261.7	1386.1	9.6	334.3	65.3	72.4	8.4	215.0	47.6
			Mean	***736.35***	***3543.23***	***1872.46***	-	***1886.40***	***1564.64***	***17.12***	***448.93***	***78.44***	***91.21***	***48.27***	***946.29***	***52.92***
			Max	1027.66	3773.8	3343.8	-	2800.4	1854.4	22.6	556.8	90.6	112.5	119.6	2968.5	60.1
312	W	2	Min	415.95	322.7	1761.4	-	30.3	2.3	-	278.6	11.9	65.3	-	1488.2	16.4
			Mean	***534.08***	***1264.46***	***2782.78***	-	***520.74***	***77.47***	-	***359.30***	***13.17***	***208.20***	***81.80***	***1755.45***	***17.38***
			Max	652.21	2206.2	3804.2	-	1011.2	152.6	-	440.0	14.5	351.1	-	2022.7	18.4
222	W	6	Min	139.91	623.4	1592.5	0.8	172.5	1258.4	7.1	111.0	13.8	332.8	5.3	12.5	26.7
			Mean	***1804.60***	***1676.79***	***4471.95***	***2.62***	***443.32***	***1596.71***	***14.36***	***153.68***	***15.19***	***395.01***	***41.02***	***91.46***	***31.11***
			Max	5198.37	4335.5	9702.8	4.5	666.1	1947.0	32.5	240.4	17.8	480.7	94.7	233.3	33.1
161	W	3	Min	286.38	3522.5	3296.5	3.9	1304.9	1280.9	56.3	757.5	41.9	77.1	41.0	43.8	60.9
			Mean	***476.63***	***4043.63***	***3878.53***	***5.63***	***1523.97***	***1434.73***	***107.11***	***797.83***	***45.18***	***88.32***	***1283.71***	***1920.47***	***66.00***
			Max	839.51	4412.4	4451.9	7.2	1846.2	1721.3	194.7	830.9	50.5	97.2	3733.6	5549.5	69.9
254	W	10	Min	74.43	891.6	589.5	1.5	583.4	2464.5	26.8	188.6	5.3	4.0	2.7	-	47.7
			Mean	***472.71***	***1201.12***	***2974.42***	***1.81***	***885.33***	***2624.01***	***48.66***	***353.78***	***24.49***	***16.58***	***408.62***	-	***57.25***
			Max	2893.14	2167.4	7138.6	2.1	1384.9	2874.3	71.2	607.0	71.1	25.2	3025.6	-	63.7
338	W	3	Min	49.46	656.5	595.4	-	851.6	4012.3	1167.3	154.5	13.1	16.4	3.7	-	42.9
			Mean	***63.65***	***743.24***	***1144.15***	-	***1822.51***	***4214.47***	***1268.03***	***204.83***	***22.23***	***21.65***	***7.93***	-	***45.65***
			Max	85.58	805.1	1691.1	-	3383.0	4564.0	1447.4	279.9	29.1	29.2	12.1	-	50.7
LCD106	W	4	Min	60.49	1229.73	631.66	0.15	893.29	405.54	1.56	86.04	21.62	25.73	0.28	7.52	24.53
			Mean	***177.70***	***1282.47***	***656.64***	***0.22***	***998.84***	***417.02***	***1.87***	***123.42***	***34.91***	***30.09***	***0.78***	***8.43***	***33.17***
			Max	278.59	1351.10	686.02	0.26	1089.02	429.86	2.18	152.94	41.91	33.76	1.56	9.08	37.56
LCD13	W	5	Min	69.5	430.1	484.1	0.3	365.3	177.0	3.5	61.4	4.6	21.2	1.2	6.7	25.4
			Mean	***106.06***	***868.07***	***792.91***	***0.74***	***882.52***	***230.97***	***3.89***	***85.66***	***16.24***	***30.38***	***4.06***	***36.86***	***27.75***
			Max	162.3	1332.0	1183.1	1.6	2070.2	322.1	4.3	107.1	60.8	47.5	7.8	81.9	29.1
1714	W	8	Min	28.51	68.6	373.4	1.4	92.1	1949.7	10.2	50.9	12.6	40.8	2.0	7.8	3.4
			Mean	***54.50***	***88.78***	***1494.13***	***2.32***	***828.37***	***2674.65***	***172.88***	***81.65***	***15.38***	***108.56***	***2.36***	***10.63***	***6.36***
			Max	99.87	151.5	5247.9	2.9	1363.8	3033.1	683.7	126.3	19.5	207.1	2.8	14.0	11.3
217	W	12	Min	61.5	311.9	873.1	0.9	222.0	1190.5	8.8	499.5	0.7	347.9	1.3	59.2	49.1
			Mean	***187.17***	***649.68***	***3280.91***	***1.24***	***410.10***	***1854.17***	***15.43***	***563.08***	***10.03***	***845.68***	***59.79***	***584.70***	***59.10***
			Max	267.73	827.0	8077.8	1.4	557.0	2448.2	37.2	666.2	97.9	1798.5	258.4	4914.6	86.5
243	W	9	Min	47.0	138.2	347.5	0.7	80.2	2.5	4.8	288.8	1.0	2006.9	10.4	30.0	13.1
			Mean	***379.92***	***467.26***	***2443.03***	***1.26***	***139.65***	***70.42***	***5.38***	***346.95***	***8.42***	***2789.03***	***135.22***	***99.78***	***17.46***
			Max	1155.8	928.7	8339.9	2.1	219.3	176.0	6.0	475.2	41.9	4903.1	271.6	184.7	23.3

Sample No	Sample Type	No of Analyses		As	Y	Zr	Mo	In	Sn	Sb	La	Ce	Hf	W	Pb	Bi	Th	U
ST1	M	3	Min	-	-	-	7.8	5.9	-	9.6	-	0.1	-	8.7	2.0	2.1	-	0.4
			Mean	-	-	-	***32.39***	***8.45***	***2.42***	***10.96***	***2.74***	***0.64***	-	***27.84***	***19.93***	***3.79***	-	***0.40***
			Max	-	-	-	74.8	11.1	-	12.3	-	1.2	-	65.5	37.9	5.5	-	0.5
OS1	M	8	Min	-	-	0.1	0.4	0.1	2.5	2.5	1.5	0.1	0.1	3.4	1.0	0.4	0.5	0.1
			Mean	***41.63***	***0.16***	***0.14***	***114.02***	***14.35***	***6.33***	***2.20***	***3.95***	***4.40***	***1.40***	***6.85***	***1.60***	***1.89***	***7.19***	***11.88***
			Max	-	-	0.3	819.7	23.2	16.7	5.1	7.8	15.3	2.8	37.7	6.1	8.4	21.0	73.1
ME	M	7	Min	2.50	0.08	0.06	2.32	0.13	0.20	0.19	0.01	0.04	0.02	0.02	1.62	0.25	0.01	0.34
			Mean	***3.85***	***0.33***	***0.41***	***144.70***	***0.98***	***1.37***	***0.46***	***1.23***	***1.11***	***0.05***	***1.40***	***2.95***	***0.70***	***0.12***	***1.88***
			Max	7.26	0.635	0.89	424.28	2.5	3.41	1.42	3.46	2.88	0.133	5.51	5.22	2.3	0.433	3.55
291	W	6	Min	-	0.4	0.2	1.4	0.1	2.1	0.7	0.3	0.9	0.8	1.3	1.2	0.8	-	1.3
			Mean	-	***0.78***	***1.25***	***3.42***	***2.66***	***4.16***	***4.79***	***0.68***	***3.11***	***1.31***	***7.24***	***7.84***	***3.06***	-	***5.82***
			Max	-	1.2	2.1	5.0	7.1	11.2	12.4	1.3	6.3	1.8	17.8	14.9	5.1	-	18.3
262	W	9	Min	19.8	0.2	1.7	4.5	0.1	9.7	1.0	0.2	0.2	0.2	4.4	0.6	0.4	0.4	0.5
			Mean	***23.83***	***0.77***	***3.37***	***52.61***	***8.71***	***18.35***	***3.05***	***0.54***	***3.38***	***0.38***	***25.64***	***18.05***	***4.32***	***1.20***	***9.22***
			Max	30.5	2.2	5.3	154.9	15.8	26.7	6.2	2.3	8.5	0.5	46.2	37.4	14.0	2.5	21.7
204	W	4	Min	-	-	-	119.8	0.3	1.9	0.6	0.1	0.2	0.2	0.2	0.4	0.5	0.2	13.2
			Mean	-	-	-	***991.26***	***0.98***	***4.71***	***7.78***	***4.28***	***1.99***	***1.45***	***3.69***	***12.08***	***14.97***	***0.34***	***13.19***
			Max	-	-	-	2639.1	1.7	9.3	15.5	9.1	3.7	2.7	5.7	33.4	46.2	0.5	13.2
168	W	5	Min	15.7	-	0.2	1.9	0.1	3.5	-	0.2	0.9	0.3	0.1	0.6	0.5	0.3	0.1
			Mean	***15.83***	-	***0.23***	***59.39***	***3.08***	***5.80***	-	***0.33***	***3.18***	***0.85***	***2.38***	***3.93***	***4.17***	***3.17***	***5.26***
			Max	15.9	-	0.3	160.2	5.5	11.8	-	0.5	6.6	1.6	7.7	5.5	9.1	6.0	8.6
312	W	2	Min	-	-	-	12.1	5.2	-	-	-	0.9	-	3.4	1.9	0.6	-	2.7
			Mean	-	-	-	***106.10***	***5.41***	-	-	-	***1.13***	-	***3.89***	***2.51***	***1.60***	-	***4.40***
			Max	-	-	-	200.1	5.6	-	-	-	1.4	-	4.4	3.1	2.6	-	6.1
222	W	6	Min	3.9	0.4	0.2	1.6	0.0	1.2	0.6	0.1	0.2	0.1	0.1	3.1	0.3	0.1	0.2
			Mean	***5.58***	***0.51***	***0.61***	***92.24***	***4.71***	***5.08***	***1.41***	***0.84***	***1.04***	***0.12***	***0.73***	***26.93***	***3.55***	***0.16***	***2.37***
			Max	7.2	0.6	1.2	184.9	13.4	12.7	3.8	2.3	2.6	0.2	1.7	83.9	16.8	0.2	5.5
161	W	3	Min	8.7	0.3	0.7	-	-	4.1	0.8	0.3	0.8	0.1	1.6	17.0	0.4	0.1	4.0
			Mean	***10.30***	***0.68***	***0.97***	***240.26***	-	***4.63***	***1.66***	***0.31***	***3.97***	***1.18***	***2.08***	***32.26***	***2.49***	***0.64***	***5.03***
			Max	11.9	1.2	1.2	-	-	5.4	2.5	0.3	9.8	3.2	2.6	43.6	5.0	1.2	6.7
254	W	10	Min	11.0	0.8	0.0	0.5	0.2	0.7	0.4	0.0	0.1	-	1.4	0.4	0.5	0.1	0.1
			Mean	***14.44***	***2.02***	***1.32***	***29.94***	***2.65***	***1.51***	***5.05***	***0.57***	***0.32***	-	***4.68***	***2.50***	***3.17***	***0.85***	***3.14***
			Max	17.4	3.2	5.4	158.5	7.4	3.4	13.9	1.5	0.7	-	12.9	9.2	9.9	3.8	9.0
338	W	3	Min	8.9	-	-	-	-	-	0.2	-	1.1	-	-	-	0.3	0.0	-
			Mean	***8.92***	-	-	***4.09***	***0.04***	***7.89***	***0.69***	-	***4.09***	-	-	***1.21***	***0.48***	***0.11***	-
			Max	8.9	-	-	-	-	-	1.1	-	7.1	-	-	-	0.6	0.2	-
LCD106	W	4	Min	-	-	0.03	0.08	-	2.03	-	0.01	-	-	-	0.12	-	-	-
			Mean	-	-	***0.07***	***0.13***	***0.02***	***2.85***	-	***0.03***	***0.02***	***0.03***	-	***0.23***	-	-	-
			Max	-	-	0.11	0.22	-	3.61	-	0.05	-	-	-	0.50	-	-	-
LCD13	W	5	Min	-	0.0	0.0	0.0	0.0	0.5	0.1	0.0	0.0	-	-	0.2	0.0	-	-
			Mean	-	***0.49***	***7.37***	***0.09***	***0.03***	***1.28***	***0.09***	***0.02***	***0.06***	-	-	***0.64***	***0.04***	-	-
			Max	-	1.0	20.5	0.2	0.0	1.9	0.1	0.0	0.2	-	-	1.1	0.1	-	-
1714	W	8	Min	-	0.1	0.1	0.6	0.2	0.8	0.7	0.0	0.1	0.2	0.3	0.3	1.2	0.1	0.1
			Mean	-	***0.16***	***0.29***	***0.73***	***4.66***	***5.00***	***1.37***	***0.04***	***2.17***	***2.33***	***3.50***	***0.73***	***4.44***	***0.61***	***0.14***
			Max	-	0.3	0.9	0.9	9.1	10.0	2.7	0.1	11.4	6.6	6.7	1.5	10.8	1.2	0.2
217	W	12	Min	6.0	0.2	0.0	0.3	0.4	0.9	0.4	0.1	0.0	0.0	0.4	2.4	0.2	0.1	0.1
			Mean	***27.54***	***0.99***	***1.39***	***3.05***	***8.07***	***6.06***	***4.32***	***3.79***	***2.82***	***0.31***	***6.00***	***15.98***	***2.37***	***0.62***	***7.97***
			Max	63.9	2.1	5.3	9.3	52.9	14.6	13.0	27.5	25.5	0.7	23.9	55.1	7.0	2.6	34.0
243	W	9	Min	7.4	0.2	0.1	0.5	1.1	1.9	1.6	0.1	0.0	0.1	1.5	2.3	0.2	0.1	1.7
			Mean	***10.44***	***0.59***	***0.19***	***2.77***	***2.09***	***2.43***	***3.21***	***0.64***	***1.50***	***0.46***	***3.04***	***13.97***	***3.51***	***0.46***	***2.79***
			Max	15.6	1.7	0.4	5.6	3.9	3.3	5.0	1.6	4.5	0.8	4.5	44.8	21.9	0.8	4.9

Table 6.4: Mean, minimum and maximum values of the trace element content of magnetite from various barren Fe oxide-rich systems in the EFB (in ppm). Sample location numbers are presented in appendix 9. Also shown is the number of analyses taken for each sample. The hyphen represent analyses that are below the detection limit.

Sample No	Sample Type	No of Analyses		Mg	Al	Si	Sc	Ti	V	Cr	Mn	Co	Ni	Cu	Zn	Ga
ST2	B	9	Min	5.62	480.22	1017.49	1.09	61.60	9.15	4.41	4.67	0.20	1.17	3.41	4.13	4.01
			Mean	***37.03***	***2954.54***	***2802.90***	***2.45***	***1032.82***	***33.49***	***13.89***	***30.27***	***15.91***	***19.66***	***94.50***	***635.48***	***6.42***
			Max	135.42	15295.30	8100.13	3.70	1576.25	44.42	22.98	165.82	54.83	67.08	400.96	3376.19	10.52
ST3	B	10	Min	102.16	510.36	451.57	1.56	111.41	47.50	4.31	139.35	14.12	8.59	7.98	17.01	7.74
			Mean	***170.66***	***790.34***	***4293.79***	***2.06***	***253.47***	***56.19***	***21.62***	***162.12***	***28.40***	***55.76***	***558.19***	***479.35***	***13.80***
			Max	261.69	1216.15	9016.23	2.46	1281.09	63.18	42.36	203.10	110.87	340.08	4661.55	1819.15	36.64
OS2	B	12	Min	282.35	501.62	510.29	0.87	6.27	195.35	3.72	69.29	14.08	20.05	6.98	9.10	22.94
			Mean	***363.33***	***576.88***	***1746.48***	***3.43***	***33.27***	***212.60***	***9.79***	***98.94***	***173.64***	***46.33***	***357.82***	***206.67***	***56.83***
			Max	627.97	982.05	5853.09	9.07	191.82	278.44	23.76	109.57	253.40	173.32	2663.89	1283.46	66.08
MPO11	B	4	Min	32.96	274.24	438.64	0.27	106.19	1177.67	221.87	40.36	10.19	139.17	2.10	2.54	24.10
			Mean	***342.58***	***871.12***	***1955.27***	***2.59***	***313.83***	***2571.30***	***1196.33***	***54.46***	***28.21***	***146.96***	***120.27***	***4.48***	***36.99***
			Max	811.85	1442.45	4003.82	6.46	469.49	3632.00	2467.62	65.68	46.72	161.41	391.63	7.36	47.20
1314	B	8	Min	72.96	145.02	331.88	0.31	33.91	425.49	185.88	88.05	41.08	83.57	0.79	14.37	20.34
			Mean	***102.04***	***193.76***	***797.34***	***0.57***	***151.22***	***718.30***	***411.68***	***131.42***	***50.50***	***91.45***	***1.49***	***22.29***	***23.11***
			Max	119.55	231.78	1168.91	1.08	310.61	878.71	687.45	178.37	58.13	101.92	1.93	75.53	25.78
MA3	B	4	Min	47.16	242.92	423.88	0.80	313.81	1454.97	11.73	188.13	3.08	19.36	14.13	15.71	5.19
			Mean	***196.94***	***987.56***	***3174.50***	***1.13***	***753.36***	***1564.82***	***48.82***	***207.57***	***6.15***	***24.81***	***49.08***	***18.71***	***9.46***
			Max	444.15	1695.01	7928.66	1.52	1397.87	1632.48	79.96	221.90	9.46	33.63	82.06	26.41	14.61
MA2	B	4	Min	10.14	77.29	508.22	-	34.39	2114.45	27.71	157.29	20.81	25.52	1.60	7.77	5.24
			Mean	***35.03***	***487.36***	***1328.11***	***-***	***231.07***	***2364.69***	***82.33***	***194.83***	***29.67***	***34.17***	***2.40***	***87.04***	***16.42***
			Max	103.21	1409.58	2120.23	-	471.04	2738.59	236.52	254.21	54.26	49.40	3.94	311.86	40.10
1375B	B	5	Min	60.43	208.55	538.37	0.82	42.97	1072.37	50.54	256.75	38.96	53.71	4.22	15.42	10.77
			Mean	***433.41***	***369.24***	***1447.79***	***1.47***	***86.13***	***1351.97***	***713.24***	***456.28***	***57.73***	***69.48***	***7.52***	***23.64***	***15.52***
			Max	1744.63	924.61	3315.98	2.08	115.65	1534.83	1205.59	564.23	64.97	84.99	10.82	31.74	19.22
SY	B	7	Min	442.84	4240.65	2740.11	5.47	659.31	1435.18	42.03	244.36	71.52	107.20	7.96	75.02	96.70
			Mean	***1052.56***	***8421.37***	***5500.73***	***12.45***	***2353.70***	***1698.51***	***203.80***	***546.70***	***91.15***	***132.41***	***3.86***	***772.20***	***124.00***
			Max	1994.25	22698.71	8373.44	28.94	5832.86	2037.59	464.21	1244.51	147.99	165.42	20.63	3648.59	194.86
LCD32	B	6	Min	78.52	485.58	399.09	0.13	828.66	263.57	1.06	318.17	106.25	44.56	0.21	44.08	22.81
			Mean	***212.69***	***1055.85***	***1784.16***	***0.17***	***980.62***	***288.67***	***5.86***	***473.31***	***110.14***	***46.71***	***4.02***	***51.25***	***24.06***
			Max	752.27	2187.04	5600.31	0.26	1137.60	327.88	8.25	628.25	114.26	50.50	9.39	60.59	25.24
LC43	B	6	Min	41.15	502.04	520.94	0.18	761.27	267.18	0.91	70.65	3.80	21.74	0.31	3.81	24.66
			Mean	***157.43***	***710.40***	***904.59***	***0.40***	***1264.40***	***286.12***	***3.04***	***199.25***	***8.56***	***25.60***	***1.99***	***21.09***	***26.80***
			Max	608.11	1022.76	1818.13	0.59	1539.04	308.08	9.52	332.97	14.57	32.58	4.94	50.35	30.16
LCF12	B	6	Min	16.75	534.81	547.92	0.89	396.18	1212.08	178.76	233.73	6.27	19.25	0.29	32.35	25.42
			Mean	***378.16***	***1827.18***	***1895.16***	***1.14***	***1009.38***	***1511.67***	***249.90***	***402.44***	***8.90***	***30.63***	***12.88***	***712.99***	***43.93***
			Max	1755.61	3386.46	6503.56	1.42	1775.58	1647.75	319.54	560.79	18.96	38.12	57.41	3883.34	63.82
1307	B	10	Min	101.90	224.97	432.90	0.25	74.27	1028.21	36.81	33.80	35.22	120.94	0.39	10.99	34.79
			Mean	***323.20***	***368.44***	***1237.30***	***0.93***	***163.24***	***1155.56***	***351.77***	***166.06***	***56.03***	***137.57***	***3.48***	***19.43***	***45.16***
			Max	1491.75	716.89	4006.57	1.99	264.03	1396.49	926.82	292.11	68.20	166.97	14.48	41.68	56.51
1310	B	4	Min	151.75	302.79	748.39	0.07	195.74	1277.41	31.83	166.39	49.33	42.75	0.29	14.07	25.57
			Mean	***166.77***	***380.61***	***784.12***	***0.48***	***320.01***	***1491.63***	***373.42***	***201.30***	***58.69***	***97.26***	***1.93***	***16.15***	***39.65***
			Max	189.24	452.55	806.89	0.71	583.12	1816.86	611.61	247.84	76.37	125.96	5.10	17.90	49.06
1351A	B	3	Min	61.57	178.80	657.98	0.52	64.15	509.81	121.04	107.31	29.74	86.28	0.91	9.21	15.81
			Mean	***92.63***	***220.79***	***882.42***	***0.80***	***111.74***	***636.75***	***212.37***	***239.25***	***39.78***	***93.78***	***4.75***	***10.04***	***17.61***
			Max	112.39	259.58	1259.99	0.95	154.59	702.21	349.79	398.01	48.58	106.07	10.29	11.22	18.74
1356A	B	6	Min	166.28	229.10	487.28	0.77	7.44	512.22	1.26	389.65	57.19	79.81	0.11	24.79	12.78
			Mean	***271.96***	***568.15***	***1384.88***	***0.90***	***19.82***	***547.88***	***3.42***	***461.67***	***59.53***	***86.68***	***7.38***	***31.06***	***13.80***
			Max	456.42	1350.54	4095.62	1.06	66.53	633.12	7.22	523.68	65.03	94.92	22.63	38.96	15.27
1375A	B	4	Min	32.72	464.59	597.49	0.21	522.43	2021.57	1.10	323.04	18.58	4.87	0.46	30.44	30.65
			Mean	***44.81***	***656.15***	***774.37***	***0.31***	***741.31***	***2442.09***	***1.44***	***363.39***	***29.54***	***5.68***	***1.09***	***41.57***	***33.41***
			Max	56.21	989.55	981.08	0.41	867.75	2721.88	2.10	406.13	43.46	7.78	1.58	58.64	38.54
1686	B	10	Min	39.38	77.91	607.46	0.98	172.66	342.81	1.86	88.37	23.59	63.37	0.35	6.57	11.48
			Mean	***360.16***	***308.79***	***1230.66***	***2.03***	***308.70***	***401.29***	***7.08***	***101.33***	***24.70***	***70.19***	***1.42***	***12.43***	***15.42***
			Max	2796.45	2055.36	4653.75	3.30	692.01	467.47	16.01	168.04	26.43	79.42	3.36	26.24	22.91
1735	B	4	Min	63.95	161.79	877.74	0.29	100.35	713.80	53.75	330.62	36.66	86.90	0.31	2.93	8.25
			Mean	***92.11***	***271.59***	***1679.31***	***0.37***	***120.37***	***809.35***	***172.79***	***366.92***	***41.02***	***99.59***	***12.89***	***8.13***	***8.91***
			Max	131.96	415.50	2179.90	0.49	141.94	867.34	251.91	424.65	45.45	114.48	47.68	19.89	9.89
1785	B	4	Min	58.97	401.87	1458.11	0.09	48.92	860.30	144.15	268.73	60.12	85.91	0.39	19.89	18.78
			Mean	***123.30***	***533.07***	***4160.01***	***0.23***	***82.66***	***1043.59***	***356.36***	***318.29***	***64.30***	***89.60***	***0.72***	***33.21***	***29.16***
			Max	236.63	655.52	9851.08	0.30	129.04	1217.89	799.74	370.84	71.27	96.43	1.41	47.20	37.92
1808	B	2	Min	2913.63	332.72	7417.58	0.51	72.51	1285.31	242.14	174.53	34.88	105.37	0.85	7.18	8.03
			Mean	***3444.03***	***941.89***	***8180.01***	***0.86***	***98.14***	***1292.11***	***922.39***	***175.85***	***36.12***	***113.73***	***1.38***	***8.33***	***8.53***
			Max	3974.42	1551.05	8942.44	1.21	123.76	1298.91	1602.63	177.17	37.36	122.08	1.91	9.48	9.03
345	B	2	Min	40.64	384.07	644.44	2.13	141.27	1226.38	101.62	53.65	35.34	225.07	1.68	3.84	75.95
			Mean	***1276.17***	***1988.19***	***4304.42***	***6.73***	***233.27***	***1383.91***	***416.53***	***541.03***	***42.57***	***298.53***	***3.93***	***4.69***	***77.35***
			Max	2511.70	3592.31	7964.39	11.32	325.26	1541.43	731.44	1028.41	49.80	371.98	6.17	5.54	78.74

Sample No	Sample Type	No of Analyses		As	Y	Zr	Mo	In	Sn	Sb	La	Ce	Hf	W	Pb	Bi	Th	U
ST2	B	9	Min	6.91	0.21	0.19	0.61	0.07	2.03	3.46	0.04	0.21	0.18	0.89	5.39	0.29	0.11	0.09
			Mean	***302.23***	***0.57***	***9.24***	***25.42***	***2.17***	***9.65***	***137.74***	***1.22***	***3.06***	***0.57***	***14.30***	***19.67***	***5.60***	***0.60***	***2.01***
			Max	1456.08	2.01	27.55	157.48	6.97	38.08	322.20	8.85	22.58	1.01	46.75	39.82	39.29	1.47	10.14
ST3	B	10	Min	7.29	0.12	0.06	0.38	1.43	0.89	1.04	0.06	0.12	0.20	0.41	31.85	0.54	0.15	1.04
			Mean	***13.34***	***0.45***	***2.85***	***33.47***	***5.71***	***5.08***	***5.99***	***0.93***	***2.42***	***0.24***	***6.35***	***68.50***	***3.42***	***0.41***	***11.41***
			Max	22.42	0.82	9.68	250.34	10.06	11.74	14.68	2.14	10.04	0.30	15.65	147.17	10.79	0.85	34.60
OS2	B	12	Min	5.96	0.26	0.04	0.25	1.17	1.02	0.51	0.10	0.06	0.13	0.54	0.47	0.22	0.03	0.18
			Mean	***15.25***	***1.72***	***2.37***	***5.41***	***2.72***	***21.96***	***2.93***	***0.86***	***2.50***	***0.69***	***17.89***	***8.06***	***1.79***	***3.16***	***3.76***
			Max	26.91	5.94	13.55	20.15	5.63	163.78	7.66	3.29	6.72	2.53	95.06	32.57	9.96	16.74	16.90
MPO11	B	4	Min	2.58	-	0.96	0.31	-	0.14	0.10	0.01	0.01	0.01	0.02	0.36	0.01	0.27	0.02
			Mean	***2.86***	-	***6.45***	***0.35***	-	***0.33***	***0.11***	***1.09***	***1.06***	***0.10***	***0.07***	***6.61***	***0.02***	***0.87***	***2.54***
			Max	3.14	-	16.34	0.39	-	0.65	0.12	2.73	2.13	0.19	0.11	16.56	0.03	1.47	6.56
1314	B	8	Min	-	-	0.06	0.50	-	-	0.65	0.03	0.07	-	-	0.18	-	0.06	-
			Mean	-	-	***0.18***	***2.35***	-	-	***1.74***	***1.47***	***0.18***	-	-	***0.67***	-	***0.33***	-
			Max	-	-	0.36	4.27	-	-	6.04	6.50	0.28	-	-	1.56	-	0.86	-
MA3	B	4	Min	-	0.18	0.06	0.18	-	0.80	0.62	0.07	0.09	0.33	0.03	0.56	0.03	1.14	7.85
			Mean	-	-	***1.14***	***0.31***	-	***1.55***	***1.06***	***0.44***	***1.73***	***0.44***	***0.10***	***1.76***	***0.03***	***7.50***	***68.51***
			Max	-	3.63	4.09	0.38	-	2.48	1.48	1.02	5.09	0.55	0.16	4.97	0.03	22.47	147.51
MA2	B	4	Min	-	-	-	-	-	0.52	1.45	-	0.32	-	-	0.27	0.10	-	-
			Mean	-	-	-	-	-	***0.57***	***2.49***	***1.26***	***1.70***	-	-	***0.57***	***0.49***	-	-
			Max	-	-	-	-	-	0.61	4.25	-	3.84	-	-	0.71	0.87	-	-
1375B	B	5	Min	-	0.04	0.13	-	-	-	0.53	-	0.05	-	0.25	0.28	-	-	-
			Mean	-	***0.07***	***0.18***	-	-	***0.75***	***2.53***	***0.07***	***0.12***	-	***2.59***	***0.76***	-	-	-
			Max	-	0.11	0.24	-	-	-	9.57	-	0.25	-	4.94	1.60	-	-	-
SY	B	7	Min	-	1.80	0.05	1.02	0.12	22.85	0.48	0.36	0.75	-	3.45	2.52	0.19	0.09	0.44
			Mean	-	***7.17***	***1.37***	***186.02***	***3.04***	***80.45***	***3.95***	***2.41***	***2.73***	-	***7.18***	***4.73***	***2.73***	***0.13***	***13.98***
			Max	-	19.42	3.83	537.13	16.38	287.43	7.34	8.18	5.91	-	16.02	10.98	8.43	0.17	43.35
LCD32	B	6	Min	0.78	0.02	0.03	0.08	0.03	0.35	-	0.02	0.01	-	0.05	0.09	0.06	-	0.05
			Mean	***1.37***	***0.07***	***0.68***	***0.12***	***0.06***	***0.61***	***0.04***	***0.04***	***0.10***	-	***0.22***	***4.82***	***0.11***	-	***0.07***
			Max	1.70	0.16	3.63	0.16	0.13	0.85	-	0.05	0.26	-	0.67	12.59	0.17	-	0.11
LC43	B	6	Min	-	0.01	0.02	0.11	0.01	0.89	-	0.01	0.01	0.02	0.04	0.10	-	0.01	0.01
			Mean	-	***0.02***	***0.17***	***0.29***	***0.02***	***1.26***	-	***0.02***	***0.05***	***0.02***	***0.69***	***1.00***	-	***0.06***	***0.40***
			Max	-	0.06	0.44	0.83	0.03	1.92	-	0.06	0.22	0.02	2.44	4.89	-	0.16	1.69
LCF12	B	6	Min	-	0.04	0.07	0.11	-	0.30	0.10	0.01	0.02	-	0.05	0.23	-	0.02	0.02
			Mean	-	***1.28***	***1.63***	***0.24***	-	***0.54***	***0.23***	***2.28***	***2.69***	***0.15***	***0.22***	***1.90***	-	***3.01***	***0.26***
			Max	-	3.73	6.24	0.41	-	0.81	0.35	10.63	15.05	-	0.41	7.03	-	11.40	0.69
1307	B	10	Min	0.76	0.01	0.02	0.03	0.01	0.20	0.08	0.00	0.01	0.01	0.02	0.26	0.01	0.01	0.01
			Mean	***1.32***	***0.11***	***0.31***	***0.10***	***0.01***	***0.85***	***0.15***	***0.23***	***0.27***	***0.02***	***0.02***	***1.66***	***0.02***	***0.12***	***0.40***
			Max	1.71	0.30	1.94	0.20	0.02	3.61	0.29	0.80	1.36	0.02	0.03	5.00	0.05	0.44	1.64
1310	B	4	Min	-	0.01	0.04	0.04	-	0.19	-	0.05	0.03	-	-	0.12	-	0.01	0.02
			Mean	-	***0.02***	***0.11***	***0.07***	-	***0.22***	-	***0.23***	***0.32***	-	-	***0.22***	-	***0.07***	***0.04***
			Max	-	0.03	0.28	0.11	-	0.25	-	0.58	1.04	-	-	0.35	-	0.19	0.08
1351A	B	3	Min	1.02	0.25	3.37	0.05	0.01	0.15	-	0.01	0.46	-	0.07	0.06	-	0.04	0.06
			Mean	***1.15***	***1.10***	***5.09***	***0.09***	***0.12***	***0.16***	-	***0.19***	***0.61***	-	***0.11***	***0.47***	-	***0.06***	***0.18***
			Max	1.36	1.95	6.80	0.13	0.23	0.18	-	0.29	0.76	-	0.16	0.95	-	0.08	0.31
1356A	B	6	Min	1.07	0.01	0.01	0.04	0.01	0.36	0.08	0.01	0.01	0.01	0.03	0.06	0.01	0.06	0.00
			Mean	***3.72***	***0.51***	***0.89***	***0.19***	***0.19***	***2.63***	***0.48***	***0.39***	***0.38***	***0.02***	***0.69***	***3.78***	***0.01***	***0.58***	***1.82***
			Max	9.53	2.29	2.43	0.47	1.00	12.19	1.77	1.29	1.75	0.04	2.78	13.60	0.01	1.11	10.57
1375A	B	4	Min	1.70	-	0.03	0.14	0.01	0.57	0.45	0.01	-	-	-	7.99	-	-	0.01
			Mean	***1.92***	-	***12.50***	***0.20***	***0.02***	***1.28***	***0.82***	***0.01***	-	-	-	***24.11***	-	-	***0.08***
			Max	2.13	-	24.97	0.23	0.02	1.57	1.16	0.01	-	-	-	33.36	-	-	0.15
1686	B	10	Min	0.43	0.00	0.02	0.03	0.00	0.24	0.04	0.01	0.01	0.00	0.05	0.14	0.02	0.01	0.02
			Mean	***0.94***	***0.57***	***0.42***	***0.07***	***0.01***	***0.69***	***0.09***	***0.12***	***0.23***	***0.04***	***0.42***	***2.07***	***0.02***	***0.07***	***0.10***
			Max	1.43	2.93	2.40	0.16	0.02	1.54	0.16	0.54	0.98	0.07	2.05	6.99	0.03	0.23	0.22
1735	B	4	Min	1.30	0.05	1.22	0.08	-	0.27	-	0.01	0.04	0.03	0.02	0.15	-	0.01	0.08
			Mean	***27.40***	***0.20***	***17.48***	***0.12***	-	***0.55***	***0.29***	***0.03***	***0.21***	***0.61***	***0.05***	***3.99***	-	***0.06***	***0.24***
			Max	53.50	0.59	62.76	0.18	-	0.99	-	0.05	0.56	1.73	0.08	15.28	-	0.15	0.61
1785	B	4	Min	-	0.06	0.20	0.05	-	0.21	0.07	0.01	0.02	1.03	0.04	0.12	0.02	0.06	0.02
			Mean	-	***0.39***	***35.15***	***0.09***	-	***0.40***	***0.10***	***0.01***	***0.04***	***1.63***	***0.10***	***0.28***	***0.04***	***0.09***	***0.38***
			Max	-	0.62	88.24	0.11	-	0.66	0.16	0.02	0.08	2.23	0.19	0.37	0.08	0.12	0.89
1808	B	2	Min	2.90	0.05	0.35	0.07	-	0.59	0.73	0.03	0.11	-	-	22.80	0.01	0.02	0.05
			Mean	***2.94***	***0.10***	***0.40***	***0.08***	-	***0.74***	***1.08***	***0.07***	***0.15***	-	-	***26.49***	***0.01***	***0.03***	***0.18***
			Max	2.97	0.15	0.45	0.10	-	0.89	1.43	0.11	0.18	-	-	30.17	0.02	0.04	0.32
345	B	2	Min	3.39	0.01	0.04	0.12	-	2.27	0.96	0.01	0.04	-	0.03	22.18	-	0.01	0.01
			Mean	***9.03***	***63.21***	***12.58***	***0.62***	-	***2.33***	***1.38***	***302.75***	***652.71***	-	***0.18***	***30.94***	-	***13.72***	***3.60***
			Max	14.67	126.41	25.13	1.13	-	2.39	1.79	605.48	1305.37	-	0.32	39.70	-	27.42	7.20

Figure 6.8: Bi-plots of trace elements identified in magnetite from various Fe oxide-rich systems in the EFB. Yellow symbols represent magnetite from Cu-Au mineralisation at Ernest Henry, Starra, Osborne, Mount Elliott and magnetite veins from the Lightning Creek Cu-Au systems. K-Fe alteration, marble matrix breccia, Na-Ca alteration from Ernest Henry, FC4NW, and FC12 and cumulate Fe oxide-rich rocks from the FC12 prospect represent weakly mineralised systems analysed. Barren 'Fe oxide-rich rocks' from Starra and Osborne hosting Cu-Au mineralisation as well as several regional barren Fe oxide-rich rocks from Mount Philp, the Gilded Rose, MFC and the Corella formation were also analysed. Fe-rich sills and monzodiorite from Lightning Creek make up the suite of rocks analysed in this study.

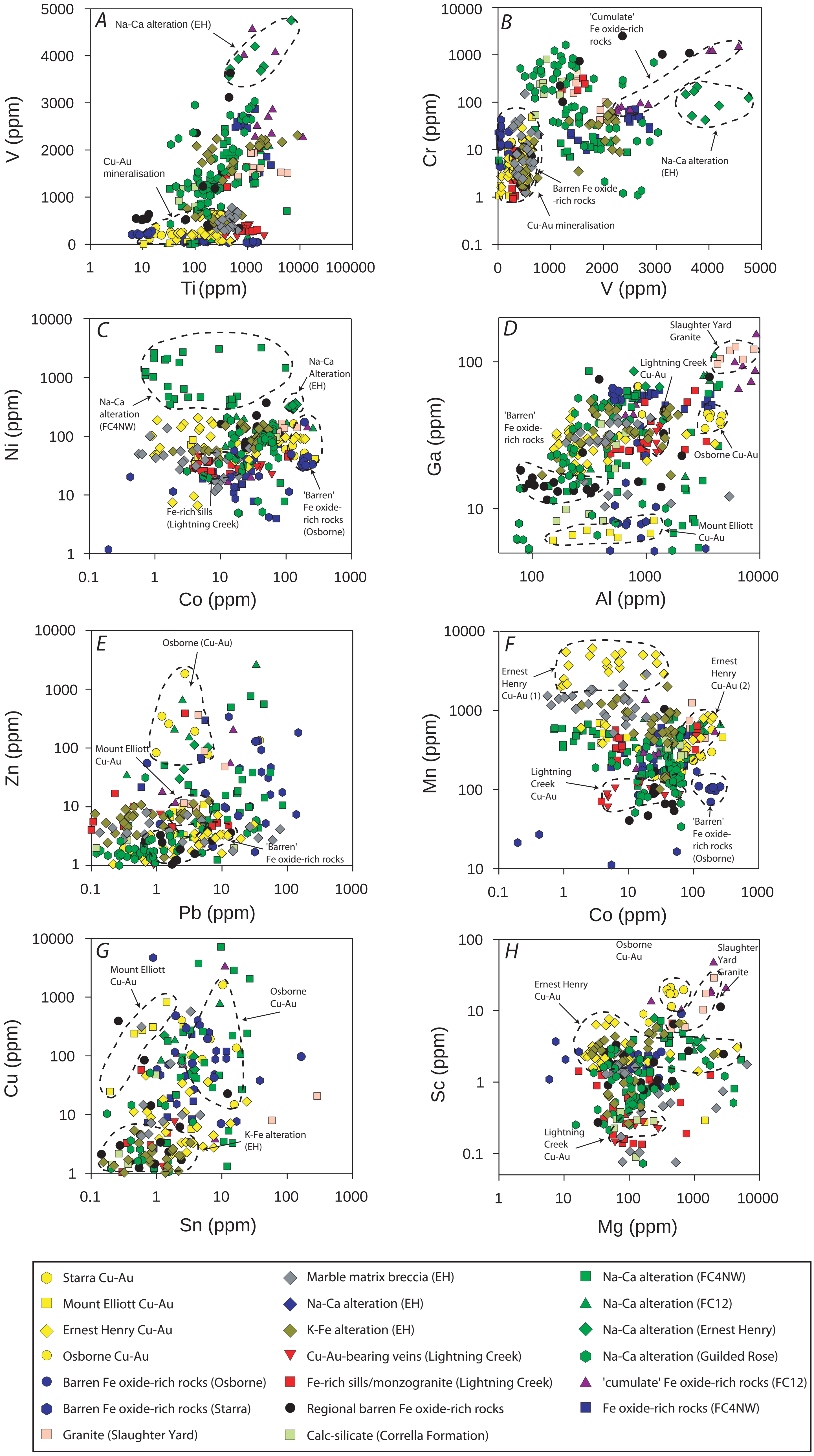
A
Na-Ca alteration (EH)
Cu-Au mineralisation
V (ppm)
Ti (ppm)
B
'Cumulate' Fe oxide-rich rocks
Na-Ca alteration (EH)
Barren Fe oxide-rich rocks
Cu-Au mineralisation
Cr (ppm)
V (ppm)
C
Na-Ca Alteration (EH)
Na-Ca alteration (FC4NW)
Fe-rich sills (Lightning Creek)
'Barren' Fe oxide-rich rocks (Osborne)
Ni (ppm)
Co (ppm)
D
Slaughter Yard Granite
Lightning Creek Cu-Au
'Barren' Fe oxide-rich rocks
Osborne Cu-Au
Mount Elliott Cu-Au
Ga (ppm)
Al (ppm)
E
Osborne (Cu-Au)
Mount Elliott Cu-Au
'Barren' Fe oxide-rich rocks
Zn (ppm)
Pb (ppm)
F
Ernest Henry Cu-Au (1)
Ernest Henry Cu-Au (2)
Lightning Creek Cu-Au
'Barren' Fe oxide-rich rocks (Osborne)
Mn (ppm)
Co (ppm)
G
Mount Elliott Cu-Au
Osborne Cu-Au
K-Fe alteration (EH)
Cu (ppm)
Sn (ppm)
H
Osborne Cu-Au
Slaughter Yard Granite
Ernest Henry Cu-Au
Lightning Creek Cu-Au
Sc (ppm)
Mg (ppm)
Starra Cu-Au
Mount Elliott Cu-Au
Ernest Henry Cu-Au
Osborne Cu-Au
Barren Fe oxide-rich rocks (Osborne)
Barren Fe oxide-rich rocks (Starra)
Granite (Slaughter Yard)
Marble matrix breccia (EH)
Na-Ca alteration (EH)
K-Fe alteration (EH)
Cu-Au-bearing veins (Lightning Creek)
Fe-rich sills/monzogranite (Lightning Creek)
Regional barren Fe oxide-rich rocks
Calc-silicate (Corrella Formation)
Na-Ca alteration (FC4NW)
Na-Ca alteration (FC12)
Na-Ca alteration (Ernest Henry)
Na-Ca alteration (Guilded Rose)
'cumulate' Fe oxide-rich rocks (FC12)
Fe oxide-rich rocks (FC4NW)

population represents values an order of magnitude higher than all other systems (>2000 ppm) while the other population is significantly lower (300-1000 ppm).

Other elements in magnetite, including Ni, Si, Cu, Co, Zn and Sn, do not readily discriminate between Cu-Au mineralisation and other Fe oxide-bearing systems (Fig. 6.8). However, these elements still define interesting populations within the dataset. Magnetite from Starra, Mount Elliott and Osborne all contain relatively high Cu values compared to Ernest Henry (Fig. 6.8g), and Osborne magnetite also contains higher Zn compared to the other deposits (Fig. 6.8e; 100-5000 ppm). Co content is highly variable at Ernest Henry (1-200 ppm). For the other Fe oxide-bearing systems in the dataset, Ni is significantly higher in magnetite (500-5000 ppm) associated with Na-Ca alteration at FC4NW compared to all other systems (~100 ppm). Co concentrations at FC4NW are significantly lower than in the other Na-Ca assemblages (i.e. Gilded Rose, Ernest Henry and FC12) (Fig. 6.8c).

Major and trace element substitution

The presence of Mn, Cr and V in magnetite can be explained by their preferential substitution for Fe^{3+} (ionic radius = 0.73 Å), while Zn, Cu and Ni will readily substitute for Fe^{2+} (ionic radius = 0.86 Å)(Deer et al., 1992; Toplis and Corgne, 2002). The Mg content in magnetite is attributed to the substitution of Mg^{2+} for Fe^{2+}, although its abundance in magnetite may be strongly influenced by the corresponding Fe:Mg ratio of neighbouring Fe-bearing silicates (Frost, 1991). In oxidised environments, both Pb and Sn are in the quadrivalent state and may also substitute for Fe^{3+} (Goldschmidt, 1958). The Al and Ga content in magnetite is consistent with other studies of iron ore deposits (e.g. Kisvarsanyi and Procter, 1967; Nystrom and Henriquez, 1994) and can substitute for Fe^{3+}. The presence of Ti in magnetite can be attributed to the similar ionic radii of Fe^{3+} and Ti^{4+} (Goldschmidt, 1958). In addition, work by Dasgupta (1967) showed that the ionisation potential (IP) between Fe^{3+} (43.25 eV) with Ti^{4+} (30.6 eV) is significantly different, and suggested that the substitution of Ti^{4+} for Fe^{3+} will introduce strain in bonds with surrounding oxygen ions within the magnetite crystal lattice. This introduced strain will necessitate the conversion of Fe^{3+} ions to the Fe^{2+} state due to the stabilization energy of Fe^{2+} being greater than Fe^{3+} when bonded with oxygen anions in spinels. This will potentially have an important control of the elements that partition into magnetite, where di- and tri- valent cations with lower ionisation potentials (e.g. Mg^{2+}, Mn^{2+} and V^{3+}) will be favoured in place of Fe^{3+} and Fe^{2+} (Dasgupta, 1967).

Discriminant analysis

A discriminant analysis of the entire dataset was undertaken using 10 groups defined on their geological setting (Table 6.1). These analyses showed that a total of nine discriminant functions account for the total variance in the data set. The variation in each of these discriminant functions is expressed as Eigenvalues (Table 6.5a), which is a representation of the degree of variance expressed by a particular discriminant function, where the larger Eigenvalues indicate separation between the pre-defined groups. For example, the Eigenvalue for the first discriminant function represents 46.8% of the total variance in the dataset (cf. Table 6.5a).

Table 6.5b shows the classification results for the discriminant analysis, showing the pre-defined groups and the predicted group membership. These groupings are compared as a percentage. For example, 94.2% of the analyses assigned as Cu-Au mineralisation were classified into group 1, and in total, 86.7% of all analyses were classified into their pre-defined groups. This table is also useful to ascertain what groups the uncategorized analyses fall into. For example, group 1 shows the three analyses not classified into this group fall into groups 4 (marble matrix breccia) and 7 (Fe oxide-rich rock (metasomatic), perhaps suggesting a genetic link. The table of group centroids shows which pre-defined groups are important in defining each discriminant function (Table 6.5c). For example, groups 1 (Cu-Au mineralisation), 4 (marble matrix breccia) and 10 (barren Fe oxide-rich rocks at Starra and Osborne) have low values for function 1 (-1,855, -1.045 and -1.563 respectively) while group 6 (cumulate magnetite) have high values (3.095). Hence, the trace element geochemistry of these mineral associations differ most with respect to function 1 which is defined by Mn and V (table 6.5d). For function 2, groups 1 and 6 differ significantly with respect to group 10 as defined by the elements Sc, Mn and Pb (table 6.5d). The results agree with the elements deemed important in section 6.1.1, with V, Mn, Co and Ni exhibiting the greatest variance between different mineral associations in the dataset, and are the most effective trace element discriminant of barren and mineralised systems in the district.

Table 6.5: Results of the stepwise discriminant analysis for magnetite.

A. *Calculated eigenvalues for each of the discriminant functions for magnetite produced from the discriminant analysis. The larger the eigenvalue, the greater the separation between the pre-defined groups. Also shown is the canonical correlation for each discriminant function, where the closer the value is to 1, the higher the degree of association between the discriminant function and the groups. % variance and cumulative % of each successive discriminant function is also shown.*
B. *Classification table showing the degree to which the discriminant functions differentiate between the groups for magnetite. Further explanation of the table is given in the text.*
C. *Table of group centroids showing the way in which each discriminant function differentiates between the pre-defined groups for magnetite. Further explanation of the table is given in the text.*
D. *Table of the standardized canonical discriminant function coefficients showing to what degree each of the elements contribute to each of the discriminant functions for magnetite.*

A

Eigenvalues

Function	Eigenvalue	% of Variance	Cumulative %	Canonical Correlation
1	1.557[a]	46.8	46.8	.780
2	.930[a]	28.0	74.7	.694
3	.448[a]	13.5	88.2	.556
4	.238[a]	7.2	95.4	.439
5	.083[a]	2.5	97.9	.277
6	.041[a]	1.2	99.1	.198
7	.025[a]	.7	99.9	.156
8	.004[a]	.1	100.0	.064
9	.001[a]	.0	100.0	.024

B

Classification Results[a]

		Mineral association	Predicted Group Membership										Total
			1	2	3	4	5	6	7	8	9	10	
Original	Count	1	49	0	0	2	0	0	1	0	0	0	52
		2	0	73	4	0	0	0	25	0	2	0	104
		3	0	0	33	0	0	0	0	0	0	0	33
		4	0	0	0	24	0	0	0	0	0	0	24
		5	0	0	0	0	9	0	0	0	0	0	9
		6	0	0	0	0	0	9	0	0	0	0	9
		7	0	1	0	0	0	0	35	0	1	0	37
		8	0	0	0	0	0	0	0	8	0	0	8
		9	0	0	0	0	0	0	3	0	22	0	25
		10	0	0	0	0	0	0	0	0	0	31	31
	%	1	94.2	.0	.0	3.8	.0	.0	1.9	.0	.0	.0	100.0
		2	.0	70.2	3.8	.0	.0	.0	24.0	.0	1.9	.0	100.0
		3	.0	.0	100.0	.0	.0	.0	.0	.0	.0	.0	100.0
		4	.0	.0	.0	100.0	.0	.0	.0	.0	.0	.0	100.0
		5	.0	.0	.0	.0	100.0	.0	.0	.0	.0	.0	100.0
		6	.0	.0	.0	.0	.0	100.0	.0	.0	.0	.0	100.0
		7	.0	2.7	.0	.0	.0	.0	94.6	.0	2.7	.0	100.0
		8	.0	.0	.0	.0	.0	.0	.0	100.0	.0	.0	100.0
		9	.0	.0	.0	.0	.0	.0	12.0	.0	88.0	.0	100.0
		10	.0	.0	.0	.0	.0	.0	.0	.0	.0	100.0	100.0

[a] 88.3% of original grouped cases correctly classified.

C

Functions at Group Centroids

Mineral association	Function								
	1	2	3	4	5	6	7	8	9
1	-1.855	1.322	-.322	.224	.163	-8.37E-02	-1.97E-02	-2.26E-02	5.886E-03
2	.997	-.359	-.582	.147	.130	8.717E-02	-4.63E-02	-1.07E-02	4.602E-05
3	.554	.546	9.993E-02	-.322	-.192	-6.20E-02	-1.48E-02	.147	3.380E-02
4	-1.045	.364	-7.97E-02	-.565	-.474	.478	.113	-4.93E-03	-2.89E-02
5	-.436	-.639	.774	-1.164	-.366	-.146	-.709	-.132	1.877E-02
6	3.095	2.621	2.031	1.375	-.364	5.069E-02	-.118	-3.47E-02	-3.08E-02
7	.709	-.176	4.911E-02	-.306	-.234	-.281	.258	-7.97E-02	8.924E-03
8	-.245	-.487	-.550	-.313	-5.91E-02	-.614	-.128	.132	-.118
9	-6.96E-03	-.273	1.359	-.594	.682	8.775E-02	8.797E-02	9.533E-03	-8.57E-03
10	-1.563	-1.898	.623	.774	-.181	-4.68E-03	1.039E-02	2.257E-02	6.485E-03

Unstandardized canonical discriminant functions evaluated at group mean

D

Standardized Canonical Discriminant Function Coefficients

	Function								
	1	2	3	4	5	6	7	8	9
SC	.028	.754	.105	.566	-.127	-.103	-.309	-.243	-.484
TI	.135	-.065	.611	-.127	.005	.317	-.491	.537	.314
V	.863	.176	-.403	.249	.014	-.060	.403	.223	-.111
MN	-.500	.670	-.304	.091	.168	.256	.291	.258	.255
CO	-.391	-.296	-.076	.510	.452	-.494	.028	.317	.463
NI	.418	-.025	-.442	.205	.495	.349	-.404	-.302	.271
GA	.186	.081	.605	-.255	-.007	.066	.482	-.644	.471
PB	-.157	-.501	.089	.651	-.314	.402	.319	.018	.038
SN	-.186	-.366	.023	-.166	.706	.227	.155	.300	-.633

6.6.2. Pyrite

Trace element content and variation

<u>Ernest Henry</u>

The most common trace elements in pyrite at Ernest Henry are Ti, Co, As, Si, Se, and Ni. Also Mg, Al, In, Cu, Sn, Sb, Ru, Mn, Pb, Bi, Cr and Ag were detected in pyrite but were either close to or below the detection limit or exhibited highly erratic values between individual analyses (appendix 9). Mean, maximum and minimum values for all analyses are shown in table 6.6, and the spatial distribution of various trace element concentrations with respect to the Ernest Henry ore-body is presented in figure 6.9. Co and As concentrations are highest in pyrite associated with Cu-Au mineralisation (Fig. 6.9 and 6.10). In contrast, Ni, Se, Ti and Si show no demonstrable difference in concentration between any alteration phase at Ernest Henry. Element maps produced by Proton Induced X-ray Emission (PIXE) shows that pyrite exhibits considerable zonation (e.g. As, Co, Ni) (Mark et al., 1999; Brodie, 2001). These patterns are consistent with the considerable range in As and Co contents in pyrite found in this study (Fig., 6.10).

<u>Other Fe oxide-rich mineralised systems</u>

The trace elements most commonly detected in pyrite outside the Ernest Henry hydrothermal system are Ti, Si, Co, Ni, As and Se. These are the same elements identified in pyrite from Ernest Henry. Also Mg, Al, In, Cu, Sn, Sb, Ru, Mn, Pb, Bi, Cr and Ag were detected. However, these elements were found to either exhibit highly erratic values between individual analyses, or were below the detection limit of the instrument. Mean, maximum and minimum values for all analyses are shown in table 6.7. Pyrite associated with Cu-Au mineralisation typically contains lower mean concentrations of Se and Ni, and higher As and Co concentrations than other mineral associations (Fig. 6.11). Within the ore systems, Ernest Henry contains an order of magnitude higher Co (>10000 ppm) and As (1000-50000 ppm) than the other IOCG deposits, while Mount Elliott and Starra contain the lowest concentrations of these elements (<10 pp Co and <100 ppm As) (Fig. 6.11b). Mount Elliott contains higher concentrations of Ni (Fig. 6.11c) with respect to the other ore deposits (500-5000 ppm), while the Lightning Creek Cu-Au occurrence contains an order of magnitude higher Se (Fig. 6.11e) than all other systems (>100 ppm). Pyrite from Cu-Au mineralisation, K-Fe alteration and marble matrix breccia associations at Ernest Henry contain low Ti values compared to most other systems (<10 ppm). Cu-Au-enriched veins from Lightning

Table 6.6: Mean, minimum and maximum values of the trace element content of pyrite from various alteration stages at the Ernest Henry (Cu-Au) deposit (in ppm). Sample location numbers are presented in appendix 9. Sample type refers to whether the rock is Cu-Au mineralised (M) or weakly mineralised. Also shown is the number of analyses taken for each sample. The hyphen represent analyses that are below the detection limit..

Sample No	Sample Type	No of Analyses		Mg	Al	Si	Ti	Mn	Co	Ni	Cu	Zn	As	Se	Zr	Mo	Ru	In	Sn	Sb	Pb	Bi
EH647	M	7	Min	0.158	0.18	195.26	10.15	0.64	6804.16	33.33	2.19	19.68	563.15	10.61	0.0092	3.22	1.79	0.0055	0.104	0.194	0.151	0.16
			Mean	***0.98***	***4.84***	***1915.41***	***18.84***	***6.07***	***17079.17***	***55.45***	***216.54***	***537.11***	***2170.92***	***12.19***	***42.78***	***19.8***	***4.06***	***0.51***	***0.65***	***0.45***	***3.12***	***1.70***
			Max	1.79	27.4	8149.19	51.93	22.9	33794.3	111.59	1057.27	2042.66	7066.02	15.99	189.65	36.3	8.66	1.76	1.3	0.6	14.08	6.54
FT8C	M	3	Min	0.409	0.338	68.52	1.19	0.054	19168.48	27.32	0.42	0.371	15852.8	15.6	0.0038	0.032	39.5	0.0288	0.041	0.092	0.0723	0.33
			Mean	***2.65***	***2.40***	***86.61***	***3.18***	***0.28***	***24484.51***	***1125.90***	***17.49***	***0.42***	***26037.70***	***16.76***	***5.33***	***7.5***	***42.88***	***0.05***	***0.06***	***0.29***	***1.39***	***15.36***
			Max	4.85	4.92	100.01	7.02	0.552	28024.19	3318.15	34.56	0.462	31870.76	17.75	15.98	22.36	45.22	0.063	0.094	0.649	3.44	30.42
EH201B	M	6	Min	0.039	0.0483	34.34	1.076	0.062	19402.33	39.51	0.397	0.266	7925.44	6.32	0.0079	0.0201	10.45	0.0134	0.0363	0.025	0.004	0.0261
			Mean	***5.35***	***7.74***	***146.14***	***19.54***	***8.31***	***24432.26***	***50.92***	***6.82***	***0.65***	***12936.83***	***10.19***	***8.07***	***0.1***	***25.22***	***0.06***	***0.08***	***0.15***	***0.26***	***1.96***
			Max	30.87	41.04	324.76	92.98	30.64	28926.73	74.23	34.04	1.31	16870.99	13.09	36.58	0.447	49.95	0.244	0.116	0.455	0.603	10.71
E184D	M	4	Min	0.0186	0.207	78.17	2.4	0.621	10898.11	41.99	1.43	0.84	8587.43	5.2	0.0278	0.0187	6.68	0.0147	0.063	0.146	0.0221	0.203
			Mean	***1.84***	***30.23***	***166.95***	***2.51***	***1.47***	***15000.30***	***57.00***	***400.66***	***1.98***	***10068.34***	***5.88***	***0.04***	***0.2***	***8.84***	***0.03***	***0.24***	***1.28***	***5.11***	***15.59***
			Max	5.39	98.3	210.74	2.7	2.31	19112.31	63.95	1212.17	4.81	11294.08	6.66	0.0501	0.441	11.24	0.066	0.477	3.28	11.74	26.38
FT8A	M	3	Min	0.472	0.126	72.8	2.08	0.337	20712.35	424.26	2.37	0.47	13786.84	23.01	0.0259	0.0181	12.52	0.0191	0.058	0.452	0.086	5.7
			Mean	***2.34***	***21.35***	***166.32***	***2.61***	***2.46***	***63704.15***	***607.50***	***6.86***	***0.56***	***69832.78***	***27.30***	***2.34***	***0.1***	***38.36***	***0.07***	***0.07***	***0.80***	***0.37***	***27.78***
			Max	4.63	59.15	279.54	3.57	6.56	94956.21	842.42	12.94	0.66	104148.83	29.52	4.65	0.087	55.16	0.112	0.074	1.09	0.79	66.88
EH201C	M	8	Min	0.0129	0.071	48.87	1.82	0.08	207.93	5.74	0.163	0.75	97.29	1.87	0.0098	0.0191	0.082	0.003	0.073	0.094	0.0095	0.0126
			Mean	***0.03***	***0.13***	***86.51***	***2.10***	***0.08***	***8832.44***	***196.79***	***64.85***	***0.98***	***4754.78***	***9.36***	***0.02***	***0.0***	***5.46***	***0.03***	***0.09***	***0.53***	***0.85***	***8.97***
			Max	0.055	0.221	188.12	2.39	0.08	20602.57	1153.97	395.46	1.18	15163.61	26.86	0.022	0.0232	12.85	0.0838	0.111	2.37	4.72	23.99
FT21A	W	5	Min	0.0218	0.06	121.3	2.12	-	4297.7	61.71	0.088	0.535	1758.92	15.13	0.0134	0.0098	1.59	0.0095	0.083	0.035	0.0241	0.0109
			Mean	***15.44***	***15.83***	***208.26***	***2.26***	-	***7437.42***	***90.28***	***0.37***	***0.75***	***2683.10***	***19.05***	***45.53***	***0.1***	***2.91***	***0.01***	***0.12***	***0.42***	***0.78***	***2.62***
			Max	76.81	78.56	294.18	2.47	-	10212.24	110.66	1.28	1.24	4182.67	26.94	213.38	0.266	3.83	0.0188	0.172	1.09	3.76	11.79
FT4A1	W	2	Min	-	0.078	162.25	2.19	-	9720.93	75.55	0.122	0.57	509.17	7.76	0.0106	-	4.05	0.0099	0.138	-	-	0.0084
			Mean	-	***0.09***	***173.98***	***2.24***	-	***19140.02***	***87.74***	***0.15***	***0.62***	***3265.94***	***8.45***	***0.16***	-	***7.95***	***0.01***	***0.15***	-	-	***0.01***
			Max	-	0.1	185.7	2.28	-	28559.11	99.93	0.175	0.67	6022.7	9.14	0.319	-	11.84	0.0177	0.163	-	-	0.014
FT4A2	W	6	Min	0.043	0.116	74.27	2.07	-0.09	74.69	24.47	0.31	1.09	36.95	-	-0.0085	-	0.074	0.0047	0.079	0.086	0.116	-0.0099
			Mean	***0.53***	***4.41***	***87.81***	***2.22***	***0.23***	***625.70***	***35.64***	***2.76***	***1.30***	***131.87***	-	***0.03***	-	***0.35***	***0.01***	***0.08***	***0.16***	***1.25***	***0.21***
			Max	1.262	29.67	107.27	2.71	0.524	1165.76	48.8	6.32	1.68	211.84	-	0.054	-	0.704	0.0074	0.083	0.235	3.08	0.428
EH184B	W	3	Min	0.486	0.46	56.81	1.3	0.127	18729.98	35.16	0.141	0.453	2446.84	7.17	0.0036	0.011	9.49	0.0071	0.062	0.0414	0.0261	0.116
			Mean	***7.40***	***8.25***	***126.13***	***9.57***	***1.04***	***20758.04***	***40.32***	***0.30***	***0.56***	***2744.52***	***7.39***	***2.90***	***0.0***	***10.30***	***0.01***	***0.08***	***0.12***	***0.03***	***1.44***
			Max	20.24	22.35	244.56	18.33	1.96	22777.35	48.21	0.512	0.77	3046.4	7.73	5.8	0.0181	11.03	0.015	0.088	0.201	0.0335	3.65
FT4A2	W	9	Min	0.043	0.116	74.27	2.07	0.089	74.69	24.47	0.31	1.09	36.95	-	0.0112	-	0.074	-	0.069	0.086	0.116	0.0088
			Mean	***0.53***	***4.41***	***87.81***	***2.22***	***0.23***	***625.70***	***35.64***	***2.76***	***1.30***	***131.87***	-	***0.03***	-	***0.35***	-	***0.08***	***0.16***	***1.25***	***0.21***
			Max	1.262	29.67	107.27	2.71	0.524	1165.76	48.8	6.32	1.68	211.84	-	0.054	-	0.704	-	0.083	0.235	3.08	0.428
FT94A	W	4	Min	0.0174	0.055	36.44	1.91	-	127.75	347.56	0.165	1.027	3.15	56.55	-	0.0147	0.1	-	0.099	0.034	0.014	0.0237
			Mean	***0.03***	***0.09***	***50.13***	***2.05***	-	***7731.15***	***553.04***	***0.25***	***1.25***	***53.13***	***88.95***	-	***0.01***	***4.71***	-	***0.11***	***0.04***	***0.07***	***0.03***
			Max	0.037	0.205	70.25	2.35	-	18134.63	701.86	0.305	1.3	199.98	177.59	-	0.285	11.34	-	0.13	0.0817	0.18	0.0362
EH151	W	7	Min	0.0251	0.079	58.6	2.34	0.096	18.04	49.27	0.241	0.92	2.56	3.27	0.006	0.0122	0.044	-	0.059	0.111	0.06	0.0095
			Mean	***0.09***	***0.19***	***107.46***	***2.63***	***1.36***	***871.18***	***198.66***	***2.47***	***1.05***	***35.22***	***5.40***	***0.46***	***0.0***	***1.27***	-	***0.08***	***0.19***	***0.18***	***1.20***
			Max	0.171	0.312	193.23	2.84	6.3	4763.27	371.1	10.62	1.18	216.59	8.23	2.23	0.08	2.71	-	0.133	0.279	0.441	7.57
FT4B	W	5	Min	0.0122	0.082	68.21	2.32	-	9692.22	50.56	0.261	0.85	1010.14	6.17	0.0058	0.0127	6.48	0.0032	0.046	0.039	0.0098	0.0169
			Mean	***0.18775***	***0.121***	***92.65***	***2.508***	-	***15175.668***	***76.824***	***0.744***	***0.916***	***5861.148***	***7.824***	***1.993425***	***0.016667***	***10.068***	***0.0114***	***0.063***	***0.0912***	***0.02355***	***0.01845***
			Max	0.69	0.147	121.35	2.68	-	25782.15	110.44	2.19	1.01	17946.94	9.39	7.95	0.0235	16.72	0.0266	0.079	0.113	0.0339	0.02

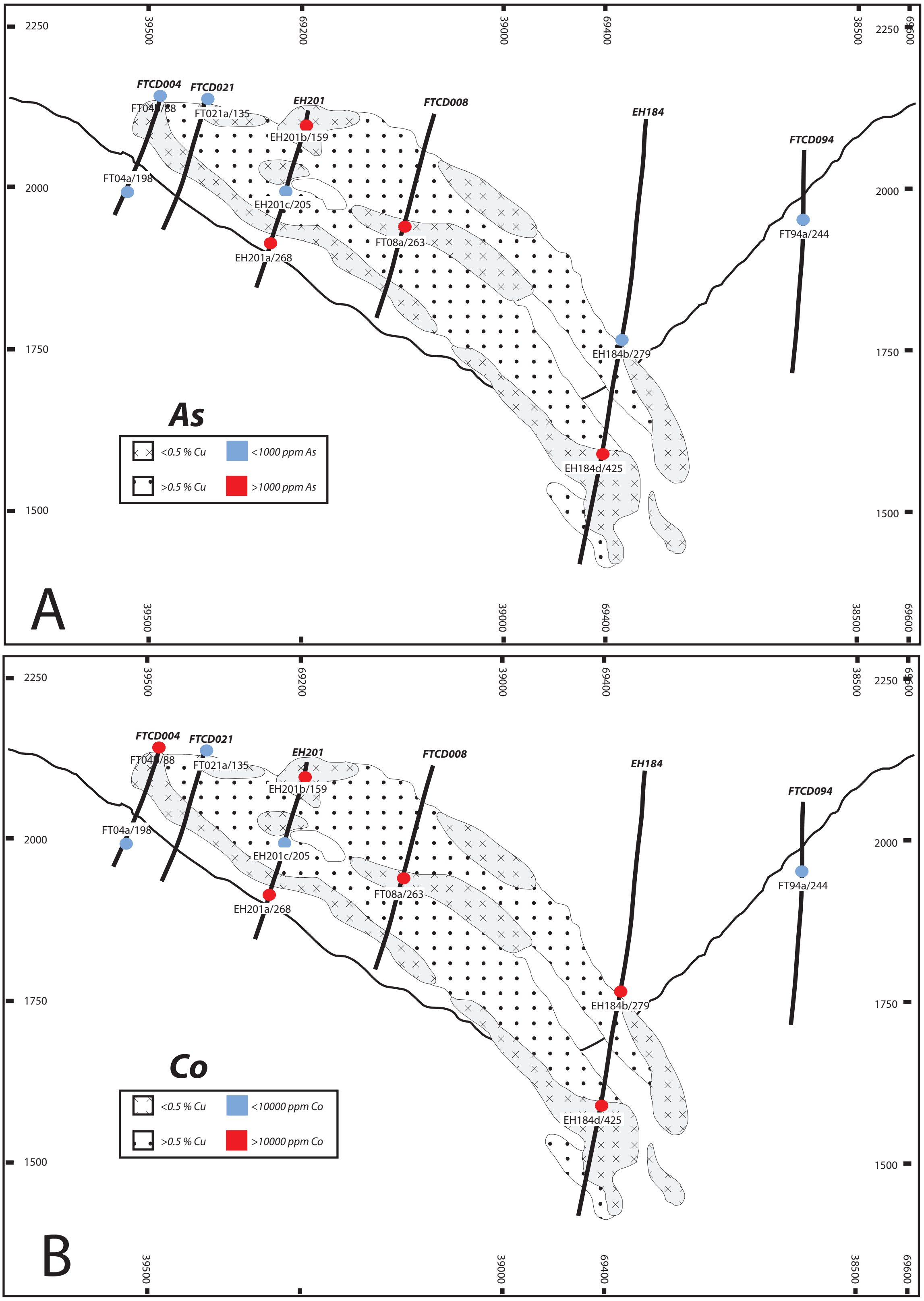

Figure 6.9a and b: As and Co contents of pyrite annotated on a crossection of the Ernest Henry ore body, looking north, with drill hole traces and location of samples used for this study. Trace element values of pyrite are averaged equivalents of individual analyses from each sample, and standard deviations of these values are given in Appendix 9. These values are divided into categories of low and high, represented as coloured circles (blue=low and red=high).

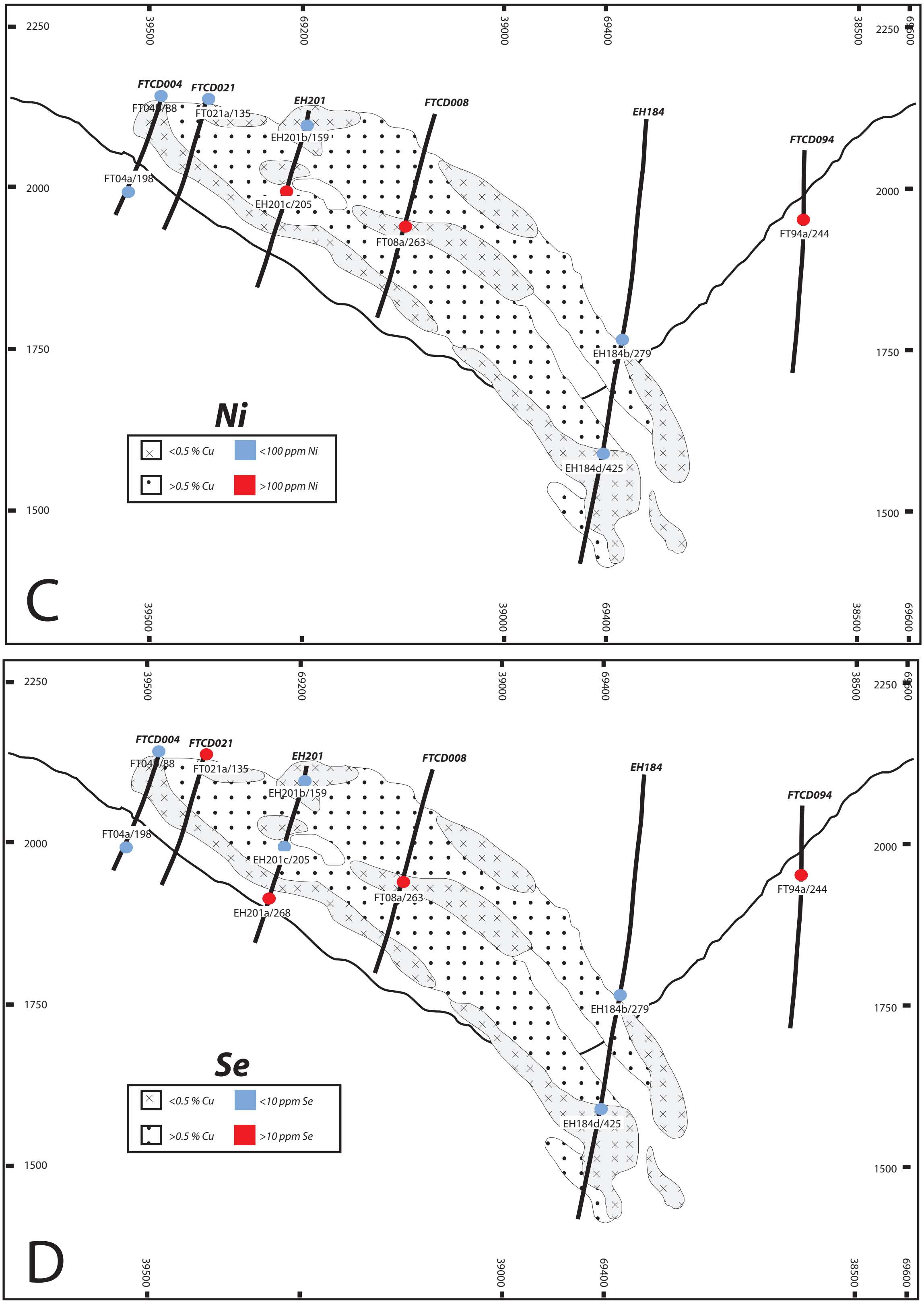

Figure 6.9c and d: Ni and Se contents of pyrite annotated on a crossection of the Ernest Henry ore body looking north, with drill hole traces and location of samples used for this study. Trace element values of pyrite are averaged equivalents of individual analyses from each sample, and standard deviations of these values are given in Appendix 9. These values are divided into categories of low and high, represented as coloured circles (blue=low and red=high).

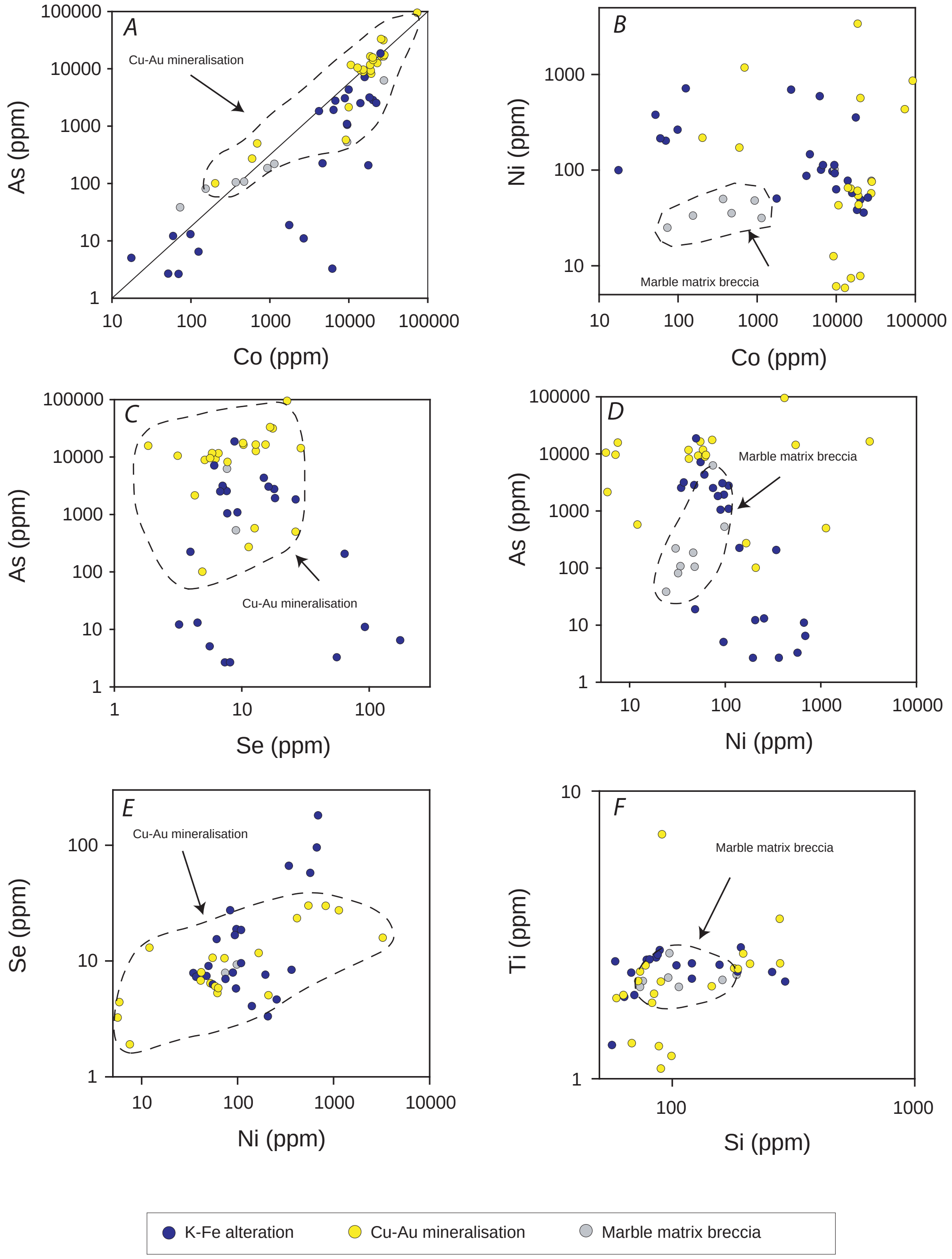

Figure 6.10: Bi-plots of trace element concentrations measured in pyrite from the Ernest Henry Cu-Au system. Various alteration phases include: Cu-Au mineralisation (Yellow), K-Fe alteration (Blue) and marble matrix breccia (Grey).

Table 6.7: Mean, minimum and maximum values of the trace element content of pyrite from various Fe oxide-rich systems in the EFB (in ppm). Sample location numbers are presented in appendix 9. Sample type refers to whether the rock is Cu-Au mineralised (M) or weakly mineralised. Also shown is the number of analyses taken for each sample. The hyphen represent analyses that are below the detection limit.

Sample No		No of Analyses		Mg	Al	Si	Ti	Cr	Mn	Co	Ni	Cu	Zn	As	Se	Mo	Ru	Ag	In	Sn	Sb	Pb	Bi
ST1	M	7	Min	0.358	0.485	100.04	9.88	0.42	0.38	74.02	30.58	2.74	3.04	4.3	15.74	0.241	0.028	0.294	0.0101	0.067	0.372	1.18	0.069
			Mean	***21.99***	***34.57***	***222.10***	***11.44***	***0.42***	***0.85***	***115.97***	***57.31***	***1025.68***	***191.84***	***12.09***	***18.71***	***0.24***	***0.03***	***1.48***	***0.48***	***0.60***	***1.55***	***9.02***	***2.54***
			Max	80.87	96.45	322.53	13.05	0.42	1.89	153.43	104.18	4617.84	592.9	28.62	21.51	0.241	0.028	4.51	1.5	1.16	2.65	17.93	7.18
OS1	M	6	Min	0.32	0.61	376.57	14.37	-	0.55	34052.86	89.13	1.34	2.6	55.83	64.85	8.1	6.32	0.233	0.132	0.27	0.134	0.163	0.226
			Mean	***4.56***	***4.34***	***597.00***	***16.48***	***-2.00***	***0.90***	***41609.38***	***137.11***	***11.36***	***52.92***	***929.85***	***91.61***	***294.33***	***7.34***	***0.67***	***3.04***	***0.71***	***9.95***	***6.05***	***20.50***
			Max	10.36	9.31	906.41	18.96	-	1.57	49315.21	190	35.82	139.54	1727.42	120.89	1009.69	8.5	1.65	13.36	1.15	57.2	22.13	73.45
ME	M	16	Min	0.6	0.68	203.46	2.85	0.227	0.85	2.8	235.19	4.93	2.23	1.5	16.5	0.07	0.0276	0.025	0.05	0.107	0.118	0.49	0.886
			Mean	***236.88***	***161.29***	***1761.12***	***24.02***	***2.02***	***97.27***	***1184.69***	***1076.00***	***867.71***	***42.67***	***8.37***	***39.20***	***4.49***	***0.48***	***0.32***	***0.61***	***0.69***	***0.59***	***4.18***	***13.73***
			Max	1335.68	510.09	5960.67	111.26	17.74	295.86	7881.4	2151.56	7625.5	234.4	52.89	104.25	57.9	2.53	0.8	1.52	3.07	1.47	9.75	48.35
262	W	5	Min	2.58	0.184	215.17	8.88	-	0.43	22.89	971.83	0.83	1.19	61.17	57.54	0.2	0.145	0.053	0.083	0.142	0.265	-	0.544
			Mean	***3.25***	***1.18***	***436.50***	***9.35***	-	***0.87***	***487.71***	***2738.87***	***94.81***	***371.66***	***191.48***	***77.78***	***17.18***	***0.22***	***0.35***	***0.28***	***0.29***	***0.91***	-	***5.28***
			Max	3.91	2.58	828.95	10.31	-	1.68	1190.94	5068.45	466.95	1799.62	368.9	112.75	82.5	0.28	0.51	0.668	0.443	1.58	-	10.79
222	W	6	Min	0.56	0.4	155.77	13.06	1.35	0.58	4229.32	160.66	2.02	1.98	82.97	20.59	0.91	1.07	0.071	0.027	0.19	0.043	2.05	0.153
			Mean	***15.59***	***135.82***	***628.41***	***921.98***	***2.28***	***24.51***	***9890.72***	***242.36***	***4.35***	***124.52***	***229.56***	***34.90***	***10.33***	***2.13***	***0.31***	***1.02***	***2.25***	***0.25***	***5.22***	***1.17***
			Max	72.56	752.35	2525.65	5463.03	4.35	140.42	11548.64	560.59	11.05	647.46	417.16	85.54	37.28	2.69	0.63	2.6	5.55	0.72	8.11	4.18
204	W	9	Min	0.405	0.104	188.8	7.55	0.33	0.657	1334.76	70.08	0.34	1.48	2.4	6.97	0.106	0.311	0.075	0.136	0.109	0.0222	0.0138	0.124
			Mean	***35.86***	***9.51***	***445.70***	***8.82***	***1.12***	***2.04***	***6240.84***	***618.18***	***2.75***	***10.75***	***57.21***	***14.27***	***2.26***	***1.54***	***0.36***	***0.32***	***0.63***	***0.28***	***0.04***	***1.14***
			Max	92.42	54.47	1457.78	9.89	1.98	4.57	14260.9	1535.1	9.87	27.51	161.82	19.58	11.74	3.33	0.9	0.64	2.32	0.605	0.063	5.45
312	W	8	Min	0.96	2.72	343.36	16.8	1.82	0.5	96.8	46.13	0.32	6.11	1.54	7.81	0.12	1.38	0.111	0.014	0.16	0.144	0.6	0.113
			Mean	***74.79***	***65.66***	***976.60***	***19.69***	***2.76***	***4.06***	***8321.97***	***1848.44***	***4.53***	***229.28***	***498.74***	***12.86***	***50.49***	***2.36***	***1.08***	***0.63***	***0.78***	***0.76***	***18.33***	***3.26***
			Max	337.66	183.16	2649.17	22.14	3.6	12.4	18674.22	4721.2	10.55	1528.59	1470.48	21.38	204.44	3.61	2.64	1.25	1.23	2.47	120.39	9.39
254	W	9	Min	0.114	0.234	171.39	2.84	0.8	0.236	565.47	8.4	0.54	0.03	62.42	23.25	0.134	0.56	0.045	-	0.099	0.045	0.047	0.09
			Mean	***75.94***	***44.76***	***267.71***	***5.46***	***0.98***	***1.18***	***8400.25***	***978.43***	***11.03***	***5.35***	***448.15***	***75.91***	***1.84***	***4.01***	***0.40***	***0.58***	***0.65***	***1.20***	***4.48***	***2.04***
			Max	453.16	239.51	445.25	7.04	1.27	4.18	12507.63	6461.53	68.67	14.63	1206.69	175.71	5.02	5.86	0.736	-	0.962	2.49	19.91	13.67
338	W	5	Min	0.181	2.102	146.6	3.99	0.52	0.35	24.67	163.52	3.56	-	44.09	44.72	0.152	0.69	0.204	0.163	0.104	0.185	0.163	1.382
			Mean	***912.98***	***702.14***	***2685.48***	***5.26***	***1.04***	***16.09***	***1744.44***	***1378.16***	***402.29***	-	***452.47***	***52.72***	***1.85***	***3.63***	***0.65***	***0.21***	***0.69***	***1.34***	***7.54***	***7.45***
			Max	2974.57	2578.6	4966.87	7.87	1.59	33.79	7161.86	2785.57	1888.22	-	971.14	64.73	5.23	6.57	1.644	0.257	1.57	4.98	14.16	23.28
LCD106	W	3	Min	0.1258	0.1334	78.42	1.574	-	0.166	221.32	755.89	-	0.484	0.254	290.41	0.007	0.132	0.0291	0.0211	0.0469	0.23	0.643	0.213
			Mean	***2.00***	***2.30***	***93.21***	***1.64***	-	***0.48***	***718.25***	***1655.63***	-	***1.55***	***2.64***	***303.40***	***0.01***	***0.41***	***0.13***	***0.11***	***0.06***	***0.88***	***3.82***	***1.92***
			Max	5.71	6.55	119.57	1.695	-	0.656	1105.87	2269.08	-	2.61	5.41	317.89	0.0129	0.613	0.282	0.1851	0.0812	2.14	8.89	4.74
LC13	W	9	Min	0.0163	0.086	25.78	1.87	-	0.117	0.067	0.146	0.383	0.45	24.44	168.68	-	0.564	0.026	0.00179	0.06	0.069	0.0183	0.06
			Mean	***4.53***	***6.80***	***144.56***	***2.22***	-	***0.33***	***3676.02***	***602.39***	***22646.52***	***20.82***	***64.82***	***250.14***	-	***2.40***	***4.00***	***1.00***	***3.20***	***0.13***	***5.00***	***0.21***
			Max	12.67	45.19	593.62	2.55	-	0.955	7622.15	1282.74	2.33	180.14	174.07	487.73	-	4.77	15.69	3.98	24.75	0.284	41.35	0.506
1714	W	3	Min	0.0199	0.094	67.26	1.22	-	-	48.62	94.06	0.615	0.521	34.07	24.8	-	0.615	-	0.007	0.042	0.234	0.0199	0.0271
			Mean	***0.02***	***6.45***	***108.97***	***1.37***	-	-	***2977.92***	***360.27***	***170.90***	***0.65***	***384.01***	***36.96***	-	***2.42***	***0.02***	***0.01***	***0.05***	***0.41***	***0.03***	***2.03***
			Max	0.023	18.27	166.36	1.61	-	-	7780.47	561.87	280.05	0.84	1056.44	44.37	-	4.22	-	0.0135	0.065	0.497	0.0399	3.62
243	W	9	Min	0.131	1.31	36.33	6.4	-	0.246	87.08	777.3	0.74	0.87	14.78	49.33	0.177	0.172	0.106	0.008	-	0.517	0.0216	0.117
			Mean	***1.88***	***2.64***	***64.58***	***7.37***	-	***0.71***	***601.36***	***1864.44***	***13.25***	***89.04***	***56.33***	***71.04***	***5.80***	***0.36***	***0.12***	***0.58***	***0.11***	***0.52***	***0.73***	***0.96***
			Max	7.3	3.87	164.41	9.09	-	1.335	1333.72	3798.54	48.72	286.7	153.08	130.44	21.45	0.64	0.132	1.152	-	0.532	2.49	3.47
125	W	3	Min	0.397	0.854	49.78	4.29	-	0.318	175.06	31.78	0.266	0.61	29.21	11.12	1.23	0.087	-	-	-	-	0.062	0.106
			Mean	***4.15***	***8.20***	***57.04***	***4.38***	-	***14.38***	***2286.08***	***111.90***	***13.30***	***0.99***	***130.97***	***17.75***	***1.23***	***0.99***	-	-	-	-	***2.21***	***0.66***
			Max	7.9	20.34	64.73	4.46	-	42.47	3391.64	201.93	36.69	1.36	232.72	29.89	1.23	1.59	-	-	-	-	6.32	1.765
273	W	7	Min	2.79	7.63	160.55	5.81	1.33	0.317	8281.35	31.1	0.75	1.38	44.84	7.56	0.049	2.82	0.025	0.0104	0.103	0.044	0.53	0.282
			Mean	***25.68***	***84.54***	***348.15***	***71.87***	***1.57***	***1.63***	***10334.82***	***57.69***	***3.54***	***69.64***	***250.56***	***10.19***	***0.35***	***3.94***	***0.15***	***0.07***	***0.27***	***0.07***	***3.33***	***1.19***
			Max	64.06	198.42	567.05	445.83	1.81	6.06	15070.36	87.18	6.66	221.89	817.59	13.65	0.98	5.61	0.43	0.122	0.39	0.104	9.15	4.73
217	W	9	Min	0.104	0.217	118.92	7.7	0.7	0.301	28.96	2049.82	2.03	0.59	46.11	37.58	0.122	0.33	0.026	0.0056	0.331	0.064	0.064	0.067
			Mean	***9.35***	***18.80***	***394.00***	***10.51***	***1.15***	***3.38***	***509.19***	***4366.04***	***25.72***	***34.74***	***82.46***	***74.99***	***5.80***	***0.66***	***0.46***	***0.50***	***1.32***	***0.59***	***2.61***	***0.49***
			Max	53.68	60.36	1042.87	27.13	1.57	13.04	1727.1	7974.77	135.78	110.93	149.85	127.42	18.02	1.16	1.93	0.93	2.33	2.21	13.97	1.79

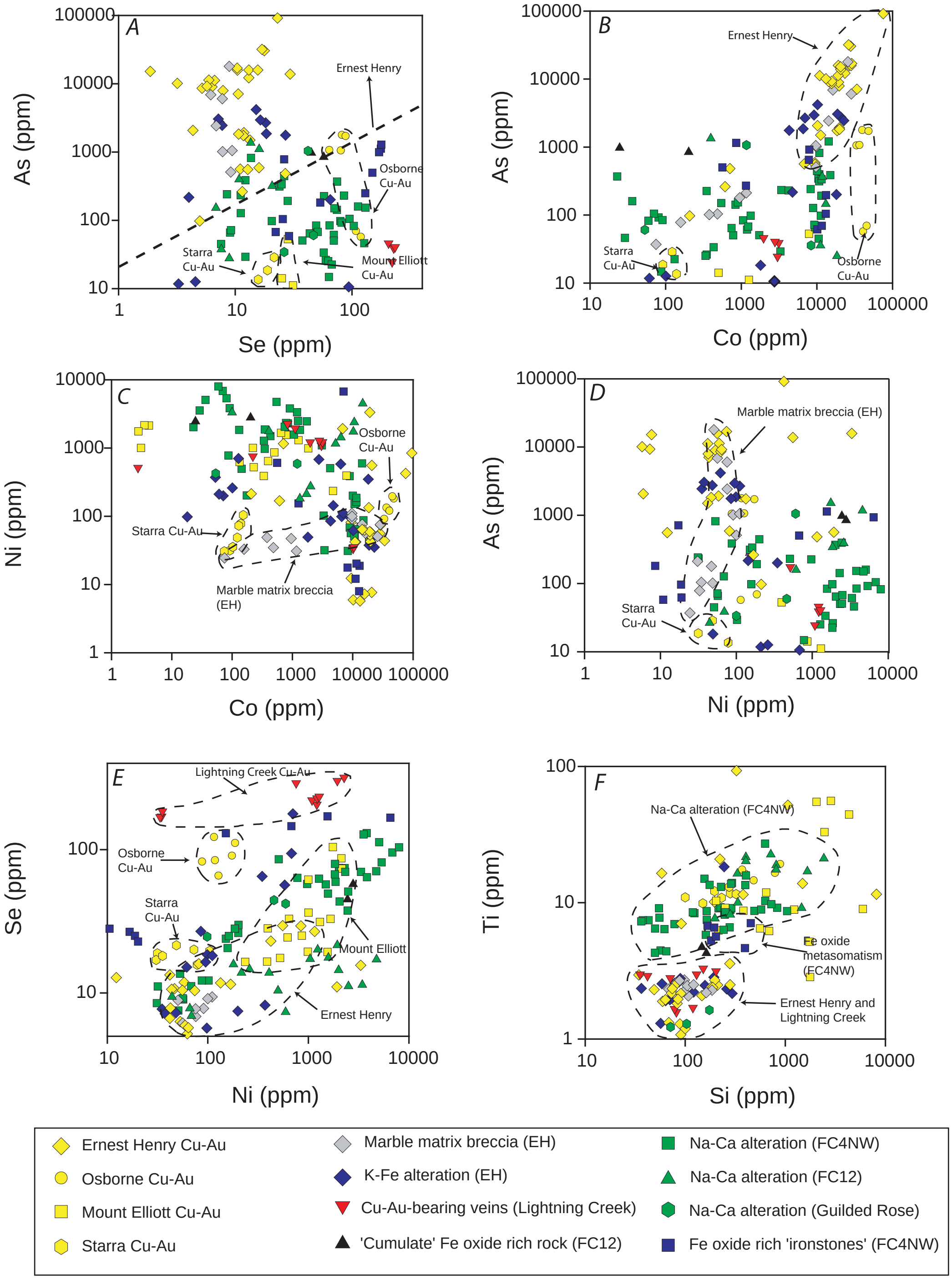

Figure 6.11: Bi-plots of trace elements identified in pyrite from various Fe oxide-rich systems in the EFB. Yellow symbols represent pyrite from Cu-Au mineralisation at Ernest Henry, Starra, Osborne and Mount Elliott. K-Fe alteration, marble matrix breccia, Na-Ca alteration from FC4NW, and FC12 and cumulate Fe oxide-rich rocks from the FC12 prospect represent weakly mineralised systems analysed. One Na-Ca vein from the Gilded Rose containing pyrite was also analysed.

Creek and Na-Ca alteration from the Gilded Rose area also contain low Ti values (Fig. 6.11f).

Major and trace element substitution

In pyrite, Co, Ni and Se substitute for Fe (Co, Ni) and S (Se) and fall into the Huston et al (1995) 'stoichiometric' group. In addition, Huston et al (1995) found that As decreased in pyrite as a result of later recrystallisation, and was therefore categorised as a 'non stoichiometric' element. Work by Cook and Chryssoulis (1990) showed that As substitution into pyrite occurs when $[AsS]^{3-}$ anion pairs substitute for $[S_2]^{2-}$ anion pairs. The presence of Si and Ti is more difficult to explain. Ti^{4+} will substitute for Fe^{3+} but is rarely identified in pyrite. It is possible that both Si and Ti may represent minor inclusions of other mineral phases.

Discriminant analysis

A discriminant analysis of the entire dataset was undertaken for pyrite using 5 groups defined by their geological setting (table 6.1) and produced four discriminating functions. The first discriminant function accounted for 84.9 % of the total variance in the dataset, while the other three discriminant functions both accounted for 10.5%, 4.5% and 0.1% of the overall variance respectively (Table 6.8a). Classification of the results, however, shows that the discriminant analysis was less successful in classifying the data into their pre-defined groups compared to magnetite (Table 6.8b). 43.3% of all analyses assigned as Cu-Au mineralisation were classified as group 1 according to the trace element geochemistry. The remaining analyses were classified as group 2 (Na-Ca alteration; 13.3%), group 3 (pre- and post- ore pyrite from Ernest Henry; 41.7%) and group 4 (Fe oxide rich rocks; 1.7%). In total, only 50.3% of all analyses were classified into their pre-defined groups based on the trace element geochemistry. The table of group centroids (Table 6.8c) shows groups 1 (Cu-Au mineralisation) and 5 (Lightning Creek) exhibiting the largest differentiation for function 1, whereas function 2 differentiates most strongly between mineral group 2 (Na-Ca alteration) and 1 (Cu-Au mineralisation). The most important contributors to the first two discriminant functions include Ni and Se (function 1) and Co and Ni (function 2) (Table 6.8d). These results are consistent with the X-Y plots in figure 6.11, where Se, Ni and Co each varies significantly between Cu-Au mineralisation and other Fe oxide and sulphide-bearing systems.

Table 6.8: Results of the stepwise discriminant analysis for pyrite

A. *Calculated eigenvalues for each of the discriminant functions for pyrite produced from the discriminant analysis. The larger the eigenvalue, the greater the separation between the pre-defined groups. Also shown is the canonical correlation for each discriminant function, where the closer the value is to 1, the higher the degree of association between the discriminant function and the groups. % variance and cumulative % of each successive discriminant function is also shown.*
B. *Classification table showing the degree to which the discriminant functions differentiate between the groups for pyrite. Further explanation of the table is given in the text.*
C. *Table of group centroids showing the way in which each discriminant function differentiates between the pre-defined groups for pyrite. Further explanation of the table is given in the text.*
D. *Table of the standardized canonical discriminant function coefficients showing to what degree each of the elements contribute to each of the discriminant functions for pyrite.*

A

Eigenvalues

Function	Eigenvalue	% of Variance	Cumulative %	Canonical Correlation
1	2.366[a]	84.9	84.9	.838
2	.292[a]	10.5	95.4	.475
3	.128[a]	4.6	99.9	.337
4	.001[a]	0.1	100.0	.029

B

Classification Results

		Mineral associations	Predicted Group Membership					Total
			1	2	3	4	5	
Original	Count	1	26	8	25	1	0	60
		2	8	23	19	9	0	59
		3	5	0	25	3	1	34
		4	0	2	5	3	1	11
		5	0	0	0	0	11	11
	%	1	43.3	13.3	41.7	1.7	.0	100.0
		2	13.6	39.0	32.2	15.3	.0	100.0
		3	14.7	.0	73.5	8.8	2.9	100.0
		4	.0	18.2	45.5	27.3	9.1	100.0
		5	.0	.0	.0	.0	100.0	100.0

a. 53.7% of original grouped cases correctly classified

C

Functions at Group Centroids

mineral association	Function			
	1	2	3	4
1	-.504	.606	.253	4.501E-04
2	-.420	-.651	.150	-1.34E-02
3	-.496	.147	-.700	-5.42E-03
4	.803	-.399	-1.56E-02	.108
5	5.730	.130	-4.72E-03	-2.16E-02

Unstandardized canonical discriminant functions evaluated at group mean

D

Standardized Canonical Discriminant Function Coefficients

	Function			
	1	2	3	4
SI	-.114	.383	.676	-.634
CO	-.130	.577	.483	.684
NI	-.468	-.719	.638	.363
SE	1.103	.112	.083	-.002

6.6.3. Chalcopyrite

Trace element content and variation

The trace elements most commonly detected in chalcopyrite are Ti, Si, Co, Ni, Zn, Se, Ag, In, Sn, Pb and Bi (appendix 9). Other elements detected in chalcopyrite are Mo, Ru, Sb, V, Mn, Au, U, Cd and W but their concentrations were typically either close to or below the detection limit or exhibited highly erratic values. Mean, maximum and minimum values for all analyses are shown in table 6.9. Chalcopyrite from the Cu-Au deposits contain higher Bi, Sn, In and Ag and lower Se contents compared to weakly mineralised systems (Fig. 6.12), whereas Pb and Ni do not readily discriminate between the Cu-Au deposits and weakly mineralised systems. Within the ore systems, Osborne and Starra contain higher Co, Zn, Pb, Ti and Ni concentrations compared to Ernest Henry and Mount Elliott (Fig. 6.12a, b, f). The Osborne and Lightning Creek Cu-Au occurrences, on the other hand, contain much higher Se concentrations (Fig. 6.12e) compared to the other ore systems (>100 ppm). Chalcopyrite associated with Na-Ca alteration at FC4NW contains higher Ag (>30 ppm), Ti (5-10 ppm) and Se (>100 ppm) but lower In (<5 ppm) compared to Na-Ca alteration from the Guilded Rose area (Fig. 6.12d, e, f).

Major and trace element substitution

This study reveals numerous similarities in trace element composition and makeup compared to previous studies described in section 5.2. However, this study found a greater variety of trace elements. As described for magnetite and pyrite, Ti, Co, In, Ni and possibly Zn can substitute for Fe and Se substitutes for S. Ag and Bi are detected in chalcopyrite only. Huston et al (1995) noted that Ag substitutes for Cu, while Goldschmidt (1958) noted that in high temperature hydrothermal deposits, Bi is commonly associated with Se. Si typically will not partition into the chalcopyrite crystal lattice; therefore, its presence in analyses may be due to minor inclusions of silicates.

Discriminant analysis

Three discriminant functions were produced for chalcopyrite from the discriminant analysis (Table 6.10a). The first discriminant function represents 70.1% of the overall variance in the dataset, and functions 2 and 3 account for 25.8% and 4.1% of the overall

Table 6.9: Mean, minimum and maximum values of the trace element content of chalcopyrite from various Fe oxide-rich systems in the EFB (in ppm). Sample location numbers are presented in appendix 9. Sample type refers to whether the rock is Cu-Au mineralised (M) or weakly mineralised (W). Also shown is the number of analyses taken for each sample. The hyphen represent analyses that are below the detection limit..

Sample No	Sample Type	No of Analyses		Mg	Al	Si	Ti	V	Cr	Mn	Co	Ni	Zn
ST1	M	8	Min	1.11	0.53	219.63	10.33	0.24	2.51	1.51	3.56	9.09	19.07
			Mean	***13.01***	***15.13***	***699.07***	***13.83***	***4.56***	***5.10***	***4.44***	***15.60***	***24.32***	***307.28***
			Max	51.44	87.75	1623.13	15.79	19.09	9.58	18.16	37.65	52.24	1743.08
OS1	M	10	Min	0.58	0.57	713.28	13.07	0.14	2.20	0.65	23.62	8.78	171.96
			Mean	***6.05***	***16.03***	***2243.30***	***19.27***	***2.72***	***2.93***	***6.29***	***42.74***	***14.07***	***396.01***
			Max	18.30	63.95	5219.64	39.52	8.53	3.66	15.55	55.83	29.77	1852.17
ME	M	4	Min	1.15	1.67	263.64	9.40	0.17	0.83	0.48	0.26	0.36	81.99
			Mean	***60.03***	***9.17***	***1140.36***	***12.82***	***0.29***	***0.86***	***1.94***	***3.27***	***3.71***	***595.34***
			Max	231.68	30.24	3015.06	22.02	0.55	0.89	4.34	6.28	7.08	1644.51
EH647	M	4	Min	1.68	4.97	373.98	10.69	0.28	4.47	0.47	9.79	4.03	55.97
			Mean	***10.99***	***32.08***	***1390.74***	***13.78***	***1.52***	***5.66***	***5.53***	***173.34***	***10.63***	***647.32***
			Max	21.64	102.88	2451.53	16.02	2.77	6.84	12.72	483.19	20.76	2102.06
EH201	M	4	Min	0.07	0.04	125.61	0.80	-	-	0.21	0.58	-	1.59
			Mean	***0.25***	***0.07***	***205.80***	***0.97***	-	-	***1.23***	***1.69***	-	***3.41***
			Max	0.37	0.10	339.67	1.07	-	-	3.96	2.40	-	4.90
EH201B	M	5	Min	0.07	0.57	173.28	2.78	-	-	0.15	1.37	-	2.83
			Mean	***0.61***	***3.18***	***301.87***	***3.18***	-	-	***0.15***	***1.82***	-	***3.26***
			Max	1.04	5.78	449.03	4.03	-	-	0.15	2.10	-	3.90
FT8A	M	10	Min	0.07	0.05	228.62	0.96	-	0.45	0.10	0.22	0.07	29.27
			Mean	***0.29***	***0.21***	***352.75***	***1.92***	-	***0.60***	***0.19***	***1.45***	***0.30***	***47.61***
			Max	0.81	0.45	772.96	2.94	-	0.75	0.28	1.97	1.14	63.88
EH184D	M	4	Min	0.15	0.17	39.87	2.19	0.02	-	1.86	0.07	0.16	5.12
			Mean	***6.55***	***3.12***	***237.45***	***2.47***	***0.03***	-	***2.61***	***0.15***	***0.18***	***6.82***
			Max	16.13	8.83	547.17	2.77	0.04	-	3.47	0.28	0.21	9.13
EH201C	M	3	Min	0.09	0.46	264.47	2.12	-	-	-	0.05	0.10	15.11
			Mean	***1.63***	***0.46***	***360.38***	***2.62***	-	-	-	***0.07***	***1.11***	***15.67***
			Max	3.17	0.46	534.90	3.13	-	-	-	0.09	2.12	16.05
262	W	9	Min	4.16	1.61	879.39	6.77	0.08	1.10	0.93	0.20	0.72	82.95
			Mean	***34.31***	***11.53***	***1124.69***	***9.75***	***0.58***	***3.39***	***1.69***	***18.28***	***32.92***	***234.89***
			Max	122.92	39.79	1384.38	14.67	1.76	5.68	3.25	121.98	113.09	349.90
338	W	8	Min	0.33	0.50	502.45	4.25	0.53	2.13	0.36	0.30	2.22	-
			Mean	***286.79***	***13.07***	***2557.83***	***5.82***	***3.99***	***30.41***	***11.73***	***4.34***	***7.92***	-
			Max	1994.74	71.84	7504.14	8.06	7.86	58.68	41.87	10.24	23.67	-
LCD106	W	7	Min	0.09	0.05	91.87	1.31	0.00	0.13	0.11	0.28	0.02	4.37
			Mean	***12.54***	***1.49***	***296.78***	***1.52***	***0.21***	***0.29***	***9.25***	***0.43***	***0.15***	***10.13***
			Max	43.33	4.84	936.44	1.62	1.15	0.60	24.85	0.62	0.53	24.97
1714	W	8	Min	0.10	0.24	163.58	1.69	0.37	-	0.96	0.19	0.37	7.17
			Mean	***1.67***	***4.38***	***317.87***	***2.25***	***0.37***	-	***0.96***	***5.98***	***1.14***	***9.77***
			Max	4.27	8.65	481.03	3.45	0.37	-	0.96	26.27	3.78	18.88
243	W	4	Min	4.28	11.62	335.32	9.89	0.14	-	2.10	0.45	17.65	102.53
			Mean	***67.59***	***98.11***	***1700.42***	***20.76***	***10.89***	-	***72.93***	***13.14***	***286.56***	***446.44***
			Max	177.32	258.73	4544.21	41.56	42.63	-	193.04	40.45	1001.31	842.70

Sample No	Sample Type	No of Analyses		Se	Mo	Ru	Ag	In	Sn	Sb	W	Pb	Bi
ST1	M	8	Min	21.63	0.43	0.23	0.87	5.42	93.16	0.20	0.03	3.07	0.57
			Mean	***28.62***	***2.60***	***0.44***	***2.11***	***8.55***	***139.21***	***4.76***	***0.56***	***16.31***	***3.04***
			Max	34.53	5.22	0.62	4.43	14.38	189.97	9.70	1.87	44.04	7.21
OS1	M	10	Min	218.81	5.34	0.18	59.88	13.77	217.40	1.00	0.03	1.52	7.27
			Mean	***279.45***	***97.27***	***0.31***	***68.40***	***17.65***	***312.28***	***3.03***	***3.06***	***10.71***	***14.92***
			Max	334.66	434.48	0.54	82.46	22.47	395.67	9.05	8.34	30.88	58.09
ME	M	4	Min	17.14	1.32	0.33	2.10	8.13	5.47	0.21	0.13	4.38	0.63
			Mean	***66.34***	***12.22***	***0.40***	***6.64***	***13.21***	***12.37***	***0.69***	***0.69***	***290.45***	***6.06***
			Max	110.56	37.04	0.48	10.67	20.95	18.06	1.18	1.39	740.67	22.02
EH647	M	4	Min	43.39	1.51	0.38	33.25	7.37	4.20	1.69	0.23	4.67	1.70
			Mean	***45.32***	***13.98***	***0.43***	***39.75***	***8.06***	***36.07***	***4.60***	***2.77***	***6.00***	***4.05***
			Max	47.34	32.74	0.49	47.12	8.63	53.77	9.43	6.75	7.38	5.12
EH201	M	4	Min	25.55	0.01	1.56	1.80	6.03	3.35	0.11	-	1.26	3.91
			Mean	***40.46***	***0.01***	***2.13***	***3.01***	***9.35***	***65.18***	***0.45***	-	***2.31***	***4.47***
			Max	65.63	0.01	2.56	4.35	10.84	91.53	0.83	-	4.09	5.74
EH201B	M	5	Min	12.47	0.04	0.42	2.65	7.74	68.95	0.35	-	0.25	3.24
			Mean	***15.97***	***3.29***	***0.51***	***3.06***	***8.65***	***78.77***	***0.87***	-	***0.54***	***5.59***
			Max	18.61	6.54	0.63	3.32	8.83	84.55	1.12	-	0.84	9.30
FT8A	M	10	Min	30.78	0.01	0.44	42.44	5.21	54.34	0.41	0.03	0.29	1.86
			Mean	***45.06***	***0.44***	***0.72***	***51.26***	***6.28***	***102.36***	***0.61***	***0.05***	***0.73***	***3.72***
			Max	59.17	0.87	1.04	68.73	8.38	149.45	0.89	0.09	1.98	7.88
EH184D	M	4	Min	17.39	-	0.32	4.89	5.21	14.15	1.43	-	0.94	5.27
			Mean	***20.40***	-	***0.60***	***5.96***	***5.94***	***24.00***	***3.27***	-	***4.70***	***7.48***
			Max	24.60	-	0.73	7.25	6.61	31.80	6.08	-	8.18	10.03
EH201C	M	3	Min	10.07	-	0.52	14.07	12.76	20.82	0.81	-	9.34	8.37
			Mean	***13.17***	-	***0.55***	***14.22***	***13.76***	***22.08***	***0.91***	-	***10.85***	***10.36***
			Max	14.76	-	0.59	14.49	14.74	23.55	1.03	-	12.08	11.81
262	W	9	Min	42.51	0.06	0.26	23.69	0.70	0.33	0.10	0.05	0.05	0.73
			Mean	***63.23***	***2.13***	***0.41***	***41.18***	***1.63***	***0.76***	***0.46***	***0.75***	***0.05***	***2.88***
			Max	103.34	4.09	0.61	55.34	4.47	1.14	1.06	2.06	0.05	7.63
338	W	8	Min	34.01	1.14	0.48	3.21	1.69	0.22	0.21	0.04	2.02	0.91
			Mean	***50.02***	***125.27***	***0.78***	***4.80***	***3.94***	***1.90***	***1.27***	***0.97***	***18.22***	***4.24***
			Max	77.56	696.33	1.25	7.01	8.42	5.07	2.61	2.10	38.68	13.75
LCD106	W	7	Min	220.27	0.02	0.52	0.07	3.71	0.46	0.12	0.11	0.74	0.09
			Mean	***338.92***	***0.05***	***0.60***	***0.49***	***6.05***	***1.03***	***0.42***	***0.94***	***43.95***	***5.63***
			Max	506.26	0.09	0.69	1.47	7.99	1.52	1.41	1.75	143.47	14.63
1714	W	8	Min	40.79	0.14	0.35	0.48	5.14	1.86	0.63	0.86	0.37	-
			Mean	***50.79***	***0.60***	***0.48***	***1.33***	***5.57***	***3.80***	***1.27***	***0.60***	***1.68***	-
			Max	58.73	1.07	0.61	3.42	5.80	6.41	2.29	3.59	1.56	-
243	W	4	Min	308.28	0.40	-	0.81	0.94	2.41	1.09	1.82	4.46	0.78
			Mean	***381.26***	***2.31***	-	***1.54***	***1.87***	***16.60***	***1.32***	***2.37***	***48.59***	***1.48***
			Max	536.18	4.80	-	2.05	3.24	57.76	1.55	2.92	130.99	2.13

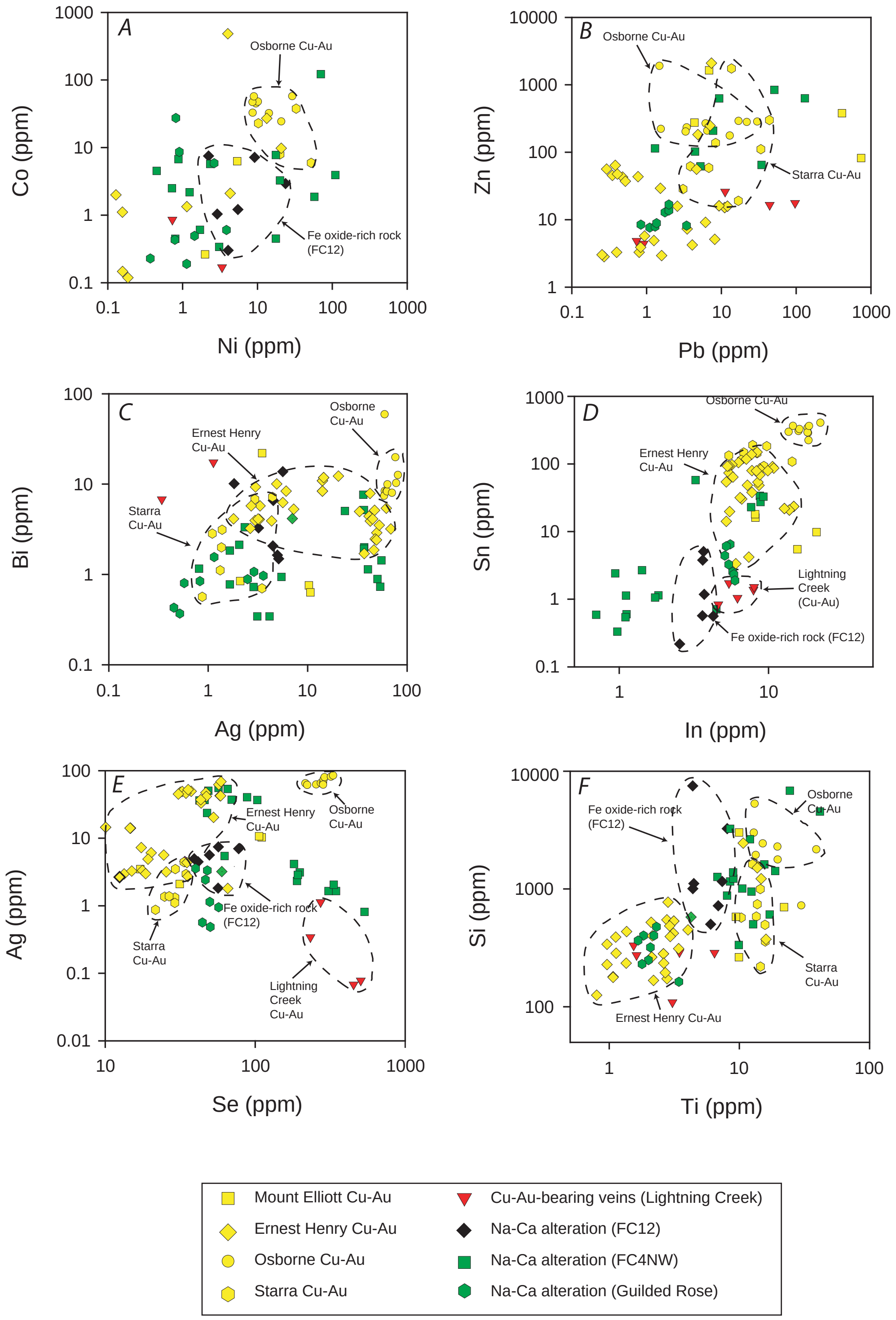

Figure 6.12: Bi-plots of trace elements identified in chalcopyrite from various Fe oxide-rich systems in the EFB. Yellow symbols represent chalcopyrite from Cu-Au mineralisation at Ernest Henry, Starra, Osborne and Mount Elliott. Magnetite-rich veins from Lightning Creek, Na-Ca alteration from FC4NW and Gilded Rose and Fe oxide rich rocks from FC12 represent the weakly mineralised systems analysed.

A **Eigenvalues**

Function	Eigenvalue	% of Variance	Cumulative %	Canonical Correlation
1	2.210[a]	70.1	70.1	.830
2	.813[a]	25.8	95.9	.670
3	.129[a]	4.1	100.0	.338

B **Classification Results**[a]

		Mineral association	Predicted Group Membership 1	2	3	4	Total
Original	Count	1	51	3	1	0	55
		2	0	21	3	2	26
		3	0	4	5	0	9
		4	0	0	0	5	5
	%	1	92.7	5.5	1.8	.0	100.0
		2	.0	80.8	11.5	7.7	100.0
		3	.0	44.4	55.6	.0	100.0
		4	.0	.0	.0	100.0	100.0

a. 86.3% of original grouped cases correctly classified

C **Functions at Group Centroids**

Mineral association	Function 1	2	3
1	1.105	.342	6.258E-03
2	-1.330	-.650	-.396
3	-.625	-1.631	.857
4	-4.111	2.552	.451

Unstandardized canonical discriminant functions evaluated at group means

D **Standardized Canonical Discriminant Function Coefficients**

	Function 1	2	3
SI	-.007	-.710	.806
TI	.066	-.438	-1.181
SE	-1.190	.752	.137
IN	.422	.721	.097
SN	.926	-.094	.230

Table 6.9: Results of the stepwise discriminant analysis for chalcopyrite

E. Calculated eigenvalues for each of the discriminant functions for chalcopyrite produced from the discriminant analysis. The larger the eigenvalue, the greater the separation between the pre-defined groups. Also shown is the canonical correlation for each discriminant function, where the closer the value is to 1, the higher the degree of association between the discriminant function and the groups. % variance and cumulative % of each successive discriminant function is also shown.

F. Classification table showing the degree to which the discriminant functions differentiate between the groups for chalcopyrite. Further explanation of the table is given in the text.

G. Table of group centroids showing the way in which each discriminant function differentiates between the pre-defined groups for chalcopyrite. Further explanation of the table is given in the text.

H. Table of the standardized canonical discriminant function coefficients showing to what degree each of the elements contribute to each of the discriminant functions for chalcopyrite.

variance respectively. Overall, 86.3% of all the analyses were categorised into their pre-defined groups (Table 6.10b). 53 of the 55 analyses assigned as Cu-Au mineralisation

were classified as group 1, whereas the remaining analyses bear a closer affinity with group 3 (cumulate magnetite). 80.8% of the analyses assigned as Na-Ca alteration were classified as group 2, and 55.6% of the analyses assigned to Fe oxide-rich rocks from FC12 were classified as group 3 based on their trace element geochemistry. The table of group centroids (table 6.9c) shows chalcopyrite from group 1 (Cu-Au mineralisation) to differ most compared to group 4 (Lightning Creek). Function 2 differentiates most strongly between group 2 (Na-Ca alteration) and group 1 (Cu-Au mineralisation). The discriminant analysis for chalcopyrite shows that Se, In, Sn and Si are the elements which best define the variation in the geochemical data.

6.6.4. Hematite

Trace element content and variation

Ti, Si, Mg, Al, Co, Ni, As, Sn, Sb, Zr, V, Mn, W, Sc, Ga and Nb were all detected in hematite from various Fe oxide systems. La, Mo, Ce, In, Hf, Bi, Pb, U and Cu were also detected but were either close to or below the detection limit or were highly erratic between individual analyses. Table 6.11 shows the mean, minimum and maximum values for all analyses of hematite. Elements that are most notably higher in hematite associated with Cu-Au mineralisation at Ernest Henry are As (100-1000 ppm), Sb (10-100 ppm), Ga (10-60 ppm) and W (50-500 ppm) (Fig. 6.13). Concentrations of other elements vary between mineral associations. The ratios Co/Ni, Co/Mn, Ti/V and Al/Mg each exhibit strong positive correlations, and may reflect strong and systematic partitioning of these elements into hematite.

Major and trace element substitution

In comparison to the previous studies described earlier, all the trace elements identified in hematite by Kisvarsanyi and Procter (1967) (V, Mg, Cu, Co and Ti) were detected in hematite also in this study. In addition to these elements, Si, Al, Ga, Sn, Zr, Sc, As, Sb, W and Nb were also detected. V, Cr, Ti, Al, Ga and Mn each substitute readily for Fe^{3+}, which is the dominant valency state of iron in hematite. However, pure hematite is a theoretical end member only and commonly occurs in solid solution with other Fe oxide minerals and spinels (Deer et al, 1992). Hence, Ni, Co, Zn and Mg most likely substitute

Table 6.11: Mean, minimum and maximum values of the trace element content of hematite from various Fe oxide-rich systems in the EFB (in ppm). Sample location numbers are presented in appendix 9. Sample type refers to whether the rock is Cu-Au mineralised (M), weakly mineralised (W) or barren (B). Also shown is the number of analyses taken for each sample. The hyphen represent analyses where values were below the detection limit and mean values could not be calculated.

Sample No	Sample Type	No of Analyses		Mg	Al	Si	Sc	Ti	V	Cr	Mn	Co	Ni	Cu	Zn	Ga	As	Zr
EH647	M	9	Min	4.73	114.60	329.58	1.27	293.49	564.30	1.51	31.44	6.38	1.80	3.43	16.14	13.43	12.86	0.89
			Mean	***54.29***	***219.47***	***1828.34***	***10.47***	***2013.34***	***980.59***	***8.26***	***623.24***	***19.96***	***29.74***	***119.38***	***567.15***	***25.32***	***187.43***	***8.38***
			Max	221.32	380.37	4629.10	44.74	6578.75	1424.03	22.61	2210.01	85.32	97.70	248.33	3311.36	41.40	458.36	32.89
R271	B	7	Min	38.08	125.31	879.34	1.95	21.12	7.66	11.70	193.52	20.50	4.40	3.20	8.65	0.96	0.00	0.33
			Mean	***72.02***	***158.06***	***2937.83***	***1.95***	***50.63***	***9.78***	***12.68***	***419.11***	***26.68***	***19.36***	***118.72***	***1297.90***	***3.96***	-	***8.28***
			Max	103.15	193.92	6575.80	1.95	136.89	14.77	13.65	621.82	56.40	73.16	295.11	5562.72	7.86	0.00	23.70
R176	B	6	Min	19.48	194.16	964.73	5.42	7730.67	248.04	9.89	14.05	1.97	20.43	3.67	13.13	4.03	10.60	1.55
			Mean	***57.12***	***768.11***	***7015.94***	***7.54***	***9719.80***	***258.52***	***17.75***	***19.75***	***4.27***	***99.53***	***10.03***	***1145.23***	***5.34***	***15.10***	***64.71***
			Max	197.22	2467.59	22162.95	11.08	11981.25	273.16	35.72	29.65	8.54	178.63	16.71	4328.17	6.81	19.60	156.41
1351A	B	2	Min	297.80	256.61	2998.48	23.65	39962.98	1236.79	696.48	165.33	8.44	7.10	0.98	6.06	10.43	1.25	77.42
			Mean	***320.11***	***513.69***	***3931.34***	***42.93***	***47698.93***	***1582.88***	***948.80***	***181.87***	***9.10***	***9.83***	***2.26***	***9.17***	***14.13***	***1.68***	***276.69***
			Max	342.41	770.76	4864.19	62.20	55434.88	1928.97	1201.12	198.41	9.76	12.55	3.54	12.28	17.82	2.11	475.96
1356A	B	6	Min	3.00	49.45	419.38	0.62	5.93	172.32	1.21	2.37	0.04	0.13	0.29	1.50	8.23	18.86	0.06
			Mean	***4.66***	***105.07***	***732.58***	***0.77***	***102.98***	***533.50***	***2.40***	***5.95***	***0.08***	***0.32***	***1.20***	***4.88***	***11.13***	***18.86***	***0.48***
			Max	7.01	191.82	1591.70	0.93	294.22	747.26	4.20	11.79	0.11	0.52	2.21	11.93	13.30	18.86	1.44
1561A	B	7	Min	172.02	474.78	695.43	4.60	2246.44	548.48	18.30	240.33	7.28	7.03	0.15	1.68	19.06	0.74	1.39
			Mean	***522.92***	***569.81***	***1623.13***	***7.46***	***7695.76***	***1562.08***	***79.84***	***853.19***	***18.76***	***20.33***	***0.33***	***3.89***	***23.30***	***0.87***	***2.89***
			Max	795.01	634.37	3777.14	10.73	12674.12	3250.40	227.67	1346.54	27.33	34.18	0.48	5.60	27.49	1.02	6.34
1561B	B	7	Min	30.58	198.19	539.62	0.29	2394.02	74.92	4.02	92.21	5.24	6.80	0.71	6.60	11.27	9.30	0.40
			Mean	***313.18***	***288.36***	***847.26***	***3.88***	***4238.61***	***293.39***	***21.61***	***903.67***	***27.13***	***28.36***	***2.05***	***11.26***	***15.03***	***9.30***	***1.33***
			Max	426.67	396.90	1127.14	11.94	6228.05	407.69	44.26	1428.25	48.14	60.06	3.41	13.84	17.81	9.30	2.20
1739	B	9	Min	8.50	88.90	577.12	0.76	552.58	49.36	7.25	1.77	0.16	0.71	0.80	3.51	2.94	0.73	3.74
			Mean	***20.45***	***156.68***	***1369.60***	***1.27***	***953.51***	***95.49***	***10.09***	***4.35***	***0.27***	***1.01***	***3.85***	***7.96***	***4.92***	***1.71***	***24.86***
			Max	65.33	241.11	3647.74	1.68	2061.69	176.81	16.07	9.75	0.48	1.55	18.48	24.99	6.23	2.89	54.09

Sample No	Sample Type	No of Analyses		Nb	Mo	In	Sn	Sb	La	Ce	Nd	Hf	W	Pb	Bi	U
EH647	M	9	Min	1.41	0.24	0.15	10.93	16.10	0.24	0.04	0.36	0.11	46.05	0.29	0.22	0.22
			Mean	***5.35***	***21.01***	***3.24***	***20.91***	***42.27***	***1.82***	***2.10***	***1.13***	***0.32***	***256.69***	***2.61***	***1.85***	***6.74***
			Max	16.06	69.78	8.21	46.36	86.40	4.34	6.91	2.54	0.67	597.01	5.77	4.52	18.91
R271	B	7	Min	0.13	1.92	0.13	2.22	0.57	0.07	0.29	1.01	0.06	1.04	0.41	0.21	1.42
			Mean	***0.67***	***79.32***	***1.03***	***20.03***	***3.27***	***1.14***	***2.05***	***2.49***	***0.22***	***8.60***	***2.37***	***0.56***	***5.98***
			Max	3.16	343.14	2.15	77.03	8.44	4.93	5.38	4.40	0.50	21.80	5.25	1.72	17.26
R176	B	6	Min	8.35	1.20	0.07	2.89	1.65	0.28	0.08	0.36	0.71	0.56	0.26	0.21	0.59
			Mean	***11.53***	***1.89***	***0.15***	***4.66***	***2.98***	***1.09***	***1.56***	***0.56***	***2.37***	***8.66***	***0.92***	***0.52***	***2.18***
			Max	14.17	2.99	0.24	6.22	5.20	2.12	3.15	0.75	3.62	21.54	1.56	1.34	4.83
1351A	B	2	Min	36.89	0.92	0.31	51.45	1.94	0.06	0.20	0.09	2.49	0.34	0.36	0.02	0.36
			Mean	***38.78***	***1.32***	***0.34***	***58.20***	***3.07***	***0.36***	***0.76***	***0.50***	***8.06***	***0.46***	***1.41***	***0.03***	***1.38***
			Max	40.66	1.72	0.36	64.94	4.19	0.67	1.32	0.91	13.63	0.58	2.46	0.05	2.39
1356A	B	6	Min	0.63	0.09	0.01	2.56	0.69	0.01	0.01	0.05	0.01	0.62	0.12	0.03	0.04
			Mean	***4.58***	***11.78***	***0.07***	***11.73***	***5.90***	***0.11***	***0.29***	***0.16***	***0.03***	***27.74***	***1.08***	***0.10***	***0.33***
			Max	7.47	43.40	0.12	24.08	13.69	0.45	1.34	0.37	0.05	94.49	2.48	0.22	1.46
1561A	B	7	Min	1.11	0.03	0.03	6.50	0.50	0.03	0.03	0.01	0.09	0.07	0.13	-	0.03
			Mean	***6.81***	***0.15***	***0.06***	***8.85***	***0.90***	***0.29***	***0.26***	***0.32***	***0.24***	***0.57***	***0.35***	***0.00***	***0.09***
			Max	18.31	0.24	0.07	11.39	1.87	0.97	0.92	0.73	0.55	1.10	0.73	-	0.23
1561B	B	7	Min	0.14	0.13	0.02	3.75	0.26	0.01	0.06	0.21	0.02	0.06	0.92	0.03	0.02
			Mean	***3.00***	***0.25***	***0.05***	***7.77***	***0.97***	***0.72***	***0.57***	***0.30***	***0.04***	***6.61***	***2.84***	***0.03***	***0.37***
			Max	18.71	0.48	0.10	15.21	3.34	1.32	1.35	0.34	0.08	16.90	4.74	0.03	0.96
1739	B	9	Min	13.51	0.27	0.63	148.03	12.29	0.03	0.04	0.02	0.16	0.21	0.50	0.01	0.18
			Mean	***23.54***	***1.34***	***0.97***	***225.99***	***52.67***	***0.13***	***0.32***	***0.12***	***1.05***	***4.40***	***1.23***	***0.04***	***0.74***
			Max	31.72	3.86	1.29	283.16	79.46	0.66	1.31	0.29	2.75	17.98	2.57	0.09	2.06

Figure 6.13: Bi-plots of trace elements identified in hematite from various Fe oxide-rich systems in the EFB. Yellow symbols represent chalcopyrite from Cu-Au mineralisation at Ernest Henry. Na-Ca alteration from the FC12 prospect and Gilded Rose area represent weakly mineralised systems analysed. Various hematite-rich Fe oxide-rich rocks from the Gilded Rose area and MFC make up the suite of samples analysed for this study.

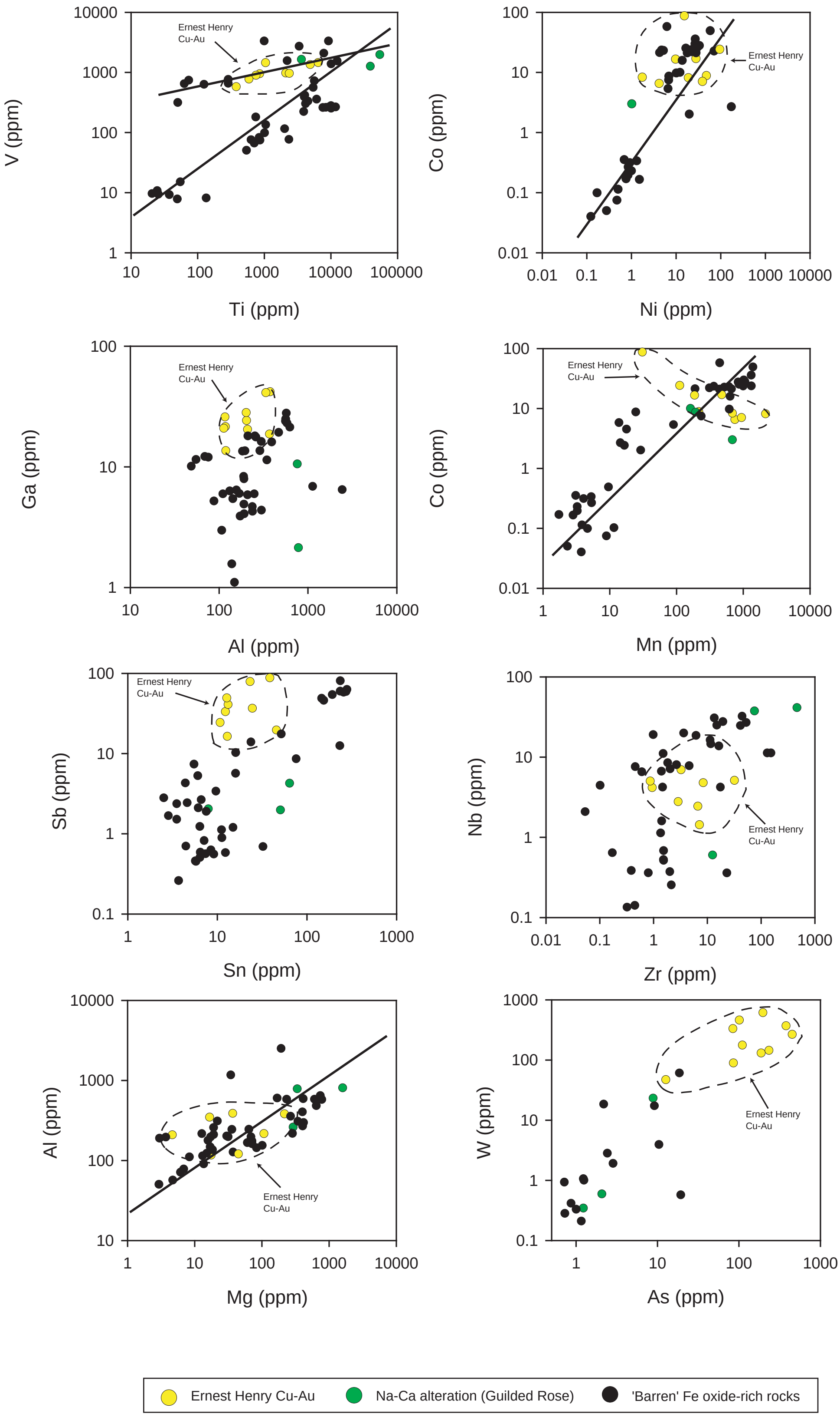
V (ppm)
Ti (ppm)
Ernest Henry Cu-Au
Co (ppm)
Ni (ppm)
Ernest Henry Cu-Au
Ga (ppm)
Al (ppm)
Ernest Henry Cu-Au
Co (ppm)
Mn (ppm)
Ernest Henry Cu-Au
Sb (ppm)
Sn (ppm)
Ernest Henry Cu-Au
Nb (ppm)
Zr (ppm)
Ernest Henry Cu-Au
Al (ppm)
Mg (ppm)
Ernest Henry Cu-Au
W (ppm)
As (ppm)
Ernest Henry Cu-Au
Ernest Henry Cu-Au
Na-Ca alteration (Guilded Rose)
'Barren' Fe oxide-rich rocks

Fe^{2+} in hematite. Both Nb^{5+} and Sb^{5+} have a similar atomic radius to Ti^{4+} and therefore substitutes for this particular element, and Ti^{4+} will substitute for Fe^{3+} (Goldschmidt, 1958). W has a close geochemical relationship to Mo due to their similar atomic size in 12-fold coordination; however, Mo in hematite was found to be sporadic between analyses, perhaps representing inclusions (appendix 9). While W may also be associated with inclusions of other phases in hematite, Goldschmidt (1955) suggested it possible that W may substitute for Fe and Mn, as illustrated by the occurrences in nature of such minerals as wolframite $(Fe,Mn)WO_4$ and ferberite ($FeWO_4$). The presence of As in hematite is unusual as As will normally partition into Fe-sulphides by substituting for S. The most likely explanation is that As substituted for Co and Fe (Goldschmidt, 1958), or that it is present in another phase as inclusions within the analysed hematite grains.

Discriminant analysis

A stepwise discriminant analysis of trace elements in hematite produced two discriminant functions (Table 6.12a). Some caution; however, is needed, as the dataset is quite small and only three pre-defined groups were used (table 6.4). The Eigenvalue for group 1 (Cu-Au mineralisation) is very large and explains 91.3% of the total variance in the dataset (table 6.12a). Classification of the results shows that 96.2% of the analyses in total were classified into their pre-defined groups based on the trace element geochemistry (table 6.12b). All analyses from Cu-Au mineralisation at Ernest Henry were classified as group 1 except one which was classified as group 2 (barren Fe oxide-rich rock). The table of group centroids (table 6.12c) shows that hematite from Cu-Au mineralisation (group 1) differs most from Na-Ca alteration (group 3), while for function 2, barren Fe oxide-rich rocks (group 2) and Na-Ca alteration (group 3) differentiate the most. The elements that define each of the functions are shown in table 6.12d, where Sc and Al appear to be the most important contributors to function 1, and W and Al are the most important for function 2. These results are partly consistent with elements exhibiting the greatest variation in figure 6.13, where W shows significant clustering between Cu-Au mineralisation at Ernest Henry and other Fe oxide-bearing systems.

6.7. DISCUSSION

This study has shown that magnetite, hematite, pyrite and chalcopyrite from various mineral assemblages throughout the EFB can accommodate a variety of trace elements

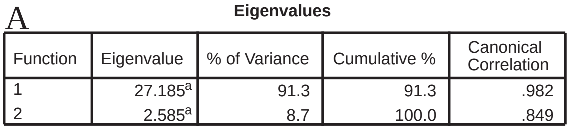

A

Eigenvalues

Function	Eigenvalue	% of Variance	Cumulative %	Canonical Correlation
1	27.185[a]	91.3	91.3	.982
2	2.585[a]	8.7	100.0	.849

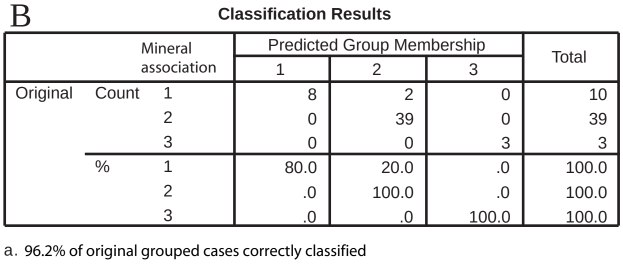

B

Classification Results

		Mineral association	Predicted Group Membership			Total
			1	2	3	
Original	Count	1	8	2	0	10
		2	0	39	0	39
		3	0	0	3	3
	%	1	80.0	20.0	.0	100.0
		2	.0	100.0	.0	100.0
		3	.0	.0	100.0	100.0

a. 96.2% of original grouped cases correctly classified

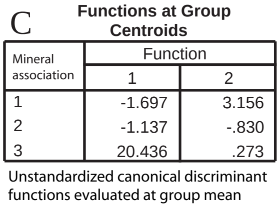

C

Functions at Group Centroids

Mineral association	Function	
	1	2
1	-1.697	3.156
2	-1.137	-.830
3	20.436	.273

Unstandardized canonical discriminant functions evaluated at group mean

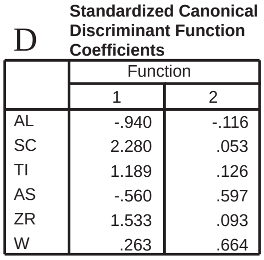

D

Standardized Canonical Discriminant Function Coefficients

	Function	
	1	2
AL	-.940	-.116
SC	2.280	.053
TI	1.189	.126
AS	-.560	.597
ZR	1.533	.093
W	.263	.664

Table 6.11: Results of the stepwise discriminant analysis for hematite

A. Calculated eigenvalues for each of the discriminant functions calculated for hematite produced from the discriminant analysis. The larger the eigenvalue, the greater the separation between the pre-defined groups. Also shown is the canonical correlation for each discriminant function, where the closer the value is to 1, the higher the degree of association between the discriminant function and the groups. % variance and cumulative % of each successive discriminant function is also shown.
B. Classification table showing the degree to which the discriminant functions differentiate between the groups for hematite. Further explanation of the table is given in the text.
C. Table of group centroids showing the way in which each discriminant function differentiates between the pre-defined groups for hematite. Further explanation of the table is given in the text.
D. Table of the standardized canonical discriminant function coefficients showing to what degree each of the elements contribute to each of the discriminant functions for hematite.

into their crystal structure. Importantly, trace element signatures of individual Fe oxide and Fe sulphide grains from ore deposits differ markedly compared to those derived from weakly mineralised and barren Fe oxide-bearing systems. This variation can be controlled by a number of factors including oxidation state, host rock geochemistry, degree of fluid-rock interaction, temperature and fluid chemistry.

6.7.1. Role of host rocks and composition on mineral chemistry

Fe oxide (±Cu-Au) mineralisation within the EFB is hosted in a variety of rock types, which can potentially play an important role in the relative trace element concentration of magnetite, hematite, pyrite and chalcopyrite between different systems. Hydrothermal alteration associated both with, and peripheral to, Cu-Au mineralisation at Ernest Henry is hosted in felsic volcanic rocks, suggesting any variation in trace element content between different alteration phases is unlikely to be caused by host rock geochemistry. In contrast, Mount Elliott is a skarn hosted deposit proximal to granite, and Cu-Au mineralisation at Starra and Osborne are distal to potential causative intrusions and are hosted in early Fe oxide-rich rocks and metasedimentary rocks (Appendix 8). In these latter two cases, any variability in trace element chemistry between different mineral associations may have been influenced by the host rock geochemistry.

Figure 6.14 presents all magnetite analyses from the EFB plotted according to host rock. Due to the small amount of data for pyrite, chalcopyrite and hematite, similar plots were not constructed for these minerals. The magnetite plots show a wide range of trace element concentrations, however clear clusters are still apparent. Magnetite hosted in felsic volcanic rocks typically contains higher Mn and lower V and Cr than other rock types. Banded Fe oxide-rich rocks at Starra and Osborne have low V and Mn, whereas Zn and Al are typically higher at Osborne compared to other ore deposits. Magnetite produced by igneous processes, including gabbro and Fe oxide-rich rocks from FC12, Fe-rich sills from Lightning Creek and the Slaughter Yard granite, contain elevated Ti, Zn, Sc and Cu, whereas skarn hosted magnetite contains lower Ga. In many cases, however, the rock type in question is associated with a single deposit or mineral association only (e.g. Skarn at Mount Elliott), therefore the apparent host rock control exhibited by these plots can be misleading. Analyses of magnetite hosted by felsic volcanic rocks are mostly from Ernest Henry, although two samples from FC4NW are

Figure 6.14: Bi-plots of trace elements identified in magnetite from various Fe oxide-rich systems in the EFB plotted according to host rock. Rock types include Gabbro from the FC12 prospect (Grey circles); Banded 'ironstone' from Starra and Osborne (origin contentious) (Red circles); Fe-rich sills (Pink circles) and granite from Lightning Creek and FC4NW (Pink squares); felsic volcanic rocks from Ernest Henry (purple circles); skarn from Mount Elliott (Light green circles); calc-silicate rocks from the Gilded Rose area and Corella (Dark green circles) and various regional Fe oxide-rich rocks (Black circles). Note discrete populations of magnetite associated with different rock types are labelled by black dashed lines.

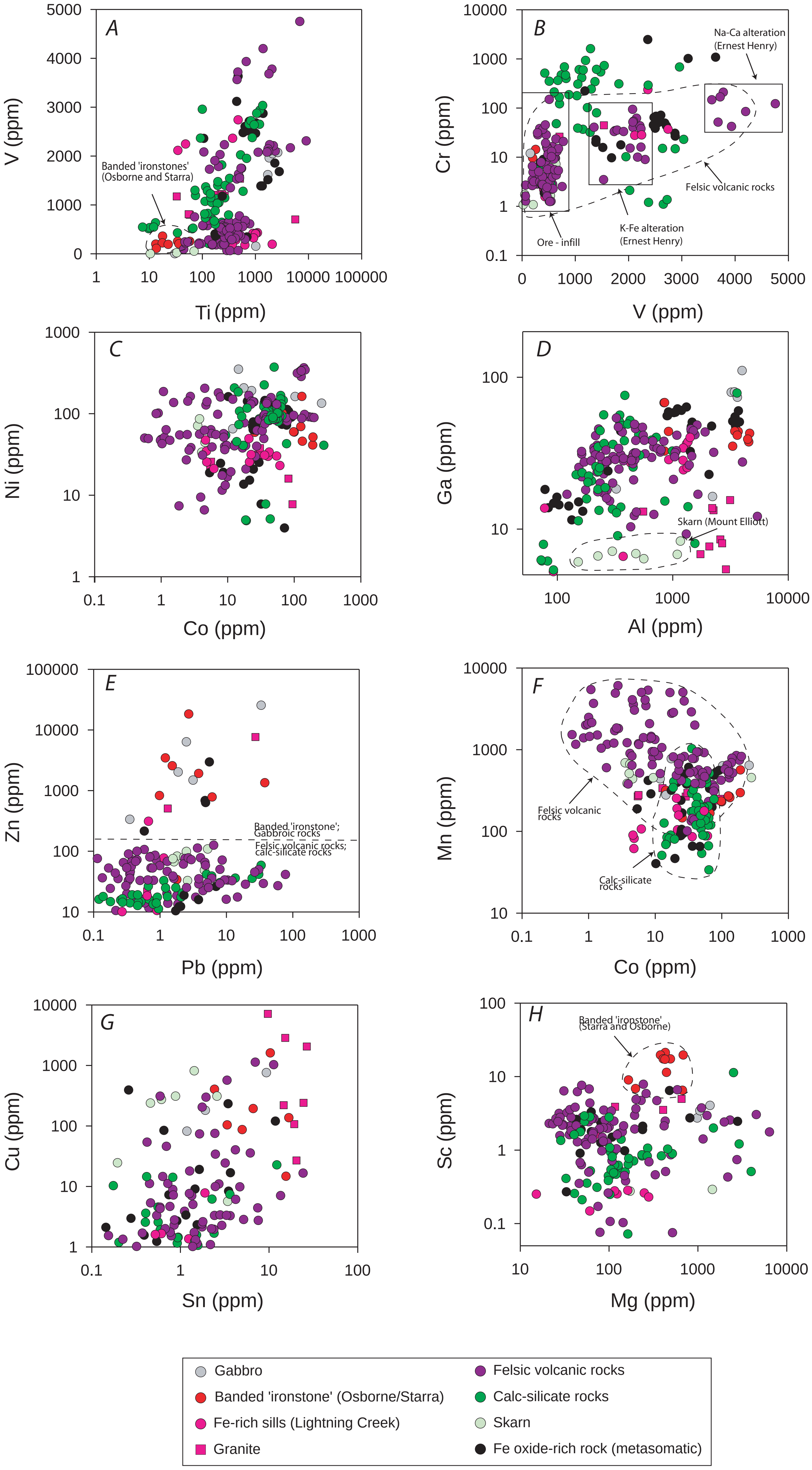
A
V (ppm)
Ti (ppm)
5000
4000
3000
2000
1000
0
1
10
100
1000
10000 100000
Banded 'ironstones' (Osborne and Starra)
B
Cr (ppm)
V (ppm)
10000
1000
100
10
1
0.1
0
1000
2000
3000
4000
5000
Na-Ca alteration (Ernest Henry)
Felsic volcanic rocks
K-Fe alteration (Ernest Henry)
Ore - infill
C
Ni (ppm)
Co (ppm)
1000
100
10
1
0.1
1
10
100
1000
D
Ga (ppm)
Al (ppm)
100
10
100
1000
10000
Skarn (Mount Elliott)
E
Zn (ppm)
Pb (ppm)
100000
10000
1000
100
10
0.1
1
10
100
1000
Banded 'ironstone'; Gabbroic rocks
Felsic volcanic rocks; calc-silicate rocks
F
Mn (ppm)
Co (ppm)
10000
1000
100
10
0.1
1
10
100
1000
Felsic volcanic rocks
Calc-silicate rocks
G
Cu (ppm)
Sn (ppm)
10000
1000
100
10
1
0.1
1
10
100
H
Sc (ppm)
Mg (ppm)
100
10
1
0.1
10
100
1000
10000
Banded 'ironstone' (Starra and Osborne)
● Gabbro
● Banded 'ironstone' (Osborne/Starra)
● Fe-rich sills (Lightning Creek)
■ Granite
● Felsic volcanic rocks
● Calc-silicate rocks
● Skarn
● Fe oxide-rich rock (metasomatic)

also hosted by felsic volcanic rocks. In the case of Ernest Henry, the control on V content does not appear to be associated with the host rock geochemistry because pre-mineralisation phases also hosted in felsic volcanic rocks contain comparatively high concentrations of this element relative to ore (Fig. 6.14b). In addition, Mark et al (1999) showed that Mn was consistently enriched in Na-Ca and K-Fe alteration assemblages compared to the original felsic volcanic host rock. This suggests that the elevated Mn in magnetite is a product of fluid chemistry or changes in physicochemical conditions rather than the host rock.

The high Ti concentrations in magnetite from gabbro and Fe oxide-rich rocks at FC12, in addition to the Fe-rich sills at Lightning Creek and the Slaughter Yard granite, is consistent with a magmatic origin. It is well known that Ti is relatively immobile compared to other elements in aqueous fluids (chapter 4, 5), therefore it would be expected that Ti is low in hydrothermal magnetite. The elevated Ti content in magnetite from Fe oxide-rich rocks at FC12 in particular supports the interpretation that these rocks are formed from crystal fractionation rather than hydrothermal processes (chapter 5).

The degree to which host rock geochemistry played a role in the relative trace element content of magnetite also depends on the degree of fluid-rock interaction. As mentioned in chapter 5, the immobile element geochemistry of an Fe oxide-rich rock produced from the replacement of a previous rock will most likely reflect its precursor. In contrast, Fe oxide-rich rocks produced from infill will contain typically low immobile element concentrations because of the very low solubility of such elements in most crustal fluids. Magnetite investigated in this study were formed by a wide range of processes including infill (Cu-Au mineralisation), replacement (K-Fe alteration at Ernest Henry), magmatic crystal fractionation (Fe oxide-rich rocks at FC12), and probable chemical sedimentation (banded Fe oxide-rich rocks at Osborne and Starra; Davidson et al., 1989), and is plotted accordingly in figure 6.15.

Figure 6.15 shows that both V and Zn are low in magnetite associated with infill. In many hydrothermal systems, V is essentially immobile in aqueous fluids (Goldschmidt, 1958). Magnetite associated with Cu-Au mineralisation mainly occurs as infill, and the low V content of magnetite from the Cu-Au veins at Lightning Creek compared to

Figure 6.15: Bi-plots of trace elements identified in magnetite from various Fe oxide-rich systems in the EFB plotted according to the degree of fluid-rock interaction (i.e. infill, replacement, magmatic, syn-sedimentary). Categories include: Infill (black circles); Banded 'ironstone' from Starra and Osborne (origin contentious) (blue circles); Replacement (red circles); Magmatically-derived magnetite (green circles); magnetite derived from cumulate Fe oxide-rich rocks at FC12 (grey circles); metamorphic – calc-silicate rocks (blue circles). Note discrete populations of magnetite associated with specific styles of magnetite precipitations are labelled by black dashed lines.

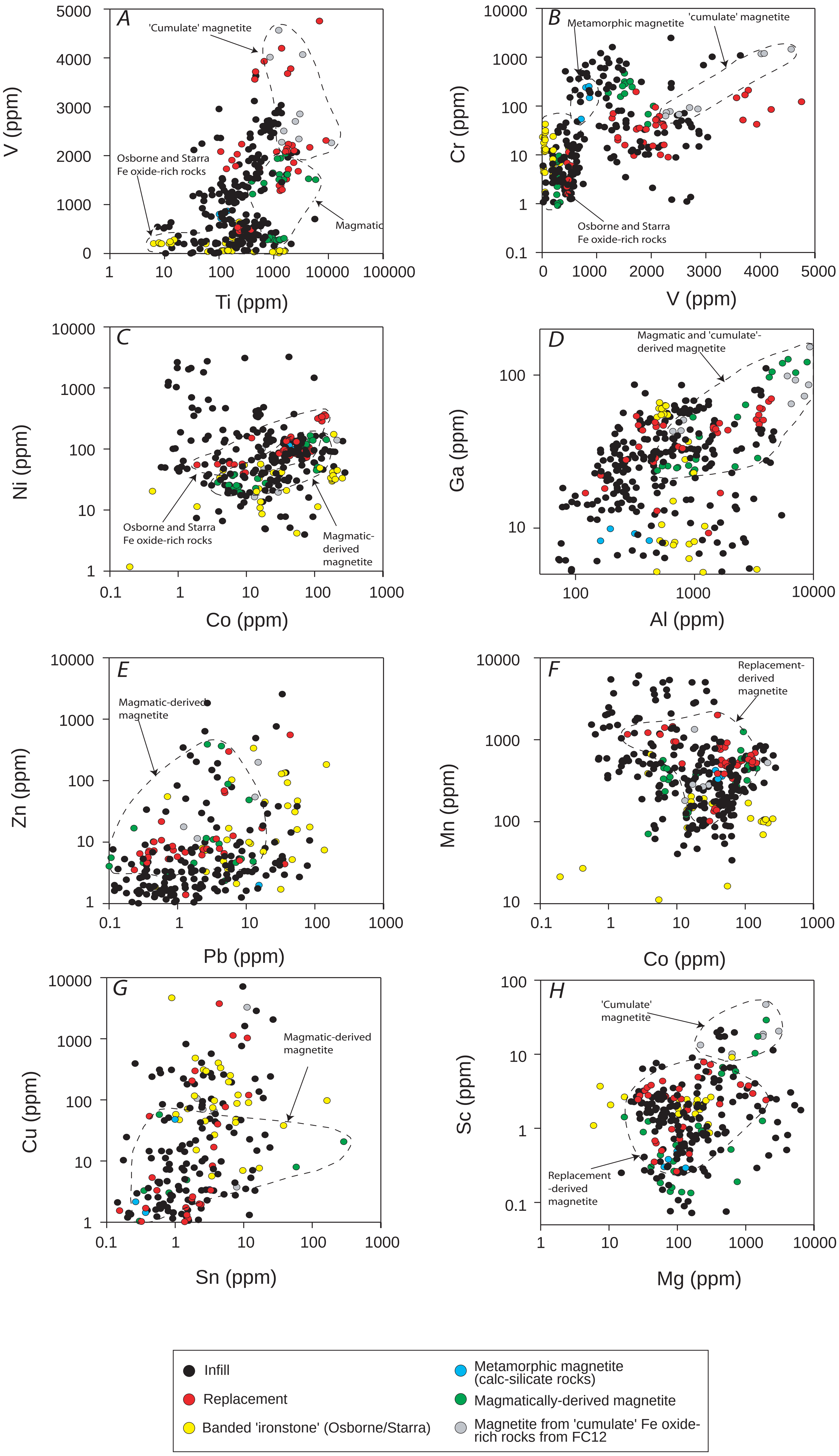A
'Cumulate' magnetite
Osborne and Starra Fe oxide-rich rocks
Magmatic
V (ppm)
5000
4000
3000
2000
1000
0
Ti (ppm)
1
10
100
1000
10000
100000
B
Metamorphic magnetite
'cumulate' magnetite
Osborne and Starra Fe oxide-rich rocks
Cr (ppm)
10000
1000
100
10
1
0.1
V (ppm)
0
1000
2000
3000
4000
5000
C
Osborne and Starra Fe oxide-rich rocks
Magmatic-derived magnetite
Ni (ppm)
10000
1000
100
10
1
Co (ppm)
0.1
1
10
100
1000
D
Magmatic and 'cumulate'-derived magnetite
Ga (ppm)
100
10
Al (ppm)
100
1000
10000
E
Magmatic-derived magnetite
Zn (ppm)
10000
1000
100
10
1
Pb (ppm)
0.1
1
10
100
1000
F
Replacement-derived magnetite
Mn (ppm)
10000
1000
100
10
Co (ppm)
0.1
1
10
100
1000
G
Magmatic-derived magnetite
Cu (ppm)
10000
1000
100
10
1
Sn (ppm)
0.1
1
10
100
1000
H
'Cumulate' magnetite
Replacement -derived magnetite
Sc (ppm)
100
10
1
0.1
Mg (ppm)
1
10
100
1000
10000
● Infill
● Replacement
● Banded 'ironstone' (Osborne/Starra)
● Metamorphic magnetite (calc-silicate rocks)
● Magmatically-derived magnetite
● Magnetite from 'cumulate' Fe oxide-rich rocks from FC12

igneous-derived magnetite from the granites and Fe-rich sills may also be attributed to the former precipitating as infill. However, figure 6.15 shows examples of infill magnetite that contain relatively high V contents including Na-Ca assemblages from FC4NW and the Gilded Rose area. In addition, figure 6.14b shows that both the K-Fe and Na-Ca alteration phases at Ernest Henry, which formed by replacement rather than infill, contain significantly different V contents despite both being hosted in felsic volcanic rocks. Therefore, while the degree of fluid-rock interaction may have played some role in the V content of magnetite in these systems, the large spread of data suggests this variability was most likely controlled by other factors.

Interestingly, V, Cr and Mn concentrations are also low in magnetite in the banded Fe oxide-rich rocks at Osborne and Starra, and may have important implications regarding their origin. Work by Nystrom and Henriquez (1994) found Fe oxide-rich rocks derived from sedimentary processes compared to the Kiruna-type ores of Chile and Sweden also containing relatively low V. The low V content in banded Fe oxide-rich rocks at Osborne and Starra supports the interpretation made in chapter 5 that they are syn-sedimentary rather than metasomatic (see also Davidson, 1994, and Marshall, 2003).

6.7.2. Physicochemical controls on trace element substitution

Little work is currently available on the effects of various physicochemical factors on the partitioning of specific elements into Fe oxide and Fe sulphide minerals (e.g. Ilton and Eugster, 1989; Huston et al., 1995; Butler and Nesbitt, 1999; Toplis and Corgne, 2002). Work by Butler and Nesbitt (1999) suggests In will partition more favourably into chalcopyrite at higher temperatures. A comparison between the deposits shows chalcopyrite from Ernest Henry contains relatively low In compared to chalcopyrite at Osborne. However, this does not correlate with the suggested temperature control of Butler and Nesbitt (1999), as Ernest Henry is interpreted to have formed at slightly higher temperatures (400-500ºC, Mark et al., 1999) than Osborne (300-400ºC, Adshead, 1995). Instead, the relative In content of chalcopyrite most likely reflects different fluid composition rather than variations in temperature.

Ilton and Eugster (1989) experimentally investigated base metal exchange reactions between magnetite and a supercritical chloride solution at 600 to 800°C and 2 kb. They found that Cu, Zn and Mn will partition more favourably into the fluid phase rather than magnetite with respect to Fe. The partitioning of Cu into the fluid phase was found to be so strong that it was considered incompatible with magnetite. The strong partitioning behaviour of Cu, Zn and Mn with respect to Fe in a chloride-rich fluid was found to be influenced by temperature, with the aforementioned elements partitioning more strongly into the fluid at lower temperatures. Ilton and Eugster (1989) suggest that even minor to trace concentrations of Cu, Zn and Mn in magnetite indicate very strong enrichment of these components (relative to Fe) in chloride-rich hydrothermal fluids.

The high Cu and Zn content in magnetite associated with Cu-Au mineralisation at Osborne (Fig. 6.8) may imply elevated levels of these components in the fluid compared to the other deposits. In contrast, Cu in ore magnetite at Ernest Henry is low compared to the other deposits. The low Cu values in magnetite at Ernest Henry also correlate with PIXE data for fluid inclusions (Mark et al, 1999), which are similarly depleted in Cu compared to Starra and Lightning Creek. Additionally, the high Mn concentration in magnetite from Ernest Henry implies the fluids were extremely enriched in Mn compared to the other deposits. This also correlates with PIXE data for fluid inclusions (cf. chapter 4) which shows that Mn concentrations are an order of magnitude higher at Ernest Henry compared to magnetite from Starra and Lightning Creek (cf. Mark et al., 1999; Williams et al., 2001). These results imply that the relative concentration of Cu and Mn in magnetite between different systems is most likely dominated by the fluid chemistry.

Whether temperature also played a significant role in the relative concentration of Cu, Zn and Mn in magnetite is difficult to assess due to the effects of other physicochemical factors including redox, fluid chemistry and pH. At Lightning Creek, high temperature (500-600°C) quartz-magnetite-albite-clinopyroxene-rich veins contain significant amounts of Fe (~1 wt%) and Cu (~0.1 wt%) (Perring et al., 2000; chapter 4), and are interpreted to represent a window on the transition from magmatic to hydrothermal conditions. These Cu and Fe concentrations are significantly higher than fluids associated with Cu-Au mineralisation at Ernest Henry and Starra (Mark et al., 1999; Perring et al., 2000; Williams et al., 2001; chapter 4). Overprinting these veins are low temperature (<200) calcite-chlorite-magnetite-pyrite-chalcopyrite veins, which were interpreted by Perring et al., (2000) to have formed by the admixture of a meteoric component to the aforementioned high temperature Cu-Fe-rich fluids (Perring et al., 2000). In contrast to the high Cu content associated with these fluids, this study found Cu was very low (<10 ppm) in magnetite associated with the late-stage Cu-Au-bearing veins at Lightning Creek. Thus, the low temperatures during formation of the Cu-bearing veins at Lightning Creek may have inhibited the partitioning of Cu into magnetite, despite the fluids associated with alteration at Lightning Creek exhibiting extremely high Cu values.

Experimental work by Toplis and Corgne (2002) suggested that f_{O2} may affect the degree of V partitioning into magnetite, while Co and Ni show no relation to f_{O2}.. Toplis and Corgne (2002) showed that the synchronous change in valence state as well as the ionic radius of V with respect to redox (NNO = -6 to 4) will drastically affect the degree of substitution into magnetite at constant temperature (1068°C). They concluded that increasing f_{O2} would decrease the partition coefficient of V into magnetite from an iron-bearing silicate liquid/melt. Rotherham (1997) and Mark et al (1999) proposed that fluids responsible for Cu-Au mineralisation at Starra and Ernest Henry respectively were relatively oxidised compared to fluids associated with Cu-Au mineralisation at Osborne and Mount Elliott (cf. Adshead, 1995; Wang and Williams, 2001). Rotherham (1997) inferred that the higher oxidation state of the fluid at Starra was also responsible for the high Au:Cu ratios. Interestingly, magnetite associated with Cu-Au mineralisation at Starra contains lower V (<100 ppm) than Ernest Henry, Osborne and Mount Elliott, whereas the other deposits in the EFB mostly contain higher V concentrations (100-1000 ppm) corresponding to more reduced conditions during Cu-Au mineralisation (Fig. 6.16).

Mark et al (1999) noted a change from magnetite associated with stage 1 Cu-Au mineralisation to hematite and bladed magnetite associated with stage 2 Cu-Au mineralisation at Ernest Henry. This led Mark et al (1999) to suggest that changes in the stability of magnetite and hematite were induced by increasing f_{O2} and/or decreasing temperature. The concentration of V in magnetite is typically high in early Na-Ca alteration assemblages at Ernest Henry. In contrast, magnetite associated with K-Fe alteration peripheral to the ore body contains lower V contents, while V in magnetite associated with Cu-Au mineralisation is even lower (Fig. 6.7b). This progressive decrease in V and increased stability of hematite may imply an increase in f_{O2} over time. Huston et al (1995) demonstrated that the Se content in pyrite can be affected by both

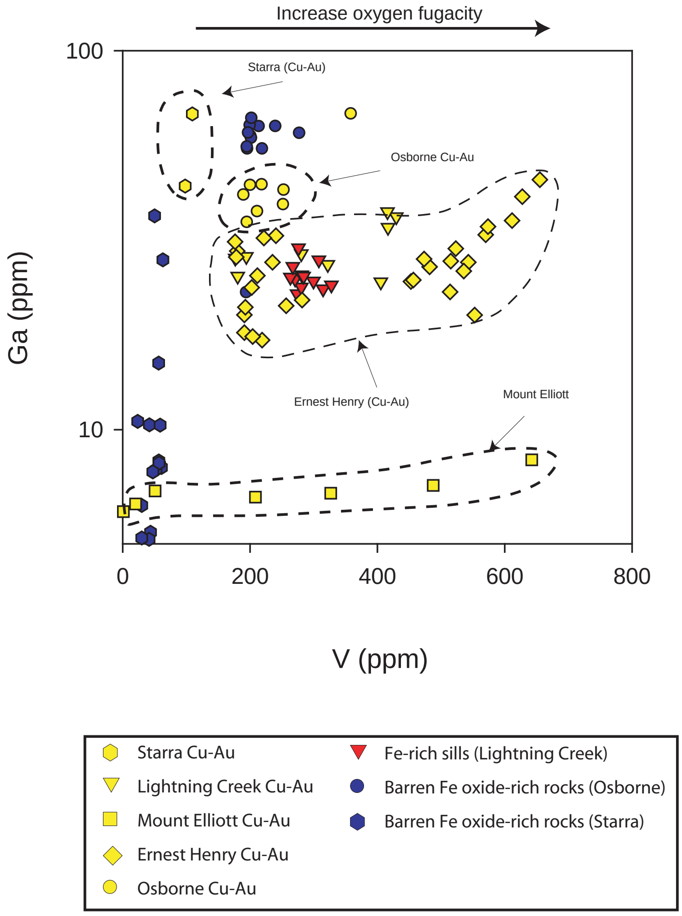

Figure 6.16: Bi-plot of V (ppm) vs Ga (ppm) in magnetite from Cu-Au mineralised systems, Fe-rich sills from Lightning Creek and barren Fe oxide-rich rocks hosting the ore at Starra and Osborne. Note magnetite associated with the Starra Cu-Au mineralisation contains low V compared to most the other deposits.

temperature and changes in redox and/or pH conditions in various VHMS-type deposits. Their study showed that at constant mH_2Se / mH_2S (where m = molarity), Se levels in pyrite decrease with increasing temperature (Fig. 6.17). The H_2Se/H_2S ratio of a fluid was shown to decrease exponentially as pH increases in the HSe^{-} dominant field, resulting in the Se content in pyrite being lowered (Fig. 6.17). As a result, pyrite deposited from oxidised fluids should have high, and variable, Se contents. In contrast, if the fluid evolves in more reduced conditions, the Se content of pyrite will decrease until the H_2S field is reached and then level off. In this study, the relative redox state of fluids from the aforementioned deposits is not reflected in the Se content of pyrite. Instead, Starra contains lower Se compared to Osborne, despite the former being associated with more oxidised fluids. The oxidation state of the fluid does not appear to be a major factor in controlling the relative Se content in pyrite in these systems.

In contrast, pyrite from the Lightning Creek Cu-Au occurrence contains an order of magnitude higher Se than all other systems. The late-stage Cu-bearing veins at Lightning Creek are interpreted to have formed at lower temperatures (<200°C) compared to Ernest Henry (400-500ºC; Mark et al., 1999), Osborne (300-400ºC; Adshead, 1995), Starra (200-350ºC; Rotherham, 1997) and Mount Elliott (ca. 350ºC; Little, 1997). Se was also found to be higher in chalcopyrite from Lightning Creek with respect to other mineral associations in the dataset. The high Se content within pyrite and chalcopyrite at Lightning Creek supports the experimental work by Huston et al (1995) that Se will more favourably partition into pyrite at lower temperatures.

6.7.2. Effects of different minerals phases on trace element partitioning

The presence of other minerals within the mineral assemblage may also have a significant effect on their trace element chemistry. Other mineral phases may preferentially partition certain elements, effectively diluting their concentration within a particular mineral. If this is the case, then Fe oxides and Fe sulphides co-existing with other minerals (i.e. Cu-Au mineralisation) might contain lower concentrations of certain elements compared to assemblages with fewer associated minerals (e.g. barren Fe oxide-rich rocks), for a given fluid chemistry. A comparison between the trace element content of Fe oxides and Fe sulphides associated with ore and non-ore assemblages suggests any effects were most likely to be small (Tables 6.2 to 6.4, 6.6 to 6.7, 6.9, 6.11). Not only is ore magnetite associated with a greater variety of elements, but in

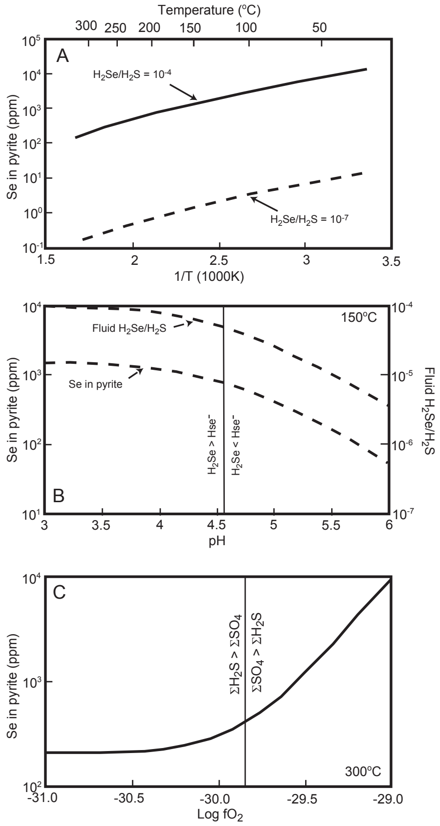

Figure 6.17: Diagrams showing variations in the Se content of pyrite (and in the H_2Se/H_2S ratio of coexisting fluids): A. With temperature assuming constant H_2Se/H_2S ratios in the fluid; B. With pH at 150ºC assuming a constant SSe/SS ratio of 10-4 and reduced conditions (f_{O2} < 10-47) in the fluid; C. With f_{O2} at 300ºC and pH = 4.5. After Huston et al (1995).

most cases, elements that are found to be anomalous in all mineral assemblage types were more enriched in the deposits. The exceptions include Ti, V and Cr in magnetite and Se and Ni in pyrite, which were found to be higher in barren and weakly mineralised sulphide-bearing systems compared to Cu-Au mineralised systems. Experimental work has shown that V, Ti and Cr will more favourably partition into magnetite compared to other mineral phases (cf. Nielsen, 2003 and references therin). Therefore, it is unlikely that the presence of additional mineral phases will greatly affect the concentration of these elements in magnetite. In contrast, both Ni and Se will strongly partition into a variety of other mineral phases including magnetite, hematite (Ni only) and chalcopyrite (Se only). This is illustrated in figure 6.18, which shows a positive correlation between Ni in pyrite and Ni in magnetite. Where the Ni content is low (<100 ppm), both pyrite and magnetite will partition Ni in equal amounts, although above 100 ppm, Ni concentrations are much higher in pyrite compared to magnetite. It is apparent from figure 6.18 that the presence or absence of pyrite in the same mineral assemblage may affect the amount of Ni in magnetite. However, tables 6.6 and 6.7 show that assemblages which contain a high pyrite content do not contain lower Ni in magnetite (with the exception of Na-Ca alteration at FC4NW) suggesting any effect of pyrite and magnetite on Ni content was most likely small. Figure 6.18 also shows that samples associated with infill and replacement exhibit a broad range of values for Ni, suggesting that the Ni content of pyrite and magnetite was mostly controlled by fluid chemistry and other physicochemical factors rather than the degree of fluid-rock interaction and host-rock geochemistry as described above.

One significant difference between the deposits shown in figure 6.18 is the proximity of igneous intrusions at Lightning Creek and Mount Elliott, although temperatures derived from fluid inclusion studies at these deposits do not support a dominant temperature control. As discussed earlier, Mount Elliott formed at similar temperatures to Osborne and Starra, whereas the Cu-Au-bearing veins at Lightning Creek formed at significantly lower temperatures. Instead, the high Ni content in both pyrite and magnetite at Lightning Creek and Mount Elliott may reflect the fluid (magmatic) source, although other physicochemical factors, which may also affect the partioning of Ni into magnetite and pyrite, cannot be discounted. One possibility is that the sources of the fluids responsible for mineralisation at Lightning Creek and Mount Elliott were more

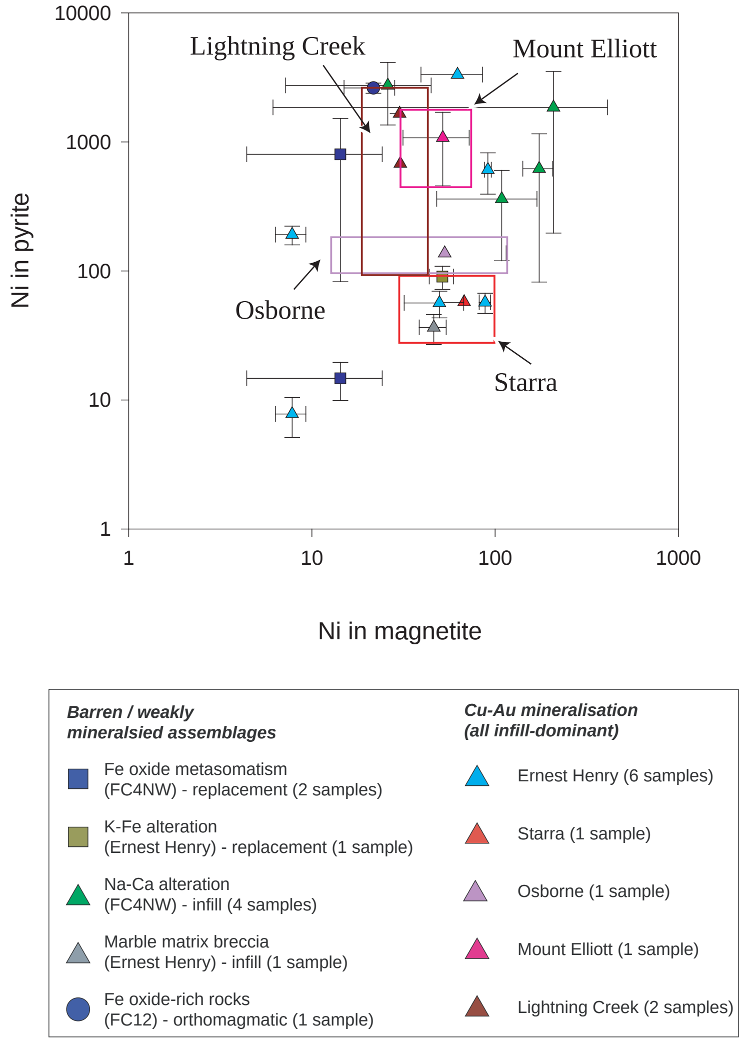

Figure 6.18: Bi-plot comparing the Ni content of magnetite and pyrite from Cu-Au mineralised and weakly mineralised systems in the EFB. The shape of each point in the diagram corresponds to the formational process whereby the magnetite and pyrite formed: infill (triangles), replacement (squares) and orthomagmatic crystal fractionation (circles). Standard deviations for data from Cu-Au mineralisation at Mount Elliott, Lightning Creek, Starra and Osborne are replaced by a colour-coded rectangular box. Also noted in the legend is the number of samples used in the plot for each mineral association. Note the positive correlation between Ni from magnetite and pyrite below 100 ppm Ni.

mafic in composition compared to Osborne and Starra, as Ni is more abundant in mafic igneous rocks (Goldschmidt, 1958). In turn, the broad range of Ni concentrations at Ernest Henry may reflect mixing of two or more fluids of both mafic and felsic source as proposed by Mark et al (1999).

6.7.4. Implications for fluid chemistry and vectors towards mineralisation

The suite of elements found in magnetite, hematite, pyrite and chalcopyrite can provide important information regarding the source of fluids and physicochemical conditions responsible for Fe oxide (±Cu-Au) mineralisation. IOCG deposits are associated with extremely complex chemistries, reflected in the large number of associated mineral phases (Adshead, 1995; Rotherham, 1997; Mark et al., 1999; Williams et al., 2001). Pollard (2000), Pollard (2000) and Williams and Skirrow (2000) suggested that fluids derived from contemporaneous magmas played a major role in the formation of Na-Ca alteration and Fe oxide (Cu-Au) mineralisation (discussed in chapter 5). Furthermore, work by Ulrich et al (2001) demonstrated from fluid inclusion studies using LA-ICP-MS that both fluid chemistry and relative metal ratios at the Bajo de la Alumbrera porphyry Cu-Au-Mo deposit are primarily controlled by the magmatic source of the ore brines, and concluded that a similar case could be made for many other porphyry-style ore deposits.

As mentioned above, magnetite associated with Cu-Au mineralisation at Osborne, Starra and Mount Elliott contained high concentrations of Mo. In contrast, Mo concentrations at Ernest Henry are typically lower, corresponding with the precipitation of molybdenite during Cu-Au mineralisation. Mo, W, U and Th were also found to be low to absent in magnetite from barren Fe oxide-rich rocks and regional Na-Ca assemblages. Molybdenite is commonly associated with porphyry molybdenum (Mo) and copper-molybdenum deposits and is typically carried in oxidised, high temperature hydrothermal fluids (White et al., 1981). Mark et al (1999) interpreted the presence of Mo at Ernest Henry to reflect the fluid composition, with Mo probably carried as a molybdenate complex ($MoO_2(OH)_2$). Therefore, the presence of Mo, W, Th and U in magnetite, in addition to the higher Co, As, Mn, Sc, Ag, In, Sc and Bi within Fe oxides and Fe sulphides in the Cu-Au deposits compared to barren hydrothermal systems, may also be a product of the fluid chemistry.

This interpretation is supported by PIXE analysis of fluid inclusions from Cu-Au mineralisation at Ernest Henry, Starra and Lightning Creek. The present work has shown that the fluids responsible for Cu-Au mineralisation were chemically complex, and contained higher concentrations of Mn, Cu, Fe, Zn and Ba compared to fluids associated with Na-Ca alteration at MFC and Mount Angelay (chapter 4). Mark et al (1999) noted that the complex chemistry associated with ore at Ernest Henry could not be derived from the one fluid, as many of the elements enriched there are soluble under different conditions. The chemical differences between Cu-Au mineralisation at the deposits compared to weakly mineralised and barren hydrothermal systems may be the result of one or more of the following scenarios:

1) Fluids associated with barren and weakly mineralised hydrothermal systems did not interact with another fluid of distinctly different composition;
2) Fluids associated with barren and weakly mineralised hydrothermal systems were derived from different magmatic sources; and/or
3) Physicochemical conditions (e.g. T, f_{O2}) prevented the above elements becoming insoluble at the time of mineral deposition in non-ore systems.

Ni, Se, Co and Si in sulphides distinguish between Na-Ca alteration and Cu-Au mineralisation particularly well. Pyrite and chalcopyrite associated with ore are consistently enriched in Co and Si, and depleted in Ni and Se. Interestingly, magnetite, pyrite and chalcopyrite from sulphide-bearing Na-Ca assemblages at FC4NW contain much higher Ni compared to other Na-Ca assemblages. Mo, W and U were also found to be relatively more common in magnetite from weakly mineralised Na-Ca assemblages from FC4NW compared to barren Na-Ca assemblages. In chapter 4, it was noted that the chemistry of fluid inclusions associated with weakly mineralised Na-Ca assemblages at FC4NW were very similar to barren Na-Ca assemblages, despite FC4NW containing anomalous Cu. These high Ni concentrations suggest that fluids responsible for sulphide-bearing Na-Ca alteration at FC4NW may have been chemically distinct from regional examples, and may explain the presence of sulphide at FC4NW.

Perhaps the most striking aspect of this study is not the fact that the trace element chemistry of specific mineral phases can differentiate between Cu-Au mineralised systems and weakly mineralised to barren counterparts, but that in some cases, mineral associations both peripheral and distal to the deposits contain trace element signatures that closely resemble the ore deposits. Magnetite and pyrite associated with Cu-Au mineralisation at Ernest Henry contain much higher As, Co and Mn contents compared to all other deposits and mineral associations in the dataset. The marble matrix breccia in the footwall of the deposit, which was interpreted to post-date Cu-Au mineralisation (Mark et al., 1999), also contains these elevated trace element signatures. In addition, most of the other trace elements in magnetite, pyrite and chalcopyrite from both ore and marble matrix breccia also exhibit virtually identical trace element signatures, suggesting that both may be genetically linked.

Two other mineral associations that contain similar trace element signatures to the Cu-Au deposits include the barren Fe oxide-rich rocks at Osborne and Starra and Fe oxide-rich rock at the Gilded Rose Breccia. As described above, the low V, Co, Mn and Ni associated with the Fe oxide-rich rocks from Osborne and Starra most likely reflects different genetic processes (chapter 5). In contrast, the breccias from the Gilded Rose area contain no textural features which would imply a syn-sedimentary origin, particularly as the breccia pipe discordantly cuts metamorphic foliation in the surrounding amphibolites (Marshall, 2003). The low V content of magnetite in these rocks correlates well with the low V associated with Cu-Au mineralisation. The geochemical patterns associated with magnetite from the Gilded Rose area may reflect similar fluid chemistry and/or f_{O2} compared to fluids responsible for ore. This fits well with the suggestion by Marshall (2003) that the Gilded Rose Breccias may have been fluid conduits for overlying IOCG deposits.

6.7.5 Comparisons with Kiruna-type systems (Sweden and Chile)

A classification of IOCG deposits by Hitzman et al (1992) proposed a link between Kiruna-type Fe oxide-apatite and IOCG deposits, although more recently Hitzman (2000) suggested the two were formed by essentially unrelated hydrothermal processes. However, many features observed in the Kiruna-type deposits are texturally and mineralogically similar to barren Fe oxide-rich rocks observed throughout the EFB (chapter 5). The trace element data for magnetite was normalised to magnetite from the El Laco iron deposit in western Chile (Nystrom and Henriquez, 1994) (Fig. 6.19). Magnetite from the Kiruna-type ores of Chile and Sweden (Fig. 6.19b, c) exhibit a smooth, flat trend, although negative Al and Mg anomalies are apparent in iron ores

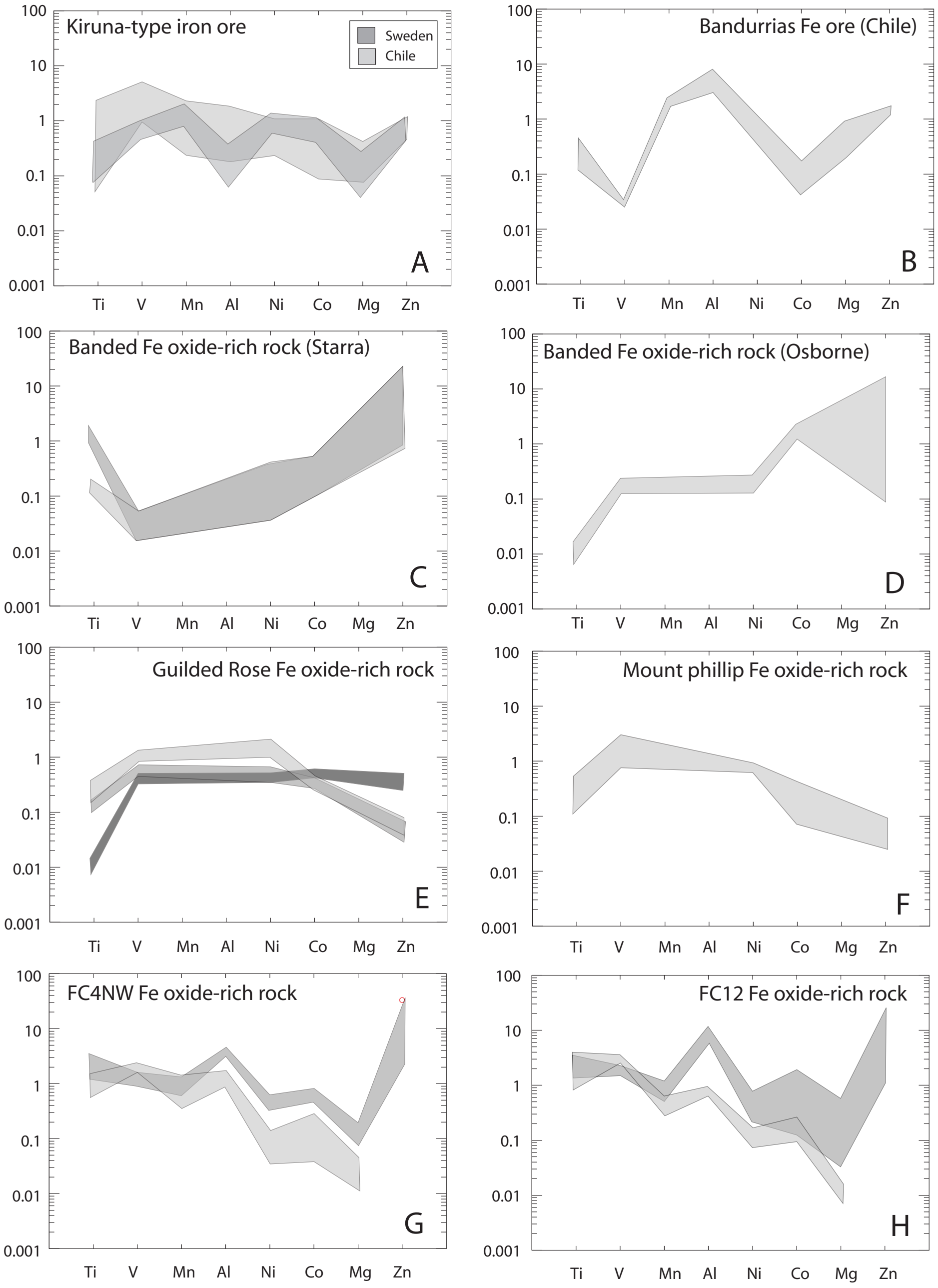

Figure 6.19: Geochemical patterns for magnetite Kiruna-type iron ores in Sweden and Chile and Fe oxide-rich rocks from the EFB normalised against the average composition of the El Laco magnetite taken from Nystrom and Henriquez (1994): Ti=933, V=1360, Mn=486, Al=944, Ni=201, Co=124, Mg=5990 and Zn=90; all in ppm).

A. Kiruna type iron ores from Sweden and Chile
B. The Bandurrias deposit in the Chilean Iron Belt
C. Banded Fe oxide-rich rock from Starra, EFB
D. Banded Fe oxide-rich rock from Osborne, EFB
E. Fe oxide-rich rock from the Guilded Rose area, EFB
F. Fe oxide-rich rock from Mount Phillip, EFB
G. 'Cumulate' Fe oxide rich rock from the FC12 prospect, EFB
H. Fe oxide-rich rock from the FC4NW prospect, EFB

from Sweden (Nystrom and Henriquez, 1994). The Bandurrias deposit of Chile is distinctly different and was interpreted by Nystrom and Henriquez (1994) to be syn-sedimentary in origin (section 6.5). Comparisons between the Kiruna iron ores and magnetite derived from the Cu-Au deposits and alteration peripheral to Ernest Henry indicate distinct differences. Each of the deposits in the EFB are characterised by a pronounced negative Mg anomaly (Fig. 6.20). In contrast, the Mg anomalies from the Kiruna iron ores of Sweden and Chile are less pronounced. The Kiruna iron ores are also markedly different to barren Fe oxide-rich rocks from Starra, Osborne, and Fe oxide-rich rocks from the MFC exploration lease (Fig. 6.19a, b, c, d). Two exceptions are the magnetite-bearing Fe oxide-rich rocks from Mount Philp and the Gilded Rose area (Fig. 6.19e, f), which exhibit even flatter and smoother trends than the Kiruna iron ores.

The different trace element trends associated with the Kiruna-type iron ores of Chile and Sweden and the Cu-Au mineralised Fe oxide deposits of the EFB supports the interpretation by Hitzman (2000) that the Kiruna-type iron ores and IOCG deposits are related to different hydrothermal processes. As described in this chapter and in chapter 5, the banded Fe oxide-rich rocks hosting Cu-Au mineralisation at Starra and Osborne contain both textural and geochemical features which invoke a syn-sedimentary origin (cf. Davidson et al., 1989). However, the Fe oxide-rich rocks from Starra and Osborne differ significantly compared to the Kiruna-type iron ores from Sweden and Chile, as well as magnetite from the Bandurrias deposit. In addition, magnetite associated with these rocks contain common Mo, W and U which are largely absent in most other barren Fe oxide-rich rocks in the EFB (Table 6.2 to 6.4). The different trends exhibited by the Starra and Osborne Fe oxide-rich rocks (this study) and magnetite from the Bandurrias deposit are at odds with the interpretation that all are sedimentary in origin (Nystrom and Henriquez, 1994). One possibility is that the Starra and Osborne Fe oxide-rich rocks have been affected by later metasomatic processes which altered their original trace element signature. In contrast, the similar trends between the Kiruna-type iron ores and Fe oxide-rich rocks from Mount Philp and Gilded Rose suggests that some barren Fe oxide-rich rocks in the EFB may have formed from similar processes to those that produced the Kiruna iron ores of Sweden and Chile (Hitzman, 2000) such as leaching and subsequent re-precipitation from regional (Na±Ca) hydrothermal systems (Oliver et al., 2004) (see chapter 7).

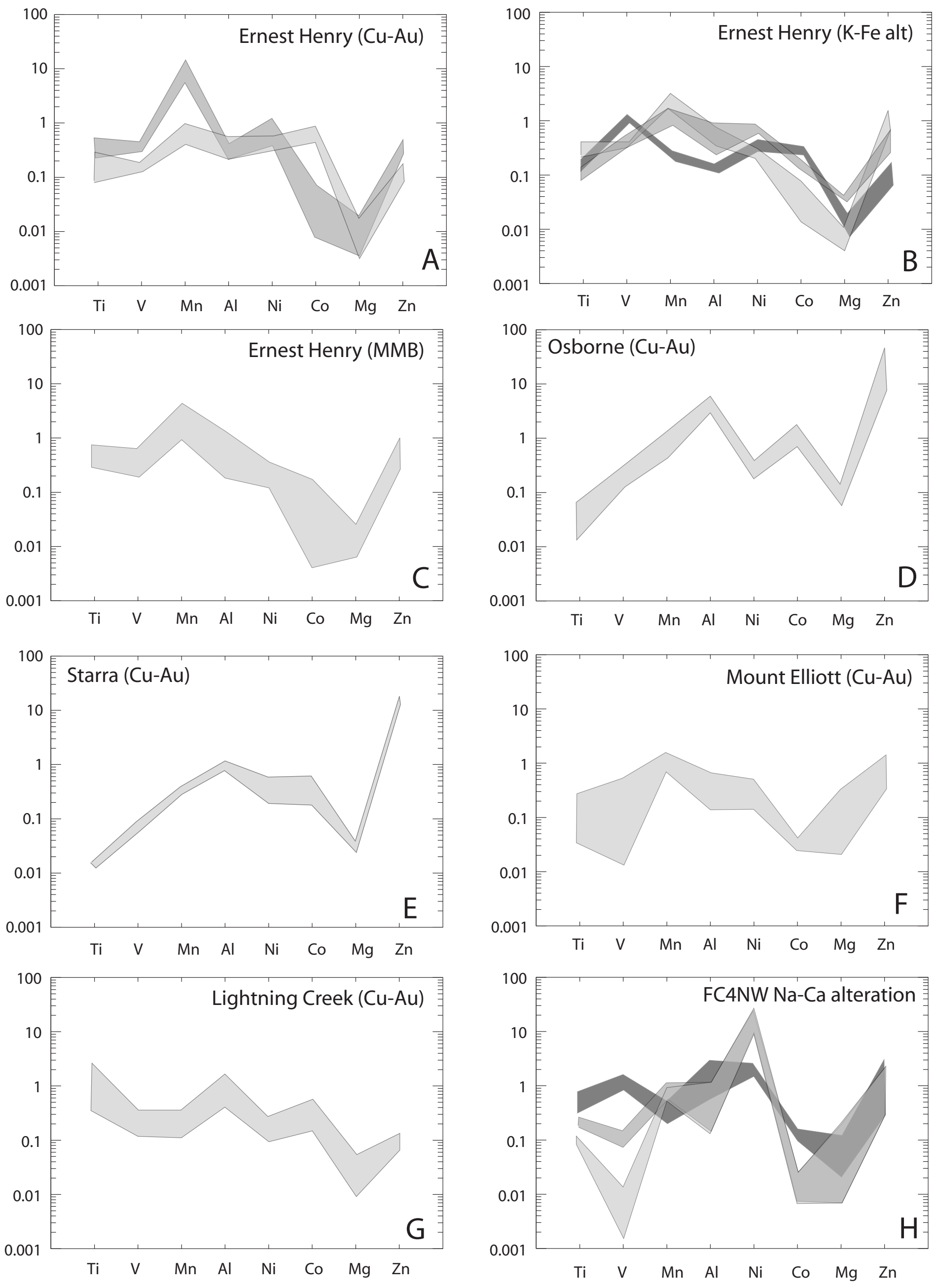

Figure 6.20: Geochemical patterns for magnetite from the major Fe oxide (Cu-Au) deposits in the EFB normalised against the average composition of the El Laco magnetite taken from Nystrom and Henriquez (1994): Ti=933, V=1360, Mn=486, Al=944, Ni=201, Co=124, Mg=5990 and Zn=90; all in ppm). Also shown are pre- and post- mineralisation phases peripheral to the Ernest Henry ore body and sulphide-bearing Na-Ca alteration from the FC4NW prospect.

A. Ernest Henry (Cu-Au)
B. Ernest Henry (K-Fe alteration
C. Ernest Henry (Marble matrix breccia
D. Osborne (Cu-Au)
E. Starra (Cu-Au)
F. Mount Elliott (Cu-Au)
G. Lightning Creek Cu-Au-bearing veins
H Sulphide-bearing Na-Ca veins from the FC4NW prospect

6.8. CONCLUSION

The trace element geochemistry of magnetite, hematite, pyrite and chalcopyrite in various mineral assemblages throughout the EFB provides crucial information regarding the chemical composition of fluids and possible processes involved in the formation of IOCG deposits. Trace elements detected in magnetite, hematite, pyrite and chalcopyrite can typically be explained by their regular substitution into the crystal lattice of each mineral (Table 6.13). Many of these elements exhibit considerable variation between Cu-Au mineralised systems and other mineral associations (Table 6.13). This study has shown that host rock geochemistry, associated mineral assemblage and depositional mechanism most likely played a limited role in controlling the relative concentrations of trace elements in magnetite, hematite, pyrite and chalcopyrite between the deposits and other mineral associations. Instead, a combination of fluid composition and other physicochemical factors such as temperature and f_{O2} appear to be the most important factors responsible for variations in trace element concentrations in the aforementioned minerals. Abundant Cu, Zn and Mn in magnetite suggests the fluids were highly enriched in these components with respect to Fe, as these components will more favourably partition into the fluid rather than magnetite (Ilton and Eugster, 1989). Additionally, temperature can greatly affect the base metal exchange between chloride-rich aqueous fluids and magnetite. Late Cu-Au-bearing veins at Lightning Creek were interpreted by Perring et al (2000) to reflect high-temperature, Cu-Fe-rich fluids that interacted with low-temperature meteoric fluids. Despite the high Cu concentrations associated with fluids at Lightning Creek, magnetite associated with these veins contains very low Cu values. These low Cu values may be a function of the low temperatures (<200°C) associated with these veins (chapter 4).

V content in magnetite differentiates ore magnetite and magnetite from other mineral assemblages, with all the deposits containing <1000 ppm V. One important control on the partitioning of V into magnetite is f_{O2}, where the partition coefficient of V into magnetite will increase with decreasing f_{O2}. This is consistent with the low V content in Starra which was interpreted by Rotherham (1997) to have formed under more oxidised conditions reflected in the high Au:Cu ratios. Huston et al (1995) showed that temperature, redox and pH can all affect the partitioning of Se into pyrite. However, the oxidation state of the fluid was not a significant factor in controlling Se content in pyrite, as Starra contains less Se than Osborne despite the former being more oxidised.

Fe oxide system	***Mineral***	***Detected elements***	***Elements which distinguish between Fe oxide systems***
Ernest Henry	Magnetite	Ti, Si, Al, Mg, V, Cr, Mn, Co, Ni, Cu, Zn, Ga, Sn, Pb, As, Zr, Y, U, Hf, La, Ce, Bi, Sb, In, Mo, W and Sn	Cu-Au mineralisation: -Higher Sn and Mn -Lower V, Ti, Mg, Si, Cr and Zn
	Pyrite	Ti, Si, Co, As, Se, Ni, Mg, Al, In, Cu, Sn, Sb, Ru, Mn, Pb, Bi, Cr and Ag	Cu-Au mineralisation: -Higher Co and As
Other Fe oxide systems	Magnetite	Ti, Si, Al, Mg, V, Cr, Mn, Co, Ni, Cu, Zn, Ga, Sn, Pb, Sc, As, Zr, Y, U, Hf, La, Ce, Bi, Sb, In, Mo, W and Sn	Cu-Au mineralisation: -Higher Sc and Mn -Lower V, Ti and Cr Mo, W, U also more higher and more common in Cu-Au mineralised and weakly mineralised assemblages
	Pyrite	Ti, Si, Co, Ni, As, Se, Mg, Al, In, Cu, Sn, Sb, Ru, Mn, Pb, Bi, Cr and Ag	Cu-Au mineralisation: -Higher Co and As -Lower Se and Ni
	Hematite	Ti, Si, Mg, Al, Co, Ni, As, Sn, Sb, Zr, V, Mn, W, Sc, Ga, Nb, La, Ce, In, Hf, Bi, Pb, U and Cu	Cu-Au mineralisation: -Higher As, Ga, Sb and W
	Chalcopyrite	Ti, Si, Co, Ni, Zn, Se, Ag, In, Sn, Pb, Bi, Mo, Ru, Sb, V, Mn, Au, U, Cd and W	Cu-Au mineralisation: -Higher Bi, Sn, In and Ag -Lower Se

Table 6.13: Summary of the important trace elements analysed for magnetite, hematite, pyrite and chalcopyrite in this study, as well as the elements which appear to discriminate between magnetite, hematite, pyrite and chalcopyrite from mineral associations containing variable degrees of Cu-Au mineralisation.

However, Se concentrations in pyrite at Lightning Creek are significantly higher than in any other system in the dataset, coinciding with the low temperatures (<200°C) at the time of formation, and implying that temperature was the strongest control on Se in pyrite in the EFB.

Although physicochemical factors including f_{O2} and temperature can control the degree of partitioning between certain elements and mineral phases, the chemical composition of magnetite, hematite, pyrite and chalcopyrite is probably a reflection of fluid chemistry. In particular, Mo, W and U, were found to be either more common and / or in higher concentrations in magnetite from the ore deposits compared to weakly mineralised and barren Fe oxide-bearing associations (Table 6.2 to 6.4). The high Mo, W, U and Th at the deposits coincides with their more complex mineralogy, and the enrichment of these elements in many porphyry systems (*cf.* Audetat and Guenther, 2000; Ulrich et al, 2001). The elevated concentrations of Co, As, Mn, Sc, Ag, In, Sc and Bi in Fe oxides and Fe sulphides from ore, together with the more complex fluid inclusion chemistry associated with both Ernest Henry and Starra, suggests that fluids associated with Cu-Au mineralisation in the EFB were chemically more complex, although the physicochemical factors discussed above may also have inhibited the precipitation of these elements in non-ore systems. Nevertheless, this may also suggest a different magmatic source for fluids associated with Cu-Au mineralisation compared to other mineral associations.

These chemical patterns also differ considerably to Kiruna-type iron ores in Sweden and Chile, with the exception of two barren Fe oxide-rich rocks from Mount Philp and the Gilded Rose area. This supports the interpretation by Hitzman (2000) who suggested different hydrothermal processes were involved in the formation of IOCG deposits and Kiruna-type iron ores. On the other hand, many barren Fe oxide-rich rocks in the EFB are texturally, mineralogically and chemically similar to Kiruna iron ores, and may hence have formed by similar processes.

Not only can trace element chemistry be used to discriminate between magnetite, hematite, pyrite and chalcopyrite from ore-related systems and other mineral associations in the EFB, it also has the potential to identify distal parts of hydrothermal systems related to Cu-Au mineralisation. For example, some magnetite-bearing Fe oxide-rich rocks from the Gilded Rose area contain V concentrations similar to the ore deposits being significantly lower in V content than most other mineral associations in the district, potentially indicating a regional pathway of one of the ore fluids.

CHAPTER 7:

SYNTHESIS: CONTROLS ON CU-AU MINERALISATION AND FE OXIDE METASOMATISM IN THE EASTERN FOLD BELT

SYNTHESIS: CONTROLS ON Cu-Au MINERALISATION AND Fe OXIDE METASOMATISM IN THE EASTERN FOLD BELT

7.1. INTRODUCTION

The EFB of the Mount Isa Inlier is host to a variety of Fe oxide-rich rocks that bear a number of spatial and temporal relationships to several major IOCG deposits in the district. However, prior to this study, the genetic relationship between the Fe oxide-rich rocks hosting Cu-Au mineralisation and those distal to these deposits was previously poorly understood. Of particular interest are: 1) the role played by intrusions as a source of fluid, heat and metals in the formation of Cu-Au mineralised and ‘barren’ Fe oxide-rich rocks, and 2) the relationship of Fe oxide-rich rocks and Cu-Au deposits to regional Na-Ca-K alteration.

Textural and geochemical criteria indicate that a variety of depositional processes were responsible for the formation of Fe oxide-rich rocks in the EFB. To-date, four major interrelationships between Fe oxide-rich rocks and Cu-Au mineralisation have been described by workers in the EFB, as summarised in figure 7.1. This study has aimed to develop a new classification scheme for Fe oxide-rich rocks in the EFB and their potential relationships to Cu-Au mineralisation, with particular emphasis on rocks in the MFC exploration lease peripheral to the Ernest Henry (Cu-Au) deposit.

7.2. DEPOSITIONAL PROCESSES FOR Fe OXIDE-RICH ROCKS

Four distinct processes are responsible for the formation of Fe oxide-rich rocks in the EFB: 1) syn-sedimentary (BIF), 2) orthomagmatic, 3) replacement, and 4) infill. Geochemical analyses and textural observations have aided in determining the origins of these Fe oxide-rich rocks. Figure 7.2 provides a detailed summary of the possible relationships between Fe oxide-rich rocks and Cu-Au mineralisation in the EFB. In addition, the main chemical signatures that appear to distinguish between Fe oxide-rich rocks of different affinities are also shown.

There has been considerable debate regarding the origin of Fe oxide-rich rocks that host Cu-Au mineralisation at the Osborne and Starra (Cu-Au) deposits (Davidson, 1989; Williams, 1994; Rotherham, 1997; chapter 5). This study has shown that these rocks

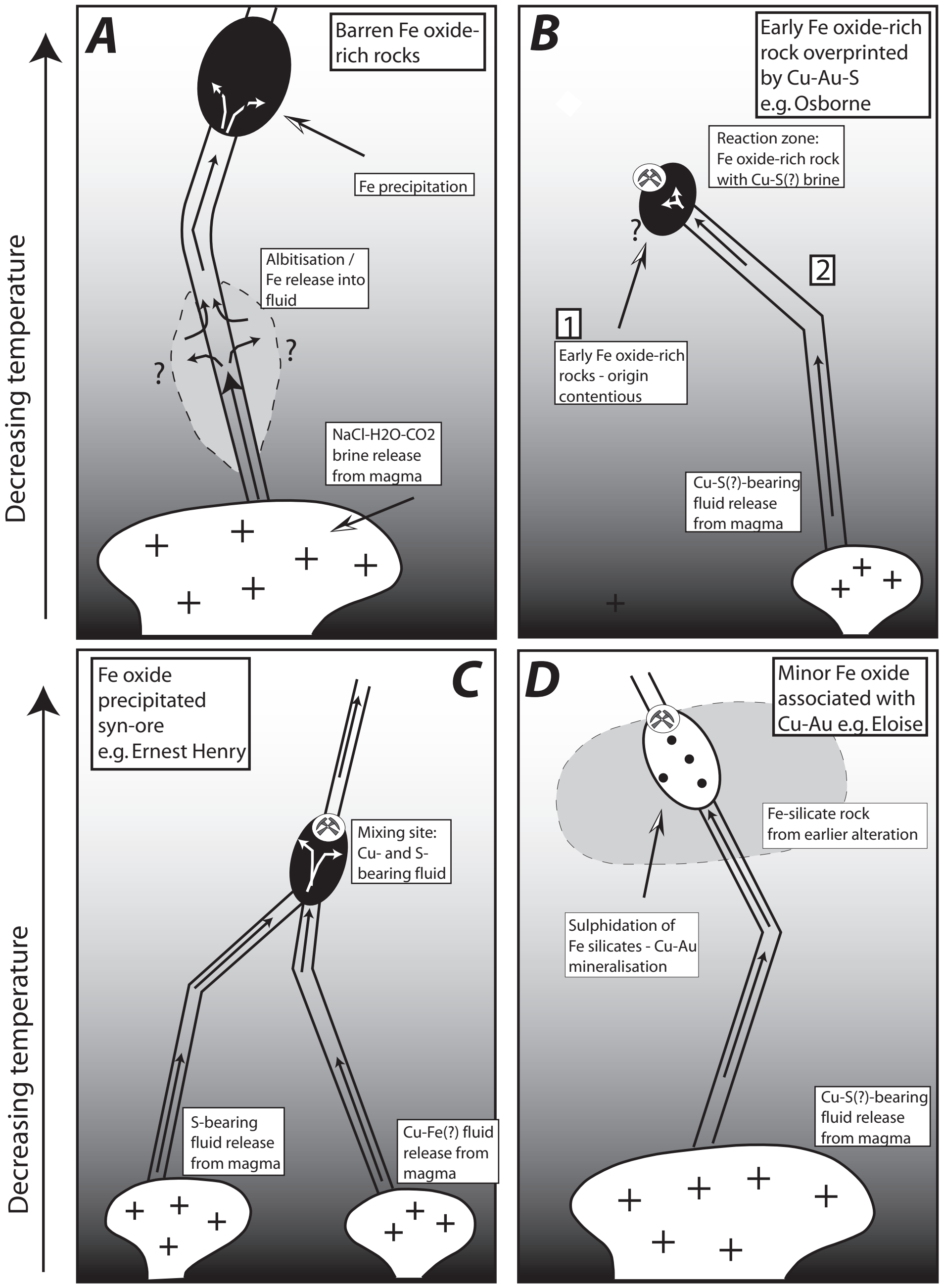

Figure 7.1: Schematic diagram illustrating the possible relationships between Cu-Au mineralisation and Fe oxide-rich rocks. A more detailed explanation of each category is given in chapter 5.
A. Barren Fe oxide-rich rocks - various processes implicated in their formation (e.g. Roxmere irontone; this study) (see figure 7.2).
B. Fe oxide-rich rocks overprinted by later Cu-Au-bearing fluids (e.g. Osborne; Adshead, 1995).
C. Fe oxide and Cu-Au mineralisation precipitated co-genetically (e.g. Ernest Henry; Mark et al., 1999)
D. Cu-Au mineralisation is not spatially associated with significant Fe oxide enrichment. (e.g. Eloise; Baker, 1998)

Figure 7.2: Schematic representation of the possible relationships between Fe oxide-rich rocks formed from different depositional processes and Cu-Au mineralisation. Also shown are the important immobile and trace elements that can be used to discriminate between these different formational processes (low V, Ti, Ga and Cr, and high Mn). Hydrothermal Fe oxide-rich rocks formed either by the replacement of a precursor rock (high immobile element content) or as infill (low immobile element content) may relate to Cu-Au mineralisation where both are precipitated co-genetically (e.g. Ernest Henry) or the Fe oxide-rich rock acts as a reactive host (e.g. Osborne). Both orthomagmatic (high immobile element content) and sedimentary (low immobile element content) processes can also form Fe oxide-rich rocks. However, these rocks can only be related to Cu-Au mineralisation by acting as reactive hosts to Cu-bearing fluids (e.g. Osborne and Starra?). The relative trace and immobile element concentration of Fe oxide-rich rocks are colour coded according to the two graphs at the bottom of the diagram.

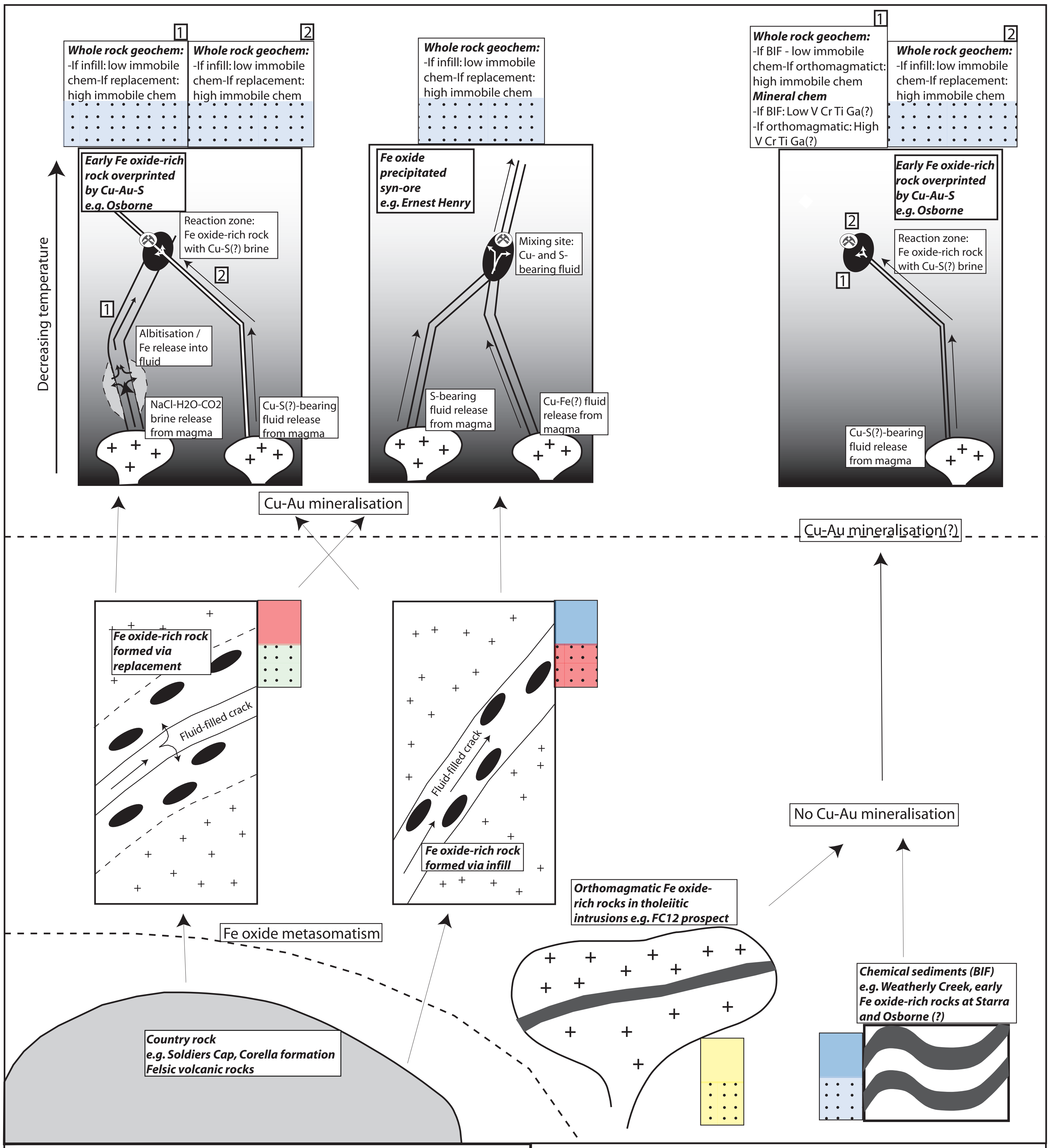

Whole-rock geochemistry of Fe oxide-rich rocks

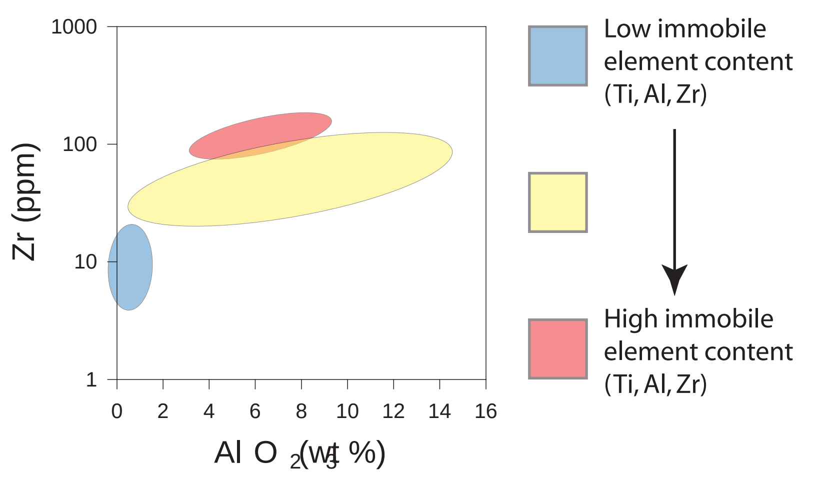

Trace element mineral chemistry of magnetite

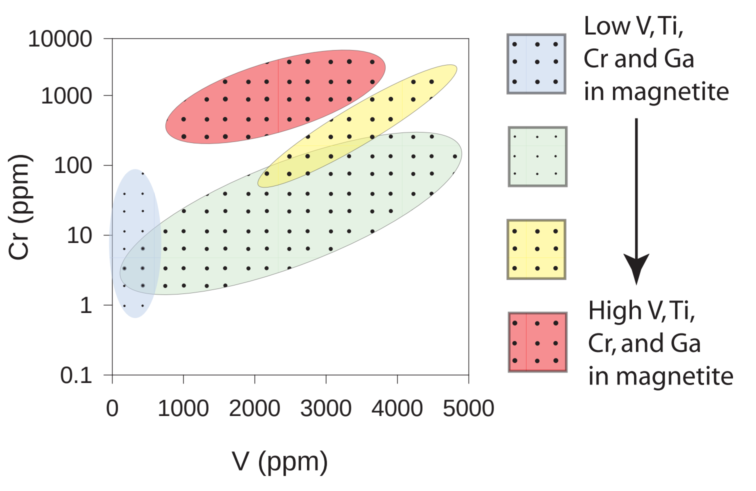

exhibit normalized REE patterns similar to BIF from the Hamersley Province in Western Australia, and elsewhere in the Selwyn Range district implying a chemical sedimentary origin. In addition, Zr and Al_2O_3 (whole rock geochemistry) and V, Cr, Ga and Ti (magnetite mineral chemistry) concentrations are lower in these rocks compared to Fe oxide-rich rocks that form by other processes. Fe oxide-rich rocks formed from orthomagmatic processes, such as at FC12, contain relatively high Al_2O_3, TiO_2 and Zr (whole rock geochemistry) and V, Cr, Ga and Ti (magnetite mineral chemistry), whereas REE patterns are nearly identical to their gabbroic hosts. These rocks are texturally and chemically reminiscent of magnetite-rich layers found in other layered tholeiitic sequences including the Bushveld Complex in South Africa, and are interpreted to have formed from episodic fluctuation in f_{O2} and alternating fractional crystallisation of silicate and oxide minerals (*cf.* Reynolds, 1985; Jiren et al., 1988; Kariyanna et al., 1996; Karkkainen, 1999; Vinayaka et al., 1999). Fe oxide-rich rocks formed by orthomagmatic processes have not previously been documented in the EFB.

Fe oxide-rich rocks formed by secondary (hydrothermal) processes may not display distinctive textures that reflect their origin. This is especially the case for Fe oxide-rich rocks formed by infill. The magnetite pit to the south of the MFC hill (Fig. 2.8) and the Roxmere ‘ironstone’ are such examples. Isocon analyses show that these Fe oxide-rich rocks did not have the same precursor as their adjacent hosts. In addition, the low concentration of Ti, Al and Zr in these rocks is consistent with their low solubility in aqueous solutions, suggesting that these rocks are a product of infill rather than replacement. In contrast, Fe oxide-rich rocks within the FC4NW prospect exhibit higher immobile element concentrations, and formed by replacement of their immediate host rocks.

7.3. RELATIONSHIP BETWEEN Fe OXIDE (±Cu-Au) MINERALISATION AND Na-Ca ALTERATION

7.3.1. Na-Ca alteration

Na-Ca alteration at both the FC4NW and FC12 prospects exhibit characteristics that suggest a different hydrothermal history in each case. At FC12, sulphide-bearing, fracture-controlled Na-Ca veins cut orthomagmatic Fe oxide-rich rocks. At FC4NW, a strong spatial and temporal relationship between Fe oxide metasomatism and ductile-brittle style clinopyroxene-rich Na-Ca alteration is apparent. Clinopyroxene-rich Na-Ca alteration and Fe oxide metasomatism at FC4NW contain similar mineral assemblages, exhibit a close spatial and temporal association with post-peak metamorphic intrusions, and are cut by lower temperature, fracture-controlled amphibole-rich Na-Ca alteration representing the main Cu-bearing mineral assemblage at FC4NW.

Fluid inclusions associated with Na-Ca alteration at FC4NW record a wide range of salinities and temperatures, from primary, high temperature and highly saline (260 to 452ºC; 35 to 59 wt% NaCl), multiphase (e.g., sylvite, halite and hematite) fluid inclusions enriched in a variety of components including K, Cl and Fe, through to later generation fluid inclusions that exhibit lower temperatures and salinities, consistent with progressive cooling over time. Fluids associated with these later hydrothermal stages typically contain greater Cu, but are generally geochemically simpler, than the multiphase inclusions. The progressive cooling shown in the fluid inclusion data is inferred to reflect the transition from clinopyroxene-rich Na-Ca alteration to the later sulphide-bearing amphibole-rich Na-Ca alteration at FC4NW. In addition, the low Mn, Ba and Zn in fluid inclusions from FC4NW suggests sulphide-bearing Na-Ca alteration is more closely associated with barren regional Na-Ca assemblages (Fu et al, unpublished data) than fluids responsible for pre- and syn- Cu-Au mineralisation stages at Starra, Lightning Creek and Ernest Henry. Fluids associated with sulphide-bearing Na-Ca assemblages at FC4NW more closely resemble fluids associated with regional Na-Ca alteration rather than Cu-Au mineralisation at the deposits

In contrast, geochemical mass transfer associated with Na-Ca alteration at FC12 is not consistent with regional Na-Ca assemblages described by Williams (1994), Rubenach and Lewthwaite (2001) and Oliver et al. (2004). At FC12, Fe is consistently depleted and the mobility of Mg, REE, Cu and S were found to be variable. In addition, although Na is enriched in some samples at FC12, other regional Na-Ca systems in the EFB commonly show more highly enriched Na during alteration (Rubenach and Lewthwaite, 2001; Oliver et al., 2004). It is unlikely that host rock geochemistry alone caused the above geochemical patterns at FC12, as previous studies on regional Na-Ca assemblages found similar chemical patterns associated with a variety of rock types (Rubenach and Lewthwaite, 2001; Oliver et al., 2004). In addition, a comparison between the mass transfer associated with Fe oxide metasomatism at FC4NW and Na-

Ca alteration at FC12 does not exhibit patterns that would implicate a genetic link. The mineral assemblage and geochemical mass balance associated with Na-Ca alteration at FC12, in particular the considerable addition of Fe and minor enrichment of Na, suggest a different fluid chemistry to regional Na-Ca alteration and Na-Ca alteration at FC4NW. One possibility is that Na-Ca alteration at FC12 was produced by more evolved fluids that interacted with country rocks, producing albitisation, thus altering the fluid chemistry with time and later precipitating chlorite-calcite-magnetite-hematite-chalcopyrite-pyrite mineral assemblages at cooler temperatures. If this is the case, then it is unlikely that Na-Ca alteration is related to the felsic intrusive rocks at FC12, as opposed to FC4NW where there is a more obvious genetic link (discussed below).

Although the FC12 and FC4NW rocks contain more sulphides than regionally Na-Ca altered rocks, sulphide mineralisation in both cases is relatively minor compared to the main Cu-Au deposits at Ernest Henry and Starra. Despite this, the presence of Cu and Fe at FC4NW, together with the apparent diffusion of Cu into the vein from the adjacent rock at FC12, suggests that these fluids had the potential to transport significant amounts of these metals. The higher Mn, Zn and Fe content of fluids associated with ore at Ernest Henry and Starra compared with fluids responsible for Na-Ca alteration at FC4NW coincides with the diverse mineral assemblages at these deposits. The most likely explanation for the low sulphide content at FC4NW and FC12 is that the fluids simply did not contain enough Cu and/or S to produce significant ore. Given previous comments about the control on the trace element chemistry of sulphides and oxides, this is most likely a reflection of a relatively Cu and S-poor fluid source.

Interestingly, magnetite, pyrite and chalcopyrite from sulphide-bearing Na-Ca assemblages at FC4NW contain much higher Ni, Mo, W and U compared to regional Na-Ca assemblages. Together with the presence of sulphide in Na-Ca veins at FC4NW, this may suggest another fluid either interacted with, or overprinted the fluids associated with Na-Ca alteration. The high Ni content in magnetite from FC4NW may also reflect a more mafic intrusive source as discussed in chapter 6. Another possibility is that the FC4NW area represents the start of a Cu-Au depositional regime where conditions were more suitable for voluminous sulphide mineralisation of the Ernest Henry style (discussed below).

7.3.2. Fe oxide metasomatism

Previous studies (Williams, 1994; Rubenach and Lewthwaite, 2001; Oliver et al., 2004) have shown that a potential link exists between Fe oxide metasomatism and Na-Ca alteration in the EFB. However, together with the apparent orthomagmatic origin of Fe oxide-rich rocks at FC12, the geochemistry of similar rocks that clearly formed by metasomatic processes suggest Fe oxide metasomatism and Na-Ca alteration are not always implicitly linked. The fluids associated with Fe oxide-rich rocks in outcrop at MFC are geochemically distinct compared to those responsible for Na-Ca alteration at FC4NW and elsewhere. In particular, fluid inclusion homogenisation temperatures are significantly lower and exhibit more variability than equivalents at FC4NW. The broader temperature range of the fluids associated with some Na-Ca alteration may suggest that they interacted with lower-temperature fluids (e.g., meteoric waters).

At FC4NW, Fe oxide metasomatism exhibits significantly different mass transfer patterns compared to similar rocks described by the above authors (e.g. K-Fe alteration and Ernest Henry). Fe oxide metasomatism is associated with significant mass gain, Na is immobile to slightly depleted, and Sr, K and Ba are consistently depleted. The depletion in K, Sr and Ba at FC4NW can be attributed to biotite breakdown in the metasedimentary rocks, whereas secondary biotite is deposited during K-Fe alteration at Ernest Henry. Fe oxide metasomatism at FC4NW more closely resembles Fe-Ca alteration at Lightning Creek (Perring et al., 2000). Considering the close spatial and temporal association between Fe oxide metasomatism and igneous intrusions at FC4NW, it is unlikely that the Fe was derived primarily from fluid-rock interaction as regionally envisaged by Oliver et al. (2004). A more likely explanation is that the Fe was sourced from a nearby magmatic intrusion, similar to that proposed by Perring et al (2000) for the Lightning Creek prospect. This association between Fe oxide metasomatism and magmatic intrusions at Lightning Creek also suggests that Fe associated with Fe oxide (±Cu-Au) mineralisation in the EFB may be derived from multiple sources.

7.3.3. Fe oxide (Cu-Au) mineralisation

The mineral chemistry of magnetite, hematite, pyrite and chalcopyrite can be used to discriminate between Cu-Au-mineralised systems and systems which are weakly mineralised and barren. Although factors including the degree of fluid-rock interaction, whole-rock geochemistry and the presence of other mineral phases in the mineral assemblage will most likely contribute to the trace element composition of oxides and sulphides, this influence is interpreted to be small compared to other factors. In particular, the more common presence of Mo, W and U in ore magnetite, together with the high concentrations of Sc, Mn, As, Co, Bi, Sn, In, Ag, Sb and Ga (elements in relatively low abundance in the host rocks), is most likely a reflection of fluid chemistry, but is probably also influenced by other physicochemical factors, including temperature (cf. Cu, Zn and Mn in magnetite and Se in pyrite) and redox (V in magnetite).

The concentration of V in magnetite exhibits the greatest separation between ore systems and barren to weakly mineralised equivalents. The low V content within ore magnetite may imply two things. Fluids associated with Cu-Au mineralisation are depleted in V compared to fluids associated with other alteration events, and/or fluids associated Cu-Au mineralisation are relatively oxidised (cf. Toplis and Corgne, 2002). It has already been shown that Cu-Au fluids are clearly geochemically distinct from Na-Ca fluids at Mount Angelay, FC4NW and FC12. It is therefore reasonable to assume that fluid chemistry was also a major contributing factor to the variable V content between the aforementioned mineral associations, although this does not preclude the effect of redox. In cases where fluid chemistries may be similar (i.e. Cu-Au fluids), a stronger case can be argued for the effects of changing redox. Rotherham (1997) suggested that the high Au:Cu ratios at Starra may be attributed to the fluids being more oxidised compared to Ernest Henry, Osborne and Mount Elliott where Au:Cu ratios are distinctly lower. This coincides with V being relatively low in magnetite at Starra, and implies that changes in redox may have been the dominant control on the partitioning of V in magnetite in this case.

The trace element chemistry of magnetite, pyrite, hematite and chalcopyrite associated with Cu-Au mineralisation at Ernest Henry and Starra strengthens the argument for the interaction of multi-sourced fluids of magmatic origin (Mark et al., 1999; Pollard, 2000; Williams and Skirrow, 2000; Williams et al., 2001). Magnetite associated with ore at Ernest Henry, Starra, Osborne and Mount Elliott are enriched in Mo, W and U and are commonly identified in many porphyry (Cu-Au) deposits (Audètat and Guenther, 2000; Ulrich et al., 2001). This supports the interpretation by Pollard (2000) that Fe oxide

(Cu-Au) and porphyry (Cu-Au) deposits form part of a broad spectrum of intrusion related Cu-Au deposits. Ulrich et al (2001) recognised that fluid chemistry and metal ratios at the Alumbrera porphyry Cu-Au-Mo deposit is primarily controlled by the magmatic source of the ore brines. The minor to absent Mo, U and W in magnetite from barren regional Na-Ca assemblages and Fe oxide-rich rocks suggests they are products of fluids derived from geochemically different (magmatic) sources.

7.4. RELATIONSHIP BETWEEN MFC AND ERNEST HENRY

Cu-Au mineralisation at Ernest Henry is associated with a complex (Cu-Au-Mo-U-REE-As-K-Ba-Mn) geochemical signature and mineral assemblage that is absent at MFC. Furthermore, sulphide mineralisation at FC12 and FC4NW is more akin to the Na-Ca-Fe assemblages that predate ore deposition at Ernest Henry (Fig. 7.3). The relative timing between Fe oxide metasomatism and Cu-Au mineralisation at FC12 and FC4NW is reflected in the geochemistry, where poor correlations between Cu and Fe are apparent at both prospects. While Fe oxide metasomatism is associated with clinopyroxene-rich Na-Ca alteration at FC4NW, Ernest Henry records K-Fe alteration and Fe oxide–precipitation associated with the main phase of Cu-Au mineralisation. These ore-forming events post-date Na-Ca alteration and are chemically and mineralogically distinct from the Cu-Au mineralised zones at FC4NW.

Possibly the most important discriminating factor between the two areas is the low concentrations of Au at FC4NW and FC12. Gold is an important commodity in many IOCG deposits in the Cloncurry district and elsewhere. Gold concentration and distribution is commonly linked to the relative redox of individual deposits, where oxidised, hematite-, pyrite-bearing occurrences typically have more Au than reduced magnetite +/- pyrrhotite-bearing counterparts (cf. Rotherham, 1997). The lack of detectable Au and low Cu at MFC may be the result of a number of factors. The presence of felsic igneous rocks at both FC4NW and FC12 indicates the presence of a nearby igneous intrusion. In contrast, no igneous intrusions have been documented at Ernest Henry. The presence of intrusive rocks at FC4NW and FC12 suggests these areas may have been situated too close to a magmatic source, where higher temperatures or absence of initial sulphur prohibited the significant sulphide precipitation. However, whereas there is a close spatial and temporal association

Figure 7.3: Schematic representation illustrating the possible relationships between hydrothermal alteration at the FC12 and FC4NW prospects compared to the Ernest Henry (Cu-Au) system over time.

A. *Formation of clinopyroxene-rich Na-Ca alteration at FC4NW, which exhibits a close spatial and temporal relationship to granitic and pegmatitic dykes. This early Na-Ca alteration phase at FC4NW is also associated with Fe oxide metasomatism.*

B. *The igneous intrusion cools over time, and actinolite becomes the dominant mineral phase associated with Na-Ca alteration at FC4NW instead of clinopyroxene. This alteration phase is interpreted to be related to sulphide-bearing Na-Ca alteration at FC12 and pre-mineralisation Na-Ca alteration at Ernest Henry.*

C. *Cu-Au mineralisation post-dates Na-Ca alteration at FC12, FC4NW and at Ernest Henry. Fluids associated with Cu-Au mineralisation at Ernest Henry are chemically more complex and contain much higher concentrations of Ba, Zn and Mn than fluids associated with sulphide mineralisation at FC4NW and FC12. suggesting an alternative fluid source and/or fluid mixing of a Cu-Fe-bearing and S-bearing fluid. Na-Ca fluids at FC4NW may be associated with the later formation of barren Fe oxide-rich rock.*

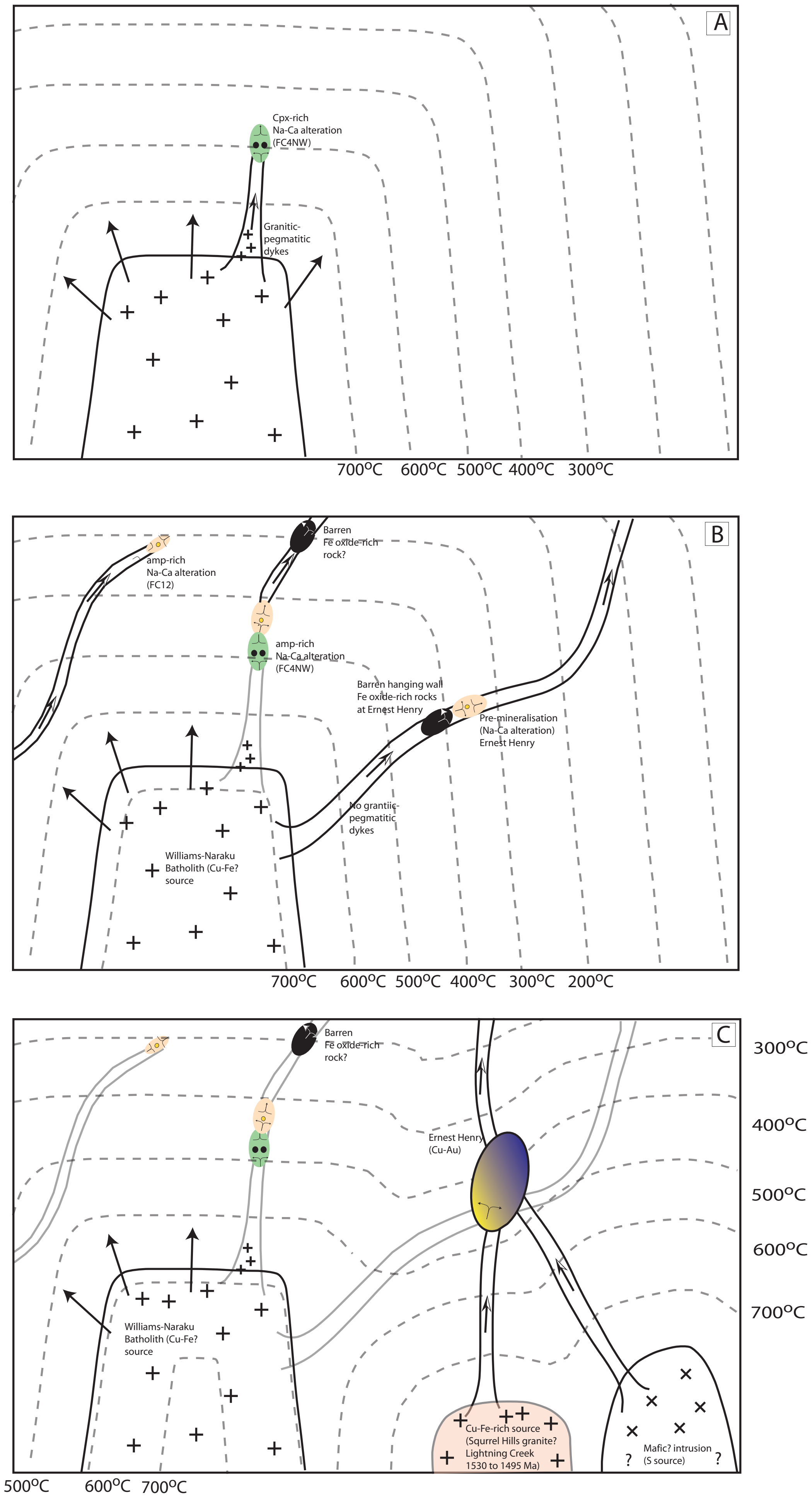
A
Cpx-rich
Na-Ca alteration
(FC4NW)
Granitic-
pegmatitic
dykes
700°C 600°C 500°C 400°C 300°C
B
Barren
Fe oxide-rich
rock?
amp-rich
Na-Ca alteration
(FC12)
amp-rich
Na-Ca alteration
(FC4NW)
Barren hanging wall
Fe oxide-rich rocks
at Ernest Henry
Pre-mineralisation
(Na-Ca alteration)
Ernest Henry
No grantiic-
pegmatitic
dykes
Williams-Naraku
Batholith (Cu-Fe?
source
700°C 600°C 500°C 400°C 300°C 200°C
C
Barren
Fe oxide-rich
rock?
Ernest Henry
(Cu-Au)
Williams-Naraku
Batholith (Cu-Fe?
source
Cu-Fe-rich source
(Squrrel Hills granite?
Lightning Creek
1530 to 1495 Ma)
Mafic? intrusion
(S source)
? ?
300°C
400°C
500°C
600°C
700°C
500°C 600°C 700°C

between Na-Ca alteration and igneous intrusions at FC4NW, Na-Ca alteration at FC12 formed at lower temperatures (chapter 3). These lower temperatures suggest that fluids associated with Na-Ca alteration at FC12 probably were more evolved with respect to their equivalents at FC4NW and most likely were not related to the felsic igneous intrusions observed in drill core. The presence of sulphide in Na-Ca assemblages from at FC12 and FC4NW shows that mineralisation occurred over a variety of temperature conditions. However, cooling appears to be an important trigger for the precipitation of sulphides, as suggested by the spatial and temporal association between sulphide and the later amphibole-rich Na-Ca alteration at FC4NW. These observations also suggest that sulphide mineralisation is unlikely to occur adjacent to high-temperature igneous intrusions.

While this and other studies (e.g. Mark et al., 1999; Pollard et al., 2000) have demonstrated that fluids associated with Na-Ca alteration and Fe oxide (Cu-Au) mineralisation by and large can contain a significant magmatic component, the paragenetic timing and fluid chemistry associated with Na-Ca alteration at MFC and Cu-Au mineralisation at Ernest Henry suggest they may be related to different sources. It is clear that sulphide-bearing Na-Ca alteration is an earlier hydrothermal event compared to the major Fe oxide (Cu-Au) mineralisation event at Ernest Henry. The fluid chemistry of the Na-Ca veins at FC4NW suggests a closer affinity to fluids responsible for regional Na-Ca assemblages rather than those directly related to Cu-Au mineralisation at Ernest Henry and Starra. However, mass transfer patterns associated with Na-Ca alteration at FC12 suggests a cooler fluid than inferred regionally which had previously undergone significant fluid-rock interaction that ultimately altered the fluid chemistry. These observations suggests that minor sulphide mineralisation at MFC is related to the early, pre-mineralisation, Na-Ca alteration at Ernest Henry. The mineral chemistry of magnetite in Na-Ca assemblages at Ernest Henry, FC12 and FC4NW and regional examples supports this interpretation, as the trace element concentrations are similar in each case (Fig. 7.4). In contrast, magnetite associated with Cu-Au mineralisation commonly contains elevated Mn and Sc and lower Ti, V, Ga and Cr compared to the aforementioned Na-Ca assemblages (Fig. 7.4) suggesting that the Cu-Au mineralisation at Ernest Henry is a later event and may be associated with younger, deep-seated, intrusions not exposed in outcrop (Fig 7.3).

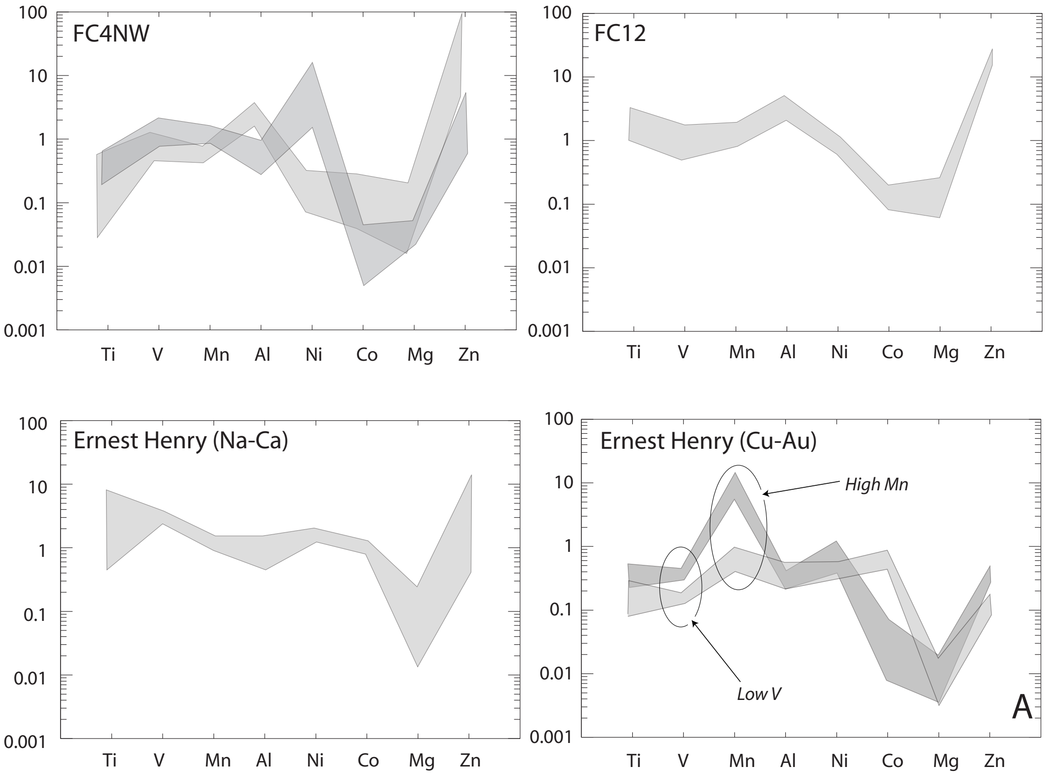

Figure 7.4: Geochemical patterns for magnetite from Na-Ca alteration at the FC4NW and FC12 prospects and Ernest Henry from the EFB. For FC4NW and Cu-Au mineralisation at Ernest Henry, the trace element mineral chemistry data defined two distinct trends. Data was normalised against the average composition of the El Laco magnetite taken from Nystrom and Henriquez (1994): Ti=933, V=1360, Mn=486, Al=944, Ni=201, Co=124, Mg=5990 and Zn=90; all in ppm).

A. Na-Ca alteration from FC4NW
B. Na-Ca alteration from FC12
C. Pre-mineralisation Na-Ca alteration from Ernest Henry
D. Cu-Au mineralisation from Ernest Henry

Note the high Mn and low V anomalies associated with Cu-Au mineralisation at Ernest Henry

The anomalous W, Mo and U in magnetite from Na-Ca assemblages at FC4NW and FC12 is minor to absent in barren regional Na-Ca assemblages, but highly enriched at Ernest Henry. The Cu-Au mineralisation at Ernest Henry may be part of an overlapping hydrothermal system, supporting the interpretation by Mark et al. (1999) that more than one fluid was responsible for Cu-Au mineralisation. Fluids responsible for sulphide mineralisation at MFC may have either been diluted by another fluid, possibly of meteoric origin, or did not mix with a more chemically complex, S-bearing fluid. Thus, although a clear distinction can be made between sulphide mineralisation at MFC and Cu-Au mineralisation at Ernest Henry both chemically and paragenetically, MFC may represent a vector towards mineralisation at Ernest Henry, because a small amount of potentially ore-bearing Ernest Henry-style fluid appears to have contributed to the MFC magnetite geochemistry.

7.6. POSSIBLE VECTORS TOWARDS Fe OXIDE (Cu-Au) MINERALISATION

Exploration for IOCG deposits in the EFB and elsewhere has largely relied on interpretation of aeromagnetic signatures, due to the apparent close spatial and temporal association between Cu-Au mineralisation and magnetite. Three of the major deposits in the EFB (Ernest Henry, Osborne and Eloise) were all discovered within, or peripheral to, major magnetic anomalies (Adshead, 1995; Baker, 1998; Mark et al., 1999). However, each deposit exhibits unique physical and chemical characteristics that make the development of a single, unified model explaining the formation of, and vectors towards, potential exploration targets extremely difficult. In particular, detailed research into the paragenetic and physicochemical characteristics associated with these deposits has revealed that the development of Fe oxide-rich rocks may not be a prerequisite for Cu-Au mineralisation (e.g. Eloise; chapter 5), highlighted by the occurrence of barren Fe oxide-rich rocks throughout the district (e.g. MFC, Roxmere ironstone).

This study has shown that a number of different processes manufactured Fe oxide-rich rocks in the district, but all were linked to Cu-Au mineralisation. Fe oxide-rich rocks formed by orthomagmatic and sedimentary processes are less likely to be involved in the formation of IOCG deposits, except possibly as a reactive host similar to the early Fe oxide-rich rocks hosting the Starra and Osborne deposits (Adshead, 1995; Rotherham, 1997) (These comprise two of the three largest deposits in the EFB).

Instead, Fe oxide-rich rocks formed from hydrothermal (infill and/or replacement) processes are more likely to be related to the formation of IOCG deposits, either as a direct precipitant synchronous with Cu-Au mineralisation (e.g. Ernest Henry; Mark et al., 1999), as a reactive host (e.g. Starra; Rotherham, 1997) or precipitated peripheral to the site of ore deposition (e.g. K-Fe alteration at Ernest Henry and Starra; Rotherham, 1997, Mark et al., 1999). Fe oxide-rich rocks formed from primary and hydrothermal processes can be discriminated by their REE and immobile element concentrations (described above), and can thus be used to better define potential exploration targets.

One common theme regarding most IOCG deposits in the EFB is their spatial relationship to magmatic intrusions. Numerous models have been put forward regarding the role played by intrusions as the source of fluids and metals associated with Cu-Au mineralisation (Barton and Johnson, 2000; Haynes, 2000; Pollard, 2000; chapter 5). Perring et al (2000), Pollard (2000) and Williams and Skirrow (2000) favoured a magmatic source for Na-Ca alteration and Cu-Au mineralisation. The distal relationship between IOCG deposits and igneous intrusions suggests a strong temperature dependence on the precipitation of sulphides from highly saline fluids. Mount Elliott represents a deposit where igneous intrusions are spatially related to ore. Early skarn development at Mount Elliott is associated with diopside-scapolite assemblages, and is overprinted by a later actinolite-dominant skarn-forming event related to the main phase of Cu-Au mineralisation. This paragenetic sequence mirrors the hydrothermal activity documented at FC4NW, where sulphide mineralisation is also related to a later actinolite-dominant event, which overprints the earlier clinopyroxene-rich Na-Ca alteration. These relationships strengthen the argument that magmatic intrusions play an integral part in the formation of IOCG deposits in the EFB, and that sulphide mineralisation is most likely due to occur along down-temperature fluid flow paths.

The mass transfer patterns associated with sulphide-bearing Na-Ca veins at FC12 differ significantly from regional Na-Ca assemblages (Oliver and Bons, 2001; Rubenach and Lewthwaite, 2002; Oliver et al., 2004). This is illustrated in figure 3.11, where FC12 appears to represent a ‘halfway’ zone between regional Na-Ca alteration and Fe oxide (Cu-Au) mineralisation. In addition, fluid inclusions associated with clinopyroxene-rich and amphibole-rich Na-Ca alteration at FC4NW are chemically very similar to regional assemblages at Mount Angelay. Thus, sulphide-bearing Na-Ca alteration at

FC12 and FC4NW is interpreted to be temporally related to pre-mineralisation Na-Ca alteration at Ernest Henry, and pre-dated the main Cu-Au mineralisation phase. Nevertheless, the presence of sulphides at both FC12 and FC4NW, in addition to the aforementioned geochemical patterns, suggests that the rocks at the FC4NW and FC12 prospects may represent the start of a depositional regime, where conditions (i.e. P, f_{o2}, and pH) were favourable for the precipitation of sulphides. Mass transfer associated with hydrothermal alteration peripheral to other deposits in the district may reveal similar patters which could be used to help track potential ore-forming fluids.

The chemical complexity of fluids associated with Cu-Au mineralisation is reflected in the trace element mineral chemistry. In particular, Mo, W and U were either more commonly detected or higher in magnetite associated with Cu-Au mineralisation. Ore magnetite also contains higher Mn and Sc compared to magnetite in other mineral assemblages. Importantly, the marble matrix breccia footwall at Ernest Henry exhibits similar V, Cr and Mn in magnetite and As, Se and Ti in pyrite as in ore associated equivalents at Ernest Henry suggesting a genetic link. Ni concentrations in oxides and sulphides in the Na-Ca alteration domain at FC4NW are high relative to regional Na-Ca alteration and may also represent a vector to ore. The chemical complexity of Cu-Au ore suggests that either parent fluids were more chemically complex, perhaps implicating fluid mixing, and/or the physicochemical conditions were more favourable for the precipitation of minerals containing Mo, U and W. In either case, these characteristics may point to an alternative magmatic source compared to fluids associated with other mineral assemblages. The mineral chemistry of Fe oxides and Fe sulphides may be used to help track alteration haloes directly associated with Cu-Au mineralised systems (e.g. marble matrix breccia at Ernest Henry), providing broader targets for exploration.

7.7. RECOMMENDATIONS FOR FUTURE RESEARCH

The following recommendations are made for future research regarding the relationship between Fe oxide-rich rocks and Cu-Au mineralisation.

1. Determine the mass transfer patterns associated with alteration peripheral to other deposits in the district. If similar patterns are found, then these may also

represent proximal 'depositional regimes', providing broader targets around ore-forming systems.

2. Geochemically characterize samples from other Fe oxide-rich rocks around the district with the aim of building a more thorough database categorising the different types of Fe oxide-rich rocks found in the EFB. This data will give a better understanding of the role played by Fe oxide-rich rocks in the formation of IOCG deposits.

3. It is recommended that type 1 fluid inclusions from FC4NW should undergo further laser Raman and PIXE analysis as the current dataset is too small, and more analyses are required for a rigorous interpretation of their relationship to surrounding alteration phases and Cu-Au mineralisation at Ernest Henry.

4. Continue the trace element characterization of magnetite, hematite, pyrite and chalcopyrite from various mineral associations in the EFB. In particular, undergo a systematic mineral geochemical study of different alteration phase's peripheral to the other major Cu-Au deposits. This should also be combined with whole-rock geochemistry to get a obtain a understanding of the role played by the composition of the host rocks on the trace element content of magnetite, hematite, pyrite and chalcopyrite, and fluid inclusion studies (PIXE and microthermometry) to more confidently determine to what degree fluid chemistry controls the trace element concentration of different minerals in various mineral associations.